

**Dynamic forcing of oxygen, iron, and manganese fluxes at the sediment-water  
interface in lakes and reservoirs**

Lee Davis Bryant

Dissertation submitted to the Faculty of the  
Virginia Polytechnic Institute and State University  
In partial fulfillment of the requirements for the degree of  
Doctor of Philosophy  
in  
Civil Engineering

John C. Little, co-Advisor

Alfred Wüest, co-Advisor

Peter Berg

Matthew J. Eick

Daniel F. McGinnis

Peter J. Vikesland

March 23, 2010

Blacksburg, Virginia

Keywords: Sediment, water, turbulence, diffusive flux, iron, manganese, oxygenation

Copyright © 2010, Lee Davis Bryant

# **Dynamic forcing of oxygen, iron, and manganese fluxes at the sediment-water interface of lakes and reservoirs – Abstract**

by Lee Davis Bryant

The National Research Council recently called for a more interdisciplinary approach to drinking water research to address the critical issue of global drinking water supplies. Hypolimnetic oxygenation systems (HOx) are being increasingly used to improve water quality in stratified reservoirs by increasing dissolved oxygen ( $O_2$ ) concentrations and subsequently suppressing the release of soluble species such as iron (Fe) and manganese (Mn) from the sediment into the water. However, while the influence of HOx on the water column has been established, little work has been done on how oxygenation affects sediment  $O_2$  uptake (i.e., sediment oxygen demand) and other sediment-water fluxes. In response to the growing need for alternative approaches for improving water quality, we conducted highly interdisciplinary research to evaluate how  $O_2$ , Fe, and Mn cycling at the sediment-water interface is influenced by both natural and HOx-induced variations in water column dynamics, chemical redox processes, and microbial activity within the sediment, all of which may govern sediment-water fluxes. Studies were performed in an alpine lake in Switzerland and in an HOx-equipped drinking-water-supply reservoir in Virginia. This research was based on in situ field campaigns paired with laboratory experiments, microbial analyses, and computer simulation to elucidate variable sediment  $O_2$  uptake and corresponding Fe and Mn cycling. This work is unique in that sediment-water fluxes were assessed using in situ data from both sides of the sediment-water interface.

Results show that sediment  $O_2$  uptake flux is strongly controlled by both wind- and HOx-induced dynamic forcing. Our findings reveal that Fe and Mn fluxes were suppressed from the bulk hypolimnion via biogeochemical cycling in the oxic benthic region. Results also indicate that the sediment microbial community structure may directly respond to HOx-induced variation in sediment  $O_2$  availability. Additionally, based on an analysis of the robustness of several commonly used methods for flux calculations, we show that flux estimates are not strongly dependent on the method chosen for analysis. Ultimately, by emphasizing the highly transient nature of sediment  $O_2$  uptake, this research will aid in accurate characterization of various sediment-water fluxes and corresponding water quality. Our results will also directly contribute to the optimization of HOx operations and lake and reservoir management.

## Acknowledgements

I am extremely grateful to my co-advisors John Little and Alfred Johnny Wüest. Without their help, support, and friendship this would not have been possible. I am also very thankful for my committee members, Peter Berg, Matt Eick, Dan McGinnis, and Peter Vikesland, who have provided invaluable advice and encouragement.

I would like to express sincere appreciation to Kevin Elam, Vickie Singleton, Lindsay Olinde, Jeff Booth, and the entire staff at Spring Hollow and Carvins Cove Reservoir treatment plants for their assistance and patience both in the field and in the laboratory. I would like to thank Helmut Bürgmann for his guidance with microbial work. I am also very grateful to Julie Petruska, Claudia Lorrain, George Filz, Andreas Brand, and Helen Hsu-Kim for their support throughout my doctoral work. I especially want to thank Paul Gantzer and Liz Rumsey for their extensive help with equipment design and field work and for their friendship.

Finally, I am so very thankful to my family and friends for their endless supply of love, support, and encouragement.

Financial support for this project came from the U.S. Environmental Protection Agency (Science to Achieve Results (STAR) fellowship), the National Science Foundation (NSF Graduate Education and Research Traineeship (IGERT) fellowship), the U.S. Department of Education (Graduate Assistance in Areas of National Need (GAANN) fellowship), Virginia Tech Via Civil and Environmental Engineering Department (Via fellowship), and the Western Virginia Water Authority (WVWA).

# Table of Contents

<b>Abstract.....</b>	<b>ii</b>
<b>Acknowledgements .....</b>	<b>iii</b>
<b>List of Tables .....</b>	<b>ix</b>
<b>List of Figures.....</b>	<b>xi</b>
<b>Author’s preface and attributions.....</b>	<b>xv</b>
<b>Chapter 1 – Executive summary on biogeochemical cycling of O<sub>2</sub>, Fe, and Mn and drinking water quality.....</b>	<b>1</b>
1.1 Introduction .....	1
1.2 Research significance .....	2
1.3 Scope and objectives .....	4
1.4 Conclusions .....	5
1.5 References .....	6
<b>Chapter 2 – Variable sediment oxygen uptake in response to dynamic forcing.....</b>	<b>10</b>
2.1 Abstract.....	10
2.2 Introduction .....	11
2.3 Methods .....	13
2.3.1 Study site and in situ instrumentation.....	13
2.3.1.1 ADV velocity measurements .....	14
2.3.1.2 ADP velocity measurements.....	14
2.3.1.3 O <sub>2</sub> and temperature logger measurements .....	14
2.3.1.4 Microsensor O <sub>2</sub> and temperature measurements across SWI .....	15
2.3.2 O <sub>2</sub> uptake and DBL analyses .....	16
2.3.3 Inertial dissipation analyses .....	19
2.3.4 Friction velocity analyses .....	20
2.4 Results .....	21
2.4.1 Seiche dynamics.....	21
2.4.2 Temperature and O <sub>2</sub> distribution.....	22
2.4.3 O <sub>2</sub> flux and $\delta_{DBL}$ .....	23
2.4.4 Sediment oxic zone.....	24

2.4.5 Profile dynamics .....	24
2.5 Discussion.....	25
2.5.1 Forcing of O <sub>2</sub> distribution .....	25
2.5.2 Variations in sediment O <sub>2</sub> consumption .....	26
2.5.3 Scale of variation .....	28
2.6 Conclusion.....	29
2.7 Acknowledgements .....	30
2.8 References .....	31

**Chapter 3 – Evaluating oxygen fluxes from both sides of the sediment-water interface .....48**

3.1 Abstract.....	48
3.2 Introduction .....	49
3.3 Materials and procedures.....	51
3.3.1 Study site and in-situ instrumentation.....	51
3.3.2 Turbulence analyses.....	51
3.3.3 Friction velocity analyses .....	52
3.3.4 Methods for J <sub>O<sub>2</sub></sub> analyses .....	52
3.3.4.1 Direct method.....	54
3.3.4.2 u* method .....	54
3.3.4.3 Curvefit method .....	55
3.3.4.4 Zonefit method.....	55
3.3.4.5 Model method .....	56
3.4 Assessment .....	57
3.4.1 Dynamic forcing of O <sub>2</sub> distribution .....	57
3.4.2 Comparison of results .....	58
3.4.3 Evaluation of each method.....	59
3.4.3.1 Direct method.....	59
3.4.3.2 u* method .....	60
3.4.3.3 Curvefit method .....	61
3.4.3.4 Zonefit method.....	62
3.4.3.5 Model method .....	63

3.5 Discussion.....	63
3.5.1 Water-side versus sediment-side.....	63
3.5.2 Sediment O <sub>2</sub> consumption.....	67
3.6 Comments and recommendations.....	68
3.7 Acknowledgements .....	70
3.8 References .....	70
<b>Chapter 4 – Oxygenation-induced variation in sediment oxygen uptake.....</b>	<b>84</b>
4.1 Abstract.....	84
4.2 Introduction .....	85
4.3 Materials and methods.....	87
4.3.1 Study site.....	87
4.3.2 Data collection and analysis.....	88
4.3.2.1 O <sub>2</sub> microprofiles.....	88
4.3.2.2 Current velocity .....	89
4.3.2.3 O <sub>2</sub> microprofile analyses.....	90
4.3.2.3 Turbulence estimations .....	91
4.4 Results and discussion.....	93
4.4.1 Vertical O <sub>2</sub> distribution at SWI.....	93
4.4.2 HOx flow and current velocity .....	95
4.4.3 HOx-induced variation in sediment O <sub>2</sub> uptake .....	96
4.4.4 J <sub>O<sub>2</sub></sub> as a function of flow rate.....	97
4.4.5 Effect of HOx on sediment O <sub>2</sub> availability.....	98
4.4.6 Influence of HOx proximity.....	100
4.4.7 Effect on source water quality .....	102
4.5 Conclusions .....	103
4.6 Acknowledgements .....	104
4.7 References .....	104
<b>Chapter 5 – Biogeochemical cycling of iron and manganese at the sediment-water interface in response to hypolimnetic oxygenation .....</b>	<b>121</b>
5.1 Abstract.....	121
5.2 Introduction .....	122

5.3	Materials and methods.....	123
5.3.1	Study site and instrumentation.....	123
5.3.1.1	O <sub>2</sub> profiles at the SWI.....	124
5.3.1.2	Fe and Mn profiles at the SWI.....	126
5.3.1.3	Water sample measurements.....	127
5.3.1.4	Bulk sediment measurements .....	127
5.3.2	Flux analyses.....	127
5.4	Results and discussion.....	129
5.4.1	Sediment-water vertical Fe and Mn distribution .....	129
5.4.2	Fe and Mn response near the SWI .....	129
5.4.3	HOx-induced variation in J <sub>O<sub>2</sub></sub> , J <sub>Fe</sub> , and J <sub>Mn</sub> .....	131
5.4.4	Amount of J <sub>O<sub>2</sub></sub> allocated to J <sub>Fe</sub> and J <sub>Mn</sub> suppression.....	133
5.4.5	Biogeochemical cycling effects .....	134
5.4.6	Influence of HOx on bulk sediment.....	135
5.4.7	Effect of J <sub>Fe</sub> and J <sub>Mn</sub> on water column .....	137
5.5	Conclusions .....	139
5.6	Acknowledgements .....	140
5.7	References .....	140
<b>Chapter 6 – Variations in sediment microbial community structure in response to hypolimnetic oxygenation.....</b>		<b>159</b>
6.1	Abstract.....	159
6.2	Introduction .....	160
6.3	Materials and procedures.....	161
6.3.1	Study site and instrumentation.....	161
6.3.2	Analytical methods .....	161
6.3.2.1	Nucleic acid extraction from CCR sediment .....	162
6.3.2.2	DNA quantification with PicoGreen.....	162
6.3.2.3	Nucleic acid amplification via PCR.....	162
6.3.2.4	Community composition via RISA.....	163
6.3.2.5	Correlation to CCR geochemical data .....	163
6.3.2.6	Identification of Mn-oxidizers via LBB .....	164

6.4 Results and discussion.....	164
6.4.1 Relative concentrations of DNA.....	164
6.4.2 Phylogenic hierarchy .....	165
6.4.3 Correlation between microbial community structure, geochemical cycling, and HOx operation.....	165
6.4.4 Presence of metal-oxidizers and reducers.....	167
6.5 Conclusions .....	168
6.6 Acknowledgements .....	169
6.7 References .....	170
<b>Chapter 7 – Global impacts and future work .....</b>	<b>182</b>
7.1 Global impacts.....	182
7.2 Future work .....	183
7.3 References .....	184
<b>Appendix A – Supporting data for Chapter 4.....</b>	<b>185</b>
<b>Appendix B – Supporting data for Chapter 5.....</b>	<b>188</b>
<b>Appendix C – Microbial method procedures .....</b>	<b>192</b>
C.1 Nucleic acid extraction .....	193
C.2 DNA quantification with PicoGreen.....	196
C.3 PCR program .....	197
<b>Appendix D – Copyright permission.....</b>	<b>199</b>

## List of Tables

### Chapter 2

Table 2.1 Acronyms and notations with corresponding units used for this study .....	36
Table 2.2 Mean estimates of friction velocity ( $u^*$ ), energy dissipation rate ( $\varepsilon$ ), and intermittency ( $\sigma_{ln(\varepsilon)}$ ) of $\varepsilon$ .....	37
Table 2.3 Results of the five analytical methods used for sediment $O_2$ uptake rate ( $J_{O_2}$ ) and diffusive boundary layer thickness ( $\delta_{DBL}$ ) calculations.....	38
Table 2.4 Average $J_{O_2}$ and vertically-integrated areal rates of change in the $O_2$ concentration over time ( $\partial C/\partial t_a$ ), areal sediment $O_2$ consumption rates ( $R_{O_2a}$ ), and mass of $O_2$ ( $M_{O_2}$ ) in the sediment .....	39

### Chapter 3

Table 3.1 Frequently-used acronyms and notations .....	76
Table 3.2 Average sediment oxygen uptake rate ( $J_{O_2}$ ), average diffusive boundary layer thickness ( $\delta_{DBL}$ ), and corresponding distributions of results ( $\pm$ as compared with averages) based on estimates from all five methods, water-side ( <i>direct</i> and $u^*$ ) and sediment-side ( <i>curvefit</i> , <i>zonefit</i> , and <i>model</i> ) approaches .....	77

### Chapter 4

Table 4.1 Average results for sediment oxygen uptake rate ( $J_{O_2}$ ), dissolved oxygen ( $O_2$ ) at the sediment-water interface ( $C_{SWI}$ ), and sediment oxic zone depth ( $z_{max}$ ) used for correlations between hypolimnetic oxygenation system (HOx) flow rate and $J_{O_2}$ (Fig. 4.8) and $z_{max}$ (Fig. 4.10) .....	109
Table 4.2 Spatial variation in average $J_{O_2}$ and areal sediment $O_2$ consumption rate ( $R_{O_2a}$ ) during summer 2008 .....	110

### Chapter 5

Table 5.1 Estimation of proportion of measured sediment $O_2$ uptake rate ( $J_{O_2}$ ; based on microprofile data) utilized for oxidation of iron (Fe) and manganese (Mn) fluxes ( $J_{Fe}$ and $J_{Mn}$ ; based on peeper data) .....	146
---	-----

### Chapter 6

Table 6.1 Sediment sampling strategy and nomenclature used in microbial analytical techniques .....	173
---	-----

**Appendix B**

Table B.1 Comparison of sediment core and in situ MP4 microprofiler data from  
summer 2007.....189

## List of Figures

### Chapter 2

Figure 2.1 The key components of a dissolved oxygen ( $O_2$ ) profile are defined, illustrating the relationship between seiche, turbulent mixing, and the vertical distribution of $O_2$ on both sides of the sediment-water interface (SWI; modified from Jørgensen and Revsbech 1985).....	40
Figure 2.2 (a) The measured longitudinal velocity spectrum $\varphi_{11}$ (with $k^{-5/3}$ slope characteristic in the inertial subrange) is multiplied by $k^{5/3}$ to be independent of wavenumber $k$ . The constant value of $\varphi_{11} \times k^{5/3}$ , indicated by the horizontal bar, is used to calculate the mean energy dissipation ( $\varepsilon$ ). (b) Dissipation rates ( $\varepsilon$ ) calculated by inertial dissipation method using longitudinal, planar, and vertical velocity data as measured via acoustic Doppler velocimeter (ADV).....	41
Figure 2.3 (a) Seiche cycle in Lake Alpnach and location of experiment site during 27 – 28 Aug 07 campaign. (b) East and north velocity components at 10 cm above the sediment as measured by the ADV .....	42
Figure 2.4 Temperature and $O_2$ data obtained on 27 – 28 Aug 07 .....	43
Figure 2.5 $O_2$ microprofiles obtained at approximately 50-min intervals relative to the ADV velocity time series.....	44
Figure 2.6 Correlation between $\varepsilon$ and sediment $O_2$ uptake rate ( $J_{O_2}$ ) .....	45
Figure 2.7 Time series of current velocity, turbulence (as defined by $\varepsilon$ ), and $\delta_{DBL}$ showing close correlation between all three parameters with only a slight phase lag (on the order of minutes) between velocity and $\varepsilon$ .....	46
Figure 2.8 PROFILE model results defining zones of varying volumetric sediment $O_2$ consumption rates ( $R_{O_2v}$ ) for periods of active and inactive turbulence as characterized by $\varepsilon$ in (a) .....	47

### Chapter 3

Figure 3.1 Components of a dissolved oxygen ( $O_2$ ) profile (a) and the five analytical methods (b-f) used to estimate sediment $O_2$ uptake rate ( $J_{O_2}$ ) and diffusive boundary layer thickness ( $\delta_{DBL}$ ) are detailed using a sample $O_2$ profile (profile 14, obtained at 08:16 h on 28 Aug 07) .....	78
Figure 3.2 (a) Time series of $J_{O_2}$ , energy dissipation ( $\varepsilon$ ), and friction velocity ( $u_*$ ) as a function of $O_2$ profile number. (b) Turbulence-induced variations in the vertical $O_2$ distribution (as characterized by $\delta_{DBL}$ and $z_{max}$ ) on both sides of the SWI.....	80

Figure 3.3 Comparison of analytical method results for (a) $J_{O_2}$ and (b) $\delta_{DBL}$ for all 14 profiles .....	81
Figure 3.4 The universal scaling law (Fig. 3.1c) could be fit with the <i>u* method</i> to a majority of our $O_2$ profiles, e.g., profile 3 in (a).....	82
Figure 3.5 Relationship between $O_2$ Batchelor length scale ( $L_B$ ) and $\delta_{DBL}$ .....	82
Figure 3.6 $R_{O_2v}$ as predicted by the <i>zonefit method</i> (PROFILE; based on zero-order kinetics; green) and the <i>model method</i> (AQUASIM; based on Monod kinetics; red).....	83

## Chapter 4

Figure 4.1 Map of Carvin’s Cove Reservoir (CCR) showing sampling sites (near-field locations CC and CVCB; central, mid-reservoir locations CE, C1, C2, and C3; back-reservoir location CR) and linear bubble-plume hypolimnetic oxygenation system (HOx).....	111
Figure 4.2 Variations in oxygen flow during CCR HOx operations in 2007 and 2008 .....	112
Figure 4.3 Summary of in situ dissolved oxygen ( $O_2$ ) profile data obtained at the sediment-water interface (SWI) with the MP4 microprofiler during the August 2008 campaign at C3 .....	113
Figure 4.4 Contour plots of $O_2$ levels at the SWI (a; MP4 $O_2$ microsensor data), in the water overlying the sediment (b; MP4 $O_2$ microsensor data), and in the hypolimnion (c; CTD (conductivity-temperature- $O_2$ as a function of depth) profile data).....	114
Figure 4.5 Variations in $O_2$ levels at the SWI ( $C_{SWI}$ ), at 5 cm above the SWI ( $C_5$ ), and within the sediment (as characterized by sediment oxic zone depth $z_{max}$ ) in response to turning off the HOx.....	115
Figure 4.6 Current velocity time series (as measured via acoustic Doppler current profiler; ADCP) in relation to HOx flow during the August 2008 C3 campaign.....	116
Figure 4.7 The response of $J_{O_2}$ and the vertical $O_2$ distribution at the SWI (a; as characterized by diffusive boundary layer thickness ( $\delta_{DBL}$ ) and $z_{max}$ ) to turning off the HOx corresponds directly to variations in near-sediment mixing (b) as characterized by current velocity (obtained via ADCP) and turbulence (defined by energy dissipation rate $\epsilon$ , which was estimated as a function of water-side $\delta_{DBL}$ ).....	117
Figure 4.8 Variation in $J_{O_2}$ as a function of HOx flow rate .....	118
Figure 4.9 Correlation between $J_{O_2}$ and both $C_{SWI}$ (a) and $C_5$ (b) .....	119
Figure 4.10 Variation in $z_{max}$ as a function of HOx flow rate.....	120

## Chapter 5

Figure 5.1 Map of Carvin’s Cove Reservoir (CCR) showing locations of the seven sampling sites (CC, CVCB, CE, C1, C2, C3, and CR) and the hypolimnetic oxygenation system (HOx).....	147
Figure 5.2 Profiles of soluble iron (Fe) and manganese (Mn) at the sediment-water interface (SWI) were obtained using in situ porewater analyzers (peepers) .....	148
Figure 5.3 Contour plots based on peeper data obtained near the HOx at site CC in 2006 (a and d) and at site CVCB in 2007 (b and e) and 2008 (c and f).....	149
Figure 5.4 Total and soluble Fe and Mn data obtained from near-sediment core water samples collected throughout 2006 HOx operations .....	150
Figure 5.5 Correlation between near-sediment Fe and Mn levels (as characterized by sediment core water sample data), HOx flow, and dissolved oxygen (O <sub>2</sub> ) levels at the SWI (as characterized by MP4 microprofile data) during the August 2008 campaign at C3 .....	151
Figure 5.6 Time series of sediment O <sub>2</sub> uptake rate (J <sub>O<sub>2</sub></sub> ), diffusive fluxes of soluble Fe and Mn (J <sub>Fe</sub> and J <sub>Mn</sub> , respectively) at the SWI, and HOx flow rate both near the HOx (a; site CVCB) and mid-reservoir (b; site C3) .....	152
Figure 5.7 Evaluation of the proportion of measured J <sub>O<sub>2</sub></sub> utilized for oxidation of reduced Fe and Mn (based solely on diffusive fluxes J <sub>Fe</sub> and J <sub>Mn</sub> ; the additional influence of microbial and surface-mediated processes were not taken into account) .....	153
Figure 5.8 Correlation between J <sub>Mn</sub> , HOx flow, and Mn concentrations directly at the SWI, 1 m above the sediment (benthic region), and 4 m above the sediment (mid-hypolimnion).....	154
Figure 5.9 The effect of near-sediment biogeochemical cycling was evaluated using a mass balance based on J <sub>Mn</sub> (a), J <sub>Fe</sub> (b), and average volume of the benthic region (1m depth) and the average hypolimnion (7m depth) .....	155
Figure 5.10 Bulk sediment total Fe and Mn data, soluble Fe and Mn concentrations at the SWI (peeper data), and corresponding sediment O <sub>2</sub> conditions as characterized by depth of the sediment oxic zone (z <sub>max</sub> ) and O <sub>2</sub> concentration 5 cm above and directly at the SWI (microprofile data) .....	156
Figure 5.11 Time series of total organic carbon (TOC), total Fe, and total Mn in bulk sediment characterizing the near field region from before CCR HOx operations began in 2005 through 2008 (no data collected in 2007) .....	157
Figure 5.12 The influence of fall turnover as compared to HOx on total and soluble Fe and Mn concentrations in the lower hypolimnion and average hypolimnetic O <sub>2</sub> .....	158

## Chapter 6

Figure 6.1 Map of Carvin’s Cove Reservoir (CCR) showing sampling sites for microbial analyses (near field locations CC and CVCB; central, mid-reservoir locations C1, C2, C3, and CE; back-reservoir location CR) and linear bubble-plume hypolimnetic oxygenation system (HOx) .....	174
Figure 6.2 Oxygen flow rates of the CCR HOx and dates of sediment core sampling ..	175
Figure 6.3 Gel image of ribosomal intergenic spacer analysis (RISA) of rRNA isolated from CCR sediment showing variable banding patterns indicating different sediment bacteria phylotypes .....	176
Figure 6.4 Nucleic-acid-concentration data obtained via PicoGreen analyses.....	177
Figure 6.5 Average linkage hierarchical cluster analysis of community similarity (Raup-Crick distances) of CCR sediment samples based on presence-absence data of RISA phylotypes.....	178
Figure 6.6 Biplots of ordination analysis of the RISA community dataset and environmental variables.....	179
Figure 6.7 Constrained CCA ordination including all environmental (geochemical) variables .....	180
Figure 6.8 Constrained CCA ordination specifically for site CC which includes soluble Fe and Mn data obtained via in situ porewater analyzer (peeper) .....	181

## Appendix A

Figure A.1 Correlation between diffusive boundary layer thickness ( $\delta_{DBL}$ ) estimates obtained using in situ water-side ( $\delta_{DBL-W}$ ) and sediment-side ( $\delta_{DBL-S}$ ) oxygen ( $O_2$ ) microprofile data.....	186
Figure A.2 Comparison of near-sediment current velocity and wind speed time series	186
Figure A.3 Correlation between $J_{O_2}$ and water-side $\delta_{DBL}$ based on in situ MP4 data from 2007-2008 .....	187

## Appendix B

Figure B.2 Contour plots based on peeper data obtained mid-reservoir (site C3) and corresponding HOx flow pattern during 2007 and 2008 .....	190
Figure B.3 Total and soluble Fe and Mn data obtained from near-sediment core water samples collected throughout 2008 HOx operations .....	191

## **Author's preface and attributions**

This dissertation is a compilation of five manuscripts included as separate chapters spanning multiple disciplines. Primary fields of applications include aquatic science research, sediment-water flux analysis, and lake and reservoir management. Each manuscript is intended to stand alone and includes a comprehensive introduction and review of the scientific literature specific to the manuscript topic. Co-authors, acknowledgements, and an abstract summarizing results are provided for each manuscript chapter.

All five of the manuscripts presented as chapters in this dissertation are intended for publication. Chapter 2 has been published as a scientific article in *Limnology & Oceanography*. Chapter 3 was recently submitted for publication as a companion methods evaluation in *Limnology & Oceanography: Methods*. Chapters 4 and 5 are currently in preparation for submission to *Water Research*. Additional microbial analyses supporting Chapter 6 will be performed as part of the author's post-doctoral work to finalize this manuscript for publication.

Chapters 4 and 5, which characterize the influence of hypolimnetic oxygenation on sediment-water fluxes and corresponding water quality, are companion papers to studies performed by Gantzer et al. (2009a,b) that focused specifically on the water column. Overall effects of oxygenation on source water quality are hence evaluated in Chapters 4 and 5 predominantly from a sediment-side perspective and by Gantzer et al. (2009a,b) from a water-side perspective. Furthermore, Chapters 4 and 5 are intended to serve as scientific and conceptual studies of oxygenation-induced variation in physical and chemical controls on sediment-water fluxes while the companion works by Gantzer et al. are meant to provide a more applied perspective to oxygenation operations. These combined studies will hopefully contribute significantly to lake and reservoir management and optimization of oxygenation systems for improved water quality and aquatic ecosystem health.

### **Attributions**

Several colleagues contributed to the research presented in this dissertation. A brief description of their background and their contributions are included here. Ms. Lee Bryant (doctoral candidate) and Dr. John Little (Professor, Civil & Environmental Engineering Dept.,

Virginia Tech; co-Advisor and Committee co-Chair) contributed to every chapter and therefore their specific contributions will not be discussed in detail.

Chapters 2 and 3: Dr. Alfred Wüest (Professor and Group Leader of Aquatic Physics, Surface Waters Dept., Swiss Federal Institute for Aquatic Science and Technology (Eawag), co-Advisor and Committee co-Chair) helped develop the research intellectually, provided insight on data analysis, and reviewed the manuscripts extensively before submission. Ms. Claudia Lorrai (doctoral candidate, Surface Waters Dept., Eawag) performed turbulence analyses, provided guidance on turbulence interpretation, and assisted with figures. Dr. Daniel McGinnis (Research scientist, Marine Biogeochemistry Dept., IFM-GEOMAR Leibniz Institute of Marine Sciences) also assisted in turbulence interpretation and with figures. Dr. Andreas Brand (Post-doctoral scientist, Civil & Environmental Engineering Dept., University of California, Berkeley) developed and provided guidance on the AQUASIM numerical model used in these chapters. Ms. Lorrai and Drs. McGinnis and Brand also reviewed the manuscripts prior to submission. Dr. Peter Berg (Professor, Dept. of Environmental Science, University of Virginia) developed and provided guidance on the PROFILE numerical model used in this research.

Chapters 4 and 5: Dr. Paul Gantzer (Gantzer Water Resources LLC) obtained water column data and performed supporting analyses. The Western Virginia Water Authority staff at Spring Hollow Treatment plant performed laboratory analyses for water and sediment samples.

Chapter 6: Dr. Helmut Bürgmann (Professor and Group Leader of Microbial Ecology, Surface Waters Dept., Eawag) contributed by providing instruction on microbial analytical methods, statistically analyzing data, and reviewing the document. Ms. Mary-Theresa Pendergast performed Leukoberbelin Blue (LBB) analyses and assisted in evaluating LBB results.

## **References**

- Gantzer, P. A., L. D. Bryant, and J. C. Little. 2009a. Effect of hypolimnetic oxygenation on oxygen depletion rates in two water-supply reservoirs. *Water Res.* **43**:1700-1710.
- Gantzer, P. A., L. D. Bryant, and J. C. Little. 2009b. Controlling soluble iron and manganese in a water-supply reservoir using hypolimnetic oxygenation. *Water Res.* **43**: 1285-1294.

# Chapter 1 – Executive summary on biogeochemical cycling of O<sub>2</sub>, Fe, and Mn and drinking water quality

## 1.1 Introduction

In response to the growing water crisis, the National Research Council (NRC) recently called for a more interdisciplinary approach to drinking water research. As the limitations of discipline-specific perspectives have become apparent in light of the pending water crisis, scientists and utilities have come to realize that truly successful solutions cannot be adequately addressed within the traditional confines of solitary disciplines but must be based on novel approaches and collaborations that merge physical, chemical, biological, and social science boundaries (NRC 2004). Alternative approaches for improving water quality are being explored to address the critical issue of global drinking water supplies. Our research largely focused on improving water quality via hypolimnetic oxygenation systems (HO<sub>x</sub>) which are being increasingly used in stratified reservoirs to elevate dissolved oxygen (O<sub>2</sub>) concentrations in the hypolimnion (bottom water) and thereby suppress the release of manganese (Mn), iron (Fe), and other soluble metals from the sediment (Beutel 2003; Gantzer et al. 2009a,b). Mn and Fe enter lakes, groundwater, and other water bodies as a result of O<sub>2</sub> depletion, which leads to reductive dissolution of metal-oxides in the sediment and a flux of reduced, soluble metals into the water. Release of metals from the sediment to the water column is one of the most common natural sources of increased metal concentrations in reservoirs, particularly during periods of hypolimnetic hypoxia.

Mn specifically is becoming a serious problem for water treatment on a global scale (Kohl and Medlar 2006). Although Mn is regulated in drinking water for aesthetic reasons (odor, taste, color), neurological health risks associated with excess Mn in drinking water are now emerging for populations in the U.S. and around the world (Wasserman et al. 2006; Buschmann et al. 2007; Hafeman et al. 2007; Walker et al. 2007). Wasserman et al. (2006) found that children in Bangladesh who had been exposed to drinking water with Mn levels > 3 mg L<sup>-1</sup> had lower IQ scores than children not exposed to increased levels of Mn. Taking into consideration these neurotoxic concerns and the fact that approximately 6% of U.S. household wells have been found to have Mn levels exceeding the EPA lifetime health advisory limit for

Mn in drinking water ( $0.3 \text{ mg L}^{-1}$ ), there is a strong possibility that some U.S. children may also be at risk for Mn-induced neurotoxicity (Walker et al. 2007). Additionally, treatment of source water with elevated Mn concentrations can be difficult and expensive due to the complexity of Mn redox kinetics (Balzer 1982; Nealson 1997). Although the removal of metals from source water during water treatment is feasible, the process is not always effective and requires the use of chemical oxidants that can react with naturally occurring organic matter to form carcinogenic compounds, thus posing serious health risks (Budd et al. 2007; Brandhuber and Clark 2008; Nattress 2008).

An HOx was installed in Carvins Cove Reservoir, one of the primary drinking water supply reservoirs for Roanoke, Virginia, in 2005 as a source-water management strategy to address Fe and Mn issues resulting from hypolimnetic hypoxia. Since installation of the Carvins Cove HOx, experiments have been performed to characterize the influence of HOx operations on source water quality, sediment  $\text{O}_2$  uptake, and soluble Fe and Mn fluxes at the sediment-water interface (SWI). An unusually holistic approach to drinking water treatment is used in this project that focuses on improving the quality of the source water prior to the treatment process. By improving the source water, the overall conditions of the aquatic ecosystem (e.g., trophic state, fish health, aquatic biodiversity, and reservoir appearance) are enhanced while drinking water quality is improved by increasing  $\text{O}_2$  and reducing metal concentrations entering the treatment plant. Although an engineering approach is typically used in designing and managing HOx, many of the factors controlling the success of source water oxygenation are in fact deeply rooted in limnology, sediment science, chemistry, aquatic physics, and microbiology. Our novel interdisciplinary research thus emphasizes the complex interactions between physical, chemical, and biological processes governing sediment-water fluxes and subsequent water quality.

## **1.2 Research significance**

The condition of water supplies in many regions of the world, including the U.S., is deteriorating and water may soon prove to be the most critical natural resource governing human and ecosystem health (Gleick 2003; NRC 2004; Lodge 2010). It has been established that oxygenation of surface waters can effectively improve water quality and reduce treatment costs (Geney 1988; Geney 1992; van der Tak et al. 1992; Beutel et al. 2007). However, HOx are

currently a relatively underused drinking water treatment method. This may be due to the fact that while the mechanisms of O<sub>2</sub> addition have been studied in great detail (McGinnis et al. 2004; Singleton and Little 2006; Gantzer et al. 2009a), the impacts of HOx on sediment O<sub>2</sub> uptake and soluble metal release have not been comprehensively evaluated.

Sediment O<sub>2</sub> uptake is a function of both physical limitations on O<sub>2</sub> transfer to the sediment and sediment O<sub>2</sub> consumption processes (e.g., benthic mineralization and re-oxidation of reduced species; Jørgensen and Boudreau 2001). Resolving the vertical distribution of O<sub>2</sub> at the SWI allows for quantification of the sediment O<sub>2</sub> uptake rate (J<sub>O<sub>2</sub></sub>), which is a fundamental parameter for the characterization of O<sub>2</sub> dynamics in aquatic systems (Wetzel 2001). Consequently, considerable effort has been devoted to elucidating the water-side and sediment-side factors controlling sediment O<sub>2</sub> uptake in freshwater and marine systems (Bouldin 1968; Jørgensen and Revsbech 1985; Boudreau 2001). Turbulence and O<sub>2</sub> levels in the lower hypolimnion have been shown to have a direct effect on O<sub>2</sub> transport to the sediment and subsequent O<sub>2</sub> consumption processes within the sediment (Lorke et al. 2003; Brand et al. 2009). However, recent work by Glud et al. (2009) has also shown that the vertical distribution of O<sub>2</sub> at the SWI and corresponding sediment O<sub>2</sub> consumption processes are much more dynamic than previously thought. Variable near-sediment turbulence and O<sub>2</sub> conditions (e.g., due to internal currents forced naturally by wind or mechanically by HOx) may have significant influence on sediment-water fluxes. Thus, while HOx are designed to suppress the release of reduced species from the sediment by elevating hypolimnetic O<sub>2</sub>, increased levels of near-sediment O<sub>2</sub> and turbulence could theoretically enhance sediment-water fluxes. Correspondingly, the failure of HOx to sufficiently oxygenate the bulk water in several reservoirs has been attributed to induced sediment O<sub>2</sub> uptake (Beutel 2003).

Therefore, we performed research based primarily on in situ measurements to investigate critical and often highly variable processes governing sediment O<sub>2</sub> uptake and Fe and Mn cycling at the SWI, with particular focus on the influence of wind- and HOx-induced changes in dynamic forcing. While it has been established by previous work that sediment-water fluxes are frequently controlled by physical transport limitations (e.g., diffusive boundary layer; Lorke et al. 2003), these studies have largely been theoretical or laboratory based (Mackenthun and Stefan 1998; Higashino et al. 2004; O'Connor and Hondzo 2008). To our knowledge, this is one of the first studies based on in situ data to assess how the vertical O<sub>2</sub> distribution at the SWI, sediment

O<sub>2</sub> uptake, and soluble metal fluxes vary in response to changes in near-sediment turbulence and O<sub>2</sub> levels. Additionally, while sediment-water fluxes are acknowledged to be influenced by both hydrodynamics and biogeochemical uptake processes within the sediment, these fluxes are almost always analyzed from either a water- or sediment-side perspective. This research expands on previous work by comparing water-side (hydrodynamics and resulting diffusive boundary layer thickness) and sediment-side (O<sub>2</sub> consumption and resulting sediment oxic zone) approaches for evaluating sediment-water flux.

### **1.3 Scope and objectives**

This doctoral research specifically investigated how O<sub>2</sub>, Fe, and Mn cycling at the SWI and corresponding water quality is influenced by variable water column dynamics, chemical redox processes, and microbial activity within the sediment. This work is unique in that it quantified processes controlling biogeochemical cycling on both sides of the SWI based on in situ sediment and water data. We used a research strategy that combined in situ field campaigns with laboratory experiments, microbial analyses, and computer simulation to elucidate sediment O<sub>2</sub> uptake and Fe and Mn cycling as a function of O<sub>2</sub> availability and turbulence.

Research investigating the effect of wind-induced (i.e., seiche) turbulence on sediment O<sub>2</sub> uptake was based on data obtained in Lake Alpnach, Switzerland. Lake Alpnach is characterized by steep O<sub>2</sub> gradients at the SWI due to relatively high J<sub>O<sub>2</sub></sub> and by basin-scale movements caused by daily alpine winds; thus, this was an ideal location for our research on natural dynamic forcing. Work focused on the influence of HO<sub>x</sub> on sediment-water fluxes used an innovative approach that employed a Virginia drinking-water-supply reservoir oxygenation system as an experimental tool to artificially control redox conditions within an otherwise entirely natural aquatic ecosystem. These field-scale facilities provided an opportunity to perform a real-world study of the interplay between sediment O<sub>2</sub> uptake, Fe and Mn biotransformation, and diffusive transport at the ecosystem level.

Specific objectives of this research were to:

- (1) Determine how seiche-induced turbulence affects sediment O<sub>2</sub> uptake rate (J<sub>O<sub>2</sub></sub>) on a very rapid (sub-hourly) time scale in an alpine freshwater lake (Chapter 2);

- (2) Evaluate five common analytical methods used to estimate  $O_2$  flux from both sides of the sediment-water interface (Chapter 3);
- (3) Quantify  $J_{O_2}$  and sediment  $O_2$  availability as a function of HOx operations in a drinking-water-supply reservoir (Chapter 4);
- (4) Identify how hypolimnetic oxygenation affects sediment-water fluxes of Fe and Mn, with particular focus on water-quality implications (Chapter 5);
- (5) Characterize how sediment microbial populations change as a function of HOx-induced variations in sediment  $O_2$  availability (Chapter 6).

## 1.4 Conclusions

Results from this interdisciplinary research provide important scientific, methodological, and practical contributions to a range of disciplines, with primary fields of application including aquatic science research, sediment-water flux analysis, and lake and reservoir management. Our evaluation of natural, wind-forced variation in turbulence revealed that  $J_{O_2}$  and corresponding  $O_2$  availability in the sediment is strongly controlled by dynamic forcing (Chapter 2). Results of this research highlight the importance of using multiple measurements to resolve average conditions at the SWI. Currently, single measurements evaluating  $J_{O_2}$  under conditions assumed constant are sometimes extrapolated to characterize an aquatic system, thereby ignoring the influence of intermittent hydrodynamic processes (Veenstra and Nolen 1991; Beutel 2003). Additionally, we show that while flux estimates are not strongly dependent on the method chosen for analysis, there are benefits and limitations involved with evaluating data from both the water- and sediment-side of the SWI (Chapter 3).

We expanded on these results via practical application in a local HOx-equipped drinking-water supply reservoir managed by the Western Virginia Water Authority (WVWA). Results of our HOx studies (Chapters 4-5), to our knowledge the first of their kind performed in situ, revealed a strong correlation between HOx use and increased  $J_{O_2}$  which verifies previous theoretical and laboratory studies (Moore et al. 1996; Beutel 2003). Furthermore, our findings show that while oxygenation did facilitate Fe and Mn flux out of the sediment, these fluxes were

suppressed from the bulk hypolimnion via biogeochemical cycling in the oxic benthic region. Supporting microbial analyses indicated that the sediment microbial community structure may directly respond to HO<sub>x</sub>-induced variation in sediment O<sub>2</sub> availability (Chapter 6). Ultimately, hypolimnetic Fe and Mn concentrations were significantly decreased by Carvins Cove HO<sub>x</sub> operations thereby supporting the viability of using oxygenation to control metal levels in source water (Chapters 4-5; Gantzer et al. 2009b).

By emphasizing the dynamic nature of sediment-water flux, our results will hopefully help shape future experiments in lakes and reservoirs. Results may also be used to improve operation of HO<sub>x</sub> installed around the world by providing mechanistic understanding of water-quality effects in relation to system operation. Specifically, HO<sub>x</sub> can be used to improve water quality on a broader scale by establishing the water-supply reservoir as the initial stage in the treatment process. HO<sub>x</sub> will become more important in the face of dwindling water supplies (e.g., in the western and southeastern U.S.) as water re-use and utilization of unconventional water supplies become more common.

## 1.5 References

- Balzer, W. 1982. On the distribution of iron and manganese at the sediment / water interface: thermodynamic versus kinetic control. *Geochem. Cosmochim. Acta* **46**: 1153-1161.
- Beutel, M. W. 2003. Hypolimnetic anoxia and sediment oxygen demand in California drinking water reservoirs." *Lake Reserv. Manage.* **19**: 208-221.
- Beutel, M. W., I. Hannoun, J. Pasek, and K. Bowman Kavanagh. 2007. Evaluation of hypolimnetic oxygen demand in a large eutrophic raw water reservoir, San Vicente Reservoir, Calif. *J. Environ. Eng. - ASCE* **133**: 130-138.
- Boudreau, B. P. 2001. Solute transport above the sediment-water interface, p. 104-126. *In* B. P. Boudreau and B. B. Jørgensen [eds.], *The benthic boundary layer: transport processes and biogeochemistry*. Oxford University Press.
- Bouldin, D. R. 1968. Models for describing the diffusion of oxygen and other mobile constituents across the mud-water interface. *J. Ecol.* **56**: 77-87.

- Brand, A., C. Dinkel, and B. Wehrli. 2009. Influence of the diffusive boundary layer on the solute dynamics in the sediments of a seiche-driven lake: A model study. *J. Geophys. Res.* **114**: G01010, doi:10.1029/2008JG000755.
- Brandhuber, P., and S. C. Clark. 2008. Assessing the sources and treatment of iron and manganese in surface water - a case study. AWWA 2008 Inorganic Contaminants Workshop, Albuquerque, NM.
- Budd, G., W. Knocke, J. Hanchak, C. Rice, and M. Billman. 2007. Manganese control issues with changing treatment sequences - Need for understanding manganese and related profile in a plant. VWEA & VA-AWWA Joint Annual Meeting Water Jam.
- Buschmann, J., M. Berg, C. Stengel, and M. L. Sampson. 2007. Arsenic and manganese contamination of drinking water resources in Cambodia: coincidence of risk areas with low relief topography. *Environ. Sci. Technol.* **41**: 2146-2152.
- Gantzer, P. A., L. D. Bryant, and J. C. Little. 2009a. Effect of hypolimnetic oxygenation on oxygen depletion rates in two water-supply reservoirs. *Water Res.* **43**:1700-1710.
- Gantzer, P. A., L. D. Bryant, and J. C. Little 2009b. Controlling soluble iron and manganese in a water-supply reservoir using hypolimnetic oxygenation. *Water Res.* **43**: 1285-1294.
- Geney, R. S. 1988. Reservoir management for water quality improvement. AWWA Annual Conference, Orlando, FL, AWWA.
- Geney, R. S. 1992. A cost-effective approach to water treatment. AWWA Water Quality Conference, Toronto, Ontario, AWWA.
- Gleick, P. H. 2003. Global freshwater resources: Soft-path solutions for the 21st century. *Science* **302**: 1524-1528.
- Glud, R. N., H. Stahl, P. Berg, F. Wenzhöfer, K. Oguri, and H. Kitazato. 2009. In situ microscale variation in distribution and consumption of O<sub>2</sub>: A case study from a deep ocean margin sediment (Sagami Bay, Japan). *Limnol. Oceanogr.* **54**: 1-12.
- Hafeman, D., P. Factor-Litvak, et al. 2007. Association between manganese exposure through drinking water and infant mortality in Bangladesh. *Environ. Health Persp.* **115**: 1107-1112.
- Higashino, M., C. J. Gantzer, and H. G. Stefan. 2004. Unsteady diffusional mass transfer at the sediment/water interface: Theory and significance for SOD measurement. *Water Res.* **38**: 1-12.

- Jørgensen, B. B., and B. P. Boudreau. 2001. Diagenesis and sediment-water exchange, p. 211-244. *In* B. P. Boudreau and B. B. Jørgensen [eds.], *The benthic boundary layer: transport processes and biogeochemistry*. Oxford University Press.
- Jørgensen, B. B., and N. P. Revsbech. 1985. Diffusive boundary layers and the oxygen uptake of sediments and detritus. *Limnol. Oceanogr.* **30**: 111-122.
- Kohl, P. M., and S. J. Medlar. 2006. *Occurrence of Manganese in Drinking Water and Manganese Control*. AWWA and USEPA. Philadelphia, IWA Publishing.
- Lodge, D. M. 2010. It's the water, stupid! *Bioscience* **60**: 6-7.
- Lorke, A., B. Müller, M. Maerki, and A. Wüest. 2003. Breathing sediments: the control of diffusive transport across the sediment-water interface by periodic boundary-layer turbulence. *Limnol. Oceanogr.* **46**: 2077-2085.
- Mackenthun, A. A., and H. G. Stefan. 1998. Effect of flow velocity on sediment oxygen demand: Experiments. *J. Environ. Eng.-ASCE*. **124**: 222-230.
- McGinnis, D. F., A. Lorke, A. Wüest, A. Stöckli, and J. C. Little. 2004. Interaction between a bubble plume and the near field in a stratified lake. *Water Resour. Res.* **40**: W10206, doi:10.1029/2004WR003038.
- Moore, B. C., P. H. Chen, W. H. Funk, and D. Yonge. 1996. A model for predicting lake sediment oxygen demand following hypolimnetic aeration. *Wat. Resour. Bull.* **32**:1-9.
- NRC (National Research Council). 2004. *Confronting the Nation's Water Problems: The Role of Research*. Washington, D.C., National Academies Press.
- Nattress, J. M. 2008. Chlorine dioxide as a preferential oxidant for manganese in the presence of TOC in surface waters. *American Water Works Association 2008 Inorganic Contaminants Workshop*, Albuquerque, NM.
- Nealson, K. H. 1997. "Sediment bacteria: Who's there, what are they doing, and what's new?" *Annual Rev. Earth Planet. Sci.* **25**: 403-434.
- O'Connor, B. L., and M. Hondzo. 2008. Dissolved oxygen transfer to sediments by sweep and eject motions in aquatic environments. *Limnol. and Oceanogr.* **53**: 566-578.
- Singleton, V. L., and J. C. Little. 2006. Designing hypolimnetic aeration and oxygenation systems: a review. *Environ. Sci. Technol.* **40**: 7512-7520.

- van der Tak, L., E. Snyder, T. Martens, G. Schafran, F. Scully, C. Ziesmar, and P. Fortin. 1992. Partial aeration of a Virginia reservoir for iron, manganese and THM control. AWWA Water Quality Technology Conference, Toronto, Ontario, AWWA.
- Veenstra, J. N., and S. L. Nolen. 1991. In situ sediment oxygen demand in five southwestern U.S. lakes. *Water Res.* **25**: 351-354.
- Walker, S. P., T. D. Wachs, J. M. Gardner, B. Lozoff, G. A. Wasserman, E. Pollitt, J. A. Carter, and the International Child Development Steering Group. 2007. Child development: risk factors for adverse outcomes in developing countries. *Lancet* **369**: 145-157.
- Wasserman, G. A., X. Liu, F. Parvez, H. Ahsan, D. Levy, P. Factor-Litvak, J. Kline, A. van Green, V. Slavkovich, N. J. Lolacano, Z. Cheng, Y. Zheng, and J. H. Graziano. 2006. Water manganese exposure and children's intellectual function in Araihasar, Bangladesh. *Environ. Health Persp.* **114**: 124-129.
- Wetzel, R. G. 2001. *Limnology: Lake and River Ecosystems*. San Diego, Academic Press.

## Chapter 2 – Variable sediment oxygen uptake in response to dynamic forcing

Bryant, Lee D.,<sup>a</sup> Claudia Lorrai,<sup>b,c</sup> Daniel F. McGinnis,<sup>b,1</sup> Andreas Brand,<sup>b,2</sup> Alfred Wüest,<sup>b,c</sup> John C. Little<sup>a</sup>

<sup>a</sup>Civil and Environmental Engineering, Virginia Tech, Blacksburg, Virginia.

<sup>b</sup>Eawag (Swiss Federal Institute of Aquatic Science and Technology), Surface Waters – Research and Management, Kastanienbaum, Switzerland.

<sup>c</sup>Institute of Biogeochemistry and Pollutant Dynamics, ETH Zurich, Zurich, Switzerland.

Present addresses:

<sup>1</sup>IFM-GEOMAR, Leibniz Institute of Marine Sciences, RD2 Marine Biogeochemistry, Kiel, Germany.

<sup>2</sup>University of California, Berkeley.

Published in 2010 in *Limnology and Oceanography* **55**:950-964. Used with kind permission from and copyrighted 2010 by the American Society of Limnology and Oceanography, Inc.

### 2.1 Abstract

Seiche-induced turbulence and the vertical distribution of dissolved oxygen above and within the sediment were analyzed to evaluate the sediment oxygen uptake rate ( $J_{O_2}$ ), diffusive boundary layer thickness ( $\delta_{DBL}$ ), and sediment oxic zone depth ( $z_{max}$ ) in situ. High temporal-resolution microprofiles across the sediment-water interface and current velocity data within the bottom boundary layer in a medium-sized mesotrophic lake were obtained during a 12-h field study. We resolved the dynamic forcing of a full 8-h seiche cycle and evaluated  $J_{O_2}$  from both sides of the sediment-water interface. Turbulence (characterized by the energy dissipation rate,  $\epsilon$ ), the vertical distribution of dissolved oxygen across the sediment-water interface (characterized by  $\delta_{DBL}$  and  $z_{max}$ ),  $J_{O_2}$ , and the sediment oxygen consumption rate ( $R_{O_2}$ ) are all strongly correlated in our freshwater system. Seiche-induced turbulence shifted from relatively active ( $\epsilon = 1.2 \times 10^{-8} \text{ W kg}^{-1}$ ) to inactive ( $\epsilon = 7.8 \times 10^{-12} \text{ W kg}^{-1}$ ). In response to this dynamic forcing,  $\delta_{DBL}$  increased from 1.0 mm to the point of becoming undefined,  $z_{max}$  decreased from 2.2 to 0.3 mm as oxygen was depleted from the sediment, and  $J_{O_2}$  decreased from 7.0 to 1.1  $\text{mmol m}^{-2} \text{ d}^{-1}$  over a time span of hours.  $J_{O_2}$  and oxygen consumption were found to be almost equivalent (within ~5% and thus close to steady-state), with  $R_{O_2}$  adjusting rapidly to changes in

$J_{O_2}$ . Our results reveal the transient nature of sediment oxygen uptake and the importance of accurately characterizing turbulence when estimating  $J_{O_2}$ .

## 2.2 Introduction

Dissolved oxygen ( $O_2$ ) is one of the most critical ecological parameters affecting natural aquatic systems with benthic diversity, ecosystem health, and overall water quality all negatively influenced by depleted  $O_2$  levels (Wetzel 2001; Stachowitsch et al. 2007). The amount of  $O_2$  taken up by the sediment largely governs  $O_2$  depletion in stratified waters with organic-rich sediment (Bouldin 1968; Veenstra and Nolen 1991). Sediment  $O_2$  uptake is a function of both physical limitations on  $O_2$  transfer to the sediment and sediment  $O_2$  consumption processes (Jørgensen and Boudreau 2001). Resolving the vertical distribution of  $O_2$  at the sediment-water interface (SWI) allows for the quantification of the sediment  $O_2$  uptake flux ( $J_{O_2}$ ), which is a fundamental parameter for the characterization of  $O_2$  dynamics in aquatic systems (Wetzel 2001). Consequently, considerable effort has been devoted to elucidating the water-side and sediment-side factors controlling sediment  $O_2$  uptake in freshwater and marine systems (Bouldin 1968; Jørgensen and Revsbech 1985; Boudreau 2001).

Molecular diffusion typically becomes the controlling transport process for dissolved species (e.g.,  $O_2$ ) at approximately 1 mm above the SWI in non-advective systems (e.g., cohesive freshwater and marine sediment; Jørgensen and Revsbech 1985; Røy et al. 2004). This mm-scale region immediately above the SWI is referred to as the diffusive boundary layer (DBL; Jørgensen and Revsbech 1985). Diffusion through the DBL is often the rate-limiting step restricting the supply of  $O_2$  to the sediment in systems (e.g., lakes) where steep gradients occur at the SWI (Jørgensen and Revsbech 1985; Wüest and Lorke 2003).  $O_2$  transport to the SWI is driven by the concentration gradient in the DBL and is therefore a function of the thickness of the DBL ( $\delta_{DBL}$ ), which is controlled by turbulent mixing in the bottom boundary layer (BBL), and  $O_2$  concentrations within the bulk BBL ( $C_{bulk}$ ) and at the SWI ( $C_{SWI}$ ), as depicted in Fig. 2.1. Upon reaching the sediment,  $O_2$  is utilized for various biogeochemical processes (e.g., benthic organic matter mineralization and oxidation of reduced compounds) within the sediment oxic zone (quantified by depth  $z_{max}$ ; Fig. 2.1). A balance between the rate at which  $O_2$  is supplied to the sediment, quantified by flux  $J_{O_2}$  ( $mmol\ m^{-2}\ d^{-1}$ ), and the rate at which  $O_2$  is consumed within

the sediment, quantified by the O<sub>2</sub> consumption rate (R<sub>O<sub>2</sub></sub>) which may be defined volumetrically (R<sub>O<sub>2v</sub></sub>; mmol m<sup>-3</sup> d<sup>-1</sup>) or areally (R<sub>O<sub>2a</sub></sub>; mmol m<sup>-2</sup> d<sup>-1</sup>), establishes the extent of the sediment oxic zone (Jørgensen and Boudreau 2001; Higashino et al. 2004). It is important to note that R<sub>O<sub>2</sub></sub> describes the utilization of available O<sub>2</sub> supplied to the sediment rather than the potential sediment O<sub>2</sub> demand (PSOD), which is often evaluated as a constant volumetric O<sub>2</sub> consumption rate. PSOD is a function of available electron acceptors in the sediment; while R<sub>O<sub>2v</sub></sub> may approach PSOD in systems where R<sub>O<sub>2v</sub></sub> controls O<sub>2</sub> diffusion at the SWI (e.g., marine sediment), PSOD would be much greater than R<sub>O<sub>2v</sub></sub> in highly organic, transport-limited systems (e.g., lake sediment; Wüest and Lorke 2003). Furthermore, while R<sub>O<sub>2v</sub></sub> may be strongly influenced by J<sub>O<sub>2</sub></sub>, PSOD is a relatively inherent property unaffected by short-term variations in O<sub>2</sub> availability.

Turbulence in the BBL (e.g., due to internal currents forced by wind or tide) has a direct effect on O<sub>2</sub> transport to the sediment and thus also influences O<sub>2</sub> consumption processes within the sediment. Significant insight has been gained from theoretical studies on how turbulence-induced variations in  $\delta_{\text{DBL}}$  affect O<sub>2</sub> uptake (Higashino et al. 2004, 2008), the relative contributions of O<sub>2</sub>-consuming processes (Glud et al. 2007; Brand et al. 2009), and sediment microbial activity (Gantzer and Stefan 2003; Higashino and Stefan 2005). Rapid changes in  $\delta_{\text{DBL}}$  in response to dynamic forcing have been observed both in the laboratory (Mackenthun and Stefan 1998; Røy et al. 2004; O'Connor and Hondzo 2008) and in situ (Gundersen and Jørgensen 1990; Lorke et al. 2003). Glud et al. (2009) document that the vertical distribution of O<sub>2</sub> at the SWI of marine sediment can vary temporally (on the order of minutes to hours) by a factor > 3, which is within the range of seasonal variability for many aquatic systems. Results of these studies highlight the importance of using multiple measurements to resolve average conditions at the SWI. However, single measurements evaluating J<sub>O<sub>2</sub></sub> under conditions assumed constant are sometimes extrapolated to characterize an aquatic system, thereby ignoring the influence of intermittent hydrodynamic processes (Veenstra and Nolen 1991; Beutel 2003).

Despite the established relationship between turbulence and the vertical O<sub>2</sub> distribution near the SWI, relatively few studies have incorporated simultaneous measurements of in situ current velocity and  $\delta_{\text{DBL}}$  into the assessment of J<sub>O<sub>2</sub></sub>. Previous work has focused predominantly on marine systems (Gundersen and Jørgensen 1990; Glud et al. 2007). Several freshwater experiments were performed to resolve turbulent O<sub>2</sub> transport within the BBL (Brand et al. 2008) and the effect of BBL dynamics on  $\delta_{\text{DBL}}$  (Lorke et al. 2003); however, these studies primarily

characterized turbulence. To our knowledge, no in situ work has been done that focuses on how  $J_{O_2}$ ,  $\delta_{DBL}$ , and the sediment oxic zone vary in response to rapid changes in velocity and direction of basin-scale (i.e., seiche) currents. Additionally, while sediment  $O_2$  uptake may be influenced by both hydrodynamics and consumption processes within the sediment (Fig. 2.1),  $J_{O_2}$  is almost always interpreted exclusively from either a water- or sediment-side perspective (Higashino et al. 2004). We performed an in situ study that evaluated data from the water- and sediment-side of the SWI to determine how seiche-induced turbulence affects  $\delta_{DBL}$ , the sediment oxic zone, and corresponding  $J_{O_2}$  and  $R_{O_2}$  on a rapid (sub-hourly) time scale. This research is therefore unique in that it assesses the transient nature of sediment  $O_2$  uptake by investigating the effect of seiche-induced dynamic forcing on the vertical  $O_2$  distribution under natural, in situ conditions from both sides of the SWI.

## 2.3 Methods

**2.3.1 Study site and in situ instrumentation** – We performed a 12-h field campaign (21:00 h on 27 August to 09:00 h on 28 August 2007) to obtain high-resolution SWI profile data ( $O_2$  and temperature) and velocity data in Lake Alpnach, Switzerland. Lake Alpnach has a simple elliptical shape, a well-established deep current structure, and mesotrophic production (Wüest et al. 2000). The lake is characterized by a relatively high  $J_{O_2}$  (ranging annually from  $\sim 10$  to  $\sim 20$   $\text{mmol m}^{-2} \text{d}^{-1}$ ) and a shallow sediment oxic zone ( $< 3$  mm) that establish steep  $O_2$  gradients at the SWI (Müller et al. 2002; Lorke et al. 2003). Alpine mountain ridges direct thermal winds over the lake causing basin-scale movements of the water body. Two seiche modes are typically observed in summer: a first horizontal-first vertical mode with a period of 8 to 12 h and a first horizontal-second vertical mode with a period of  $\sim 24$  h (Münnich et al. 1992; Lorke et al. 2003). The dynamic  $O_2$  conditions at the SWI and daily wind forcing make Lake Alpnach an ideal location for this study.

During the campaign, an instrumentation array was deployed on the southwestern slope of Lake Alpnach ( $46^{\circ}57'21''$  N,  $8^{\circ}17'53''$  E) at a depth of 22 m. Velocity data were collected continuously at a single point using an acoustic Doppler velocimeter (ADV; Vector, Nortek) and as vertical profiles using an acoustic Doppler profiler (ADP; Aquadopp, Nortek). Thermistors (TR-1060, RBR Ltd.) were placed on the ADP tripod to resolve the temperature structure. A

micro-profiler (MP4, Unisense A/S) was used to measure high-resolution O<sub>2</sub> and temperature profiles across the SWI. A Conductivity-Temperature-Depth (CTD; SBE-19, Seabird Electronics) profiler, which also measured O<sub>2</sub>, was used to profile the water column near the experiment site every 2 h for background information on O<sub>2</sub> and density stratification. Detailed information about the primary components of the experimental setup is provided below. Frequently used acronyms and notations are defined in Table 2.1.

*2.3.1.1 ADV velocity measurements* – An ADV was used to continuously measure three-dimensional current time series at 32 Hz, positioned via tripod at 10 cm above the SWI. Accuracy of the velocity measurements is 0.5% of measured value  $\pm 0.1 \text{ cm s}^{-1}$ . ADV velocity data were used to analyze the current structure and to estimate energy dissipation rate and friction velocity at 10 cm above the SWI.

*2.3.1.2 ADP velocity measurements* – A 2-MHz ADP equipped with three acoustic beams slanted at 25° was used to measure BBL current profiles. Accuracy of the velocity measurements is 1% of measured value  $\pm 0.5 \text{ cm s}^{-1}$ . The ADP was positioned (via tripod) downward looking and measured profiles from 1.60 m to 0 m above the sediment, with 32 measurement cells (5-cm bin size). Samples were obtained in burst mode with 1024 samples per ensemble at a rate of 8 Hz. ADP velocity data were used to estimate bottom drag coefficients at 1 m above the SWI as an independent verification of ADV velocity data.

*2.3.1.3 O<sub>2</sub> and temperature logger measurements* – BBL temperature (i.e., density) structure was continuously measured using a string of 20 thermistors positioned every 25 cm on the leg of the ADP tripod from 0 m to 4.75 m above the sediment. Measurements were obtained using TR-1060 thermistors, which have a response time of  $< 3 \text{ s}$ , accuracy of  $\pm 2 \times 10^{-3} \text{ }^\circ\text{C}$ , resolution of  $< 5 \times 10^{-5} \text{ }^\circ\text{C}$ , and drift of  $< 2 \times 10^{-3} \text{ }^\circ\text{C yr}^{-1}$ . A logger measuring both temperature and O<sub>2</sub> (TDO-2050, RBR Ltd.) was mounted on the micro-profiler at 8 cm above the sediment. In addition to TR-1060 temperature specifications, the TDO-2050 has a measurement range of 0% to 150% O<sub>2</sub> saturation, with an accuracy of  $\pm 1\%$ . TDO-2050 O<sub>2</sub> data were calibrated via Winkler titration of BBL water sampled at the same depth using a Niskin bottle. The calibrated

TDO time series and a zero reading from anoxic sediment were then used for calibration of micro-profiler O<sub>2</sub> measurements.

*2.3.1.4 Microsensor O<sub>2</sub> and temperature measurements across SWI* – An in situ autonomous micro-profiler equipped with microsensors (one Clark-type O<sub>2</sub> sensor and one thermo-coupled temperature sensor, Unisense A/S) was used for microprofiling across the SWI. The sensors have tip diameters of 100 μm, which allow for fast response time (90% in < 8 s), negligible stirring sensitivity, and ~100-μm spatial resolution. Vertical alignment of the microsensors was established by lowering the group of microsensors toward quiescent water and adjusting sensors until all tips touched the water surface simultaneously. Profiles were obtained every ~50 min and were acquired as follows: 10-mm resolution from 10 cm to 1 cm above the SWI, 1-mm resolution from 1 cm to 0.5 cm above the SWI, 0.1-mm resolution from 0.5 cm above to 0.5 cm below the SWI. Following a brief pause to establish equilibrium, ten data points were collected at each depth at a rate of 1 Hz (inspection of measurement set showed no trend in variation, thus confirming data aliasing did not occur).

We measured 14 O<sub>2</sub> profiles during the experiment. The O<sub>2</sub> profile number (1 – 14) corresponds to the time each profile was obtained and is used as the reference for comparison with other parameters (e.g., turbulence). In the absence of a video camera, the location of the SWI was determined by both visual interpretation of each profile (based on identifying linear DBL regions and kinks in the profiles due to porosity differences between the sediment and the water column; Røy et al. 2004) and using standard deviations of O<sub>2</sub> profile data (variation should decrease approaching the SWI due to reduced fluctuations in turbulence; Müller et al. 2002; Brand et al. 2007). Estimates of the SWI using O<sub>2</sub> standard deviations were comparable to estimates based on visual interpretation, though consistently ~1 mm deeper. Correspondingly, previous work has shown the variance method to systematically overestimate  $\delta_{\text{DBL}}$  due to concentration fluctuations protruding into the sediment (Røy et al. 2004). The SWI location predicted by both methods did remain relatively constant across our profile series however. Hence, even if the estimated SWI location was slightly erroneous, this would not affect comparison among profiles.

**2.3.2 O<sub>2</sub> uptake and DBL analyses** – O<sub>2</sub> uptake is frequently evaluated for cohesive sediment using a water-side approach based on Fick’s first law of diffusion (Rasmussen and Jørgensen 1992):

$$J_{O_2} = \varphi D \frac{\partial C}{\partial z} = \varphi D \frac{C_{\text{bulk}} - C_{\text{SWI}}}{\delta_{\text{DBL}}} \quad [\text{mmol m}^{-2} \text{ d}^{-1}] \quad (2.1)$$

where  $D$  is the molecular diffusion coefficient for O<sub>2</sub> in water (m<sup>2</sup> d<sup>-1</sup>),  $\varphi$  is porosity (m<sup>3</sup> voids m<sup>-3</sup> total volume; taken as unity in the water column), and  $\partial C/\partial z$  is the O<sub>2</sub> concentration gradient in the linear portion of the DBL immediately above the SWI (i.e., the change in the O<sub>2</sub> concentration,  $C$ , over distance  $z$ ; mmol m<sup>-4</sup>).

While this is one of the most direct approaches for evaluating  $J_{O_2}$ , there are several problems associated with quantifying  $\delta_{\text{DBL}}$ . The short residence time of O<sub>2</sub> near the SWI and rapid variations in  $\delta_{\text{DBL}}$  due to BBL turbulence make it difficult to accurately characterize the DBL with microsensor measurements (Røy et al. 2004; O’Connor and Hondzo 2008). Furthermore, the transition from the linear DBL to the bulk BBL region is often indistinct (Wüest and Lorke 2003). To address this issue, Jørgensen and Revsbech (1985) established an ‘effective’ DBL, obtained by extrapolating  $\partial C/\partial z$  at the SWI to the point where O<sub>2</sub> levels reach the average concentration of the BBL ( $C_{\text{bulk}}$ ; Fig. 2.1) as defined by the second part of Eq. 2.1 (on the right-hand side). It has been shown, however, that  $\delta_{\text{DBL}}$  is often overestimated by the effective DBL (Hondzo et al. 2005; O’Connor and Hondzo 2008). Additionally, microsensors have been found to alter the structure of the DBL by ~25-45%, possibly due to increased flow around the microsensor shaft compressing the DBL below the sensor tip (Glud et al. 1994; Glud 2008). A decreased  $\delta_{\text{DBL}}$  caused by microsensor compression would obviously result in an overestimation of  $J_{O_2}$ . Considering the variability of the DBL and subsequent difficulties in characterizing  $\delta_{\text{DBL}}$ , it may be more appropriate to regard  $\delta_{\text{DBL}}$  as a conceptual parameter rather than as a physical quantity.

Although problems with quantifying  $\delta_{\text{DBL}}$  are avoided when using sediment-side methods, these methods are often more intensive due to relatively complex sediment processes. In addition to accounting for  $\varphi$  effects (Eq. 2.1), changes in O<sub>2</sub> consumption and storage in the sediment must also be accurately quantified. The balance between the amount of O<sub>2</sub> taken up by

the sediment (characterized by  $J_{O_2}$ ) and the amount consumed within the sediment (characterized by  $R_{O_2}$ ) is shown by:

$$J_{O_2} = \int_0^{z_{\max}} R_{O_{2v}} dz + \int_0^{z_{\max}} \frac{\partial C}{\partial t_v} dz \quad [\text{mmol m}^{-2} \text{ d}^{-1}] \quad (2.2)$$

where volumetric  $R_{O_{2v}}$  ( $\text{mmol m}^{-3} \text{ d}^{-1}$ ) and the change in  $O_2$  concentration over time ( $\partial C/\partial t_v$ ;  $\text{mmol m}^{-3} \text{ d}^{-1}$ ) are integrated over the sediment profile to  $z_{\max}$  (designated in this study as the depth where  $O_2 < 3 \mu\text{mol L}^{-1}$ ). The first term on the right-hand side of Eq. 2.2 represents the amount of  $O_2$  consumed per unit time while the second term represents the temporal change of the  $O_2$  content in the sediment (Higashino et al. 2004). Depth-integrated values from Eq. 2.2 are defined by areal  $R_{O_{2a}}$  and  $\partial C/\partial t_a$ , respectively ( $\text{mmol m}^{-2} \text{ d}^{-1}$ ; Table 2.1), for each profile to allow for direct comparison with  $J_{O_2}$ . Eq. 2.2 shows that  $J_{O_2}$  and  $R_{O_{2a}}$  are equal at steady-state whereas  $O_2$  accumulation or depletion ( $\partial C/\partial t_a$ ) occurs during transient conditions.

To comprehensively assess how dynamic forcing affects sediment  $O_2$  uptake, we analyzed  $J_{O_2}$  and  $\delta_{DBL}$  for each microsensor profile with five different methods using data from both the water-side (*direct* and *u\* methods*) and sediment-side (*curvefit*, *zonefit*, and *model methods*) of the SWI. These five methods were selected to evaluate  $J_{O_2}$  as a function of  $O_2$  microsensor and velocity data. Problems with specific measurement techniques (e.g., measuring  $\delta_{DBL}$ ) or analytical methods should be minimized by the use of a combination of methods based on water-side velocities and water- and sediment-side microsensor data. A more detailed comparison of the methods used to estimate sediment  $O_2$  uptake will be presented in a companion paper (Ch. 3).

For the *direct method*,  $\partial C/\partial z$  was obtained directly from the DBL region of  $O_2$  microsensor profiles and then incorporated into Eq. 2.1 to evaluate  $\delta_{DBL}$  and  $J_{O_2}$  (Jørgensen and Revsbech 1985). For the *u\* method* (Hondzo et al. 2005), dimensionless power law scaling was applied to friction velocity ( $u_*$ ) data derived from ADV velocity series to universally scale the vertical  $O_2$  distribution in the BBL for  $\delta_{DBL}$ , which was then used to solve for  $J_{O_2}$  via Eq. 2.1.

$O_2$  profile data from the sediment side were evaluated by fitting a polynomial equation  $C(z)$  to the porewater region of each  $O_2$  profile, focusing on the region immediately below the SWI (*curvefit method*). The derivative of  $C(z)$  can then be incorporated into Eq. 2.1 to solve for

$J_{O_2}$  and  $\delta_{DBL}$  (Glud 2008). Third-order  $C(z)$  polynomial equations were found to best fit the series of profile data, with the exception of profile 6 which required a fourth-order polynomial.

Porewater data were also evaluated using the numerical model PROFILE (Berg et al. 1998), which analyzes data based on a numerical analysis that defines multiple zones of constant consumption to best describe each  $O_2$  profile (*zonefit method*). Integrating depth-specific  $R_{O_2v}$  (evaluated at 0.1-mm increments) over the depth of the sediment oxic zone yields the overall areal  $R_{O_2a}$  per profile.  $R_{O_2a}$  can then be used to calculate  $J_{O_2}$  via Eq. 2.2. Model parameters used include  $D = 1.97 \times 10^{-9} \text{ m}^2 \text{ s}^{-1}$  at  $20^\circ\text{C}$  (corrected for temperature using the Stokes-Einstein relationship; Li and Gregory 1974; Agregá and Lee 2005), with irrigation and bioturbation effects assumed negligible and boundary conditions (evaluated at the bottom of each profile) of  $J_{O_2} = 0 \text{ mmol m}^{-2} \text{ d}^{-1}$  and  $C = 0 \text{ } \mu\text{mol L}^{-1}$ .

We further analyzed sediment porewater data with the sediment module of the aquatic system simulation software AQUASIM (Reichert 1994), which was used to predict the  $\delta_{DBL}$  required to model  $O_2$  porewater profiles via a simple Monod model for  $O_2$  consumption (*model method*). Model parameters and setup details for the AQUASIM model utilized in this study are defined by Brand et al. (2009). We were able to accurately model our series of sediment  $O_2$  profiles in AQUASIM with a single set of Monod parameters (maximum oxidation rate ( $\mu$ ) =  $5920 \text{ mmol m}^{-3} \text{ d}^{-1}$  and half-saturation constant ( $K_{O_2}$ ) =  $19.1 \text{ } \mu\text{mol L}^{-1}$ ) and  $C_{SWI}$  as the only variable. We then incorporated these Monod parameters into a second model (see Eq. 6 in Brand et al. 2009) in which  $C_{bulk}$  was designated as the upper boundary condition and  $\delta_{DBL}$  was used as the sole fitting parameter to reproduce our sediment  $O_2$  profiles.

Sediment cores from our experiment site were analyzed for  $\phi$  (porewater volume per total volume) following Dalsgaard et al. (2000) to characterize diffusive transport in the sediment and  $\phi$  values of 0.97 and 0.91 in the upper 5 mm were obtained. Using these  $\phi$  results as a point of reference and  $J_{O_2}$  values from an independent set of profiles (obtained  $\sim 1 \text{ m}$  from our experiment site, measured prior to the series of 14 assessed in the primary study) as goals,  $\phi$  was also estimated on a mm-scale with PROFILE (which uses  $\phi$  as an input parameter) via a trial-and-error approach. Similar porosities (0.95 in the upper 1 mm of sediment and 0.90 below) were obtained and these  $\phi$  values were used in Eq. 2.1 and/or as model parameters.

The transience of our system and sediment  $O_2$  consumption as a function of  $O_2$  availability were evaluated using Eq. 2.2. Proximity to steady-state was determined by

calculating  $\partial C/\partial t_a$  for each profile by comparing the preceding and following profiles, evaluating  $\partial C/\partial t_v$  at each depth, and integrating over  $z_{\max}$ . Because the *direct*, *u\**, *curvefit*, and *model methods* estimate  $J_{O_2}$  directly, results from these methods were used to evaluate  $O_2$  consumption (as characterized by  $R_{O_{2a}}$ ) via Eq. 2.2 as a function of  $\partial C/\partial t_a$ . The *zonefit method* predicts depth-specific  $O_2$  consumption directly and hence Eq. 2.2 was used to estimate  $J_{O_2}$  from  $R_{O_{2a}}$  values based on PROFILE results.

Based on results of the five methods, mean values of  $J_{O_2}$ ,  $R_{O_{2a}}$ , and  $\delta_{DBL}$  were calculated for each profile. These parameters were statistically analyzed based on a normal distribution. Standard deviations ( $\sigma$ ) were calculated for  $J_{O_2}$  and  $\delta_{DBL}$  data ( $\sigma$  calculations for  $R_{O_{2a}}$  were unnecessary since  $J_{O_2}$  and  $R_{O_{2a}}$  are directly correlated via Eq. 2.2). Estimates obtained from the five methods were comparable, as shown below.

**2.3.3 Inertial dissipation analyses** – The dissipation rate of turbulent kinetic energy,  $\varepsilon$  ( $W\ kg^{-1}$ ), was estimated using the inertial dissipation method (Grant et al. 1962). The analysis is based on the inertial subrange where the spectrum is expressed in the wavenumber ( $k$ ) domain:

$$E(k) = \alpha \varepsilon^{2/3} k^{-5/3} \quad [m^3\ s^{-2}] \quad (2.3)$$

where velocity fluctuation follows a  $k^{-5/3}$  slope for eddy sizes of typically dm to m (Fig. 2.2a). We used  $\alpha = 1.56$  for the experimentally estimated, three-dimensional Kolmogorov constant (Wyngaard and Coté 1971). With the ADV, we measured horizontal (longitudinal and lateral) and vertical velocity fluctuations 10 cm above the sediment. Dissipation rates can be obtained from the longitudinal component of the one dimensional spectrum expressed in the wavenumber ( $k_1$ ) domain:

$$\varphi_{11}(k_1) = \alpha_1 \varepsilon^{2/3} k_1^{-5/3} \quad [m^3\ s^{-2}] \quad (2.4)$$

and the two transversal components of the power spectrum:

$$\varphi_{22}(k_1) = \varphi_{33}(k_1) = \alpha_2 \varepsilon^{2/3} k_1^{-5/3} \quad [m^3\ s^{-2}] \quad (2.5)$$

where  $\alpha_1 = \frac{18}{55} \alpha$  and  $\alpha_2 = \frac{4}{3} \alpha_1$ . Rather than fitting the -5/3 slope to the inertial subrange, the respective power spectrum (Eqs. 2.4 and 2.5) is multiplied by  $k^{5/3}$ . This procedure transforms the spectrum so that it is only dependent on  $\varepsilon$  as  $E(k) \times k^{5/3}$  becomes constant (Fig. 2.2a). Dissipation ( $\varepsilon$ ) is then calculated by taking the average of the inertial subrange. All three velocity fluctuation records were used to quantify the value of  $\varepsilon$  (longitudinal, transversal planar, and transversal vertical; Eqs. 2.4 and 2.5) over a time span of approximately 50 min (Fig. 2.2b), which corresponds to the measurement period of each O<sub>2</sub> profile.

To account for the intermittency of turbulence,  $\varepsilon$  is averaged by assuming a lognormal distribution (Baker and Gibson 1987). The most likely average of the three  $\varepsilon$  values ( $\bar{\varepsilon}$ ) is

$$\bar{\varepsilon} = \exp\left(\overline{\ln(\varepsilon)} + \frac{\sigma_{\ln(\varepsilon)}^2}{2}\right) \quad [\text{W kg}^{-1}] \quad (2.6)$$

where  $\overline{\ln(\varepsilon)}$  is the average of the ln-value of  $\varepsilon$  and  $\sigma_{\ln(\varepsilon)}$  is the standard deviation, or intermittency, of the ln( $\varepsilon$ ) values (Table 2.2).

**2.3.4 Friction velocity analyses** – Friction velocities ( $u_*$ ) were calculated at a height ( $h$ ) of 10 cm above the sediment from the estimated  $\varepsilon$  values using the law-of-the-wall assumption:

$$u_* = \sqrt[3]{\varepsilon \kappa h} \quad [\text{m s}^{-1}] \quad (2.7)$$

where  $\kappa$  (the von Karman constant) is 0.41. The resulting  $u_*$  values (Table 2.2) quantify the frictional stress of BBL currents on the sediment and thus, similar to  $\varepsilon$ , describe the level of turbulence in the BBL.

## 2.4 Results

**2.4.1 Seiche dynamics** – We acquired data for 12 hours and captured a full 8-h seiche cycle. During the campaign, bottom currents moved initially from the southwest toward the northeast, reached the current reversal point and then reversed direction toward the southwest, similar to the motion of a pendulum (as depicted in Fig. 2.3a, where the schematics show the water body moving back and forth relative to our experiment site). Corresponding changes in current velocity are shown in Fig. 2.3b. During the observed seiche cycle, water from higher elevations in the BBL moved down the southwestern slope with increasing velocity toward the northeast. Current velocity reached a maximum of  $2.3 \text{ cm s}^{-1}$  (at 23:50 h) during this period. At the current reversal point (~04:00 h), velocities in the BBL reached a minimum value of  $0.6 \text{ cm s}^{-1}$ . When the water mass then shifted back toward the southwest, water from the central region of the BBL moved toward the southwestern slope and velocities increased to levels observed prior to current reversal, reaching a maximum value of  $2.3 \text{ cm s}^{-1}$  (at 07:44 h).

Lorke et al. (2002) demonstrated that law-of-the-wall theory (used to estimate  $u_*$ ) only applies in cases of turbulence where longitudinal velocity is greater than  $1 \text{ cm s}^{-1}$  at 1 m above the sediment. Most of our velocities (obtained at 10 cm above the sediment) were within this range, with only velocities during the period of current reversal (profiles 7 – 9) falling significantly below this level (Fig. 2.3b). Accordingly, a majority of our profiles were consistent with the law-of-the-wall profile. However, for velocities smaller than this threshold, the logarithmic profile broke down and no characteristic features of the BBL could be identified (as independently confirmed by  $\text{O}_2$  microsensor measurements). To verify the applicability of the law-of-the-wall to the full series of our velocity data, we employed the bottom drag coefficient ( $C_{1m}$ ) via:

$$u_* = \sqrt{C_{1m}} U_{1m} \quad [\text{m s}^{-1}] \quad (2.8)$$

where  $U_{1m}$  is the longitudinal velocity ( $\text{m s}^{-1}$ ) at 1 m above the sediment obtained from the downward-looking ADP. The bottom drag coefficient relates the Reynolds stress on the sediment surface and the mean current velocity at a specified height. A  $C_{1m}$  value of 0.0033 was obtained for the full set of velocity data and a  $C_{1m}$  of 0.0013 was obtained when the velocity data

below  $1 \text{ cm s}^{-1}$  were excluded. These  $C_{1m}$  values are comparable to the typical range of 0.001 – 0.003 (Wüest and Lorke 2003) for smooth-bottom boundaries (such as lake-bottom sediments).

**2.4.2 Temperature and O<sub>2</sub> distribution** – Temperature and O<sub>2</sub> in the water column and near the sediment are shown to be strongly affected by seiche-induced variations in current velocity (Fig. 2.4). At the beginning of the measurement period (21:00 h), a cold water mass from the central, well-mixed BBL moved across the experiment site (Fig. 2.4a – c). As the water mass shifted toward the northeast, warmer water from the upper BBL moved toward the experiment site (approaching 04:00 h) as the current reversal point was approached (Fig. 2.3). Following reversal of current direction, velocity increased and the cooler, well-mixed region of the BBL moved back to the experiment site as the current shifted the water mass toward the southwest.

Variations in temperature and O<sub>2</sub> in the BBL at 8 cm above the sediment are shown in Fig. 2.4a. Changes in temperature are shown as a function of depth in Fig. 2.4b (200 to 30 cm above the SWI) and Fig. 2.4c (1 cm above to 0.25 cm below the SWI). From Fig. 2.4b – c, it is apparent that while temperature varied over time (on the order of  $\sim 2^\circ\text{C}$ ), the vertical temperature profile remained relatively constant with depth but was displaced first in the positive and then negative direction. However, while changes in O<sub>2</sub> are relatively minor (on the order of  $\sim 10 \mu\text{mol L}^{-1}$ ) at 8 cm above the sediment (Fig. 2.4a), O<sub>2</sub> variations are observed on a much greater scale near the SWI (Fig. 2.4d; 1 cm above to 0.25 cm below the SWI). When velocity decreased during profiles 5 to 9, O<sub>2</sub> decreased from  $\sim 100 \mu\text{mol L}^{-1}$  to  $70 \mu\text{mol L}^{-1}$  at 1 cm above the SWI and from  $59 \mu\text{mol L}^{-1}$  to  $5 \mu\text{mol L}^{-1}$  at the SWI. Furthermore, the sediment approached anoxia as sediment O<sub>2</sub> was depleted during this period.

The controlling influence that dynamic forcing has on the vertical distribution of O<sub>2</sub> above and below the SWI is emphasized in Fig. 2.5. O<sub>2</sub> profiles are separated into panels according to the direction of profile movement, which strongly corresponds to changes in velocity magnitude. The oscillating motion of the water body is apparent in the directional shifts of the O<sub>2</sub> profiles over the seiche cycle. As currents intensify, O<sub>2</sub> levels in the water and in the sediment increase, as shown by profiles 2 – 5 (Fig. 2.5a) and 9 – 14 (Fig. 2.5c); however, as velocity decreases approaching current reversal, O<sub>2</sub> throughout the full length of the profile drops to negligible levels (profiles 5 – 9; Fig. 2.5b). Profile 1 is not shown due to a slight misalignment with the other profiles that likely resulted from equipment settling into the

sediment following deployment (discussed further below). A key point shown in Fig. 2.5 is the elasticity of the system, in that the vertical O<sub>2</sub> distribution changes significantly as it shifts from oxic (Fig. 2.5a) to nearly anoxic conditions (Fig. 2.5b) but then returns to an oxic distribution (Fig. 2.5c) close to its initial state (Fig. 2.5a).

In Fig. 2.5a (profiles 2 – 5) and Fig. 2.5c (profiles 9 – 14), the oxic zone extends further into the sediment and  $\delta_{\text{DBL}}$  decreases as velocity increases, clearly illustrating how current-induced mixing forces the vertical O<sub>2</sub> structure at the SWI. After velocity peaked at approximately 23:50 h (Fig. 2.5a),  $z_{\text{max}}$  and  $C_{\text{SWI}}$  reached maximum values (2.2 mm and 59  $\mu\text{mol L}^{-1}$ , respectively) while  $\delta_{\text{DBL}}$  reached a minimum of 1.0 mm. This relationship is shown in reverse in Fig. 2.5b (profiles 5 – 9) where, as velocity decreases during current reversal (between profiles 8 and 9 at approximately 04:00 h),  $\delta_{\text{DBL}}$  increases to the point of being undefined and the oxic zone almost completely disappears (minimum  $z_{\text{max}} = 0.3$  mm) as the sediment goes anoxic.

**2.4.3 O<sub>2</sub> flux and  $\delta_{\text{DBL}}$**  – Mean values of  $J_{\text{O}_2}$  and  $\delta_{\text{DBL}}$  were obtained by averaging results from the five analytical methods used to evaluate O<sub>2</sub> profile and  $u^*$  data (Table 2.3). Consequently, both water-side (transport) and sediment-side (consumption) influences on  $J_{\text{O}_2}$  and  $\delta_{\text{DBL}}$  are reflected in the average values. Values of  $J_{\text{O}_2}$  based on  $R_{\text{O}_2\text{a}}$  from the *zonefit model* were corrected for transient accumulation of O<sub>2</sub> per Eq. 2.2. During energetic periods (maximum  $\varepsilon = 1.2 \times 10^{-8}$  W kg<sup>-1</sup>; profile 4),  $\delta_{\text{DBL}}$  reached a minimum of 1.0 mm and  $J_{\text{O}_2}$  increased to a maximum of 7.0 mmol m<sup>-2</sup> d<sup>-1</sup> (Table 2.3). As turbulence decreased approaching the current reversal point (minimum  $\varepsilon = 7.8 \times 10^{-12}$  W kg<sup>-1</sup>; profile 9),  $\delta_{\text{DBL}}$  expanded significantly as there was no longer sufficient turbulence to maintain an established DBL (Fig. 2.5, Table 2.3). Although a DBL in the classical sense is not maintained under these quiescent conditions (Gantzer and Stefan 2003; Røy et al. 2004), we nevertheless quantified  $\delta_{\text{DBL}}$  during this period as a relative measure for comparison. Using independent results from all five methods, a maximum average  $\delta_{\text{DBL}}$  of  $7.8 \pm 2.2$  mm was estimated for profile 9 (Table 2.3).

During the period of weak turbulence and subsequently increased  $\delta_{\text{DBL}}$ ,  $J_{\text{O}_2}$  decreased by 85%, from 7.0 mmol m<sup>-2</sup> d<sup>-1</sup> to 1.1 mmol m<sup>-2</sup> d<sup>-1</sup> (Fig. 2.6). The substantial short-term variability in  $J_{\text{O}_2}$  in response to changes in turbulence is emphasized in Fig. 2.6. However, an explicit relationship between  $J_{\text{O}_2}$  and  $\varepsilon$  cannot be defined by the linear correlation shown in Fig. 2.6 as  $J_{\text{O}_2}$  is also affected by other variables (e.g.,  $C_{\text{bulk}}$  and  $R_{\text{O}_2}$ ).

The relatively small standard deviation of  $J_{O_2}$  and  $\delta_{DBL}$  obtained from the different methods per profile as compared to the overall temporal variation in averages ( $J_{O_2}$  or  $\delta_{DBL}$ ) shows that comparable estimates were obtained from the different methods (Table 2.3). Water-side methods did yield slightly but consistently higher values of  $J_{O_2}$  (with correspondingly lower values of  $\delta_{DBL}$ ) though. A comparative evaluation of method results is being performed for the companion methods study (Ch. 3). Standard deviation evolves according to changes in turbulence. When turbulence levels are low, increasing  $\delta_{DBL}$  and decreasing  $\varepsilon$  lead to greater uncertainty and subsequently higher  $\sigma$  (or intermittency) for these parameters. Thus, observed increases in variability in  $\delta_{DBL}$  and  $\varepsilon$  during the period of weak turbulence (Tables 2.2 and 2.3) are more an effect of analysis than a reflection of the quality of data. While  $J_{O_2}$ ,  $\delta_{DBL}$ , and  $\varepsilon$  values for profile 1 exhibit unusually high variability, these increased deviations are reflected in data obtained with multiple instruments (ADV and micro-profiler; Tables 2.2 and 2.3) and are observed only at the beginning of the campaign; hence, they are likely a result of equipment settling at the lake bottom following deployment.

**2.4.4 Sediment oxic zone** – Changes in the extent of the sediment oxic zone correspond to variations in  $J_{O_2}$  and  $\delta_{DBL}$  in response to turbulence. When  $O_2$  transport into the sediment escalated as the DBL was compressed by elevated turbulence (Fig. 2.6), both  $z_{max}$  (Fig. 2.5) and the vertically integrated mass of  $O_2$  ( $M_{O_2}$ ; Table 2.4) increased significantly as  $O_2$  penetrated deeper into the sediment. The oxic zone is observed to reach a maximum  $z_{max}$  of 2.2 mm during active turbulence (corresponding  $\delta_{DBL} = 1.0$  mm,  $J_{O_2} = 6.9$  mmol m<sup>-2</sup> d<sup>-1</sup>, and  $M_{O_2} = 54$  μmol m<sup>-2</sup>). Conversely,  $z_{max}$  decreased to a minimum of 0.3 mm and  $C_{SWI}$  decreased from 59 to 5 μmol L<sup>-1</sup> during negligible turbulence (corresponding  $\delta_{DBL} = 7.6$  mm,  $J_{O_2} = 1.3$  mmol m<sup>-2</sup> d<sup>-1</sup>, and  $M_{O_2} = 3$  μmol m<sup>-2</sup>) as the sediment approached anoxia. The strongly coupled behavior observed in these parameters is supported by recent modeling work based on data from Lake Alpnach (Brand et al. 2009) which shows that an increase in  $\delta_{DBL}$  (from 0.25 to 1.5 mm) results in decreased  $z_{max}$  (from 1.7 to 1.2 mm) and decreased  $J_{O_2}$  (from 15 to 9.5 mmol m<sup>-2</sup> d<sup>-1</sup>).

**2.4.5 Profile dynamics** – Eq. 2.2 was used to determine proximity to steady-state. Although significant variation was observed in our  $O_2$  profiles over the 12-h measurement period (Fig. 2.5),  $O_2$  accumulation and/or depletion within the sediment was insignificant (Table 2.4), with an

average  $\partial C/\partial t_a$  of  $\pm 0.30 \text{ mmol m}^{-2} \text{ d}^{-1}$  or  $\sim 5\%$  of the average  $J_{O_2}$  ( $5.2 \text{ mmol m}^{-2} \text{ d}^{-1}$ ) over the full measurement period. The rate at which  $O_2$  enters the sediment ( $J_{O_2}$ ) equals the areal  $O_2$  consumption rate ( $R_{O_{2a}}$ ) at steady-state (Eq. 2.2) and these values were found to be almost equivalent in our mesotrophic lake system (Table 2.4). Additionally, the average  $J_{O_2}$  and  $M_{O_2}$  ( $32 \mu\text{mol m}^{-2}$ ; Table 2.4) for the 12-h period indicate a mean  $O_2$  residence time in the sediment of 9 min. Because profiles were obtained every  $\sim 50$  minutes, quasi-steady-state conditions prevailed.

## 2.5 Discussion

**2.5.1 Forcing of  $O_2$  distribution** – Lorke et al. (2003) show that  $\delta_{DBL}$  is controlled primarily by turbulence rather than velocity based on an observed phase lag between  $\varepsilon$ ,  $\delta_{DBL}$ , and current velocity, where  $\varepsilon$  and  $\delta_{DBL}$  lagged consistently ( $\sim 1.5$  h) behind current velocity at 1 m above the sediment. Although we do observe a direct relationship between  $\varepsilon$  and  $\delta_{DBL}$ , a defined phase lag between these parameters and current velocity was not evident within the temporal resolution of our measurements (Fig. 2.7). However, it has been shown that this delay becomes greater with increasing distance from the sediment (Lorke et al. 2002). The phase lag would therefore be expected to be much shorter ( $\sim 10$  min) during our experiment.

During periods of relatively high velocity (profiles 1 – 5 and 9 – 14), turbulence increased as cold water from the deeper region of the BBL moved across our experiment site (Figs. 2.4, 2.7). The movement of this cooler water mass along the slope may have established small inverse temperature gradients that produced additional turbulence due to bottom convective mixing (Lorke et al. 2005). Turbulence compressed the DBL during these periods, which facilitated increased  $O_2$  transport from the BBL down to the sediment and resulted in greater sediment  $O_2$  uptake and an enhanced sediment oxic zone. As the water mass approached current reversal (profiles 5 – 9), decreased turbulence,  $J_{O_2}$ , and  $z_{max}$  are observed as current velocity subsided (Figs. 2.5, 2.6).

Temperatures in the BBL and near the SWI increased (Fig. 2.4a – c) in response to the influx of warm water from farther up the slope (confirmed by CTD data, not shown). Variations in temperature are reflected over the full microsensor profile depth and are not affected by changes in  $\delta_{DBL}$ , which is likely due to the relatively rapid rate of heat transfer (compared to

molecular diffusion) and the fact that temperature is not consumed by the sediment (unlike O<sub>2</sub>). Hence, once the near-surface sediment temperature equilibrates with that of the BBL, the sediment no longer behaves as a heat sink. Conversely, significant variation was observed in the vertical distribution of O<sub>2</sub> across the SWI which may be largely attributed to O<sub>2</sub> consumption. In the absence of turbulence, while O<sub>2</sub> remained at ~110 μmol L<sup>-1</sup> several cm above the SWI, the O<sub>2</sub> supply through the extended DBL was insufficient to maintain the sediment oxic zone (Figs. 2.4, 2.6). As J<sub>O<sub>2</sub></sub> diminished and O<sub>2</sub> was consumed in the sediment, O<sub>2</sub> in the water immediately overlying the sediment, C<sub>SWI</sub>, and z<sub>max</sub> decreased significantly (Figs. 2.4, 2.5). These findings emphasize that, even when O<sub>2</sub> levels in the BBL remain relatively high, the O<sub>2</sub> distribution on both sides of the SWI and the corresponding J<sub>O<sub>2</sub></sub> are strongly governed by turbulence, as supported by previous work (Jørgensen and Revsbech 1985; Brand et al. 2009; Gantzer et al. 2009a).

**2.5.2 Variations in sediment O<sub>2</sub> consumption** – Quasi-steady conditions prevailed (J<sub>O<sub>2</sub></sub> and R<sub>O<sub>2a</sub></sub> differed by only 5%) and, correspondingly, both J<sub>O<sub>2</sub></sub> and R<sub>O<sub>2</sub></sub> (quantified by R<sub>O<sub>2a</sub></sub> and R<sub>O<sub>2v</sub></sub>) varied in response to dynamic forcing, as shown by R<sub>O<sub>2a</sub></sub> data in Table 2.4. This indicates that sediment O<sub>2</sub> consumption was directly related to O<sub>2</sub> availability within the sediment as supplied via J<sub>O<sub>2</sub></sub>. Monod and first-order kinetic models are frequently used to characterize sediment O<sub>2</sub> consumption as a function of O<sub>2</sub> concentration in the sediment (Rasmussen and Jørgensen 1992; Higashino et al. 2004). However, due to the variety of O<sub>2</sub>-consuming processes and the complexity of the kinetics, simple zero-order kinetics is frequently assumed (Bouldin 1968; Jørgensen and Boudreau 2001; Røy et al. 2004). Irrespective of the kinetics, though, it has been reported that when O<sub>2</sub> uptake is at least partially governed by diffusive transport, R<sub>O<sub>2</sub></sub> does become dependent on O<sub>2</sub> concentration below O<sub>2</sub> levels of 20 – 30 μmol L<sup>-1</sup> (Santschi et al. 1990; Berg et al. 2003). Sediment O<sub>2</sub> levels remained close to this minimum range during our study (Fig. 2.5). Our results therefore demonstrate dependence of R<sub>O<sub>2</sub></sub> on O<sub>2</sub> availability under limiting O<sub>2</sub> conditions regardless of the kinetics involved. Models based on variable zones of O<sub>2</sub> consumption and Monod kinetics were used (*zonefit* and *model methods*, respectively) to evaluate J<sub>O<sub>2</sub></sub> and δ<sub>DBL</sub> with comparable results (Table 2.3; Ch. 3).

Variability in sediment O<sub>2</sub> consumption was further evaluated using PROFILE (*zonefit method*) to characterize regions of differing R<sub>O<sub>2v</sub></sub> within the sediment oxic zone as a function of

time and depth, as shown in Fig. 2.8. Zone-specific  $R_{O_2v}$  values predicted by PROFILE were corrected for  $\partial C/\partial t_v$  (Eq. 2.2). PROFILE results show that  $R_{O_2v}$  was consistently higher near the SWI and then decreased significantly with depth (Fig. 2.8). Results by O'Connor and Harvey (2008) and Brand et al. (2009) also show increased  $R_{O_2v}$  immediately below the SWI.  $O_2$  consumption in the upper sediment region is often elevated due to mineralization of freshly deposited organic matter at the sediment surface as well as re-oxidation of subsequently released reduced inorganic species (Santschi et al. 1990; Zhang et al. 1999). Accordingly, increased heterotrophic bacterial abundance and activity in the sediment surface layer is common (Fischer et al. 2002, 2005).

Variations in turbulence (Fig. 2.8a) coupled with changes in PROFILE-predicted consumption zones (Fig. 2.8b – d) support our observation of increased  $J_{O_2}$  leading to increased  $O_2$  consumption (Table 2.4). The upper sediment layer is obviously most directly affected by turbulence in the BBL and variations in  $\delta_{DBL}$ . Consumption in this upper zone is observed to increase during periods of peak turbulence when elevated  $O_2$  concentrations above the sediment and a thinner  $\delta_{DBL}$  facilitate enhanced  $J_{O_2}$ . Elevated  $R_{O_2v}$  in the upper sediment as a result of increased  $O_2$  availability implies that the intrinsic capacity of the sediment for  $O_2$  consumption (PSOD) exceeds  $J_{O_2}$ , indicating water-side control of sediment  $O_2$  uptake (O'Connor and Harvey 2008). When  $J_{O_2}$  increased during periods of elevated turbulence, the sediment oxic zone is observed to increase while  $\partial C/\partial t_a$  remained relatively small, suggesting that the additional  $O_2$  entering the sediment was being consumed rather than accumulating in the sediment (Fig. 2.8b, d, Table 2.4). However, during periods when turbulence is at a minimum and  $\delta_{DBL}$  extends to the point of becoming undefined, thereby limiting  $O_2$  transport and subsequent availability at the SWI, consumption is characterized by a minimal zone and  $R_{O_2}$  drops significantly (Fig. 2.8c, Table 2.4). At this point, the sediment oxic zone almost completely disappears. The elasticity observed in sediment-water  $O_2$  profiles shown in Fig. 2.5 is also evident in sediment  $O_2$  consumption zones shown in Fig. 2.8, although it is less direct due to the complexity of sediment processes. The distribution of  $O_2$  consumption zones for profile 13 (Fig. 2.8d) returns to a structure similar to that of profile 4 (Fig. 2.8b) as turbulence increases following a substantial shift to a smaller, single zone for profile 8 during the stagnant period (Fig. 2.8c).

Our results show that variations in  $\delta_{DBL}$  have a significant effect on  $J_{O_2}$ ,  $R_{O_2}$  (both areally and volumetrically), and resultant  $z_{max}$ . It is important to emphasize that in this study, diffusion

time for O<sub>2</sub> across the DBL and transport time through the sediment oxic zone are comparable (~10 to 20 min during the majority of the campaign when turbulence levels were high enough to maintain a defined DBL). When the timescale of O<sub>2</sub> diffusion through the DBL is short in comparison to transport through the sediment oxic zone (e.g., oligotrophic environments where z<sub>max</sub> can be measured in cm and sediment O<sub>2</sub> residence time can be on the order of days), changes in δ<sub>DBL</sub> would be unlikely to have a strong influence on J<sub>O<sub>2</sub></sub>, R<sub>O<sub>2</sub></sub>, and z<sub>max</sub> (Glud et al. 2007).

**2.5.3 Scale of variation** – Mean values for J<sub>O<sub>2</sub></sub> (Table 2.4) obtained during this study are comparable to values found in previous studies of BBL turbulence at the same location. Brand et al. (2008) estimated an average J<sub>O<sub>2</sub></sub> of 13 ± 2 mmol m<sup>-2</sup> d<sup>-1</sup> and Lorke et al. (2003) estimated J<sub>O<sub>2</sub></sub> to range from 6 to 13 mmol m<sup>-2</sup> d<sup>-1</sup>, with a corresponding δ<sub>DBL</sub> range of 0.16 to 0.84 mm. Turbulence and O<sub>2</sub> levels in the BBL were higher in these previous studies than those observed during our campaign; this is reflected in our relatively low turbulence estimates and subsequently decreased J<sub>O<sub>2</sub></sub> and increased δ<sub>DBL</sub> values. Despite the less energetic conditions, variation in J<sub>O<sub>2</sub></sub> and the vertical distribution of O<sub>2</sub> over the 12-h measurement period was still significant (Figs. 2.5 – 2.7). The fact that we observed such change in these parameters in response to dynamic, though relatively mild, turbulence conditions highlights the dependence of sediment O<sub>2</sub> uptake on turbulence.

Not only was J<sub>O<sub>2</sub></sub> found to vary significantly over the duration of a single seiche cycle (on the order of hours) during our campaign (Fig. 2.6) but it was also observed to change substantially on a sub-hourly time scale. For example, in the course of the 53-min period between profiles 9 and 10 when turbulence increased as the water body shifted back toward the southwest direction following current reversal, J<sub>O<sub>2</sub></sub> increased from 1.1 mmol m<sup>-2</sup> d<sup>-1</sup> to 5.7 mmol m<sup>-2</sup> d<sup>-1</sup> (Table 2.4). During this time, ε increased from 7.8 × 10<sup>-12</sup> to 2.5 × 10<sup>-10</sup> W kg<sup>-1</sup>, δ<sub>DBL</sub> decreased from 7.8 to 1.7 mm (Fig. 2.7), z<sub>max</sub> increased from 0.6 to 1.3 mm (Fig. 2.5), and M<sub>O<sub>2</sub></sub> increased from 5 to 24 μmol m<sup>-2</sup> (Table 2.4). The high degree of variation observed in J<sub>O<sub>2</sub></sub> and the vertical O<sub>2</sub> distribution over such a brief time period illustrates the transient nature of sediment O<sub>2</sub> uptake. While it has been shown that long-term (e.g., annual) average J<sub>O<sub>2</sub></sub> is typically not influenced by short-term (e.g., hourly) changes in δ<sub>DBL</sub> (Glud et al. 2007), our results stress the importance of taking turbulence into account when resolving O<sub>2</sub> profiles in

order to fully evaluate  $J_{O_2}$ . Under dynamic conditions, a system must be characterized in greater detail than what can be discerned from a single profile. An accurate assessment of  $J_{O_2}$  and  $R_{O_2}$  is not possible without obtaining a comprehensive series of profiles describing the full range of variation in the vertical distribution of  $O_2$ . Furthermore, extreme caution should be taken in evaluating PSOD based on  $R_{O_2v}$  analyses without considering physical limitations on  $O_2$  transport to the SWI (and subsequent  $O_2$  availability in the sediment) and proximity to long-term steady-state. Variation in PROFILE-predicted  $R_{O_2v}$  results for individual profiles (Fig. 2.8) emphasizes how evaluating  $R_{O_2v}$  based on a single profile could lead to very different estimates of PSOD. In all likelihood, the average  $R_{O_2v}$  observed during our 12-h campaign ( $3.5 \text{ mmol m}^{-3} \text{ d}^{-1}$  in upper sediment; data not shown) may still significantly underestimate actual PSOD due to the mild turbulence conditions limiting sediment  $O_2$  availability and subsequent consumption.

Technical and logistical restraints often limit the number of in situ microsensor measurements obtained during a given deployment to only a few (Glud et al. 2009), which may be an issue depending on the time scale of the dynamics in the system of interest. During this study, we were able to obtain 14 microprofiles at approximately 50-min intervals. Fluctuations in  $\delta_{DBL}$  have been previously observed at time scales on the order of seconds (Røy et al. 2004; O'Connor and Hondzo 2008). However, Brand et al. (2009) show that the influence of these rapid variations in  $\delta_{DBL}$  is negligible on evaluations of mean  $J_{O_2}$  and the vertical  $O_2$  distribution near the SWI at time scales appropriate for defining seiche cycles (e.g., min, h). The sub-hourly time scale at which we assessed data is small compared to the 8-h duration of the seiche cycle; hence, a thorough characterization of how seiche-induced variations in sediment  $O_2$  uptake was achieved.

## 2.6 Conclusion

In conclusion, our results reveal the effect of natural dynamic forcing on the vertical distribution of  $O_2$  across the SWI and on sediment  $O_2$  uptake. Although work has been done that contributes significantly to the understanding of BBL dynamics and flux pathways, these studies have been largely laboratory- or model-based (Røy et al. 2004; Glud et al. 2007; O'Connor and Hondzo 2008). Previous in situ studies have focused primarily on physical, water-side controls of  $O_2$  transport (Gundersen and Jørgensen 1990; Lorke et al. 2003) or spatial and temporal

variations in  $O_2$  distribution in sediment (Epping and Helder 1997; Glud et al. 2003, 2009). This study is novel in that we analyzed  $O_2$  uptake from both sides of the SWI. In doing so, we have expanded on previous results by analyzing the tight coupling between water-side (turbulence, as characterized by  $\varepsilon$ ) and sediment-side ( $O_2$  consumption in sediment, as characterized by  $R_{O_2}$ ) processes influencing sediment  $O_2$  uptake under actual field conditions in a freshwater system. The highly transient nature of  $J_{O_2}$  is revealed by rapid changes in the vertical distribution of  $O_2$  in both the water and the sediment in response to dynamic forcing via seiche motion.  $R_{O_2}$  was shown to adjust quickly to variations in  $J_{O_2}$  at quasi-steady-state. Although our study focused on  $O_2$  fluxes, knowledge gained regarding the relationship between turbulence and mass transfer at the SWI can be more broadly applied to fluxes of other soluble chemical species (e.g., reduced metals, hydrogen sulfide, methane) as well (Jørgensen et al. 1979; Frenzel et al. 1990; Gantzer et al. 2009b). The crucial role of turbulence is highlighted by the fact that, despite relatively high  $O_2$  levels only a few cm above the sediment,  $O_2$  transport to the SWI and the extent of the sediment oxic zone both decreased substantially during quiescent periods. The critical control that dynamic forcing can have on  $J_{O_2}$  must be considered when evaluating sediment  $O_2$  uptake via measuring devices (e.g., benthic chambers) that do not capture natural turbulence conditions. Furthermore, based on the significant changes observed in  $J_{O_2}$  during periods as brief as an hour, our results show that using isolated  $J_{O_2}$  measurements may be insufficient, particularly in systems experiencing high levels of variable turbulence.

## 2.7 Acknowledgements

We are grateful to Peter Berg and Miki Hondzo for their useful advice. We also thank Lorenzo Rovelli, Michi Schurter, Chregu Dinkel, and Mathias Kirf, who offered invaluable assistance in the field and with equipment. Helpful feedback from Ronnie Glud, Hans Røy, and an anonymous reviewer substantially improved the manuscript. The research described in this paper has been funded in part by the United States Environmental Protection Agency (EPA) under the Science to Achieve Results (STAR) Graduate Fellowship Program. EPA has not officially endorsed this publication and the views expressed herein may not reflect the views of the EPA. This research was also supported by the United States National Science Foundation (NSF) through the Integrative Graduate Education and Research Traineeship (IGERT) program

(DGE 0504196) and by the Swiss National Science Foundation, grants 200020-111763 and 200020-120128.

## 2.8 References

- Agrega, F., and J. H. W. Lee. 2005. Diffusional mass transfer at sediment-water interface of cylindrical sediment oxygen demand chamber. *J. Environ. Eng.-ASCE* **131**: 755-766.
- Baker, M. A., and C. H. Gibson. 1987. Sampling turbulence in the stratified ocean: statistical consequences of strong intermittency. *J. Phys. Oceanogr.* **17**: 1817-1836.
- Berg, P., N. Risgaard-Petersen, and S. Rysgaard. 1998. Interpretation of measured concentration profiles in sediment pore water. *Limnol. Oceanogr.* **43**: 1500-1510.
- Berg, P., S. Rysgaard, and B. Thamdrup. 2003. Dynamic modeling of early diagenesis and nutrient cycling. A case study in an arctic marine sediment. *Am. J. Sci.* **303**: 905-955.
- Beutel, M. W. 2003. Hypolimnetic anoxia and sediment oxygen demand in California drinking water reservoirs. *Lake Reserv. Manage.* **19**: 208-221.
- Boudreau, B. P. 2001. Solute transport above the sediment-water interface, p. 104-126. *In* B. P. Boudreau and B. B. Jørgensen [eds.], *The benthic boundary layer: transport processes and biogeochemistry*. Oxford University Press.
- Bouldin, D. R. 1968. Models for describing the diffusion of oxygen and other mobile constituents across the mud-water interface. *J. Ecol.* **56**: 77-87.
- Brand, A., C. Dinkel, and B. Wehrli. 2009. Influence of the diffusive boundary layer on the solute dynamics in the sediments of a seiche-driven lake: A model study. *J. Geophys. Res.* **114**: G01010, doi:10.1029/2008JG000755.
- Brand, A., D. F. McGinnis, B. Wehrli, and A. Wüest. 2008. Intermittent oxygen flux from the interior into the bottom boundary of lakes as observed by eddy correlation. *Limnol. Oceanogr.* **53**: 1997-2006.
- Brand, A., B. Müller, A. Wüest, C. Dinkel, N. P. Revsbech, L. P. Nielsen, O. Pedersen, L. R. Damgaard, L. H. Larsen, and B. Wehrli. 2007. Microsensor for in situ flow measurements in benthic boundary layers at submillimeter resolution with extremely slow flow. *Limnol. Oceanogr.: Methods.* **5**: 185-191.

- Dalsgaard, T. [ed.], L. P. Nielsen, V. Brotas, P. Viaroli, G. Underwood, D. B. Nedwell, K. Sundbäck, S. Rysgaard, A. Miles, M. Bartoli, L. Dong, D. C. O. Thornton, L. D. M. Ottosen, G. Castaldelli, and N. Risgaard-Petersen. 2000. Protocol handbook for NICE – Nitrogen Cycling in Estuaries: a project under the EU research programme: Marine Science and Technology (MAST III). National Environmental Research Institute, Silkeborg, Denmark.
- [http://www2.dmu.dk/LakeandEstuarineEcology/nice/NICE\\_handbook.pdf](http://www2.dmu.dk/LakeandEstuarineEcology/nice/NICE_handbook.pdf)
- Epping, E. H. G., and W. Helder. 1997. Oxygen budgets calculated from in situ microprofiles for Northern Adriatic sediments. *Cont. Shelf Res.* **17**:1737-1764.
- Fischer, H., F. Kloppe, S. Wilzcek, and M. T. Pusch. 2005. A river's liver - microbial processes within the hyporheic zone of a large lowland river. *Biogeochemistry* **76**: 349-371.
- Fischer, H., S. C. Wanner, and M. Pusch. 2002. Bacterial abundance and production in river sediments as related to the biochemical composition of particulate organic matter (POM). *Biogeochemistry* **61**: 37-55.
- Frenzel, P., B. Thebrath, and R. Conrad. 1990. Oxidation of methane in the oxic surface layer of a deep lake sediment (Lake Constance). *FEMS Microbiol. Ecol.* **73**: 149-158.
- Gantzer, P. A., L. D. Bryant, and J. C. Little. 2009a. Effect of hypolimnetic oxygenation on oxygen depletion rates in two water-supply reservoirs. *Water Res.* **43**: 1700-1710.
- Gantzer, P. A., L. D. Bryant, and J. C. Little. 2009b. Controlling soluble iron and manganese in a water-supply reservoir using hypolimnetic oxygenation. *Water Res.* **43**: 1285-1294.
- Gantzer, C. J., and H. G. Stefan. 2003. A model of microbial activity in lake sediments in response to periodic water-column mixing. *Water Res.* **37**: 2833-2846.
- Glud, R. N. 2008. Oxygen dynamics of marine sediments. *Mar. Biol. Res.* **4**: 243-289.
- Glud, R. N., P. Berg, H. Fossing, and B. B. Jørgensen. 2007. Effect of the diffusive boundary layer on benthic mineralization and O<sub>2</sub> distribution: A theoretical model analysis. *Limnol. Oceanogr.* **52**: 547-557.
- Glud, R. N., J. K. Gundersen, N. P. Revsbech, and B. B. Jørgensen. 1994. Effects on the benthic diffusive boundary layer imposed by microelectrodes. *Limnol. Oceanogr.* **39**: 462-467.
- Glud, R. N., J. K. Gundersen, H. Røy, and B. B. Jørgensen. 2003. Seasonal dynamics of benthic O<sub>2</sub> uptake in a semi enclosed bay: Importance of diffusion and fauna activity. *Limnol. Oceanogr.* **48**: 1265-1276.

- Glud, R. N., H. Stahl, P. Berg, F. Wenzhöfer, K. Oguri, and H. Kitazato. 2009. In situ microscale variation in distribution and consumption of O<sub>2</sub>: A case study from a deep ocean margin sediment (Sagami Bay, Japan). *Limnol. Oceanogr.* **54**: 1-12.
- Grant, H. L., R. W. Stewart, and A. Moilliet. 1962. Turbulence spectra from a tidal channel. *J. Fluid Mech.* **12**: 241-263.
- Gundersen, J. K., and B. B. Jørgensen. 1990. Microstructure of diffusive boundary layers and the oxygen uptake of the sea floor. *Nature* **345**: 604–607.
- Higashino, M., C. J. Gantzer, and H. G. Stefan. 2004. Unsteady diffusional mass transfer at the sediment/water interface: Theory and significance for SOD measurement. *Water Res.* **38**: 1-12.
- Higashino, M., B. L. O'Connor, M. Hondzo, and H. G. Stefan. 2008. Oxygen transfer from flowing water to microbes in an organic sediment bed. *Hydrobiologia* **614**: 219-231.
- Higashino, M., and H. G. Stefan. 2005. Sedimentary microbial oxygen demand for laminar flow over a sediment bed of finite length. *Water Res.* **39**: 3153-3166.
- Hondzo, M., T. Feyaerts, R. Donovan, and B. L. O'Connor. 2005. Universal scaling of dissolved oxygen distribution at the sediment-water interface: A power law. *Limnol. Oceanogr.* **50**: 1667-1676.
- Jørgensen, B. B., and B. P. Boudreau. 2001. Diagenesis and sediment-water exchange, p. 211-244. *In* B. P. Boudreau and B. B. Jørgensen [eds.], *The benthic boundary layer: transport processes and biogeochemistry*. Oxford University Press.
- Jørgensen, B. B., and N. P. Revsbech. 1985. Diffusive boundary layers and the oxygen uptake of sediments and detritus. *Limnol. Oceanogr.* **30**: 111-122.
- Jørgensen, B. B., N. P. Revsbech, T. H. Blackburn, and Y. Cohen. 1979. Diurnal cycle of oxygen and sulfide microgradients and microbial photosynthesis in a cyanobacterial mat sediment. *Appl. and Env. Microbiol.* **38**: 46-58.
- Li, Y.-H., and S. Gregory. 1974. Diffusion of ions in sea water and in deep-sea sediments. *Geochem. Cosmochim. Acta* **38**: 703-714.
- Lorke, A., B. Müller, M. Maerki, and A. Wüest. 2003. Breathing sediments: The control of diffusive transport across the sediment-water interface by periodic boundary-layer turbulence. *Limnol. Oceanogr.* **46**: 2077-2085.

- Lorke, A., F. Peeters, and A. Wüest. 2005. Shear-induced convective mixing in bottom boundary layers on slopes. *Limnol. Oceanogr.* **50**: 1612-1619.
- Lorke, A., L. Umlauf, T. Jonas, and A. Wüest. 2002. Dynamics of turbulence in low-speed oscillating bottom-boundary layers of stratified basins. *Environ. Fluid Mech.* **2**: 291-313.
- Mackenthun, A. A., and H. G. Stefan. 1998. Effect of flow velocity on sediment oxygen demand: Experiments. *J. Environ. Eng.-ASCE* **124**: 222-230.
- Müller, B., M. Maerki, C. Dinkel, R. Stierli, and B. Wehrli. 2002. In situ measurements in lake sediments using ion-selective electrodes with a profiling lander system, p. 126-143. *In* M. Taillefert and T. F. Rozan [eds.], *Environmental electrochemistry: Analyses of trace element biogeochemistry*. ACS symposium series 811, ACS, Washington DC.
- Münnich, M., A. Wüest, and D. M. Imboden. 1992. Observations of the second vertical mode of the internal seiche in an alpine lake. *Limnol. and Oceanogr.* **37**: 1705-1719.
- O'Connor, B. L., and J. W. Harvey. 2008. Scaling hyporheic exchange and its influence on biogeochemical reactions in aquatic ecosystems. *Water Resour. Res.* **44**: W12423, doi:10.1029/2008WR007160.
- O'Connor, B. L., and M. Hondzo. 2008. Dissolved oxygen transfer to sediments by sweep and eject motions in aquatic environments. *Limnol. and Oceanogr.* **53**: 566-578.
- Rasmussen, H., and B. B. Jørgensen. 1992. Microelectrode studies of seasonal oxygen uptake in a coastal sediment: role of molecular diffusion. *Mar. Ecol. Prog. Ser.* **81**: 289-303.
- Reichert, P. 1994. AQUASIM - a tool for simulation and data analysis of aquatic systems. *Water Sci. Tech.* **30**: 21-30.
- Røy, H., M. Huettel, and B. B. Jørgensen. 2004. Transmission of oxygen concentration fluctuations through the diffusive boundary layer overlying aquatic sediments. *Limnol. Oceanogr.* **49**: 686-692.
- Santschi, P., P. Höhener, G. Benoit, and M. Buchholtz-ten Brink. 1990. Chemical processes at the sediment-water interface. *Mar. Chem.* **30**: 269-315.
- Stachowitsch, M., B. Riedel, M. Zuschin, and R. Machan. 2007. Oxygen depletion and benthic mortalities: the first in situ experimental approach to documenting an elusive phenomenon. *Limnol. Oceanogr.: Methods.* **5**: 344-352.
- Veenstra, J. N., and S. L. Nolen. 1991. In situ sediment oxygen demand in five southwestern U.S. lakes. *Water Res.* **25**: 351-354.

- Wetzel, R. G. 2001. *Limnology: Lake and river ecosystems*, 3<sup>rd</sup> ed. Academic Press.
- Wüest, A., and A. Lorke. 2003. Small-scale hydrodynamics in lakes. *Annu. Rev. Fluid Mech.* **35**: 373-412.
- Wüest, A., Piepke, G., and D. C. Van Senden. 2000. Turbulent kinetic energy balance as a tool for estimating vertical diffusivity in wind-forced stratified waters. *Limnol. Oceanogr.* **45**: 1388-1400.
- Wyngaard, J. C., and O. R. Coté. 1971. The budgets of turbulent kinetic energy and temperature variance in the atmospheric surface layer. *J. Atmos. Sci.* **28**: 190-201.
- Zhang, H., W. Davison, and C. Ottley. 1999. Remobilisation of major ions in freshly deposited lacustrine sediment at overturn. *Aquat. Sci.* **61**: 354-361.

Table 2.1. Acronyms and notations with corresponding units used for this study.

ADP	Acoustic Doppler Aquadopp profiler; used to obtain velocity profile data
ADV	Acoustic Doppler velocimeter; used to obtain local (pointwise), high-frequency velocity data
BBL	Bottom boundary layer
D	Molecular O <sub>2</sub> diffusion coefficient (m <sup>2</sup> d <sup>-1</sup> )
DBL	Diffusive boundary layer
C <sub>bulk</sub>	Concentration of O <sub>2</sub> in bulk BBL (μmol L <sup>-1</sup> )
C <sub>SWI</sub>	Concentration of O <sub>2</sub> at SWI (μmol L <sup>-1</sup> )
∂C/∂t <sub>v</sub>	Volumetric change in O <sub>2</sub> concentration over time (mmol m <sup>-3</sup> d <sup>-1</sup> )
∂C/∂t <sub>a</sub>	Areal change in O <sub>2</sub> concentration over time (mmol m <sup>-2</sup> d <sup>-1</sup> )
∂C/∂z	O <sub>2</sub> concentration gradient (mmol m <sup>-4</sup> )
J <sub>O<sub>2</sub></sub>	SWI flux of O <sub>2</sub> into the sediment (mmol m <sup>-2</sup> d <sup>-1</sup> )
M <sub>O<sub>2</sub></sub>	Vertically integrated mass of O <sub>2</sub> in sediment (μmol m <sup>-2</sup> )
O <sub>2</sub>	Dissolved oxygen (μmol L <sup>-1</sup> )
PSOD	Potential sediment O <sub>2</sub> demand (mmol m <sup>-3</sup> d <sup>-1</sup> )
R <sub>O<sub>2</sub></sub>	O <sub>2</sub> consumption rate in sediment, defined volumetrically (R <sub>O<sub>2v</sub></sub> ) or areally (R <sub>O<sub>2a</sub></sub> )
R <sub>O<sub>2a</sub></sub>	Areal O <sub>2</sub> consumption rate in sediment (mmol m <sup>-2</sup> d <sup>-1</sup> ) where R <sub>O<sub>2a</sub></sub> is the vertical integral of volumetric R <sub>O<sub>2v</sub></sub> (Eq. 2.2)
R <sub>O<sub>2v</sub></sub>	Volumetric O <sub>2</sub> consumption rate in sediment (mmol m <sup>-3</sup> d <sup>-1</sup> )
SWI	Sediment-water interface
u*	Friction velocity (cm s <sup>-1</sup> )
z	Distance above or below SWI (mm)
z <sub>max</sub>	Depth of sediment oxic zone (mm)
δ <sub>DBL</sub>	DBL thickness (mm)
ε	Dissipation rate of turbulent kinetic energy (W kg <sup>-1</sup> )
φ	Porosity (void volume per total sediment volume; dimensionless)
σ	Standard deviation (units correspond to parameter of interest)

Table 2.2. Mean estimates of friction velocity ( $u_*$ ), energy dissipation rate ( $\epsilon$ ), and intermittency ( $\sigma_{\ln(\epsilon)}$ ) of  $\epsilon$ .

Profile number <sup>(1)</sup>	Time sensors contacted SWI <sup>(1)</sup>	Friction velocity, $u_*$ (cm s <sup>-1</sup> )	Energy dissipation rate, $\epsilon$ (W kg <sup>-1</sup> )	$\epsilon$ intermittency, $\sigma_{\ln(\epsilon)}$ (-)
1 <sup>(2)</sup>	27 Aug 07 21:14 h	(0.007)	( $8.4 \times 10^{-12}$ )	(2.4)
2	22:05 h	0.067	$7.5 \times 10^{-9}$	0.2
3	22:57 h	0.055	$4.0 \times 10^{-9}$	0.5
4	23:50 h	0.079	$1.2 \times 10^{-8}$	0.2
5	28 Aug 07 00:42 h	0.064	$6.5 \times 10^{-9}$	0.6
6	01:36 h	0.042	$1.8 \times 10^{-9}$	0.3
7	02:27 h	0.024	$3.2 \times 10^{-10}$	0.2
8	03:19 h	0.008	$1.3 \times 10^{-11}$	0.8
9	04:12 h	0.007	$7.8 \times 10^{-12}$	1.2
10	05:05 h	0.022	$2.5 \times 10^{-10}$	0.8
11	05:59 h	0.030	$6.7 \times 10^{-10}$	0.5
12	06:53 h	0.049	$2.9 \times 10^{-9}$	0.0
13	07:44 h	0.056	$4.2 \times 10^{-9}$	0.4
14	08:37 h	0.040	$1.6 \times 10^{-9}$	0.3

<sup>(1)</sup> Data are compared by profile number, which represents the time each microsensor profile was obtained during the Alpnach campaign. The time assigned to each profile was the time at which the microsensor encountered the SWI.

<sup>(2)</sup> Outlier data for profile 1 placed in parentheses.

Table 2.3. Results of the five analytical methods used for sediment O<sub>2</sub> uptake rate (J<sub>O<sub>2</sub></sub>) and diffusive boundary layer thickness ( $\delta_{DBL}$ ) calculations.

Method	Profile number	1	2	3	4	5	6	7	8	9	10	11	12	13	14
<i>Direct:</i> Measured gradient	$\delta_{DBL}$ (mm)	0.6	0.9	1.3	1.0	1.0	1.4	1.9	5.9	6.3	1.4	1.3	2.2	0.8	1.0
	J <sub>O<sub>2</sub></sub> (mmol m <sup>-2</sup> d <sup>-1</sup> )	9.9	8.1	5.1	7.6	7.0	6.5	4.5	1.6	1.2	6.8	7.2	4.0	7.6	5.5
<i>u*:</i> Function of friction velocity	$\delta_{DBL}$ (mm)	3.0	0.8	0.9	0.8	0.8	1.2	1.9	4.6	6.7	1.6	1.2	1.5	0.7	0.9
	J <sub>O<sub>2</sub></sub> (mmol m <sup>-2</sup> d <sup>-1</sup> )	2.0	9.0	7.6	9.6	8.2	7.8	4.6	2.0	1.2	5.8	8.0	5.7	8.1	6.4
<i>Curvefit:</i> Best-fit of single curve	$\delta_{DBL}$ (mm)	1.3	1.3	1.2	1.3	1.1	2.2	2.2	8.7	11.1	1.6	2.0	1.9	0.9	1.2
	J <sub>O<sub>2</sub></sub> (mmol m <sup>-2</sup> d <sup>-1</sup> )	4.5	6.0	5.6	5.9	6.1	4.1	3.9	1.1	0.7	5.9	4.7	4.5	6.8	4.6
<i>Zonefit:</i> Fitting multiple zones via PROFILE	$\delta_{DBL}$ (mm)	1.2	1.1	1.3	1.2	1.1	1.7	2.4	9.3	6.0	1.6	1.7	2.1	0.9	1.3
	J <sub>O<sub>2</sub></sub> (mmol m <sup>-2</sup> d <sup>-1</sup> )	5.2	7.1	5.4	6.4	6.1	5.3	3.5	1.0	1.3	5.8	5.6	4.0	6.9	4.4
<i>Model:</i> DBL estimation via AQUASIM	$\delta_{DBL}$ (mm)	1.0	1.8	1.2	1.5	0.9	1.7	2.2	9.7	9.0	2.2	2.0	1.7	1.0	0.9
	J <sub>O<sub>2</sub></sub> (mmol m <sup>-2</sup> d <sup>-1</sup> )	5.9	4.3	5.7	5.4	7.3	5.2	3.9	1.0	0.9	4.3	4.7	5.1	5.9	6.4
Average of five methods	$\delta_{DBL}$ (mm)	1.4	1.2	1.2	1.2	1.0	1.6	2.1	7.6	7.8	1.7	1.6	1.9	0.9	1.1
	J <sub>O<sub>2</sub></sub> (mmol m <sup>-2</sup> d <sup>-1</sup> )	±	±	±	±	±	±	±	±	±	±	±	±	±	±
	$\delta_{DBL}$ (mm)	0.9	0.4	0.2	0.3	0.1	0.4	0.2	2.3	2.2	0.3	0.4	0.3	0.1	0.2
	J <sub>O<sub>2</sub></sub> (mmol m <sup>-2</sup> d <sup>-1</sup> )	5.5	6.9	5.9	7.0	6.9	5.8	4.1	1.3	1.1	5.7	6.1	4.7	7.0	5.5
	$\delta_{DBL}$ (mm)	±	±	±	±	±	±	±	±	±	±	±	±	±	±
	J <sub>O<sub>2</sub></sub> (mmol m <sup>-2</sup> d <sup>-1</sup> )	2.9	1.8	1.0	1.7	0.9	1.4	0.5	0.5	0.3	0.9	1.5	0.7	0.8	0.9

Table 2.4. Average  $J_{O_2}$  and vertically-integrated areal rates of change in the  $O_2$  concentration over time ( $\partial C/\partial t_a$ ), areal sediment  $O_2$  consumption rates ( $R_{O_2a}$ ), and mass of  $O_2$  ( $M_{O_2}$ ) in the sediment.

Profile number	$J_{O_2}$ (mmol m <sup>-2</sup> d <sup>-1</sup> )	$\partial C/\partial t_a^{(1,2)}$ (mmol m <sup>-2</sup> d <sup>-1</sup> )	$R_{O_2a}^{(1)}$ (mmol m <sup>-2</sup> d <sup>-1</sup> )	$M_{O_2}^{(1)}$ ( $\mu$ mol m <sup>-2</sup> )
1	5.5	-0.68	6.2	50
2	6.9	-0.11	7.0	26
3	5.9	0.14	5.8	42
4	7.0	0.16	6.8	36
5	6.9	-0.02	7.0	54
6	5.8	-0.42	6.2	34
7	4.1	-0.44	4.5	23
8	1.3	-0.25	1.6	3
9	1.1	0.28	0.8	5
10	5.7	0.31	5.4	24
11	6.1	0.11	6.0	28
12	4.7	0.16	4.5	32
13	7.0	0.17	6.9	40
14	5.5	0.11	5.3	44
Average	5.2	$\pm 0.30$	5.3	32

<sup>(1)</sup> Profile-specific areal values of  $R_{O_2a}$ ,  $\partial C/\partial t_a$ , and  $M_{O_2}$  represent the integral over the depth of the sediment oxic zone.  $\partial C/\partial t_a$  was evaluated for each profile as follows: the profiles immediately before and after were compared (e.g., profiles 2 and 4 were compared to evaluate profile 3) to calculate the areal rate of change in  $O_2$  ( $\partial C/\partial t_a$ ).

<sup>(2)</sup> Quasi-steady-state is established by relatively insignificant values of  $\partial C/\partial t_a$  (5% of average  $J_{O_2}$ ).

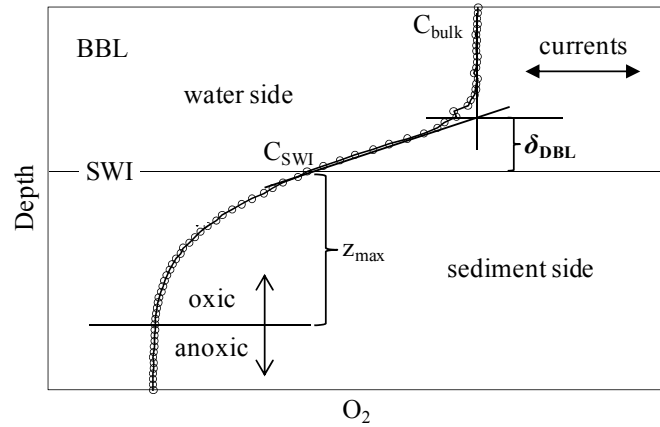


Figure 2.1. The key components of a dissolved oxygen ( $O_2$ ) profile are defined, illustrating the relationship between seicheing, turbulent mixing, and the vertical distribution of  $O_2$  on both sides of the sediment-water interface (SWI; modified from Jørgensen and Revsbech 1985). Water-side components include the bottom boundary layer (BBL), the diffusive boundary layer (of thickness  $\delta_{DBL}$ ), and  $O_2$  concentrations in the BBL ( $C_{bulk}$ ) and at the SWI ( $C_{SWI}$ ). On the sediment side,  $z_{max}$  is the depth of the sediment oxic zone.

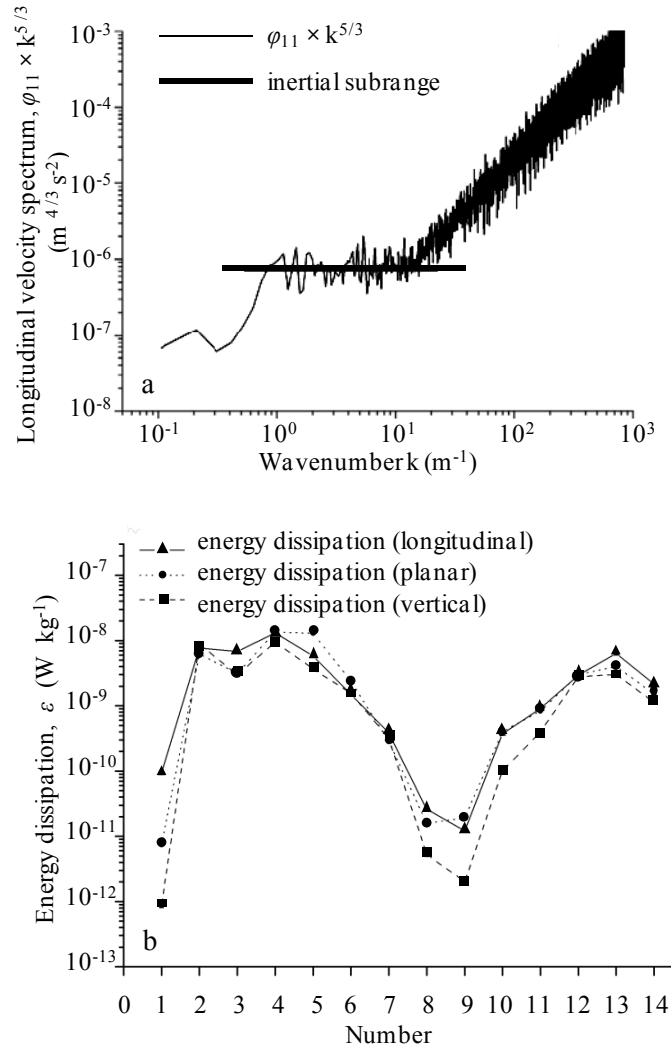


Figure 2.2. (a) The measured longitudinal velocity spectrum  $\varphi_{11}$  (with  $k^{-5/3}$  slope characteristic in the inertial subrange) is multiplied by  $k^{5/3}$  to be independent of wavenumber  $k$ . The constant value of  $\varphi_{11} \times k^{5/3}$ , indicated by the horizontal bar, is used to calculate the mean energy dissipation ( $\varepsilon$ ). (b) Dissipation rates ( $\varepsilon$ ) calculated by inertial dissipation method using longitudinal, planar, and vertical velocity data as measured via acoustic Doppler velocimeter (ADV). Note similarity in longitudinal and transversal  $\varepsilon$  values.

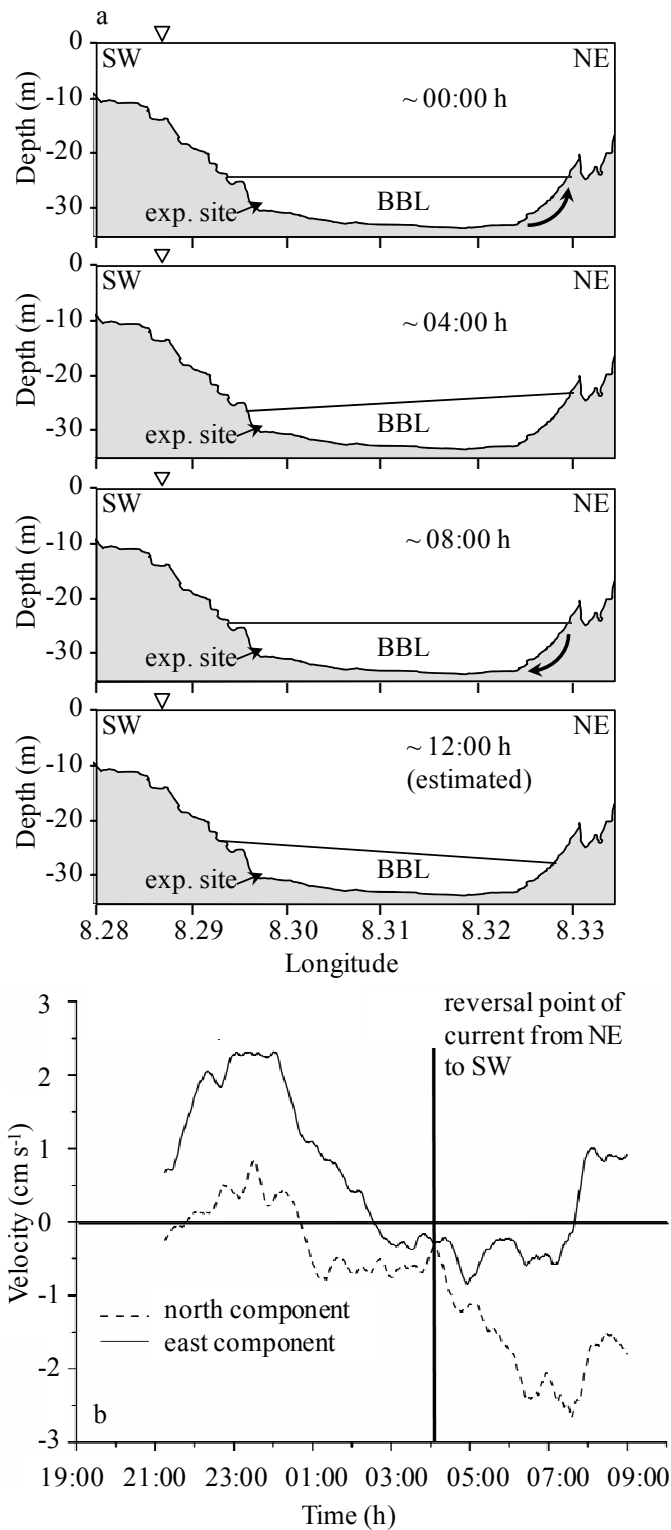


Figure 2.3. (a) Seiche cycle in Lake Alpnach and location of experiment site during 27 – 28 Aug 07 campaign. Note that water surface is indicated by downward-facing triangles and that scale of seiche is approximate. (b) East and north velocity components at 10 cm above the sediment as measured by the ADV. Bold vertical line marks the current reversal point where seiche-induced motion of the water body changed direction from northeast (NE) to southwest (SW).

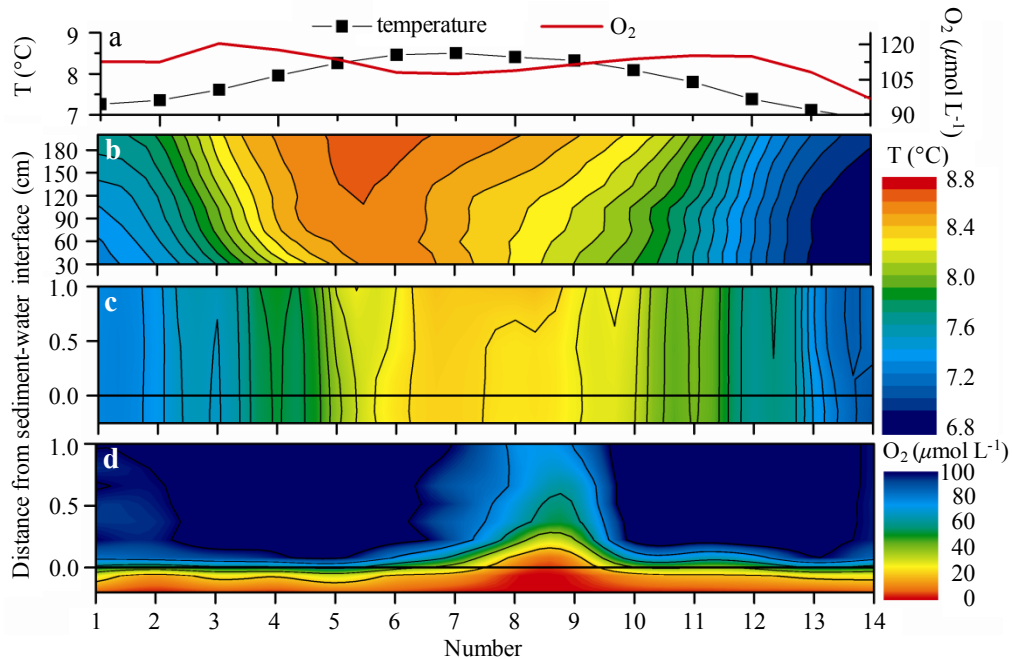


Figure 2.4. Temperature and O<sub>2</sub> data obtained on 27 – 28 Aug 07. (a) Temperature (T) and O<sub>2</sub> time series as measured using a thermistor logger at 8 cm above sediment. (b) Temperature contour plot showing data from 30 cm to 200 cm above sediment as measured via thermistors. (c and d) Temperature and O<sub>2</sub> contour plots showing data from -0.25 cm (in sediment) up to 1 cm (in water) as measured via micro-profiler microsensors (14 profiles throughout 12-h measurement period).

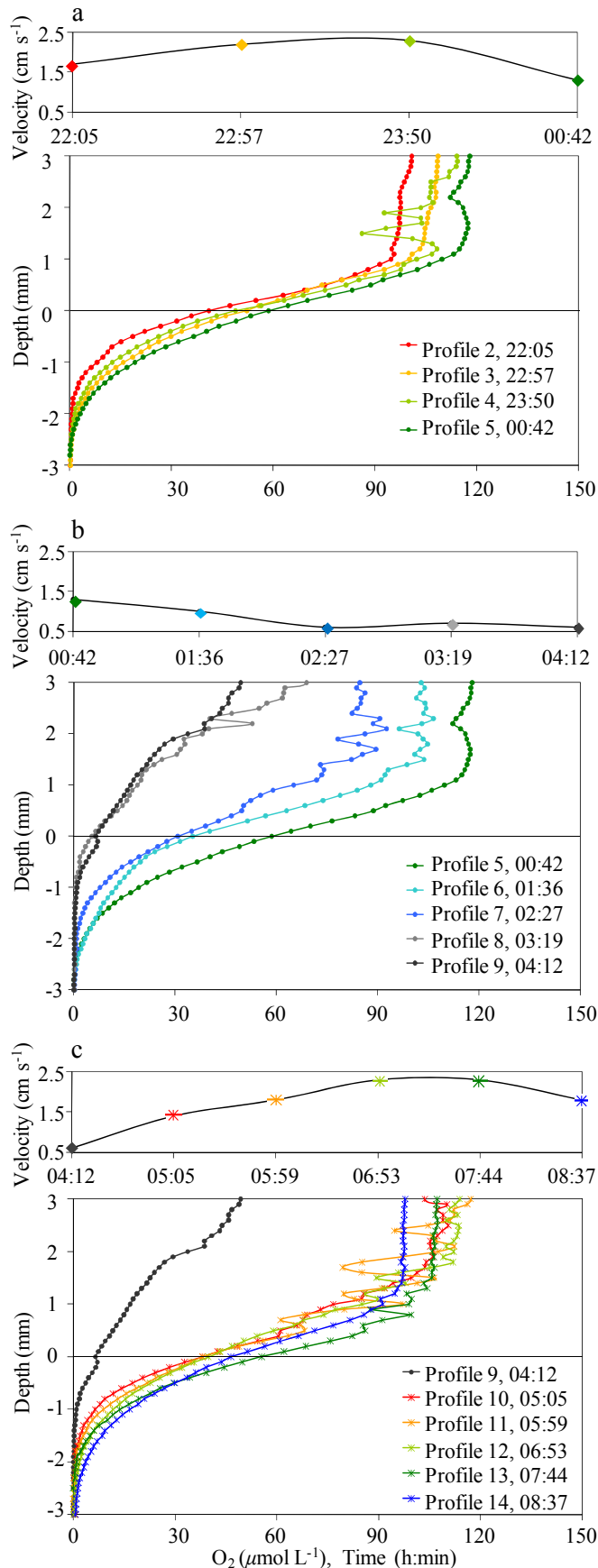


Figure 2.5. O<sub>2</sub> microprofiles obtained at approximately 50-min intervals relative to the ADV velocity time series. O<sub>2</sub> profiles are divided into three panels with corresponding section of velocity time series plotted above each O<sub>2</sub> profile panel (a – c). (a) Initially, current velocity is increasing and the O<sub>2</sub> profiles are observed to shift to the right toward more oxic conditions in both the water and the sediment with a corresponding decrease in  $\delta_{\text{DBL}}$  and increase in  $z_{\text{max}}$ . (b) As velocity decreases,  $\delta_{\text{DBL}}$  is shown to increase and  $z_{\text{max}}$  to decrease as the profiles shift to the left toward anoxic conditions in the sediment and overlying water. (c) As velocities return to initial levels, the O<sub>2</sub> profiles are observed to shift back to the right toward a more oxic distribution similar to that observed in (a).

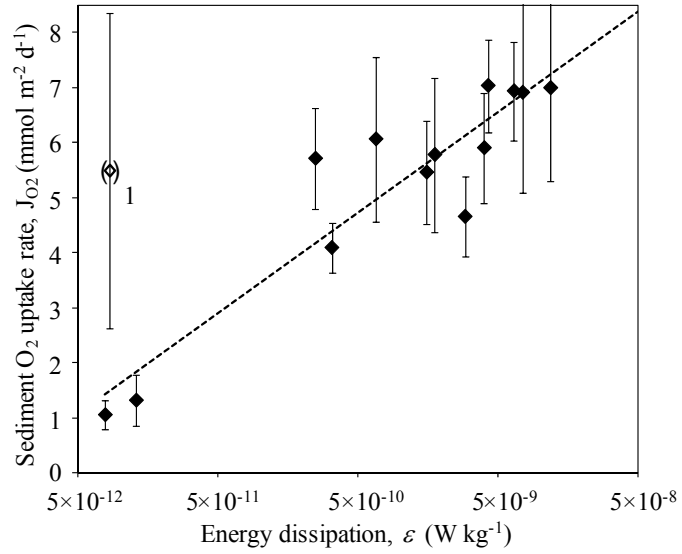


Figure 2.6. Correlation between  $\epsilon$  and sediment  $\text{O}_2$  uptake rate ( $J_{\text{O}_2}$ ). The linear trendline serves as a guide for the reader's eye and does not imply an explicit relationship between  $J_{\text{O}_2}$  and  $\epsilon$ . Because data for profile 1 are outliers, as discussed in the text, these data are placed in parentheses.

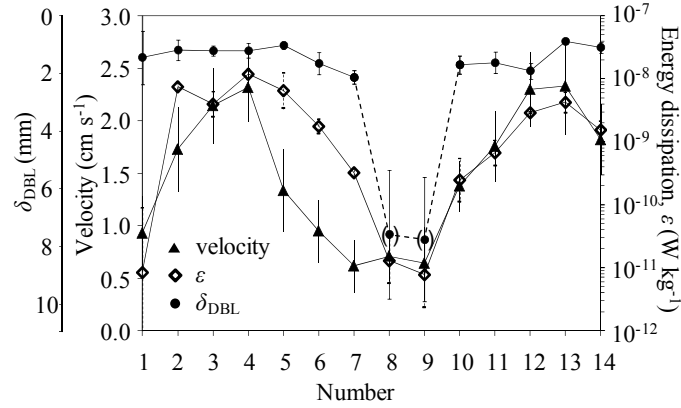


Figure 2.7. Time series of current velocity, turbulence (as defined by  $\epsilon$ ), and  $\delta_{\text{DBL}}$  showing close correlation between all three parameters with only a slight phase lag (on the order of minutes) between velocity and  $\epsilon$ . Similarity in  $\delta_{\text{DBL}}$  estimates obtained from different analytical methods is indicated by low standard deviations for  $\delta_{\text{DBL}}$ . The DBL becomes undefined during the period of negligible turbulence and thus corresponding  $\delta_{\text{DBL}}$  data (profiles 8 and 9) are placed in parentheses with dashed-line connectors to emphasize that these data are included solely as a relative comparison. Note reversed axis for  $\delta_{\text{DBL}}$ .

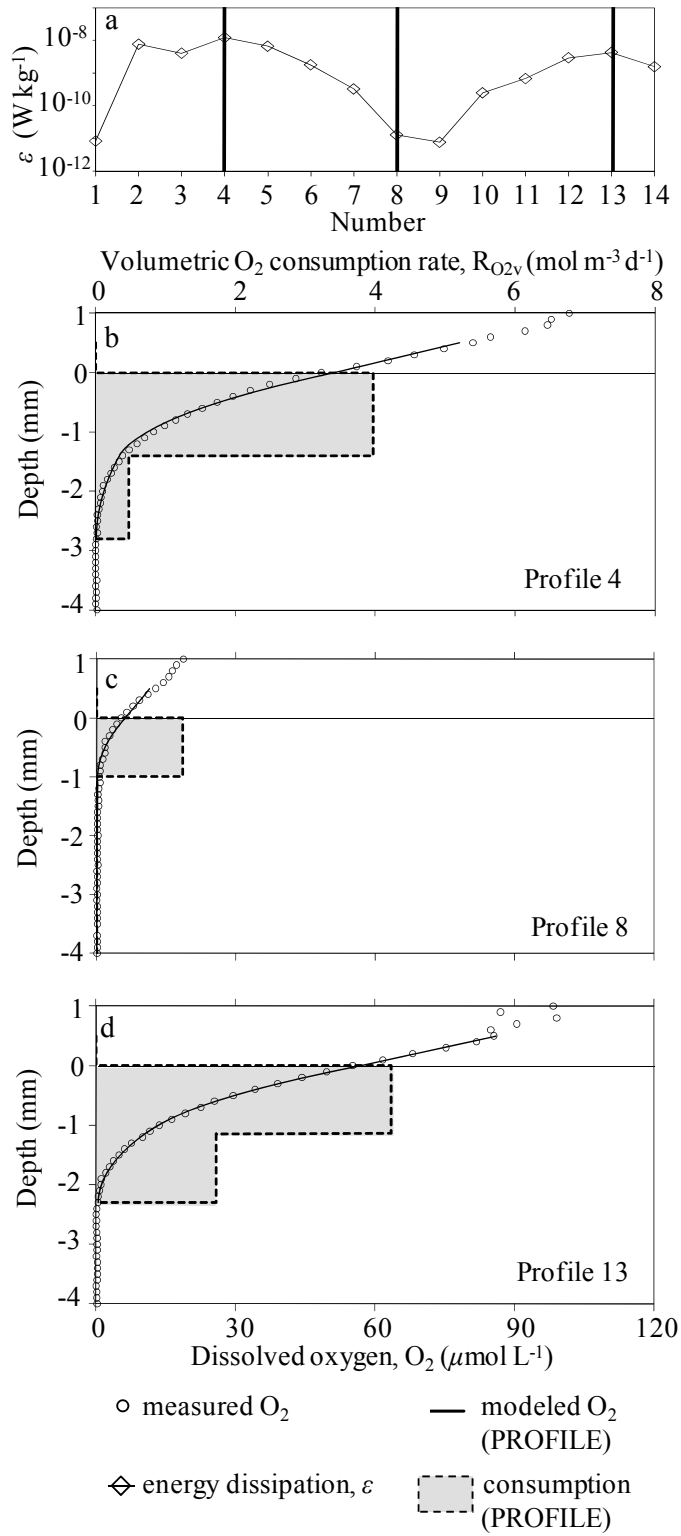


Figure 2.8. PROFILE model results defining zones of varying volumetric sediment O<sub>2</sub> consumption rates ( $R_{O_2v}$ ) for periods of active and inactive turbulence as characterized by  $\varepsilon$  in (a). During elevated turbulence (b and d), O<sub>2</sub> consumption is characterized by two zones. However, a single zone defines low consumption during the period of negligible turbulence (c).

## Chapter 3 – Evaluating oxygen fluxes from both sides of the sediment-water interface

Bryant, Lee D.<sup>a</sup>, Daniel F. McGinnis<sup>b</sup>, Claudia Lorrai<sup>c,d</sup>, Andreas Brand<sup>c,1</sup>, John C. Little<sup>a</sup>, Alfred Wüest<sup>c,d</sup>

<sup>a</sup>Civil and Environmental Engineering, Virginia Tech, Blacksburg, Virginia, USA 24061.

<sup>b</sup>IFM-GEOMAR, Leibniz Institute of Marine Sciences, RD2 Marine Biogeochemistry, Kiel, Germany D-24148.

<sup>c</sup>Eawag (Swiss Federal Institute of Aquatic Science and Technology), Surface Waters – Research and Management, Kastanienbaum, Switzerland CH-6047.

<sup>d</sup>Institute of Biogeochemistry and Pollutant Dynamics, ETH Zurich, Switzerland CH-8092.

Present address:

<sup>1</sup>Civil and Environmental Engineering, University of California, Berkeley, USA 94701.

Submitted in February 2010 to *Limnology and Oceanography: Methods*

### 3.1 Abstract

Sediment-water fluxes are influenced by both hydrodynamics and biogeochemical uptake processes within the sediment. However, fluxes at the sediment-water interface (SWI) are almost always analyzed from either a water- or sediment-side perspective. This study expands on previous work by comparing water-side (hydrodynamics and resulting diffusive boundary layer thickness  $\delta_{\text{DBL}}$ ) and sediment-side (oxygen consumption and resulting sediment oxic zone) approaches for evaluating sediment oxygen uptake rate ( $J_{\text{O}_2}$ ). Dissolved oxygen microprofile and current velocity data were analyzed using five common methods to estimate  $J_{\text{O}_2}$  and  $\delta_{\text{DBL}}$  and to assess the robustness of the approaches. Comparable values for both  $J_{\text{O}_2}$  and  $\delta_{\text{DBL}}$  were obtained (agreement within 20%) and turbulence-induced variations in these parameters were uniformly characterized with all five methods.  $J_{\text{O}_2}$  estimates based on water-side data were consistently higher (+1.8 mmol m<sup>-2</sup> d<sup>-1</sup> or 25% on average) and  $\delta_{\text{DBL}}$  estimates correspondingly lower (-0.4 mm or 35% on average) than those obtained using sediment-side data. This deviation may be attributed to artifacts of the methods themselves, assumptions made on sediment properties, and/or local variability in sediment oxygen uptake processes. Regardless, our overall results show clearly that calculations of  $J_{\text{O}_2}$  and  $\delta_{\text{DBL}}$  are not strongly dependent on

the method chosen for analysis. Benefits and limitations of each analytical method used are discussed.

### 3.2 Introduction

Problems related to low dissolved oxygen ( $O_2$ ) levels in aquatic ecosystems are growing on a global scale (Jankowski et al. 2006; Zimmerman et al. 2008).  $O_2$  depletion in stratified waters is largely controlled by sediment  $O_2$  uptake, particularly in organic-rich environments (Higashino et al. 2004). Flux of  $O_2$  across the sediment-water interface (SWI) may be governed by near-sediment hydrodynamic processes or by  $O_2$  consumption within the sediment (Gundersen and Jørgensen 1990; Jørgensen and Boudreau 2001; Glud et al. 2007). Turbulence in the bottom boundary layer (BBL) controls the thickness ( $\delta_{DBL}$ ) of the diffusive boundary layer (DBL), the mm-scale region immediately above the sediment that typically regulates mass transport of  $O_2$  to the SWI in non-advective systems (Jørgensen and Revsbech 1985; Lorke et al. 2003; Bryant et al. 2010; Ch. 2). Within the sediment, the distribution of  $O_2$  is determined by a balance between the amount of  $O_2$  supplied via diffusion and the amount of  $O_2$  used by biogeochemical oxidation processes (Berg et al. 2003). Quantifying the sediment  $O_2$  uptake rate ( $J_{O_2}$ ) is fundamental in characterizing the availability of  $O_2$  and corresponding ecological conditions in an aquatic system.

A wealth of literature exists on the various methods used for estimating  $J_{O_2}$  (Jørgensen and Revsbech 1985; Nishihara and Ackerman 2007; Glud 2008).  $J_{O_2}$  is typically evaluated from either a water- or sediment-side perspective (O'Connor et al. 2009). Considerable research has focused on hydrodynamic controls of  $\delta_{DBL}$  and corresponding  $O_2$  transport to the sediment (Boudreau 2001; Lorke et al. 2003; Hondzo et al. 2005). Water-side,  $\delta_{DBL}$ -based approaches are simpler because they do not account for  $O_2$  consumption within the sediment and thus only diffusive mass transfer is considered (Glud 2008; O'Connor and Harvey 2008). However, both rapid turbulence-driven variations in  $\delta_{DBL}$  and the short residence time of  $O_2$  in the DBL cause  $\delta_{DBL}$  to be a difficult parameter to resolve (Røy et al. 2004; O'Connor and Hondzo 2008). Furthermore, microsensors measurements of the DBL can disrupt boundary layer flow, leading to compression of the DBL and thus changing  $\delta_{DBL}$  (Glud et al. 1994).

While water-side problems are avoided by using sediment-side methods, there are additional complexities related to O<sub>2</sub> transport and consumption processes within the sediment (Glud 2008). Sediment-side data are often more difficult to interpret due to natural sediment heterogeneity (e.g., porosity and grain size; Maerki et al. 2004). Also, while lateral advection and mixing maintains a fairly uniform O<sub>2</sub> concentration in the BBL, variations in sediment O<sub>2</sub> levels are much more site-specific due to sediment heterogeneity (O'Connor and Hondzo 2008). Sediment O<sub>2</sub> consumption processes can vary either spatially (e.g., increased reactive surface area due to microtopography; Røy et al. 2002) or occur non-locally (e.g., small-scale variation in benthic communities; Rabouille et al. 2003; Glud et al. 2009). Despite these complications, porewater O<sub>2</sub> profile data can reveal important information about the sediment O<sub>2</sub> consumption rate (R<sub>O<sub>2</sub></sub>), the extent of the sediment oxic zone (Epping and Helder 1997; Berg et al. 1998; Bryant et al. 2010; Ch. 2), and solute dynamics (Berg et al. 2007a; Glud et al. 2007; Brand et al. 2009).

While numerous approaches are used for assessing J<sub>O<sub>2</sub></sub>, no single method has been shown to be optimal and further evaluation of how the various methods compare is needed (Nishihara and Ackerman 2007; Glud 2008). Furthermore, because sediment O<sub>2</sub> uptake can be affected by processes on both sides of the SWI, evaluating J<sub>O<sub>2</sub></sub> from a one-sided perspective could result in different and biased interpretations of J<sub>O<sub>2</sub></sub> and R<sub>O<sub>2</sub></sub>. Using in situ velocity and O<sub>2</sub> microprofile data obtained during a companion study on the dynamic nature of J<sub>O<sub>2</sub></sub> (Bryant et al. 2010; Ch. 2), the present work evaluates the robustness of several established methods for flux estimation based on both water- and sediment-side approaches. Some of the methods assessed have thus far been applied primarily in theoretical or laboratory-based studies (O'Connor and Hondzo 2008; Brand et al. 2009). The advantages and limitations of the different methods are discussed with respect to analytical approach and applicability. To our knowledge, while estimations of J<sub>O<sub>2</sub></sub> based on (1) hydrodynamics, (2) the vertical distribution of O<sub>2</sub> above the sediment, and (3) sediment porewater concentration data have been well justified in previous work (Jørgensen and Revsbech 1985; Rasmussen and Jørgensen 1992; Lorke et al. 2003), this is one of the first studies that incorporates all three of these components into a comprehensive evaluation of J<sub>O<sub>2</sub></sub> and  $\delta_{\text{DBL}}$  using in situ data.

### 3.3 Materials and procedures

**3.3.1 Study site and in-situ instrumentation** – During a 12-h field campaign in Lake Alpnach, Switzerland on 27 to 28 August 2007, high-resolution SWI microprofile data and velocity data were collected at a depth of 22 m to determine  $J_{O_2}$  and  $\delta_{DBL}$ . Basic information on the experimental set-up used is described here, with additional details included in the companion paper (Bryant et al. 2010; Ch. 2). Frequently-used acronyms and notations are defined in Table 3.1.

High-resolution  $O_2$  profiles were measured across the SWI using a micro-profiler (MP4, Unisense A/S) equipped with a Clark-type  $O_2$  microsensor (100- $\mu$ m diameter and depth resolution; 90% response time in  $< 8$  s). Profiles were measured continuously (profile duration of  $\sim 50$  min) at the following resolution: 10-mm increments from 10 cm to 1 cm above the SWI, 1-mm increments from 1 cm to 0.5 cm above the SWI, 0.1-mm increments from 0.5 cm above to 0.5 cm below the SWI. Following a pause between measurements to establish equilibrium, 10 data points were collected at a rate of 1 Hz at each depth (no trend in variation of the data set was evident, confirming that data aliasing did not occur). Fourteen  $O_2$  profiles were obtained during our 12-h campaign and the  $O_2$  profile number (1 – 14) is used for comparison of results. An  $O_2$  logger (TDO-2050; RBR Ltd.) was mounted on the micro-profiler to obtain measurements of 1 Hz at 8 cm above the sediment for calibration of the  $O_2$  microsensor. The TDO-2050 has a 90% response time of  $< 10$  s, a measurement range of 0% to 150%  $O_2$  saturation, resolution of  $\pm 1\%$  and accuracy of  $\pm 2\%$   $O_2$  saturation. TDO-2050 data were calibrated via Winkler titration of water samples obtained from the same depth with a Niskin bottle.

Water velocity time series corresponding to each  $O_2$  profile were collected continuously at a single point using an acoustic Doppler velocimeter (ADV; Vector, Nortek). The ADV, positioned at 10 cm above the SWI via tripod, continuously measured three-dimensional velocity data at 32 Hz with an accuracy of 0.5% of the measured value or  $\pm 0.1$  cm s<sup>-1</sup>. ADV velocity data were used to analyze the current structure and to characterize turbulence and friction velocity within the law-of-the-wall layer.

**3.3.2 Turbulence analyses** – Turbulence in the BBL was defined by the rate of dissipation of turbulent kinetic energy  $\varepsilon$  (W kg<sup>-1</sup>) using the inertial dissipation method (Grant et al. 1962).

Additional details on how turbulence was analyzed may be found in Bryant et al. (2010; Ch. 2). Average  $\varepsilon$  values were assessed based on the duration of each O<sub>2</sub> profile and hence  $\varepsilon$  estimates represent a time span of ~50 min. Because turbulence is highly intermittent, dissipation is averaged by assuming lognormal distribution. Standard deviations of  $\ln(\varepsilon)$ , or the intermittency of  $\varepsilon$ , were evaluated using the method defined by Baker and Gibson (1987).

**3.3.3 Friction velocity analyses** – Friction velocity ( $u_*$ ) quantifies the frictional stress of BBL currents on the sediment. Law-of-the-wall theory and estimated mean  $\varepsilon$  values were used to calculate  $u_*$  at a height ( $h$ ) of 10 cm above the sediment (Lorke et al. 2003):

$$u_* = \sqrt[3]{\varepsilon \kappa h} \quad [\text{m s}^{-1}] \quad (3.1)$$

where  $\kappa$  (von Karman constant) is 0.41.

**3.3.4 Methods for J<sub>O<sub>2</sub></sub> analyses** – Five different methods (*direct*, *u\**, *curvefit*, *zonefit*, and *model*; Table 3.1) were used to analyze J<sub>O<sub>2</sub></sub> and  $\delta_{\text{DBL}}$  from both sides of the SWI (Fig. 3.1). Water-side O<sub>2</sub> microsensor data were used for the *direct method* and the *u\* method*, which also incorporates ADV velocity data. Sediment-side O<sub>2</sub> microsensor data were analyzed with polynomial curve equations (*curvefit method*) and/or numerical procedures (*zonefit and model methods*). Key components of the vertical O<sub>2</sub> distribution used in these calculations are shown schematically in Fig. 3.1a.

Each method yielded results for either J<sub>O<sub>2</sub></sub> or  $\delta_{\text{DBL}}$  and then the corresponding parameter ( $\delta_{\text{DBL}}$  or J<sub>O<sub>2</sub></sub>, respectively) was evaluated using Fick's first law of diffusion (Rasmussen and Jørgensen 1992; Lavery 2001; Higashino et al. 2004):

$$J_{\text{O}_2} = -\varphi D_s \frac{\partial C}{\partial z} = -D \frac{\partial C}{\partial z} = D \frac{C_{\text{bulk}} - C_{\text{SWI}}}{\delta_{\text{DBL}}} \quad [\text{mmol m}^{-2} \text{d}^{-1}] \quad (3.2)$$

where  $\varphi$  is sediment porosity (m<sup>3</sup> voids m<sup>-3</sup> total volume),  $D_s$  is the diffusion coefficient for O<sub>2</sub> in sediment (m<sup>2</sup> s<sup>-1</sup>),  $D$  is the diffusion coefficient for O<sub>2</sub> in water (m<sup>2</sup> s<sup>-1</sup>),  $\partial C/\partial z$  is the linear O<sub>2</sub>

concentration gradient in the DBL immediately above or below the SWI ( $\mu\text{mol m}^{-4}$ ),  $C_{\text{bulk}}$  is the  $\text{O}_2$  concentration in the bulk BBL ( $\mu\text{mol L}^{-1}$ ), and  $C_{\text{SWI}}$  is the  $\text{O}_2$  concentration at the SWI ( $\mu\text{mol L}^{-1}$ ), as shown in Fig. 3.1a. Diffusive transport is hence defined in the sediment by the second term in Eq. 3.2 and in the water by the third and fourth terms. Values for  $D$  were based on  $D = 1.97 \times 10^{-9} \text{ m}^2 \text{ s}^{-1}$  at  $20^\circ\text{C}$  and correcting for temperature using the Stokes-Einstein relationship (Li and Gregory 1974; Arega and Lee 2005).  $D_s$  was defined as  $D_s = \phi D$  (multiplying by  $\phi$  provides a simple correction for tortuosity that ignores other possible higher-order corrections; Berg et al. 1998; Glud 2008). This simple tortuosity correction thus increases the influence of  $\phi$  on diffusive transport in the sediment ( $\phi D_s = \phi^2 D$  in the second term of Eq. 3.2) as compared to the usual term which only corrects for  $\phi$  (e.g., using  $\phi D$  rather than  $\phi D_s = \phi^2 D$  in the second term of Eq. 3.2; Higashino et al. 2004; Bryant et al. 2010; Ch. 2). The temporal change in  $\text{O}_2$  concentration ( $\partial C/\partial t$ ) was evaluated for our series of 14  $\text{O}_2$  profiles by comparing profiles immediately before and after one another and calculating the rate of change in  $\text{O}_2$  at each depth;  $\partial C/\partial t$  was found to be on average  $\sim 5\%$  of  $J_{\text{O}_2}$  (Bryant et al. 2010; Ch. 2), thus establishing that our profiles were at quasi-steady state.

In the absence of a video camera, SWI estimation was based on both visual interpretation of each profile (identifying linear DBL regions and profile kinks related to  $\phi$  differences between the water and the sediment; Røy et al. 2004) and assessment of  $\text{O}_2$  standard deviations (variation should decrease approaching the SWI due to reduced turbulence fluctuations; Müller et al. 2002; Brand et al. 2007). To account for sediment  $\phi$  when Eq. 3.2 was applied to porewater for the sediment-side methods,  $\phi$  measurements were performed on sediment cores taken from our experiment site (following protocol per Dalsgaard et al. 2000). Supporting  $\phi$  predictions were also obtained using the numerical model PROFILE (Berg et al. 1998) to analyze  $\phi$  at a greater depth resolution than possible with core tests (Bryant et al. 2010; Ch. 2). From these evaluations, average  $\phi$  values of 0.95 in the upper 1 mm and 0.90 at  $> 1$  mm below the SWI were obtained and subsequently used in  $J_{\text{O}_2}$  calculations and/or as model input parameters.

$J_{\text{O}_2}$  estimates obtained using Fick's law (Eq. 3.2) describe diffusive, not total,  $\text{O}_2$  uptake. Thus, influences on non-diffusive  $\text{O}_2$  uptake, such as variations in sediment topography, advective porewater flow (typical of porous sediment), and irrigation, are not taken into account (Berg et al. 1998; Jørgensen 2001). With the exception of the *zonefit method* (which evaluates  $J_{\text{O}_2}$  as a function of  $R_{\text{O}_2}$ ), all methods used in this study are based on estimating  $J_{\text{O}_2}$  directly from

Eq. 3.2 and thus characterize diffusive uptake. While non-diffusive O<sub>2</sub> uptake processes could have been incorporated into some of our analyses, these effects were neglected for the sake of comparison between methods.

*3.3.4.1 Direct method* – J<sub>O<sub>2</sub></sub> was evaluated directly from the linear slope of the DBL, as measured via the O<sub>2</sub> microsensor (Fig. 3.1b). The DBL slope  $\partial C/\partial z$  was incorporated into Eq. 3.2 to obtain J<sub>O<sub>2</sub></sub> and corresponding  $\delta_{\text{DBL}}$ . The right-hand term in Eq. 3.2 quantifies  $\delta_{\text{DBL}}$  in terms of an ‘effective’ DBL (Jørgensen and Revsbech 1985), which is obtained by extrapolating  $\partial C/\partial z$  at the SWI to C<sub>bulk</sub> in the water column. This conceptual definition of the DBL corresponds to the extension of the ‘true’ DBL (based solely on the actual linear region) from the laminar region above the SWI to the mixed bulk region.

*3.3.4.2 u\* method* – Because accurate microsensor measurements of the DBL are challenging, an alternative method has been developed that estimates  $\delta_{\text{DBL}}$  as a function of hydrodynamics (Hondzo et al. 2005; O’Connor and Hondzo 2008). This method uses a simplified dimensionless power law for the universal scaling of the vertical O<sub>2</sub> distribution in the bulk water to estimate  $\delta_{\text{DBL}}$  (Fig. 3.1c). Dimensionless power law scaling was applied to friction velocity (u\*) data derived from ADV velocity series to solve for a non-dimensional DBL thickness ( $\delta_{\text{DBL}}^+$ ; Hondzo et al. 2005):

$$C^+ = \begin{cases} z^+ \frac{\nu}{D} & \text{for } z^+ < \delta_{\text{DBL}}^+ \\ \delta_{\text{DBL}}^+ \frac{\nu}{D} + B\text{Sc}_t \left( \frac{1}{\delta_{\text{DBL}}^{+2}} - \frac{1}{z^{+2}} \right) & \text{for } z^+ \geq \delta_{\text{DBL}}^+ \end{cases} \quad \text{[dimensionless]} \quad (3.3)$$

where  $C^+$ ,  $z^+$ , and  $\delta_{\text{DBL}}^+$  are non-dimensional parameters for concentration, depth, and estimated  $\delta_{\text{DBL}}$  from the power law, respectively.  $\nu$  is kinematic viscosity (corrected for temperature), B is an integration constant, and  $\text{Sc}_t$  is the turbulent Schmidt number. We found the product  $B\text{Sc}_t$  to have a functional dependence on the Reynolds number ( $\text{Re} = u_* \delta_{\text{DBL}} \nu^{-1}$ ) across the series of 14 profiles during our relatively low in situ turbulence conditions.  $B\text{Sc}_t$  and the profile-specific  $\delta_{\text{DBL}}^+$  were used to fit the power law to water-side O<sub>2</sub> profile data immediately above the SWI and

evaluate the point at which the two curves defining  $C^+$  ( $z^+ < \delta_{\text{DBL}}^+$  and  $z^+ \geq \delta_{\text{DBL}}^+$ , as defined in Eq. 3.3) converge. Once  $\delta_{\text{DBL}}^+$  was estimated (Fig. 3.1c), it was used to obtain the actual DBL thickness ( $\delta_{\text{DBL}}$ ):

$$\delta_{\text{DBL}} = \frac{v \delta_{\text{DBL}}^+}{u_*} \quad [\text{m}] \quad (3.4)$$

The corresponding  $J_{\text{O}_2}$  was then calculated using the right-hand term in Eq. 3.2.

**3.3.4.3 Curvefit method** – This method is based on characterizing the sediment oxic zone with the polynomial  $C(z)$  that best fits the profile curve (Fig. 3.1d) immediately below the SWI (Urban et al. 1997; Glud 2008). A majority of our data were described most accurately by third-order polynomials (profile 6 required a fourth-order equation). Taking the first derivative of  $C(z)$ , which defines  $\text{O}_2$  as a function of depth ( $z$ ), and evaluating at the sediment surface ( $z_{\text{SWI}} = 0$ ) yields a constant  $\partial C/\partial z$ , which can then be incorporated into Eq. 3.2 to solve for  $J_{\text{O}_2}$  and  $\delta_{\text{DBL}}$ .

**3.3.4.4 Zonefit method** – Sediment porewater  $\text{O}_2$  data were analyzed using PROFILE, a one-dimensional, numerical procedure for biogeochemical interpretation of sediment porewater profiles (Berg et al. 1998). PROFILE uses a numerical analysis based on zero-order kinetics that defines zones of constant volumetric  $\text{O}_2$  consumption ( $R_{\text{O}_2\text{v}}$ ; Table 3.1) to best characterize a sediment  $\text{O}_2$  profile (Fig. 3.1e). At steady-state,  $R_{\text{O}_2\text{v}}$  may be defined by the derivative of Eq. 3.2 (Rasmussen and Jørgensen 1992; Glud 2008):

$$R_{\text{O}_2\text{v}} = \frac{\partial}{\partial z} \left( \phi D_s \frac{\partial C}{\partial z} \right) \quad [\text{mmol m}^{-3} \text{d}^{-1}] \quad (3.5)$$

The PROFILE algorithm solves Eq. 3.5 numerically and reduces the number of zones necessary for obtaining an optimal fit using statistical F-testing. From this statistical analysis, the simplest  $\text{O}_2$  consumption-production profile is selected that best models the porewater profile data. We found that the full set of 14 profiles was typically characterized by one or two consumption zones, as also shown by Brand et al. (2008). Data from our 14  $\text{O}_2$  profiles were used as input for

the numerical procedure. Boundary conditions were defined by O<sub>2</sub> flux and concentration evaluated at the bottom of the profile ( $J_{O_2} = 0 \text{ mmol m}^{-2} \text{ d}^{-1}$  and  $C = 0 \text{ } \mu\text{mol L}^{-1}$ , respectively). Parameters used for the model include  $D$ ,  $D_s$ , and  $\phi$  as defined above. Irrigation and bioturbation effects were assumed negligible.

Balancing O<sub>2</sub> transport and consumption results in

$$J_{O_2} = \int_0^{z_{\max}} R_{O_{2v}} dz + \int_0^{z_{\max}} \frac{\partial C}{\partial t} dz \quad [\text{mmol m}^{-2} \text{ d}^{-1}] \quad (3.6)$$

where  $R_{O_{2v}}$  ( $\text{mmol m}^{-3} \text{ d}^{-1}$ ) and the change in O<sub>2</sub> over time ( $\partial C/\partial t$ ;  $\text{mmol m}^{-3} \text{ d}^{-1}$ ) are integrated over the sediment profile depth to  $z_{\max}$  (designated as the depth where O<sub>2</sub> drops to  $< 3 \text{ } \mu\text{mol L}^{-1}$ ). Depth-integrated values of  $R_{O_{2v}}$  and  $\partial C/\partial t$  are defined by areal parameters  $R_{O_{2a}}$  and  $\partial C/\partial t_a$ , respectively ( $\text{mmol m}^{-2} \text{ d}^{-1}$ ; Table 3.1), to allow for direct comparison with  $J_{O_2}$ .  $J_{O_2}$  values based on PROFILE results were incorporated into Eq. 3.2 to obtain corresponding  $\delta_{\text{DBL}}$ .

**3.3.4.5 Model method** – We used AQUASIM (Reichert 1994), an aquatic system simulation and data analysis software, to fit measured O<sub>2</sub> porewater data to the transport-reaction equation

$$\frac{\partial C}{\partial t} = \frac{\partial}{\partial z} \left( \phi D_s \frac{\partial C}{\partial z} \right) - \mu \frac{C}{K_{O_2} + C} \quad [\text{mmol m}^{-3} \text{ d}^{-1}] \quad (3.7)$$

which defines diffusion and consumption by Monod kinetics, where  $\mu$  is the maximum oxidation rate ( $\text{mmol m}^{-3} \text{ d}^{-1}$ ) and  $K_{O_2}$  is the half-saturation constant ( $\mu\text{mol L}^{-1}$ ). The second term on the right-hand side of Eq. 3.7 thus characterizes  $R_{O_{2v}}$  in terms of Monod kinetics. The Monod parameters were obtained using a diffusion-reaction model developed with the sediment module of AQUASIM version 2.1e (Reichert 1994; Brand et al. 2009), which was adapted to include tortuosity effects via  $D_s$ . Monod kinetic data were used to predict  $\delta_{\text{DBL}}$  required to model sediment O<sub>2</sub> profile data (Fig. 3.1f), allowing us to assess an alternative kinetic approach and to model  $\delta_{\text{DBL}}$  directly from sediment-side data (the *zonefit method* is based on zero-order O<sub>2</sub> consumption and does not predict  $\delta_{\text{DBL}}$ ).

To solve the partial differential in Eq. 3.7 numerically, the vertical derivatives were discretized using a conservative finite difference scheme (LeVeque 1992). These spatially-discretized equations were then integrated over time using the differential/algebraic system solver (DASSL; Petzold 1983) algorithm and the backward-differencing, variable-step, and variable-order GEAR technique (Gear 1971). Routines for parameter estimation, based on the secant method of Ralston and Jennrich (1987), minimized the sum of weighted squares of the deviations between measured data and model results (Reichert 1994).

A single set of Monod parameters ( $\mu = 3620 \text{ mmol m}^{-3} \text{ d}^{-1}$  and  $K_{O_2} = 8.0 \text{ } \mu\text{mol L}^{-1}$ ) was found to characterize steady-state  $O_2$  consumption for the series of 14  $O_2$  profiles with  $C_{SWI}$  as the only variable. These Monod parameters were subsequently used in a second model run with  $C_{bulk}$  as the upper boundary condition and  $\delta_{DBL}$  as the sole fitting parameter to reproduce our sediment  $O_2$  data, thus enabling us to predict  $\delta_{DBL}$  for the full set of profiles.  $J_{O_2}$  was estimated by incorporating the AQUASIM-modeled  $\delta_{DBL}$  into Eq. 3.2.

### 3.4 Assessment

**3.4.1 Dynamic forcing of  $O_2$  distribution** – Turbulence-induced variation in our  $O_2$  profile data allowed us to assess the performance and applicability of the different analytical methods for  $J_{O_2}$  over a range of turbulence levels. The vertical distribution of  $O_2$  on both sides of the SWI (as characterized by  $\delta_{DBL}$  and  $z_{max}$ , respectively) and  $J_{O_2}$  were found to be strongly influenced by BBL turbulence during the 12-h measurement period (Fig. 3.2; Bryant et al. 2010; Ch. 2).  $J_{O_2}$  and  $\delta_{DBL}$  values shown in Fig. 3.2 are based on average results of the five methods. Quantified values presented in this study differ slightly ( $< 5\%$  on average) from those in Bryant et al. (2010; Ch. 2) due to a difference in how sediment tortuosity was accounted for ( $D_s$ ; discussed below); however, overall results were not affected.  $J_{O_2}$  ranged from  $6.8 \pm 1.9 \text{ mmol m}^{-2} \text{ d}^{-1}$  during peak turbulence ( $\varepsilon = 1.2 \times 10^{-8} \text{ W kg}^{-1}$ ) to  $1.0 \pm 0.3 \text{ mmol m}^{-2} \text{ d}^{-1}$  during negligible turbulence ( $\varepsilon = 7.8 \times 10^{-12} \text{ W kg}^{-1}$ ), as shown in Fig. 3.2a. Corresponding variation in  $u_*$  is also shown. The DBL was suppressed to a minimum  $\delta_{DBL}$  of  $1.1 \pm 0.1 \text{ mm}$  and  $z_{max}$  increased to  $2.2 \text{ mm}$  during peak turbulence (Fig. 3.2b). When turbulence levels dropped,  $z_{max}$  decreased to  $0.3 \text{ mm}$  and  $\delta_{DBL}$  increased to the point of becoming technically undefined (Gantzer and Stefan 2003; Røy et al. 2004). However, a conceptual  $\delta_{DBL}$  was quantified for the sake of comparison during this

quiescent period and a nominal maximum  $\delta_{\text{DBL}}$  of  $8.0 \pm 2.4$  mm was obtained. Average  $\delta_{\text{DBL}}$  and  $J_{\text{O}_2}$  (characterizing the full  $\text{O}_2$  profile set) used for comparative assessment of methods were based on data obtained during active turbulence when a defined  $\delta_{\text{DBL}}$  was maintained (excluding profiles 8 and 9).

**3.4.2 Comparison of results** – We found  $J_{\text{O}_2}$  and  $\delta_{\text{DBL}}$  estimates from the different methods to be comparable within 20% on average relative to overall change (85%) throughout the experiment (Fig. 3.3). The range in  $J_{\text{O}_2}$  and  $\delta_{\text{DBL}}$  values obtained per profile from the different methods (e.g., the five individual  $J_{\text{O}_2}$  values for profile 5) is relatively small compared to overall temporal variation in averages (e.g., the mean  $J_{\text{O}_2}$  values for profiles 5 and 7). Furthermore, the trend in turbulence-induced changes in  $J_{\text{O}_2}$  (and corresponding  $\delta_{\text{DBL}}$ ) is well preserved by all five methods (Fig. 3.2, 3.3). Although there are acknowledged conceptual and methodological difficulties with quantifying  $\delta_{\text{DBL}}$  during quiescent conditions, the methods performed reasonably well during the period of negligible turbulence, with no significant increase in variation relative to average  $\delta_{\text{DBL}}$  (or  $J_{\text{O}_2}$ ).

Estimates of  $J_{\text{O}_2}$  obtained with water-side (*direct* and  $u^*$ ) methods were consistently higher (and  $\delta_{\text{DBL}}$  estimates correspondingly lower) than those obtained via sediment-side (*curvefit*, *zonefit*, and *model*) methods (Fig. 3.3).  $J_{\text{O}_2}$  based on water-side data were on average 25% higher than estimates based on sediment-side data while  $\delta_{\text{DBL}}$  values were on average 35% lower (relative to water-side  $J_{\text{O}_2}$  and  $\delta_{\text{DBL}}$ ; differences of  $+1.8 \text{ mmol m}^{-2} \text{ d}^{-1}$  and  $-0.4 \text{ mm}$ , respectively) during active turbulence. Potential reasons for deviation between water- and sediment-side results are discussed below.

In order to measure the statistical range of results from the five methods, standard deviations ( $\sigma$ ) were calculated assuming a normal distribution. Data for  $\sigma_{J_{\text{O}_2}}$  and  $\sigma_{\text{DBL}}$  are shown in Fig. 3.2. Standard deviations remained relatively low although variation was observed at certain points during the campaign. During periods of inactive turbulence, increasing  $\delta_{\text{DBL}}$  and decreasing  $\varepsilon$  lead to greater uncertainty and subsequent increases in  $\sigma$  and  $\varepsilon$  intermittency. While increased variability in  $\delta_{\text{DBL}}$  and  $\varepsilon$  was observed during the quiescent period, this was most likely an effect of analysis rather than an indication of poor data quality. Increased variation in  $J_{\text{O}_2}$ ,  $\delta_{\text{DBL}}$ , and  $\varepsilon$  estimates for profile 1 was attributed to equipment settling (Bryant et al. 2010; Ch. 2) and hence these data were considered outliers.

**3.4.3 Evaluation of each method** – In general, each method could be applied to the full profile set for estimations of  $J_{O_2}$  and  $\delta_{DBL}$ . Data were more difficult to analyze during periods of negligible turbulence (profiles 8 and 9) due to the disintegration of a measurable DBL (*direct method*), increased uncertainty in  $u^*$  estimates ( *$u^*$  method*), and the breakdown of curvature of sediment porewater  $O_2$  profiles (*curvefit, zonefit, and model methods*). Furthermore, as with all analytical approaches, each of the methods was found to have both benefits and limitations that had to be considered during analysis and/or assessment. Unless otherwise noted, method results are compared using percent difference calculated with respect to average  $J_{O_2}$  or  $\delta_{DBL}$ .

*3.4.3.1 Direct method* – This method is the most traditional and straight-forward (Jørgensen and Revsbech 1985). However, while the  $O_2$  gradient  $\partial C/\partial z$  is relatively simple to measure for the quantification of  $J_{O_2}$  (Eq. 3.2), estimating the actual  $\delta_{DBL}$  directly from  $O_2$  profiles is more problematic due to rapid changes in  $\delta_{DBL}$  (Røy et al. 2004). The true endpoint of the linear  $\partial C/\partial z$  gradient in the DBL is also often undefined. Jørgensen and Revsbech (1985) addressed this issue by establishing the effective DBL, as characterized in Eq. 3.2 for the evaluation of  $\delta_{DBL}$ . Due to the disintegration of the intersection point between the linear DBL region and the constant bulk region in many of our  $O_2$  profiles (observed in profile 14, Fig. 3.1b), we were unable to precisely capture the true DBL because of turbulence-induced variations in the  $C_{bulk}$  endpoint during the ~50-min period required to measure a full profile. Estimating the true  $\delta_{DBL}$  visually from the strictly linear region of our measured  $O_2$  profiles yielded values 71% less than average  $\delta_{DBL}$  results (not shown).

While the effective  $\delta_{DBL}$  approach has been shown to overestimate  $\delta_{DBL}$  (Nishihara and Ackerman 2007; O'Connor et al. 2009), *direct method*  $\delta_{DBL}$  was typically slightly lower (11% on average) than mean  $\delta_{DBL}$  (Fig. 3.3). Our results are in agreement with those obtained by Jørgensen (2001), who found effective  $\delta_{DBL}$  to be similar to  $\delta_{DBL}$  estimated as a function of hydrodynamics using alabaster plate measurements. While the *direct method* was relatively easy to apply to our  $O_2$  profiles with comparable results, Nishihara and Ackerman (2007) have suggested a similar but alternate approach using a hyperbolic tangent (rather than a straight line) to define  $\partial C/\partial z$ , which may be optimal for profiles exhibiting nonlinearity in the DBL.

3.4.3.2 *u\* method* – While the other four methods are based purely on O<sub>2</sub> microsensor data, the *u\* method* is unique in that it incorporates water column hydrodynamics (as characterized by  $u^*$ ) into the assessment of  $\delta_{\text{DBL}}$ . Estimations of  $\delta_{\text{DBL}}$  from the *u\* method* are based on both O<sub>2</sub> microsensor data and ADV velocity data (used to assess  $u^*$ ), thus allowing for a more rigorous evaluation of mean  $\delta_{\text{DBL}}$  and  $J_{\text{O}_2}$ . The *u\* method* was shown by Hondzo et al. (2005) to predict  $\delta_{\text{DBL}}$  values ~30% lower than the effective  $\delta_{\text{DBL}}$  (i.e., *direct method*). Similarly, our  $u^*$ -based  $\delta_{\text{DBL}}$  estimates were consistently lower than *direct method* estimates (though within  $\pm 14\%$ ; relative to *direct method*; Fig. 3.3) and 23% less than average  $\delta_{\text{DBL}}$ .

As previously defined, the *u\* method* estimates  $\delta_{\text{DBL}}$  as a function of the fitting parameter  $\delta_{\text{DBL}}^+$  and Reynolds-number-dependent  $\text{BSc}_t$  using power law scaling of water-side O<sub>2</sub> data. While the power law easily fit most of our data (e.g., profile 14 in Fig. 3.1c and profile 3 in Fig. 3.4a), the fit was less than ideal for several profiles that had increased scatter in bulk water O<sub>2</sub> (e.g, profile 11, Fig. 3.4b). Because the fits were affected by both  $\delta_{\text{DBL}}^+$  and  $\text{BSc}_t$ , in several cases the fit was not particularly sensitive to  $\delta_{\text{DBL}}^+$ . These cases were unsystematic and the resulting combinations varied only slightly from one another, with  $\delta_{\text{DBL}}$  estimations differing by up to  $\pm 0.1$  mm ( $< 10\%$  of average  $\delta_{\text{DBL}}$  during active turbulence). For these situations, the larger, more conservative value of  $\delta_{\text{DBL}}$  was chosen. Nonetheless, the *u\* method* provided consistent approximations of  $\delta_{\text{DBL}}$ .

Although  $J_{\text{O}_2}$  and/or  $\delta_{\text{DBL}}$  are commonly assessed as a function of current velocity or  $u^*$  data in laboratory studies (Mackenthun and Stefan 1998; Røy et al. 2004; Hondzo et al. 2005), our study is one of the few that have evaluated  $J_{\text{O}_2}$  and  $\delta_{\text{DBL}}$  as a function of turbulence based on in situ current velocity. It is acknowledged that velocity-based approaches may not always be appropriate in low-energy systems (e.g., periodically-forced lakes and reservoirs) due to the fact that turbulence, rather than velocity, controls  $\delta_{\text{DBL}}$  in these environments (Lorke et al. 2003). During periods of inactive turbulence, law-of-the-wall theory does not apply (Lorke et al. 2002) and  $u^*$  is conceptually not defined. The *u\* method* may not be as applicable during these periods. Variation between  $u^*$ -based estimates and the other methods was not observed to increase during the period of inactive turbulence (profiles 8 and 9, Fig. 3.3) however, indicating that the *u\* method* performed adequately even under low- $\varepsilon$  conditions.

To further evaluate the validity of estimating  $\delta_{\text{DBL}}$  as a function of in-situ velocity during low turbulence, values of  $u^*$ -based  $\delta_{\text{DBL}}$  and average  $\delta_{\text{DBL}}$  were compared to the Batchelor length

scale ( $L_B$ ) for  $O_2$ . This comparison also allowed us to test the robustness of our other microsensor-based  $\delta_{DBL}$  estimates using an independent approach.  $L_B$  characterizes the minimum length scale of concentration where molecular diffusion begins to reduce concentration gradients (Lorke et al. 2003). Elevated turbulence ( $\varepsilon$ ) sustains concentration fluctuations at a smaller scale, which parallels  $\delta_{DBL}$  behavior.  $L_B$  may hence be used as an alternative method of estimating  $\delta_{DBL}$  as a function of  $\varepsilon$ , as developed by Hearn and Robson (2000):

$$L_B = 2\pi \left( \frac{\nu D^2}{\varepsilon} \right)^{1/4} \quad [m] \quad (3.8)$$

While  $L_B$  was defined conceptually for open flow rather than for a boundary layer, Lorke et al. (2003) show agreement between  $L_B$  and  $\delta_{DBL}$ , despite a substantial spatial gap ( $\sim 1$  m) between their points of measurement for  $\varepsilon$  and  $O_2$ . Taking into account the much smaller spatial gap ( $\sim 0.1$  m) between our measurements, the strong correlation observed in Fig. 3.5 further validates  $\delta_{DBL}$  scaling based on  $L_B$ .

Because both  $L_B$  and  $u^*$  are a function of  $\varepsilon$ , we specifically evaluated the relationship between  $L_B$  and  $u^*$  *method* results for  $\delta_{DBL}$ . We also compared  $L_B$  to average  $\delta_{DBL}$  (both including all methods and excluding  $u^*$  *method* to isolate the influence of  $u^*$  results). As shown in Fig. 3.5, all three estimates of  $\delta_{DBL}$  correlate well with  $L_B$  ( $R^2 = 0.95$  to  $0.96$ ). O'Connor and Hondzo (2009) observed similarity between  $L_B$  and  $u^*$ -based  $\delta_{DBL}$  as well, while  $\delta_{DBL}$  based on  $O_2$  profile data was overestimated in comparison. In contrast, we observed a strong relationship between  $L_B$  and both  $\delta_{DBL}$  averages (Fig. 3.5). Our  $\delta_{DBL}$  estimates based on  $u^*$  and purely on  $O_2$  profile data were thus supported by  $L_B$  results.

**3.4.3.3 Curvefit method** – Mean values of  $J_{O_2}$  and  $\delta_{DBL}$  based on *curvefit* results were within  $\sim 10\%$  of the average (Fig. 3.3). Fitting curves to porewater profiles has been used effectively to mathematically describe kinetic rates of  $O_2$  consumption and corresponding  $O_2$  fluxes in several studies (Nielsen et al. 1990). Ideally, derivatives of the best-fitting curve equations can be used to evaluate  $J_{O_2}$  and  $R_{O_2v}$  (Rasmussen and Jørgensen 1992). Zero-order kinetics are characterized by second-order polynomials and first-order kinetics by exponential equations (Bouldin 1968). Third-order polynomials, though, were found to best fit a majority of

the sediment O<sub>2</sub> profiles in our data set. It was also difficult to fit a single curve throughout the full depth of the oxic zone for any of our profiles. Therefore, emphasis was placed on precisely fitting the region of the curve immediately at the SWI and incorporating the derivative of this curve into Eq. 3.2. The fact that our data could not be defined by a single second-order polynomial indicates that consumption rates were dependent on depth, which was further explored using multiple zero-order consumption zones (*zonefit method*) and Monod kinetics (*model method*).

3.4.3.4 *Zonefit method* – The *zonefit method* yielded mean J<sub>O<sub>2</sub></sub> and δ<sub>DBL</sub> estimates that were 5% lower and 2% higher, respectively, than average values (Fig. 3.3). The approach used for this method, based on splining multiple second-order polynomials together to best fit a sediment O<sub>2</sub> profile, is advantageous because it does not assume complex reaction laws and assigns zero-order kinetic rates to as many different zones as needed to accurately reproduce the measured profile. The use of multiple zones allows for a good fit to be obtained even for atypical profiles (Maerki et al. 2006). Key benefits of the PROFILE numerical model include simplicity and broad-ranging applicability. PROFILE may be used for any solute that is produced or consumed. Also, variations in φ, bioturbation, and irrigation may be easily incorporated into PROFILE as a function of profile depth. As with most numerical modeling work, the *zonefit method* (as well as the *model method*) was initially more work-intensive than the non-model-based methods. However, once the PROFILE model is set up, the algorithm used in PROFILE is fast as compared to AQUASIM (*model method*).

Results from both the *zonefit* and *model methods* were used to infer additional information about the sediment. In addition to evaluating J<sub>O<sub>2</sub></sub> and δ<sub>DBL</sub>, both of these methods were used to predict how O<sub>2</sub> consumption varied as a function of depth and O<sub>2</sub> availability within the sediment oxic zone. Variations in PROFILE-predicted R<sub>O<sub>2v</sub></sub> and zero-order O<sub>2</sub> consumption zones in response to turbulence-induced changes in J<sub>O<sub>2</sub></sub> and subsequent O<sub>2</sub> availability are shown in green in Fig. 3.6 (discussed further below). While ∂C/∂t was minimal (5% on average per profile) for our quasi-steady-state system, zone-specific R<sub>O<sub>2v</sub></sub> values in Fig. 3.6 were corrected for ∂C/∂t by establishing a mass balance (Eq. 3.6) based on J<sub>O<sub>2</sub></sub>, R<sub>O<sub>2v</sub></sub>, and ∂C/∂t between O<sub>2</sub> consumption zones over the depth of each profile.

**3.4.3.5 Model method** – The *model method* is the only method assessed in this study that evaluates both sides of the SWI simultaneously to predict  $\delta_{\text{DBL}}$ . While the model we used, formulated in the sediment module of AQUASIM, is largely based on fitting porewater  $\text{O}_2$  data and defining sediment  $\text{O}_2$  consumption (hence, considered a sediment-side method), water-side data ( $C_{\text{bulk}}$ ) were also used to define the upper boundary condition (the lower boundary condition was defined by zero flux). Because our diffusion-reaction model provided  $\delta_{\text{DBL}}$  as an output parameter for a steady-state solution, we were thus able to predict  $\delta_{\text{DBL}}$  directly from porewater and bulk water data. Alternatively, the *curvefit* and *zonefit methods* evaluate  $J_{\text{O}_2}$  from porewater data and then  $\delta_{\text{DBL}}$  was calculated via Eq. 3.2. On average, model method predictions of  $\delta_{\text{DBL}}$  were found to be 21% higher ( $J_{\text{O}_2}$  correspondingly 20% lower) than the overall mean (Fig. 3.3). AQUASIM-predicted  $\delta_{\text{DBL}}$  are delineated by the red water-side  $\text{O}_2$  profile fit lines shown in Fig. 3.6.

Monod parameters predicted by AQUASIM to best characterize our  $\text{O}_2$  profile data and model  $\delta_{\text{DBL}}$  were also used to estimate how  $R_{\text{O}_2\text{v}}$  changed as a function of depth and time (Fig. 3.6). Although we incorporated only a single Monod formulation in this study, the sediment module of AQUASIM can be used to implement process-based sediment reaction models with more complex kinetics (e.g., Brand et al. 2009). The AQUASIM model can also be used to predict variation in  $\text{O}_2$  consumption pathways if several terminal electron acceptors which compete for  $\text{O}_2$  are considered as parameters in the model. More complex reaction patterns may however require further input parameters based on detailed measurements of other species involved in  $\text{O}_2$  dynamics, resulting in over-parameterization and longer calculation times.

## 3.5 Discussion

**3.5.1 Water-side versus sediment-side** – The general applicability of each of the methods is established by the fact that differences between method results are small relative to overall variation in  $J_{\text{O}_2}$  and  $\delta_{\text{DBL}}$ . While some deviation between water- and sediment-side estimates was observed, trends in  $J_{\text{O}_2}$  and  $\delta_{\text{DBL}}$  were sufficiently captured by both water- and sediment-side methods (Fig. 3.2, 3.3). Nevertheless, this deviation warrants further evaluation. As previously mentioned, water-side methods yielded comparable but consistently higher  $J_{\text{O}_2}$  and correspondingly lower  $\delta_{\text{DBL}}$  than sediment-side methods (differences of  $1.8 \text{ mmol m}^{-2} \text{ d}^{-1}$  (25%))

and 0.4 mm (35%) on average, respectively). Our results are similar to those obtained in a study of total and diffusive O<sub>2</sub> uptake in marine sediment by Rabouille et al. (2003), which found that while total O<sub>2</sub> flux was in very close agreement with J<sub>O<sub>2</sub></sub> based on the interface gradient (*direct method*), PROFILE-predicted (*zonefit method*) J<sub>O<sub>2</sub></sub> was 20% less. Relative to the differences observed between our water- and sediment-side results, variation is much smaller within the water-side group ( $\pm 7\%$ ) and the sediment-side group ( $\pm 10\%$ ), as shown in Table 3.2 and Fig. 3.3. Deviation between water- and sediment-side estimates occurs throughout the full data set for our 12-h experiment, with no evident correlation to turbulence and corresponding  $u^*$  (Table 3.2; Fig. 3.2). Methodological issues, assumptions made on sediment properties, and localized sediment O<sub>2</sub> transport and consumption processes however may have contributed to the difference in water- and sediment-side estimates.

Estimation of the SWI location was not trivial and may have affected results, although this would have influenced both water- and sediment-side approaches. While the *u\* method* evaluates the water O<sub>2</sub> profile up to several mm above the SWI and the *zonefit* and *model methods* assess the full porewater O<sub>2</sub> profile, the *direct* and *curvefit* methods are focused immediately on the SWI and are thus much more sensitive to the SWI location (Rabouille et al. 2003). Water-side estimates obtained via the *direct method* could also have been influenced by difficulties associated with quantifying  $\delta_{\text{DBL}}$  directly from O<sub>2</sub> profiles. Recent work has suggested that it is inadequate to classify the DBL as quiescent because  $\delta_{\text{DBL}}$  varies continuously as a function of BBL currents (Røy et al. 2004; O'Connor and Hondzo 2008). Brand et al. (2009), however, do show that the use of a quiescent DBL is a valid model for the study of O<sub>2</sub> dynamics over time scales of several minutes to hours (i.e., the 8-h seiche cycle inducing variations in turbulence observed during this study) and that high-frequency fluctuations have no significant effect on time-averaged flux.

Results for  $\delta_{\text{DBL}}$  from both water-side methods were typically less than average  $\delta_{\text{DBL}}$  (Fig. 3.3); *direct* estimates were 11% lower and *u\** estimates were 23% lower on average. The established tendency of the *u\* method* to predict thinner  $\delta_{\text{DBL}}$ , shown both in this study and also by Hondzo et al. (2005), was a likely factor in variation between water- and sediment-side results. While no defined trend was observed between turbulence and deviation in *direct* and *u\* method* results, conceptual issues with quantifying  $\epsilon$  and  $u^*$  during low turbulence conditions are a possible influence.

Sediment O<sub>2</sub> transport processes were defined for sediment-side methods using experimentally-obtained and/or assumed parameters (e.g.,  $\phi$  and bioturbation, respectively). The relatively high degree of uncertainty in these sediment parameters (P. Berg, pers. comm.) could have been a source of deviation between water- and sediment-side results. Quantifying diffusive transport and the relationship between  $\phi$  and D<sub>s</sub> in sediment is complicated by the heterogeneous nature of typical sediment matrices (Glud 2008). Previous work has shown that the influence of tortuosity on diffusion may be negligible in freshwater sediment, particularly near the SWI, where  $\phi$  approaches unity (Maerki et al. 2004). Our measured sediment  $\phi$  was  $\geq 0.95$  in the upper sediment. In addition, only slight changes in O<sub>2</sub> profile slope were evident at the SWI. For these reasons, we did not correct for tortuosity in *curvefit* and *model method* analyses in Bryant et al. (2010; Ch. 2). PROFILE (*zonefit method*), however, requires tortuosity to be defined via input parameter D<sub>s</sub>. To maintain consistency when evaluating the methods, D<sub>s</sub> (which we parameterized as  $D_s = \phi D$ ) was hence incorporated into all sediment-side analyses in this comparative study. Accounting for tortuosity in all sediment-side analyses changed results by ~5% which directly reflects the additional influence of  $\phi$  due to the tortuosity correction ( $\phi D_s = 0.90D$  per Eq. 3.2 as compared to  $\phi D = 0.95D$  per Bryant et al. 2010; Ch. 2), as discussed previously.

To further equate method comparisons and simplify assumptions made for unknown input parameters, bioturbation and irrigation effects were assumed negligible. However, bioturbation (i.e., the mixing of solutes and solids in sediment due to fauna movement; Berg et al. 2001) has been shown to increase J<sub>O<sub>2</sub></sub> estimates based on total sediment O<sub>2</sub> uptake by up to 85% in marine sediment (Glud 2008). Thus, enhanced O<sub>2</sub> flux into the sediment due to these processes would not have been accounted for in J<sub>O<sub>2</sub></sub> estimates based solely on diffusive transport (as our results were; Eq. 3.2). To investigate the influence of bioturbation (characterized via biodiffusivity; D<sub>b</sub>) as a possible source of deviation between water- and sediment-side J<sub>O<sub>2</sub></sub> values, we performed a follow-up analysis using PROFILE that evaluated D<sub>b</sub> required to estimate J<sub>O<sub>2</sub></sub> equivalent to water-side J<sub>O<sub>2</sub></sub>. Average J<sub>O<sub>2</sub></sub> initially predicted by PROFILE via the *zonefit method* was 5.5 mmol m<sup>2</sup> d<sup>-1</sup> (input D<sub>b</sub> = 0 m<sup>2</sup> s<sup>-1</sup>). By changing the D<sub>b</sub> value used to model our O<sub>2</sub> porewater data, we found that a D<sub>b</sub> of  $5.0 \times 10^{-10}$  m<sup>2</sup> s<sup>-1</sup> increased J<sub>O<sub>2</sub></sub> to the average water-side J<sub>O<sub>2</sub></sub> value (6.9 mmol m<sup>2</sup> d<sup>-1</sup>; Table 3.2). These results are comparable to work by Berg et al. (2001), who showed that including bioturbation in their O<sub>2</sub> flux evaluation caused J<sub>O<sub>2</sub></sub> to increase

from  $4.1 \text{ mmol m}^{-2} \text{ d}^{-1}$  ( $D_b = 0 \text{ m}^2 \text{ s}^{-1}$ ) to  $6.5 \text{ mmol m}^{-2} \text{ d}^{-1}$  ( $D_b = 4.6 \times 10^{-10} \text{ m}^2 \text{ s}^{-1}$ ). Uncertainties in assumed sediment parameters could therefore have contributed to differing sediment- and water-side results.

In addition to difficulties associated with defining bulk sediment properties, sediment-side estimates of  $J_{O_2}$  are further complicated by localized sediment  $O_2$  transport and consumption processes that may not be accurately characterized by  $O_2$  porewater data. Variable sediment microtopography effects, as well as bioturbation and irrigation, can have site-specific effects on diffusive  $O_2$  transport (Jørgensen and Des Marais 1990; Røy et al. 2002; Rabouille et al. 2003). Small-scale heterogeneity in mineralization of newly-deposited organic matter at the sediment surface (Zhang et al. 1999; Lewandowski et al. 2002) and  $O_2$  consumption via benthic fauna (Krantzberg 1985; Polerecky et al. 2006; Lewandowski et al. 2007) can also cause localized variation in sediment  $O_2$  uptake. Glud et al. (2009) have shown that small-scale disparities in labile organic matter distribution can result in significant variability in surface sediment  $O_2$  concentrations and localized ‘hot spots’ of benthic  $O_2$  consumption.

The impact of spatially heterogeneous  $O_2$  uptake may not have been accurately characterized by microsensor porewater measurements due to localized  $O_2$  uptake within the sediment occurring at a location near, but not directly impacting, the location of  $O_2$  microsensor measurements (Brand et al. 2008). Water-side estimates remain relatively unaffected by small-scale variation in site-specific sediment processes due to the homogenizing effect of turbulence on  $C_{\text{bulk}}$ . Water-side estimates may therefore be more representative of a larger areal ‘footprint’ than sediment-side estimates (Berg et al. 2007b; O’Connor and Hondzo 2008). If significant localized sediment  $O_2$  uptake processes were occurring near our  $O_2$  microsensor location but were not captured in profile data, then  $J_{O_2}$  estimates based on water-column data (representing a broader region) would be higher than porewater-based  $J_{O_2}$  (representing a site-specific location). Our sediment  $O_2$  profiles are parabolic in shape with no kinks or shifts in the curvature (Jørgensen and Revsbech 1985) and the difference between water- and sediment-side estimates of  $J_{O_2}$  is relatively small, indicating that the influence of localized  $O_2$  uptake processes on the vertical  $O_2$  distribution was likely not significant. It should be emphasized though that while in-situ microsensor measurements provide a robust method for  $J_{O_2}$  estimation under a wide range of turbulence conditions (Lorke et al. 2003; Bryant et al. 2010; Ch. 2), results (particularly those based on sediment-side data) are extremely localized to the microsensor profiling site.

**3.5.2 Sediment O<sub>2</sub> consumption** – Further evaluation of porewater O<sub>2</sub> data provided beneficial information on O<sub>2</sub> consumption processes within the sediment that could not have been discerned from a water-side assessment. Because we were unable to fully characterize the profiles using second-order polynomial or exponential equations, zero- and first-order kinetic models could not be directly applied to our data set using the *curvefit method*. However, zero-order and Monod kinetic models were applied using the *zonefit* and *model* methods, respectively. Based on these results, variations in R<sub>O<sub>2v</sub></sub> as a function of depth and time are shown in Fig. 3.6 (*zonefit* (PROFILE) in green; *model* (AQUASIM) in red). Sediment O<sub>2</sub> consumption during turbulent periods was typically characterized by PROFILE with two consumption zones (Fig. 3.6). R<sub>O<sub>2v</sub></sub> was consistently higher in the upper region of the sediment (immediately below the SWI) and decreased significantly with depth during periods of active turbulence (e.g., profiles 2 to 5 and 11 to 14; Fig. 3.2a). Conversely, during the period when turbulence was negligible (profiles 8 to 9), R<sub>O<sub>2v</sub></sub> decreased and O<sub>2</sub> consumption was characterized by a single zone. AQUASIM results for Monod-based R<sub>O<sub>2v</sub></sub> and the corresponding region of sediment O<sub>2</sub> consumption generally followed the same trend as the zero-order O<sub>2</sub> consumption zones and R<sub>O<sub>2v</sub></sub> values predicted by PROFILE (Fig. 3.6). Corresponding profile-specific R<sub>O<sub>2a</sub></sub> estimates based on *zonefit* and *model method* results were within ~20% on average (data not shown). Similar characterization of sediment O<sub>2</sub> consumption by multiple kinetic models verifies results from both methods and also emphasizes the influence that turbulence-induced changes in O<sub>2</sub> availability had on R<sub>O<sub>2</sub></sub> (Fig. 3.6). While zero-order kinetics are frequently used to characterize sediment O<sub>2</sub> consumption independent of O<sub>2</sub> concentration (Rasmussen and Jørgensen 1992; Jørgensen and Boudreau 2001), it has been shown that R<sub>O<sub>2v</sub></sub> can become dependent on O<sub>2</sub> concentration under limiting O<sub>2</sub> conditions such as those observed during our study (Santschi et al. 1990; Berg et al. 2003; Bryant et al. 2010; Ch. 2).

Our results, which show elevated O<sub>2</sub> consumption in the upper sediment in response to increased O<sub>2</sub> availability at the SWI, indicate water-side control of J<sub>O<sub>2</sub></sub> with the potential sediment O<sub>2</sub> demand surpassing the amount of O<sub>2</sub> supplied to the sediment (O'Connor and Harvey 2008). O<sub>2</sub> consumption can alternatively be the rate-limiting step to mass transport in physiologically active systems experiencing moderate flow (Nishihara and Ackerman 2009). We observed R<sub>O<sub>2v</sub></sub> to decrease with depth, suggesting that R<sub>O<sub>2v</sub></sub> may have been dominated by

mineralization of newly-deposited organic matter at the sediment surface (Santschi et al. 1990; Zhang et al. 1999). Similarly, Brand et al. (2009) showed that Alpnach sediment can be sufficiently modeled as a uniform layer of organic matter with a high intrinsic capacity for O<sub>2</sub> uptake and transport-limited J<sub>O<sub>2</sub></sub>. R<sub>O<sub>2v</sub></sub> has been found to increase with depth in environments (e.g., oligotrophic) where re-oxidation of reduced compounds dominates O<sub>2</sub> consumption (Glud et al. 2007; Jørgensen and Boudreau 2001).

### 3.6 Comments and recommendations

While analogous results were obtained from all five methods, each of the methods had advantages and disadvantages that may influence applicability for specific experiments. The *direct method* is the least complicated, though rapid variations in the DBL may have influenced effective  $\delta_{\text{DBL}}$  estimates during the ~50 min measurement period of each profile. The *u\* method* incorporates velocity as an independent variable and provided comparable results; however, we had difficulties in fitting the power law to the full set of profiles, particularly for profiles exhibiting scatter in bulk O<sub>2</sub> data. While water-side approaches may lose validity during periods of weak turbulence due to disintegration of the DBL and/or insignificant u\* values, the strong correlation between L<sub>B</sub> and  $\delta_{\text{DBL}}$  estimates indicates that velocity-based estimates of  $\delta_{\text{DBL}}$  may be adequate even for low turbulence. Our results also support the use of L<sub>B</sub> to estimate  $\delta_{\text{DBL}}$  as a function of hydrodynamics, which is somewhat unexpected considering that  $\varepsilon$  becomes undefined during inactive periods.

As with the *direct method*, the *curvefit method* proved to be relatively uncomplicated. Because we could not characterize our sediment profile data with a single curve, we basically applied a sediment-side version of the *direct method* to O<sub>2</sub> porewater data. While sediment  $\phi$  and tortuosity must be accounted for, the O<sub>2</sub> profile immediately below the SWI may be less variable (and thus easier to accurately measure) than the DBL in many environments. Thus, the *curvefit method* may be optimal as a straightforward J<sub>O<sub>2</sub></sub> estimation when porewater data are available and detailed information on variation in R<sub>O<sub>2</sub></sub> within the sediment is not desired.

Estimates of J<sub>O<sub>2</sub></sub> and  $\delta_{\text{DBL}}$  from the *zonefit method* were the closest to average values (within 5% and 2%, respectively). Although the *zonefit* and *model methods* were more laborious than the other methods, significant information on how O<sub>2</sub> consumption varied with sediment

depth was obtained. Advantages of the *zonefit method* include the direct analytical approach, the relative ease in which the PROFILE model can be set up and applied, and the broad applicability of PROFILE. However, PROFILE does not include dynamic processes and thus predictions of how  $J_{O_2}$  and other fluxes vary over time are dependent on the number of profiles available to characterize transient conditions. A benefit of the AQUASIM diffusion-reaction model used for the *model method* is that it can predict how the vertical  $O_2$  distribution and corresponding SWI fluxes are affected by dynamic conditions (e.g., variations in  $\delta_{DBL}$ ; Brand et al. 2009). This is especially advantageous if only a few profiles and/or proxies for  $\delta_{DBL}$  (e.g.,  $u_*$ ,  $\varepsilon$ ) are available. Fortunately, we obtained a sufficient number of profiles over a brief time period to use PROFILE to evaluate the vertical  $O_2$  distribution and  $J_{O_2}$  under dynamic conditions. If our data set had not been as extensive, AQUASIM may have been the more appropriate approach.

During this study, a direct correlation between  $O_2$  availability in the sediment and sediment  $O_2$  consumption was observed (as characterized by  $J_{O_2}$  and  $R_{O_2}$ ), indicating that  $O_2$  dynamics were water-side controlled in our highly-organic, cohesive sediment. However, O'Connor et al. (2009) showed that in porous sediment where  $J_{O_2}$  is sediment-side controlled,  $C_{SWI}$  may approach  $C_{bulk}$  under highly turbulent conditions; in this case,  $J_{O_2}$  would be inaccurately estimated as zero via Eq. 3.2. This highlights the point that the approaches evaluated in this study are applicable only to diffusive  $J_{O_2}$ , as controlled by the driving forces ( $C_{bulk} - C_{SWI}$ ) and  $\delta_{DBL}$ , and would not apply in systems dominated by advective transport.

In conclusion, by evaluating the robustness of five established methods used to analyze  $J_{O_2}$  and  $\delta_{DBL}$  at the molecular level, we show that estimations of these parameters are not strongly dependent on the method chosen for analysis. Increased correlation was observed in method results based on the same side of the SWI. Although water-side estimates of  $J_{O_2}$  were observed to be consistently higher (and estimates of  $\delta_{DBL}$  lower) than sediment-side estimates, turbulence-induced variations in  $J_{O_2}$  and  $\delta_{DBL}$  were reliably characterized by all five methods. Our results reveal that the effectiveness and applicability of each of the methods depends largely on available data on the vertical  $O_2$  distribution (e.g., data set sufficiently defining effects of dynamic conditions) and sediment properties (e.g.,  $\phi$  and  $D_b$ ). Environmental conditions at the experiment site (e.g., turbulence levels) and information desired from the experiment (e.g.,  $J_{O_2}$  and/or  $R_{O_2}$ ) are also factors. Observed variation in water- and sediment-side estimates of  $J_{O_2}$  does emphasize however that by focusing solely on a single side of the SWI, difficulties in

analyzing relatively transient water-side data and/or effects of site-specific sediment porewater data could potentially result in significantly different interpretations of sediment-water flux. By evaluating the vertical O<sub>2</sub> distribution on both sides of the SWI, a comprehensive assessment of the balance between in situ hydrodynamic and sediment O<sub>2</sub> consumption processes and resulting J<sub>O<sub>2</sub></sub> and R<sub>O<sub>2</sub></sub> is attained.

### **3.7 Acknowledgements**

We are grateful to Peter Berg, Miki Hondzo, Ronnie Glud, and Hans Røy for discussion and advice. We also thank Lorenzo Rovelli, Michi Schurter, Christian Dinkel, and Mathias Kirf, who offered invaluable assistance in the field and with equipment. Gay Bryant kindly improved grammar and figures. This research has been funded in part by the United States Environmental Protection Agency (EPA) under the Science to Achieve Results (STAR) Graduate Fellowship Program. EPA has not officially endorsed this publication and the views expressed herein may not reflect the views of the EPA. This research was also supported by the United States National Science Foundation (NSF) through the Integrative Graduate Education and Research Traineeship (IGERT) program (DGE 0504196) and the Swiss National Science Foundation, grants 200020-111763 and 200020-120128.

### **3.8 References**

- Arega, F., and J. H. W. Lee. 2005. Diffusional mass transfer at sediment-water interface of cylindrical sediment oxygen demand chamber. *J. Environ. Eng.-ASCE* **131**: 755-766.
- Baker, M. A., and C. H. Gibson. 1987. Sampling turbulence in the stratified ocean: statistical consequences of strong intermittency. *J. Phys. Oceanogr.* **17**: 1817-1836.
- Berg, P., N. Risgaard-Petersen, and S. Rysgaard. 1998. Interpretation of measured concentration profiles in sediment pore water. *Limnol. Oceanogr.* **43**: 1500-1510.
- Berg, P., H. Røy, F. Janssen, V. Meyer, B. B. Jørgensen, M. Huettel, and D. de Beer. 2003. Oxygen uptake by aquatic sediments measured with a novel non-invasive eddy-correlation technique. *Mar. Ecol. Prog. Ser.* **261**: 75-83.

- Berg, P., H. Røy, and P. L. Wiberg. 2007b. Eddy correlation flux measurements: the sediment surface area that contributes to the flux. *Limnol. Oceanogr.* **52**: 1672-1684.
- Berg, P., S. Rysgaard, P. Funch, and M. K. Sejr. 2001. Effects of bioturbation on solutes and solids in marine sediments. *Aquat. Microb. Ecol.* **26**: 81-94.
- Berg, P., D. Swaney, S. Rysgaard, B. Thamdrup, and H. Fossing. 2007a. A fast numerical solution to the general mass-conservation equation for solutes and solids in aquatic sediments. *J. Mar. Res.* **65**: 317-343.
- Bouldin, D.R. 1968. Models for describing the diffusion of oxygen and other mobile constituents across the mud-water interface. *J. Ecol.* **56**: 77-87.
- Boudreau, B. P. 2001. Solute transport above the sediment-water interface, p. 104-126. In B. P. Boudreau and B. B. Jørgensen [eds.], *The benthic boundary layer: transport processes and biogeochemistry*. Oxford University Press.
- Brand, A., C. Dinkel, and B. Wehrli. 2009. Influence of the diffusive boundary layer on the solute dynamics in the sediments of a seiche-driven lake: A model study. *J. Geophys. Res.* **114**: G01010, doi:10.1029/2008JG000755.
- Brand, A., D. F. McGinnis, B. Wehrli, and A. Wüest. 2008. Intermittent oxygen flux from the interior into the bottom boundary of lakes as observed by eddy correlation. *Limnol. Oceanogr.* **53**: 1997-2006.
- Brand, A., B. Müller, A. Wüest, C. Dinkel, N. P. Revsbech, L. P. Nielsen, O. Pedersen, L. R. Damgaard, L. H. Larsen, and B. Wehrli. 2007. Microsensor for in situ flow measurements in benthic boundary layers at submillimeter resolution with extremely slow flow. *Limnol. Oceanogr.: Methods.* **5**: 185-191.
- Bryant, L. D., C. Lorrai, D. F. McGinnis, A. Brand, A. Wüest, and J. C. Little. 2010. Variable sediment oxygen uptake in response to dynamic forcing. *Limnol. Oceanogr.* **55**: 950-964.
- Dalsgaard, T. [ed.], L. P. Nielsen, V. Brotas, P. Viaroli, G. Underwood, D. B. Nedwell, K. Sundbäck, S. Rysgaard, A. Miles, M. Bartoli, L. Dong, D. C. O. Thornton, L. D. M. Ottosen, G. Castaldelli, and N. Risgaard-Petersen. 2000. *Protocol handbook for NICE – Nitrogen Cycling in Estuaries: a project under the EU research programme: Marine Science and Technology (MAST III)*. National Environmental Research Institute, Silkeborg, Denmark.
- [http://www2.dmu.dk/LakeandEstuarineEcology/nice/NICE\\_handbook.pdf](http://www2.dmu.dk/LakeandEstuarineEcology/nice/NICE_handbook.pdf)

- Epping, E. H. G., and W. Helder. 1997. Oxygen budgets calculated from in situ microprofiles for Northern Adriatic sediments. *Cont. Shelf Res.* **17**:1737-1764.
- Gantzer, C. J., and H. G. Stefan. 2003. A model of microbial activity in lake sediments in response to periodic water-column mixing. *Water Res.* **37**: 2833-2846.
- Gear, C. W. 1971. The automatic integration of ordinary differential equations. *Commun. ACM* **14**: 176-179, doi:10.1145/362566.362571.
- Glud, R. N. 2008. Oxygen dynamics of marine sediments. *Mar. Biol. Res.* **4**: 243-289.
- Glud, R. N., P. Berg, H. Fossing, and B. B. Jørgensen. 2007. Effect of the diffusive boundary layer on benthic mineralization and O<sub>2</sub> distribution: A theoretical model analysis. *Limnol. Oceanogr.* **52**: 547-557.
- Glud, R. N., J. K. Gundersen, N. P. Revsbech, and B. B. Jørgensen. 1994. Effects on the benthic diffusive boundary layer imposed by microelectrodes. *Limnol. Oceanogr.* **39**:462-467.
- Glud, R. N., H. Stahl, P. Berg, F. Wenzhöfer, K. Oguri, and H. Kitazato. 2009. In situ microscale variation in distribution and consumption of O<sub>2</sub>: A case study from a deep ocean margin sediment (Sagami Bay, Japan). *Limnol. Oceanogr.* **54**: 1-12.
- Grant, H. L., R. W. Stewart, and A. Moilliet. 1962. Turbulence spectra from a tidal channel. *J. Fluid Mech.* **12**: 241-268.
- Gundersen, J. K., and B. B. Jørgensen. 1990. Microstructure of diffusive boundary layers and the oxygen uptake of the sea floor. *Nature* **345**: 604–607.
- Hearn, C. J., and B. J. Robson. 2000. Modelling a bottom diurnal boundary layer and its control of massive alga blooms in an estuary. *Appl. Math. Mod.* **24**: 843–859.
- Higashino, M., C. J. Gantzer, and H. G. Stefan. 2004. Unsteady diffusional mass transfer at the sediment/water interface: Theory and significance for SOD measurement. *Water Res.* **38**: 1-12.
- Hondzo, M., T. Feyaerts, R. Donovan, and B. L. O'Connor. 2005. Universal scaling of dissolved oxygen distribution at the sediment-water interface: A power law. *Limnol. Oceanogr.* **50**: 1667-1676.
- Jankowski, T., D. M. Livingstone, H. Bührer, R. Forster, and P. Niederhauser. 2006. Consequences of the 2003 European heat wave for lake temperature profiles, thermal stability, and hypolimnetic oxygen depletion: Implications for a warmer world. *Limnol. Oceanogr.* **51**: 815-819.

- Jørgensen, B. B. 2001. Life in the diffusive boundary layer, p. 348-373. In B. P. Boudreau and B. B. Jørgensen [eds.], The benthic boundary layer: transport processes and biogeochemistry. Oxford University Press.
- Jørgensen, B. B., and B. P. Boudreau. 2001. Diagenesis and sediment-water exchange, p. 211-244. In B. P. Boudreau and B. B. Jørgensen [eds.], The benthic boundary layer: transport processes and biogeochemistry. Oxford University Press.
- Jørgensen, B. B., and D. J. Des Marais 1990. The diffusive boundary layer of sediments: Oxygen microgradients over a microbial mat. *Limnol. Oceanogr.* **35**: 1343-1355.
- Jørgensen, B. B., and N. P. Revsbech. 1985. Diffusive boundary layers and the oxygen uptake of sediments and detritus. *Limnol. Oceanogr.* **30**: 111-122.
- Krantzberg, G. 1985. The influence of bioturbation on physical, chemical and biological parameters in aquatic environments: A review. *Environ. Pollut. Ser. A.* **39**: 99-122.
- Lavery, P. S., C. E. Oldham, and M. Ghisalberti. 2001. The use of Fick's First Law for predicting porewater nutrient fluxes under diffusive conditions. *Hydrol. Process.* **15**: 2435-2451.
- LeVeque, R. J. 1992. Numerical methods for conservation laws. Birkhäuser, Boston.
- Lewandowski, J., C. Laskov, and M. Hupfer. 2007. The relationship between *Chironomus plumosus* burrows and the spatial distribution of pore-water phosphate, iron and ammonium in lake sediments. *Freshwater Biol.* **52**: 331-343.
- Lewandowski, J., K. Rüter, and M. Hupfer. 2002. Two-dimensional small-scale variability of pore water phosphate in freshwater lakes: results from a novel dialysis sampler. *Environ. Sci. Technol.* **36**: 2039-2047.
- Li, Y.-H., and S. Gregory. 1974. Diffusion of ions in sea water and in deep-sea sediments. *Geochem. Cosmochim. Acta* **38**: 703-714.
- Lorke, A., B. Müller, M. Maerki, and A. Wüest. 2003. Breathing sediments: The control of diffusive transport across the sediment-water interface by periodic boundary-layer turbulence. *Limnol. Oceanogr.* **48**: 2077-2085.
- Lorke, A., L. Umlauf, T. Jonas, and A. Wüest. 2002. Dynamics of turbulence in low-speed oscillating bottom-boundary layers of stratified basins. *Environ. Fluid Mech.* **2**: 291-313.
- Mackenthun, A. A., and H. G. Stefan. 1998. Effect of flow velocity on sediment oxygen demand: Experiments. *J. Environ. Eng.-ASCE* **124**: 222-230.

- Maerki, M., B. Müller, and B. Wehrli. 2006. Microscale mineralization pathways in surface sediments: a chemical sensor study in Lake Baikal. *Limnol. Oceanogr.* **51**: 1342-1354.
- Maerki, M., B. Wehrli, C. Dinkel, and B. Müller. 2004. The influence of tortuosity on molecular diffusion in freshwater sediments of high porosity. *Geochem. Cosmochim. Acta* **68**: 1519-1528.
- Nielsen, L. P., P. B. Christensen, N. P. Revsbech, and J. Sørensen. 1990. Denitrification and oxygen respiration in biofilms studied with a microsensor for nitrous oxide and oxygen. *Microb. Ecol.* **19**: 63-72.
- Nishihara, G. N., and J. D. Ackerman. 2007. On the determination of mass transfer in a concentration boundary layer. *Limnol. Oceanogr.: Methods* **5**: 88-96.
- Nishihara, G. N., and J. D. Ackerman. 2009. Diffusive boundary layers do not limit the photosynthesis of the aquatic macrophyte *Vallisneria Americana* at moderate flows and saturating light levels. *Limnol. Oceanogr.* **54**: 1874-1882.
- O'Connor, B. L., and J. W. Harvey. 2008. Scaling hyporheic exchange and its influence on biogeochemical reactions in aquatic ecosystems. *Water Resour. Res.* **44**: W12423, doi:10.1029/2008WR007160.
- O'Connor, B. L., and M. Hondzo. 2008. Dissolved oxygen transfer to sediments by sweep and eject motions in aquatic environments. *Limnol. Oceanogr.* **53**: 566-578.
- O'Connor, B. L., M. Hondzo, and J. W. Harvey. 2009. Incorporating both physical and kinetic limitations in quantifying dissolved oxygen flux to aquatic sediments. *J. Environ. Eng.-ASCE* **135**: 1304-1314.
- Petzold, L. 1983. A description of DASSL: a differential/algebraic system solver, p. 65-68. In R. S. Stepleman [ed.], *Scientific computing: applications of mathematics and computing to the physical sciences*. North-Holland.
- Polerecky, L., N. Volkenborn, and P. Stief. 2006. High temporal resolution oxygen imaging in bioirrigated sediments. *Environ. Sci. Technol.* **40**: 5763-5769.
- Rabouille, C., L. Denis, K. Dedieu, G. Stora, B. Lansard, and C. Grenz. 2003. Oxygen demand in coastal marine sediments: comparing in situ microelectrodes and laboratory core incubations. *J. Exp. Mar. Biol. Ecol.* **285**:49-69.
- Ralston, M. L., and R. I. Jennrich. 1978. DUD: a derivative-free algorithm for nonlinear least squares. *Technometrics* **20**: 7-14, doi:10.2307/1268154.

- Rasmussen, H., and B. B. Jørgensen. 1992. Microelectrode studies of seasonal oxygen uptake in a coastal sediment: role of molecular diffusion. *Mar. Ecol. Prog. Ser.* **81**: 289-303.
- Reichert, P. 1994. AQUASIM: a tool for simulation and data analysis of aquatic systems. *Water Sci. Tech.* **30**: 21-30.
- Røy, H., M. Huettel, and B. B. Jørgensen. 2002. The role of small-scale sediment topography for oxygen flux across the diffusive boundary layer. *Limnol. Oceanogr.* **47**: 837-847.
- Røy, H., M. Huettel, and B. B. Jørgensen. 2004. Transmission of oxygen concentration fluctuations through the diffusive boundary layer overlying aquatic sediments. *Limnol. Oceanogr.* **49**: 686-692.
- Santschi, P., P. Höhener, G. Benoit, and M. Buchholtz-ten Brink. 1990. Chemical processes at the sediment-water interface. *Mar. Chem.* **30**: 269-315.
- Urban, N. R., C. Dinkel, and B. Wehrli. 1997. Solute transfer across the sediment surface of a eutrophic lake: I. Porewater profiles from dialysis samplers. *Aquat. Sci.* **59**: 1-25.
- Zimmerman, J. B., J. R. Mihelcic, and J. Smith. 2008. Global stressors on water quality and quantity. *Environ. Sci. Technol.* **42**: 4247-4254.
- Zhang, H., W. Davison, and C. Ottley. 1999. Remobilisation of major ions in freshly deposited lacustrine sediment at overturn. *Aquat. Sci.* **61**: 354-361.

Table 3.1. Frequently-used acronyms and notations.

ADV	Acoustic Doppler velocimeter; used to obtain velocity data for $\varepsilon$ and $u_*$ estimations at 10 cm above SWI
BBL	Bottom boundary layer
D	Molecular diffusion coefficient of $O_2$ in water ( $m^2 d^{-1}$ )
$D_s$	Molecular diffusion coefficient of $O_2$ in sediment corrected for tortuosity where $D_s = \phi D$ ( $m^2 d^{-1}$ )
$D_b$	Biodiffusion coefficient for $O_2$ ( $m^2 d^{-1}$ )
DBL	Diffusive boundary layer
$C_{bulk}$	Concentration of $O_2$ in bulk BBL ( $\mu mol L^{-1}$ )
$C_{SWI}$	Concentration of $O_2$ at SWI ( $\mu mol L^{-1}$ )
$J_{O_2}$	Sediment $O_2$ uptake rate at SWI ( $mmol m^{-2} d^{-1}$ )
Method: <i>curvefit</i>	Analytical method based on best-fit of polynomial defining sediment porewater profile
Method: <i>direct</i>	Analytical method based on directly measuring $\delta_{DBL}$ from linear DBL region of microprofile
Method: <i>model</i>	Analytical method based on predicting $\delta_{DBL}$ required to model sediment porewater profile via AQUASIM
Method: $u_*$	Analytical method based on estimating $\delta_{DBL}$ as a function of friction velocity
Method: <i>zonefit</i>	Analytical method based on defining multiple zero-order consumption zones to characterize sediment porewater profile via PROFILE
$O_2$	Dissolved oxygen ( $\mu mol L^{-1}$ )
$R_{O_2}$	$O_2$ consumption rate in sediment, defined volumetrically ( $R_{O_2v}$ ) or areally ( $R_{O_2a}$ )
$R_{O_2a}$	Areal $O_2$ consumption rate in sediment ( $mmol m^{-2} d^{-1}$ ) where $R_{O_2a} = \int R_{O_2v} dz$
$R_{O_2v}$	Volumetric $O_2$ consumption rate in sediment ( $mmol m^{-3} d^{-1}$ )
SWI	Sediment-water interface
$u_*$	Friction velocity ( $cm s^{-1}$ )
$z$	Distance above or below SWI (mm)
$z_{max}$	Depth of sediment oxic zone (mm)
$\delta_{DBL}$	Diffusive boundary layer thickness (mm)
$\varepsilon$	Dissipation rate of turbulent kinetic energy ( $W kg^{-1}$ )
$\phi$	Porosity (void volume per total sediment volume; dimensionless)
$\sigma$	Standard deviation (units correspond to parameter of interest)
$\partial C/\partial z$	$O_2$ concentration gradient ( $mmol m^{-4}$ )

Table 3.2. Average sediment oxygen uptake rate ( $J_{O_2}$ ), average diffusive boundary layer thickness ( $\delta_{DBL}$ ), and corresponding distributions of results ( $\pm$  as compared with averages) based on estimates from all five methods, water-side (*direct* and  $u^*$ ) and sediment-side (*curvefit*, *zonefit*, and *model*) approaches. The percent difference between water- and sediment-side averages (relative to water-side) shows that water-side estimates of  $J_{O_2}$  were consistently higher and  $\delta_{DBL}$  consistently lower than sediment-side estimates.

Profile number	Average $J_{O_2}$ ( $\text{mmol m}^{-2} \text{d}^{-1}$ )				Average $\delta_{DBL}$ (mm)			
	All methods	Water-side	Sediment-side	Difference (%)	All methods	Water-side	Sediment-side	Difference (%)
1	$5.3 \pm 2.9$	$5.9 \pm 5.6$	$4.8 \pm 0.4$	+19	$1.5 \pm 0.9$	$1.8 \pm 1.7$	$1.3 \pm 0.1$	+32
2	$6.7 \pm 2.1$	$8.5 \pm 0.7$	$5.5 \pm 1.7$	+35	$1.2 \pm 0.5$	$0.9 \pm 0.1$	$1.5 \pm 0.5$	-66
3	$5.7 \pm 1.1$	$6.4 \pm 1.8$	$5.2 \pm 0.3$	+18	$1.2 \pm 0.2$	$1.1 \pm 0.3$	$1.3 \pm 0.1$	-18
4	$6.8 \pm 1.9$	$8.6 \pm 1.4$	$5.6 \pm 0.8$	+35	$1.2 \pm 0.3$	$0.9 \pm 0.2$	$1.4 \pm 0.2$	-54
5	$6.6 \pm 1.0$	$7.6 \pm 0.9$	$6.0 \pm 0.1$	+21	$1.1 \pm 0.1$	$0.9 \pm 0.1$	$1.2 \pm 0.0$	-26
6	$5.6 \pm 1.5$	$7.1 \pm 0.9$	$4.6 \pm 0.7$	+35	$1.7 \pm 0.4$	$1.3 \pm 0.2$	$2.0 \pm 0.3$	-55
7	$4.0 \pm 0.5$	$4.6 \pm 0.1$	$3.6 \pm 0.1$	+20	$2.2 \pm 0.3$	$1.9 \pm 0.0$	$2.4 \pm 0.1$	-26
8	$1.3 \pm 0.5$	$1.8 \pm 0.3$	$1.0 \pm 0.1$	+44	$7.6 \pm 2.3$	$5.2 \pm 0.9$	$9.2 \pm 0.7$	-77
9	$1.0 \pm 0.3$	$1.2 \pm 0.1$	$0.9 \pm 0.3$	+23	$8.0 \pm 2.4$	$6.5 \pm 0.3$	$9.0 \pm 2.7$	-40
10	$5.6 \pm 1.1$	$6.3 \pm 0.8$	$5.1 \pm 1.1$	+19	$1.7 \pm 0.4$	$1.5 \pm 0.2$	$1.9 \pm 0.5$	-26
11	$5.9 \pm 1.7$	$7.6 \pm 0.5$	$4.8 \pm 0.7$	+37	$1.7 \pm 0.5$	$1.2 \pm 0.1$	$2.0 \pm 0.3$	-62
12	$4.5 \pm 0.7$	$4.8 \pm 1.2$	$4.3 \pm 0.2$	+12	$2.0 \pm 0.3$	$1.8 \pm 0.5$	$2.0 \pm 0.1$	-10
13	$6.8 \pm 1.2$	$7.8 \pm 0.3$	$6.1 \pm 1.0$	+22	$0.9 \pm 0.2$	$0.8 \pm 0.0$	$1.0 \pm 0.2$	-31
14	$5.2 \pm 0.8$	$5.9 \pm 0.6$	$4.8 \pm 0.6$	+20	$1.1 \pm 0.2$	$1.0 \pm 0.1$	$1.2 \pm 0.1$	-25
Average <sup>(1)</sup>	$5.8 \pm 1.2$	$6.9 \pm 0.8$	$5.1 \pm 0.7$	+25	$1.5 \pm 0.3$	$1.2 \pm 0.2$	$1.6 \pm 0.2$	-36

(1) Time-averaged  $\delta_{DBL}$  and  $J_{O_2}$  (characterizing the  $O_2$  profile series) used for comparative assessment are based on data obtained during active turbulence (thus excluding profiles 8 and 9). However, including data from the quiescent period typically affected average  $J_{O_2}$  and  $\delta_{DBL}$  comparisons by  $< 5\%$ . Outlier profile 1 data also excluded.

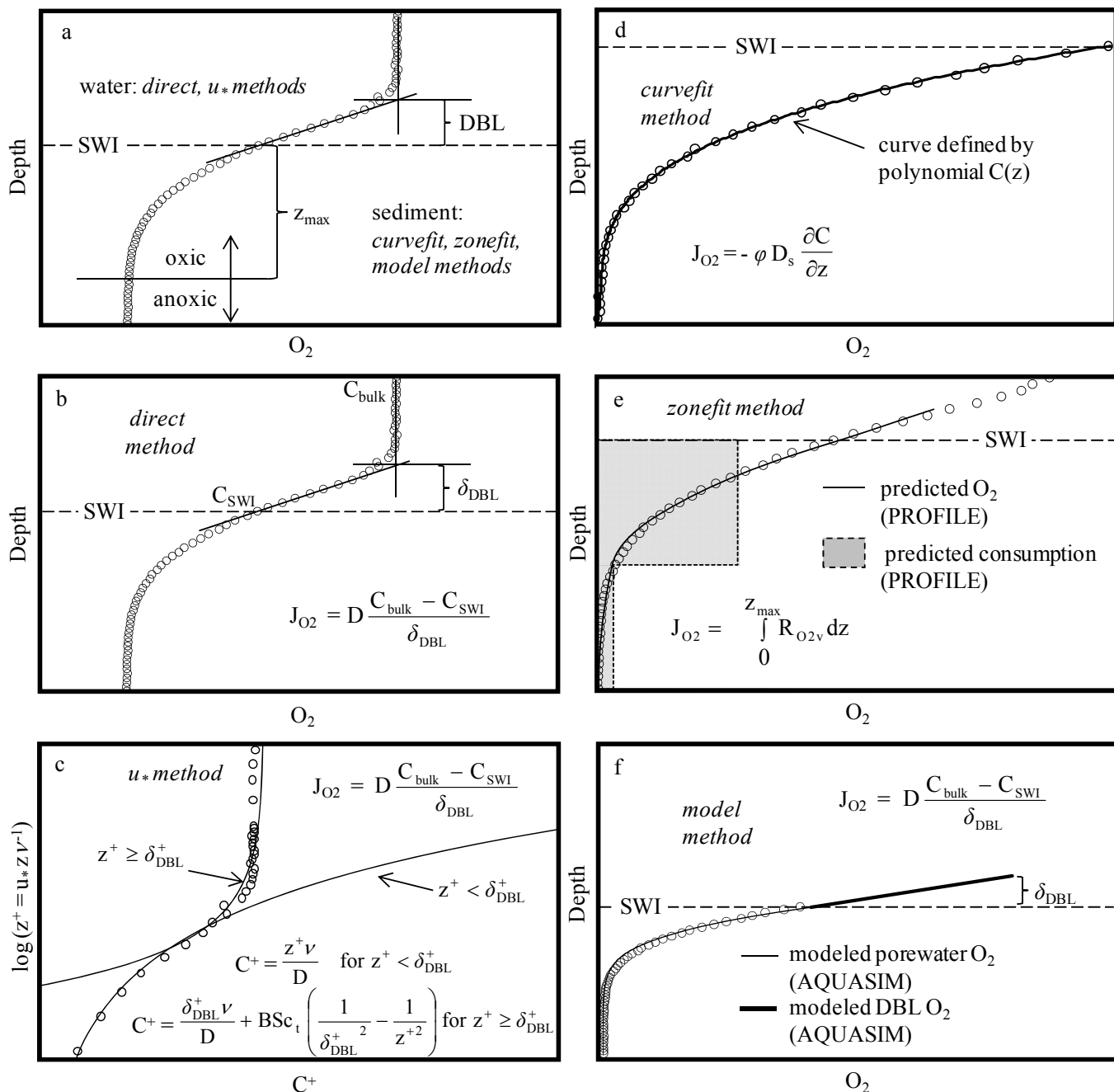


Figure 3.1. Components of a dissolved oxygen ( $O_2$ ) profile (a) and the five analytical methods (b-f) used to estimate sediment  $O_2$  uptake rate ( $J_{O_2}$ ) and diffusive boundary layer thickness ( $\delta_{DBL}$ ) are detailed using a sample  $O_2$  profile (profile 14, obtained at 08:16 h on 28 Aug 07). Open circle symbols are measured  $O_2$  profile data. (a) Key water- and sediment-side parameters include the diffusive boundary layer (DBL), sediment-water interface (SWI), and depth of the

sediment oxic zone ( $z_{\max}$ ). The five methods are defined in panels b – f. (b) *Direct method*: Fick’s first law (Eq. 3.2) applied using the concentration gradient in the DBL to calculate  $J_{O_2}$  and  $\delta_{DBL}$  with  $D$  as the diffusion coefficient for  $O_2$  in water.  $C_{\text{bulk}}$  and  $C_{\text{SWI}}$  are the  $O_2$  concentrations in the bulk water and at the SWI, respectively. (c)  *$u^*$  method*: The vertical distribution of  $O_2$  in the water column is universally scaled using a dimensionless power law for estimating  $\delta_{DBL}$  as a function of friction velocity ( $u^*$ ).  $C^+$ ,  $z^+$ , and  $\delta_{DBL}^+$  are non-dimensional parameters for  $O_2$  concentration, depth, and estimated  $\delta_{DBL}$ , respectively.  $\nu$  is kinematic viscosity,  $B$  is a constant of integration, and  $Sc_t$  is the turbulent Schmidt number. Profile-specific  $\delta_{DBL}^+$  is used to solve for  $\delta_{DBL}$ . (d) *Curvefit method*: The polynomial  $C(z)$  best describing the porewater  $O_2$  profile immediately below the SWI is identified. The vertical derivative of  $C(z)$  yields the concentration gradient  $\partial C/\partial z$ , which is used to obtain  $J_{O_2}$  as a function of the sediment  $O_2$  diffusion coefficient  $D_s$  via Eq. 3.2. (e) *Zonefit method*: Vertically-integrated PROFILE-predicted volumetric  $O_2$  consumption rates ( $R_{O_2v}$ ) over the sediment oxic zone yields the profile-specific areal  $O_2$  consumption rate ( $R_{O_2a}$ ), which is used to evaluate  $J_{O_2}$  by accounting for an areal rate of change in  $O_2$  ( $\partial C/\partial t_a$ ). (f) *Model method*: A sediment diffusion-reaction model (AQUASIM) is used to predict  $\delta_{DBL}$  required to model measured  $O_2$  porewater profiles. For definitions and units, see Table 3.1.

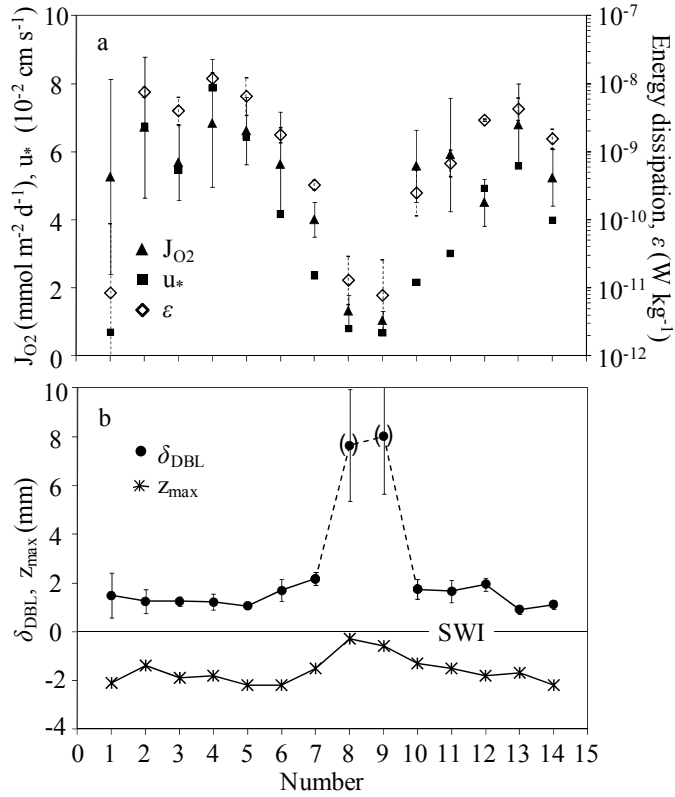


Figure 3.2. (a) Time series of  $J_{O_2}$ , energy dissipation ( $\varepsilon$ ), and friction velocity ( $u_*$ ) as a function of  $O_2$  profile number. (b) Turbulence-induced variations in the vertical  $O_2$  distribution (as characterized by  $\delta_{\text{DBL}}$  and  $z_{\text{max}}$ ) on both sides of the SWI.  $J_{O_2}$  and  $\delta_{\text{DBL}}$  values shown are the averages from the five analytical methods investigated here (Fig. 3.1). Modified from Bryant et al. (2010; Ch. 2).

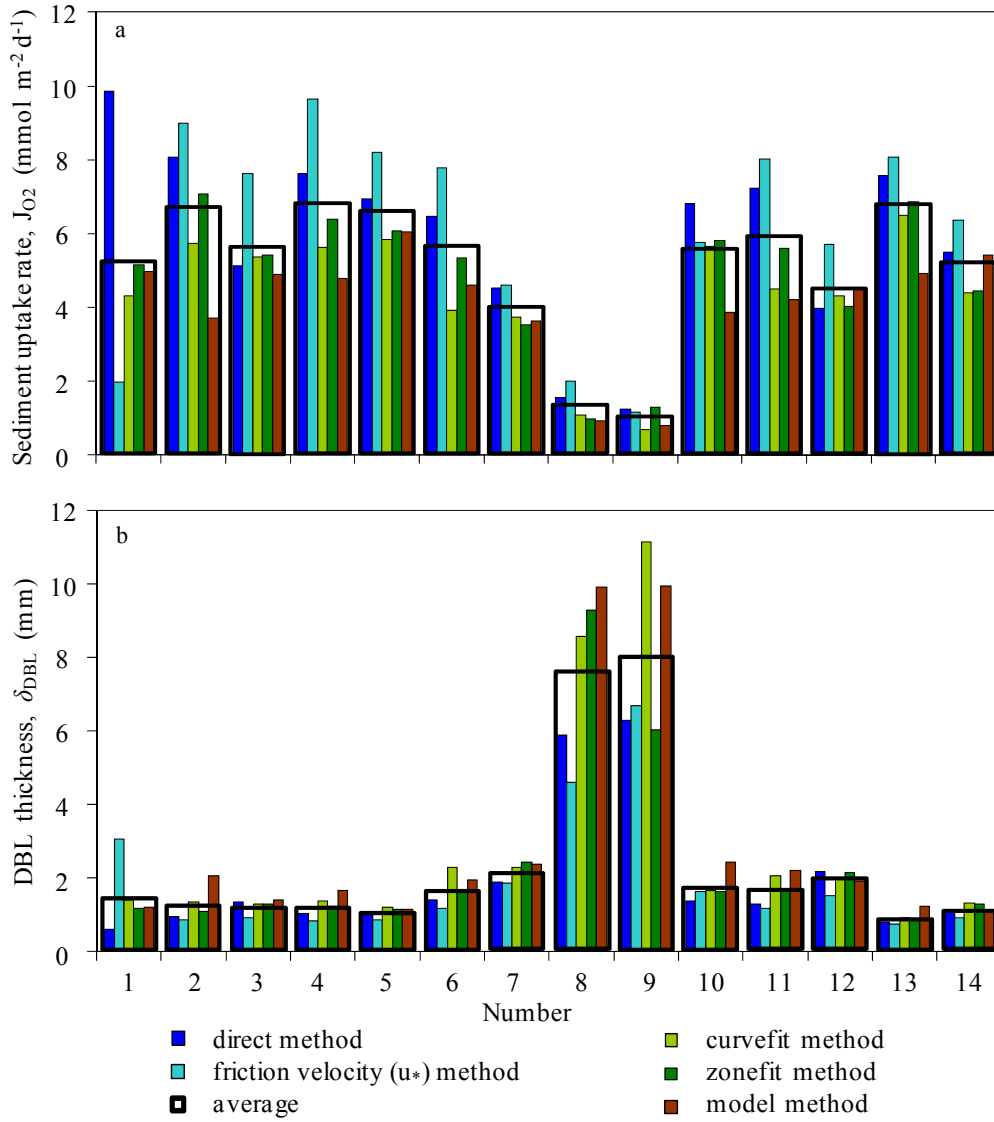


Figure 3.3. Comparison of analytical method results for (a)  $J_{O_2}$  and (b)  $\delta_{\text{DBL}}$  for all 14 profiles. Data for profile 1 considered outliers.

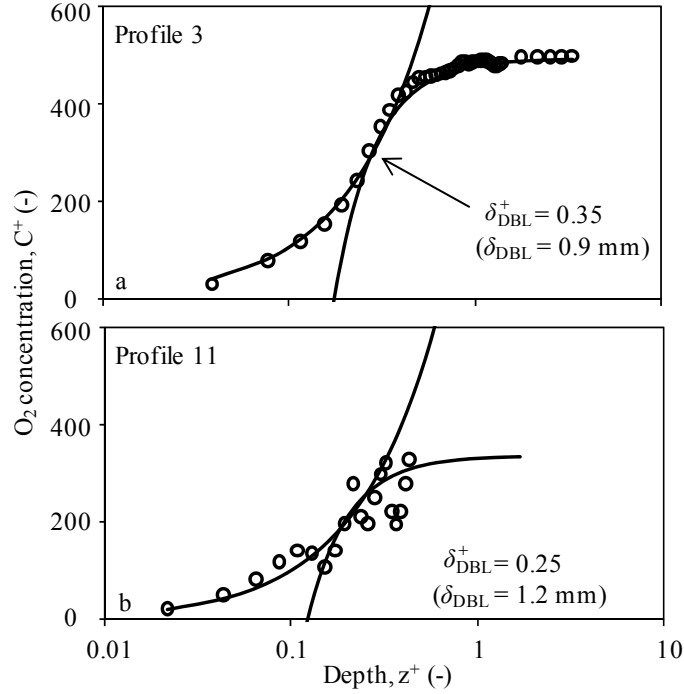


Figure 3.4. The universal scaling law (Fig. 3.1c) could be fit with the  $u^*$  method to a majority of our O<sub>2</sub> profiles, e.g., profile 3 in (a). However, the procedure was not robust for certain profiles, such as profile 11 in (b), and resulted in greater uncertainty in  $\delta_{\text{DBL}}^+$ .

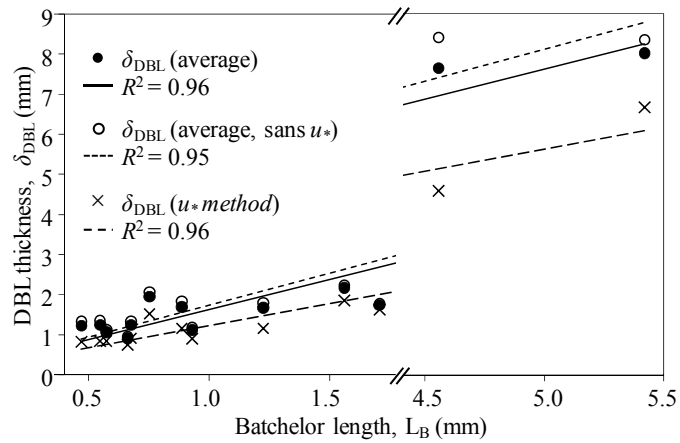


Figure 3.5. Relationship between O<sub>2</sub> Batchelor length scale ( $L_B$ ) and  $\delta_{\text{DBL}}$ . Estimates of  $\delta_{\text{DBL}}$ , based on the  $u^*$  method and the average (with and without  $u^*$  method results), are compared to  $L_B$  (Eq. 3.8). Profile 1 outlier data are excluded.

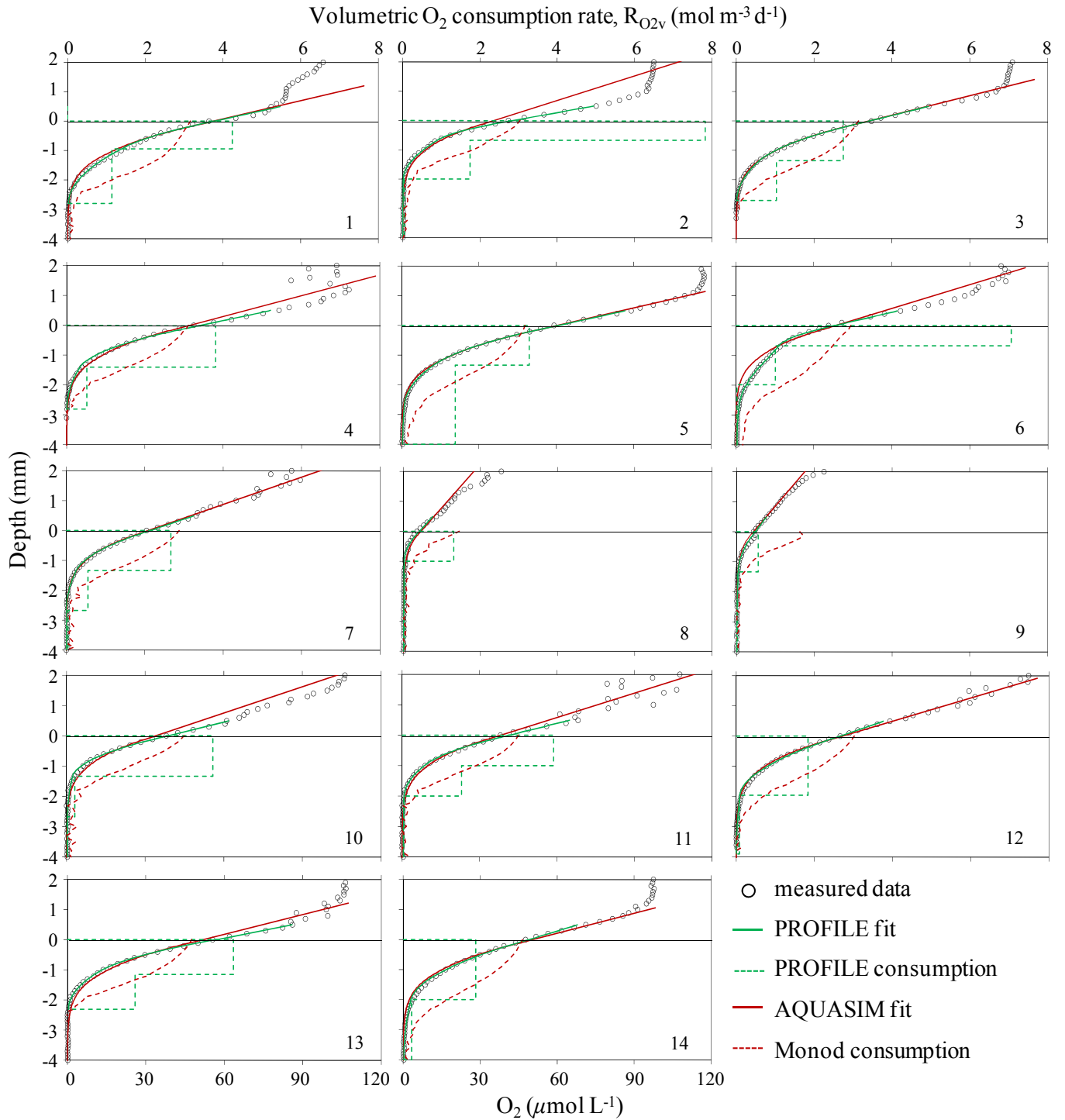


Figure 3.6.  $R_{O_2v}$  as predicted by the *zonefit method* (PROFILE; based on zero-order kinetics; green) and the *model method* (AQUASIM; based on Monod kinetics; red). Model fits designated by solid lines and model predictions of sediment  $O_2$  consumption designated by dashed lines. SWI located at depth = 0 mm.

## Chapter 4 – Oxygenation-induced variation in sediment oxygen uptake

Bryant, Lee D., Paul A. Gantzer\*, John C. Little

Civil and Environmental Engineering, Virginia Tech, Blacksburg, Virginia, 24060, USA.

\*Now at: Gantzer Water Resources LLC, Kirkland, Washington, 98084, USA.

To be submitted: *Water Research*

### 4.1 Abstract

Hypolimnetic oxygenation systems (HOx) are becoming more frequently used in lakes and reservoirs to elevate dissolved oxygen ( $O_2$ ) while preserving stratification, thereby decreasing levels of reduced chemical species in the hypolimnion. However, diminished HOx performance has been observed due to HOx-induced increases in sediment  $O_2$  uptake. Through a series of in situ  $O_2$  microprofile and current velocity measurements, we evaluated the vertical  $O_2$  distribution at the sediment-water interface as a function of HOx operation. These data were used to determine how sediment  $O_2$  uptake rate ( $J_{O_2}$ ) was affected by variable HOx flow, proximity to the HOx, and changes in near-sediment mixing and  $O_2$  levels.  $J_{O_2}$  and sediment  $O_2$  levels were found to be significantly influenced by oxygenation on a reservoir-wide basis. Increased sediment  $O_2$  uptake and an enhanced sediment oxic zone were observed in response to increasing HOx flow from low to moderately high flow rates. In contrast,  $J_{O_2}$  decreased to zero and the sediment became anoxic as the vertical  $O_2$  distribution collapsed during periods when the HOx was turned off and near-sediment mixing decreased.  $J_{O_2}$  was also observed to decrease at very high HOx flow rates, which may be a result of transient reservoir conditions, decreased water-side control of sediment  $O_2$  uptake, and/or sediment resuspension near the HOx.  $J_{O_2}$  and sediment  $O_2$  availability throughout the reservoir were found to be largely governed by HOx-induced mixing rather than  $O_2$  levels in the water column. By quantifying  $J_{O_2}$  and subsequent sediment  $O_2$  availability as a function of HOx operations, this study will contribute to the optimization of water quality and management of HOx-equipped lakes and reservoirs.

## 4.2 Introduction

Dissolved oxygen ( $O_2$ ) concentration has been identified as one of the most critical ecological factors controlling water quality and associated environmental conditions (Hondzo et al. 2005). Aquatic ecosystems, drinking water quality, and hydropower plants are all negatively affected by depleted  $O_2$  levels (Beutel and Horne 1999). Water-quality standards typically require  $O_2 > 5 \text{ mg L}^{-1}$  to protect aquatic life (EPA 2000). Hydropower plants are usually required to meet these minimum downstream  $O_2$  levels in the water they discharge downstream (Mobley et al. 2007a). It has recently been found that long-term  $O_2$  depletion in fish habitats can cause significant declines in fish populations as a result of endocrine system disruptions and subsequent reproductive impairment, with low  $O_2$  possibly having even more of an effect than anthropogenic chemicals (Wu et al. 2006). Organic or nutrient loading of thermally stratified lakes and reservoirs may lead to significant depletion of  $O_2$  in the deeper hypolimnetic water. Hypolimnetic  $O_2$  depletion may result in the release of soluble metals such as iron (Fe) and manganese (Mn) from the sediments, decreasing water quality and increasing drinking-water treatment costs. Orthophosphate release can promote excessive algal growth which stimulates eutrophication and leads to additional  $O_2$  consumption from the decomposition of settled algal detritus. Oxygen depletion in lakes and reservoirs is largely controlled by sediment  $O_2$  uptake which is regulated by near-sediment hydrodynamics and microbial and chemical reactions occurring within the sediment (Bouldin 1968; Veenstra and Nolen 1991). Understanding these processes is crucial for accurately quantifying the sediment  $O_2$  uptake flux ( $J_{O_2}$ ), optimizing water quality, and successfully managing lakes and reservoirs (Beutel 2003; Lorke et al. 2003).

$J_{O_2}$  is a fundamental parameter that is frequently used to define the overall quality of a water body (Wetzel 2001).  $O_2$  must diffuse through the diffusive boundary layer (DBL), a mm-scale laminar layer immediately above the sediment-water interface (SWI), to reach the sediment (see Fig. 2.1 in Bryant et al. 2010; Ch. 2; Jørgensen and Revsbech 1985).  $J_{O_2}$  is therefore a function of the  $O_2$  concentration driving force across the DBL, which in turn is controlled by turbulence in the overlying water of the bottom boundary layer (BBL) and subsequent DBL thickness ( $\delta_{DBL}$ ; Lorke et al. 2003; Bryant et al. 2010; Ch. 2). Upon reaching the sediment,  $O_2$  is used for various biogeochemical processes (e.g., benthic mineralization of organic matter, re-oxidation of reduced metal species). The balance between  $J_{O_2}$  and the rate of sediment  $O_2$

consumption ( $R_{O_2}$ ) governs  $O_2$  penetration into the sediment or the depth of the sediment oxic zone ( $z_{max}$ ).

Hypolimnetic oxygenation systems (HOx; e.g., bubble-plume diffusers) are used increasingly by drinking water and hydropower utilities to replenish  $O_2$  and reduce levels of soluble metals in source water while preserving stratification (McGinnis et al. 2002; Singleton and Little 2006; Gantzer et al. 2009a). Bubble-plume HOx are designed to release  $O_2$  gas from porous diffusers positioned near the reservoir bottom, thereby increasing hypolimnetic  $O_2$  levels. These systems are designed to impart relatively low levels of mixing within the hypolimnion while preserving thermal structure; this prevents destratification and the subsequent mixing of the epilimnion and hypolimnion layers (Wüest et al. 1992; McGinnis et al. 2004). Ideally, HOx increases  $O_2$  levels both in the water column and at the SWI in order to suppress the release of reduced chemical species from the sediment and to ultimately decrease concentrations of these species in the hypolimnion (Beutel 2003; Zaw and Chiswell 1999). However, oxygenation may cause additional sediment  $O_2$  uptake due to enhanced  $J_{O_2}$  resulting from HOx-induced turbulence, increased hypolimnetic  $O_2$  levels, and increased porewater concentrations of reduced chemical species, all of which would increase the  $O_2$ -concentration driving force in the DBL (Moore 2003). Unfortunately, reservoir-specific  $J_{O_2}$  measurements are rarely available and oxygenation systems are often designed based on oxygen depletion rates measured prior to installation of the HOx (Moore et al. 1996; Mobley et al. 1997b). Beutel (2003) showed that after HOx are turned on they are sometimes unable to meet the reservoir  $O_2$  demand initially, possibly because of additional HOx-induced demand.

While the relationship between near-sediment current velocity and  $J_{O_2}$  has been established (Gundersen and Jørgensen 1990; Mackenthun and Stefan 1998), little work has been done to quantify how HOx operations affect  $J_{O_2}$  and the vertical distribution of  $O_2$  at the SWI; studies that have been performed have been largely laboratory based (Moore et al. 1996; Beutel 2003). However, it has been shown that  $J_{O_2}$  can be significantly affected by variations in natural turbulence (Lorke et al. 2003; Bryant et al. 2010) and laboratory-based studies may not capture actual HOx-induced conditions. Therefore, we performed a study based on in situ  $O_2$  sediment-water microprofile and current velocity data to characterize  $J_{O_2}$  and the corresponding vertical  $O_2$  distribution at the SWI (as characterized by  $z_{max}$  and  $\delta_{DBL}$ ) as a function of HOx operation in a drinking-water-supply reservoir. We focus first on a week-long in situ campaign that shows how

$J_{O_2}$  and the vertical  $O_2$  distribution at the SWI respond to turning the HOx off and on. We then build on a multi-year data set to quantify the influence of HOx operation at a reservoir-wide scale. To our knowledge, this is one of the first studies to assess how HOx-induced variation in near-sediment mixing and  $O_2$  levels influence  $J_{O_2}$  and sediment  $O_2$  availability in situ. Corresponding effects on reservoir water quality are also evaluated.

### **4.3 Materials and methods**

**4.3.1 Study site** – Our research focused on a drinking-water-supply reservoir, Carvin’s Cove Reservoir (CCR), which is managed by the Western Virginia Water Authority (WVWA) to supply drinking water to the county of Roanoke, Virginia, USA. CCR is a stream-fed lake that has been managed by WVWA as a drinking-water-supply reservoir since the late 1940s. CCR is eutrophic and has a maximum depth of 23 m, width of ~600 m, and length of ~8000 m (Fig. 4.1). In 2005, a bubble-plume line-diffuser HOx was installed to replenish  $O_2$  depleted during summer stratification and to reduce Fe and Mn in the source water (McGinnis et al. 2002; Gantzer et al. 2009b). The CCR HOx is comprised of two parallel lines of porous tubing (each line consists of two tubes each ~1 cm in diameter and 625 m in length) located in the deepest section of the reservoir near the WVWA treatment plant outtake, as shown in Fig. 4.1. The CCR HOx delivers pure  $O_2$  gas over a wide range of flow rates, providing considerable operational flexibility for control of hypolimnetic  $O_2$  and turbulence. Hence, we had the ability to control  $O_2$  and turbulence (mixing) conditions in the reservoir by changing the HOx flow rate.

Data have been collected from 2005 through 2008 to assess how the HOx affects CCR source water, with significant improvement in water quality observed since CCR HOx operations began. Work by Gantzer et al. (2009a,b) focusing on water column conditions showed elevated  $O_2$  levels throughout summer stratification and reduced soluble Fe and Mn concentrations, with soluble Mn decreasing by > 97% from pre-HOx levels. Our study on HOx-induced variation in  $J_{O_2}$  and sediment  $O_2$  availability, as well as a companion study focused on the response of Fe and Mn fluxes to HOx (Ch. 5), support the work by Gantzer et al. by evaluating the influence of the sediment on water quality.

**4.3.2 Data collection and analysis** – This study is based on in situ data obtained primarily during CCR field campaigns performed during summer 2008. For these campaigns, an in situ microprofiler (MP4; Unisense A/S) and a Workhorse Rio Grande acoustic Doppler current profiler (ADCP; Teledyne RDI, Inc.) were used to obtain microprofiles at the SWI and current velocity series in the water column, respectively. CCR HOx flow was maintained almost continuously at  $51 \text{ m}^3 \text{ h}^{-1}$  (or  $\sim 1580 \text{ kg O}_2 \text{ d}^{-1}$ ; Fig. 4.2) in 2008. However, in the summer the HOx was turned off for two experimental campaigns (each  $\sim 1$  week in duration) to track the response of the vertical  $\text{O}_2$  distribution at the SWI and corresponding  $J_{\text{O}_2}$ . In August 2008, the MP4 and ADCP were deployed mid-reservoir,  $\sim 1000$  m upstream of the end of the HOx, at site C3 (Fig. 4.1) and data were collected continuously from August 19 to 30. Data were downloaded and batteries for the MP4 microprofiler and the ADCP were exchanged daily. The HOx was turned off for  $\sim 48$  h from August 19 to 21. A similar campaign was performed near the HOx at site CVCB from June 18 to 26. The HOx was also turned off during this period for  $\sim 48$  h from June 19 to 21. While similar results were obtained from both campaigns, analyses and results for this study are based largely on the August C3 campaign due to insufficient background MP4 data for the June CVCB campaign.

In addition to the week-long summer 2008 campaigns, MP4 and ADCP data were collected monthly from June through September 2008 at CVCB, C3, and CR, which is located  $\sim 2000$  m upstream of the end of the HOx (Fig. 4.1). Monthly MP4 microprofile measurements were also obtained from May to August 2007 downstream, alongside, and  $1000$  m upstream of the HOx at CC, CVCB, and C3, respectively, under varying flow conditions (Fig. 4.2). Every day that  $\text{O}_2$  microprofile measurements were obtained, conductivity, temperature, and  $\text{O}_2$  as a function of depth (CTD) profiles were measured at each sampling location using a Seabird Electronics SBE 19plus profiler.

*4.3.2.1  $\text{O}_2$  microprofiles* – During 2007 and 2008, the in situ autonomous MP4 microprofiler equipped with microsensors ( $\text{O}_2$ , temperature, and pH) was used to obtain microprofiles at the SWI in CCR. The  $\text{O}_2$  microsensor (OX-100; Unisense A/S) had  $100\text{-}\mu\text{m}$  tip diameter and depth resolution, fast response time (90% in  $< 8$  s), and negligible stirring sensitivity. The  $\text{O}_2$  microsensor was a Clark-type sensor with an internal reference and guard cathode. The temperature microsensor (TP-100; Unisense A/S) was a thermo-coupled sensor

with a spatial resolution of  $\sim 200 \mu\text{m}$ , resolution of  $\pm 0.1 \mu\text{V}$  per  $^{\circ}\text{C}$ , and a 90% response time of  $< 3 \text{ s}$ . The pH microsensor (PH-100; Unisense A/S) was a miniaturized conventional pH electrode with a spatial resolution of  $\sim 200 \mu\text{m}$ , detection limit of  $\pm 0.1 \text{ pH}$  unit, and a 90% response time of  $< 20 \text{ s}$ . The pH microsensor was used solely to obtain single-point measurements and not profile data; therefore, the longer response time did not affect speed of profiling. Profiles were measured continuously during the week-long campaigns and profiles were obtained in duplicate at each CCR sampling location during the monthly campaigns. Time required to obtain a full profile was  $\sim 50 \text{ min}$  and profiles were obtained as follows: 10-mm resolution from 10 cm to 1 cm above the SWI, 1-mm resolution from 1 cm to 0.5 cm above the SWI, 0.1-mm resolution from 0.5 cm above the SWI to 0.5 cm below the SWI. Ten measurements were typically taken at each depth (during the multi-day campaigns three measurements were obtained per depth increment due to data-storage limitations during overnight deployments). Following a pause between measurements for equilibrium to be established at each depth, microsensor data were collected at a rate of 1 Hz. A linear calibration of MP4 microprofile data was obtained using Winkler titration of BBL water sampled immediately above the sediment using a Kemmerer bottle and zero readings from anoxic sediment.

The SWI location was determined via both visual interpretations of  $\text{O}_2$  profiles (based on identifying linear DBL regions and kinks in the profile due to porosity differences between the sediment and the water column) and using standard deviations of  $\text{O}_2$  temporal fluctuations obtained at each sampling-depth increment. Standard deviations of solute concentration measurements decrease as the sensor approaches the sediment due to decreased eddy diffusion near the SWI; these variances were also used to determine SWI location (Müller et al. 2002). These two methods yielded consistent and comparable estimates of the SWI location (as discussed by Bryant et al. (2010); Ch. 2).

4.3.2.2 *Current velocity* – Velocity profile series were collected using a 1200 kHz RDI ZedHed ADCP equipped with four acoustic beams slanted at  $20^{\circ}$ . The ADCP, positioned adrift alongside our primary research vessel and facing downward from the water surface, profiled the full water-column depth based on a 1-m bin size. Samples were obtained in burst mode with 50 samples per ensemble at a rate of 2 Hz. Accuracy of velocity measurements was  $\pm 0.25\%$  of

water + boat velocity  $\pm 0.25 \text{ cm s}^{-1}$ . During measurements, the boat remained stationary so boat velocity was effectively zero.

A limitation of using the ADCP for water-column velocity measurements is its range of data collection, as it cannot be used to collect data over the entire water column. We were particularly interested in near-sediment velocities for this study. However, the ADCP has a blanking distance near the sediment where consistent data series are not collected due to interference from the angled acoustic beams reflecting off the sediment surface, thereby contaminating the acoustic signal returned to the ADCP. The near-sediment blank zone is  $\sim 6\%$  of the total water-column depth (as defined by RDI) or approximately the bottom 1 m in CCR. Hence, near-sediment velocities were evaluated at  $\sim 1.5$  m above the sediment, with current velocities also assessed at 3 m above the sediment and 5 m below the water surface.

*4.3.2.3 O<sub>2</sub> microprofile analyses* –  $J_{O_2}$  was evaluated based on O<sub>2</sub> microprofile data using Fick's first law of diffusion (Rasmussen and Jørgensen 1992; Lavery 2001; Higashino et al. 2004):

$$J_{O_2} = -\varphi D_s \left. \frac{\partial C}{\partial z} \right|_{\text{sed}} = -D \left. \frac{\partial C}{\partial z} \right|_{\text{water}} = D \frac{C_{\text{bulk}} - C_{\text{SWI}}}{\delta_{\text{DBL}}} \Bigg|_{\text{water}} \quad [\text{mmol m}^{-2} \text{ d}^{-1}] \quad (4.1)$$

where  $\varphi$  is sediment porosity ( $\text{m}^3$  voids  $\text{m}^{-3}$  total volume),  $D_s$  is the diffusion coefficient for O<sub>2</sub> in sediment ( $\text{m}^2 \text{ s}^{-1}$ ),  $D$  is the diffusion coefficient for O<sub>2</sub> in water ( $\text{m}^2 \text{ s}^{-1}$ ),  $\partial C/\partial z$  is the linear O<sub>2</sub> concentration gradient in the DBL immediately above or below the SWI ( $\mu\text{mol m}^{-4}$ ),  $C_{\text{bulk}}$  is the O<sub>2</sub> concentration in the bulk BBL ( $\mu\text{mol L}^{-1}$ ), and  $C_{\text{SWI}}$  is the O<sub>2</sub> concentration at the SWI ( $\mu\text{mol L}^{-1}$ ), as shown in Fig. 2.1a of Ch. 2. Diffusive transport is defined in the sediment by the second term in Eq. 4.1 and in the water by the third and fourth terms.

Sediment cores from the primary sampling locations (method detailed in Ch. 2 and 5) were evaluated for  $\varphi$  following Dalsgaard et al. (2000) and  $\varphi$  values of 0.95-0.97 were obtained. Values for  $D$  were based on  $D = 1.97 \times 10^{-9} \text{ m}^2 \text{ s}^{-1}$  at  $20^\circ\text{C}$  and correcting for temperature using the Stokes-Einstein relationship (Li and Gregory 1974; Arega and Lee 2005).  $D_s$  was defined as  $D_s = \varphi D$  to correct for sediment tortuosity as a function of  $\varphi$  (Berg et al. 1998; Glud 2008; Ch.

3). The temporal change in O<sub>2</sub> concentration ( $\partial C/\partial t$ ) was evaluated for our series of in situ O<sub>2</sub> profiles by comparing profiles immediately before and after one another and calculating the rate of change in O<sub>2</sub> at each depth.  $\partial C/\partial t$  was found to be on average <5% of J<sub>O<sub>2</sub></sub>, establishing that our profiles were at quasi-steady state and that turbulence conditions in CCR were changing slowly relative to the duration of an O<sub>2</sub> microprofile.

Because water-side O<sub>2</sub> profile data is frequently more difficult to evaluate due to rapid turbulence-induced variation in  $\delta_{\text{DBL}}$  (Bryant et al. 2010; Ch. 2), J<sub>O<sub>2</sub></sub> was evaluated from sediment O<sub>2</sub> porewater data using the second term in Eq. 4.1. The DBL was characterized from both sides of the SWI and results were compared (Appendix A.1). Water-side  $\delta_{\text{DBL}}$  was estimated as a function of the measured  $\partial C/\partial z$  in the DBL using the third and fourth terms in Eq. 4.1. Sediment-side  $\delta_{\text{DBL}}$  was estimated as a function of sediment-side J<sub>O<sub>2</sub></sub> using the second and fourth terms in Eq. 4.1. Water-side  $\delta_{\text{DBL}}$  were used in subsequent evaluations of J<sub>O<sub>2</sub></sub> to allow for independent comparison. As shown in Appendix A.1, water- and sediment-side  $\delta_{\text{DBL}}$  estimates were found to have moderately good correlation ( $R^2 = 0.76$ ).

The balance between O<sub>2</sub> transport and consumption is defined by

$$J_{\text{O}_2} = \int_0^{z_{\text{max}}} R_{\text{O}_2\text{v}} dz + \int_0^{z_{\text{max}}} \frac{\partial C}{\partial t} dz \quad [\text{mmol m}^{-2} \text{ d}^{-1}] \quad (4.2)$$

where volumetric R<sub>O<sub>2</sub></sub> (R<sub>O<sub>2</sub>v</sub>; mmol m<sup>-3</sup> d<sup>-1</sup>) and the change in O<sub>2</sub> over time ( $\partial C/\partial t$ ; mmol m<sup>-3</sup> d<sup>-1</sup>) are integrated over the sediment profile depth to z<sub>max</sub> (designated as the depth where O<sub>2</sub> drops to < 3 μmol L<sup>-1</sup>). R<sub>O<sub>2</sub>v</sub> was evaluated using the numerical procedure PROFILE (Berg et al. 1998) which characterizes zero-order sediment O<sub>2</sub> consumption as a function of depth using O<sub>2</sub> porewater profile data (Bryant et al. 2010; Ch. 2). Depth-integrated values of R<sub>O<sub>2</sub>v</sub> and  $\partial C/\partial t$  yield the areal parameters R<sub>O<sub>2</sub>a</sub> and  $\partial C/\partial t_a$ , respectively (mmol m<sup>-2</sup> d<sup>-1</sup>), which are directly comparable to J<sub>O<sub>2</sub></sub> via Eq. 4.2 (Epping and Helder 1997).

*4.3.2.4 Turbulence estimations* – As previously discussed, we were restricted in obtaining near-sediment velocities with our ADCP due to the limited accuracy approaching the sediment. Our estimates of velocity at ~1.5 m above the sediment are thus a relative measure of near-sediment mixing conditions. Additionally, turbulence has been shown by Lorke et al.

(2003) to be a controlling factor in  $\delta_{\text{DBL}}$  and  $J_{\text{O}_2}$  estimates rather than velocity. Turbulence is characterized by the dissipation rate of turbulent kinetic energy,  $\varepsilon$  ( $\text{W kg}^{-1}$ ), which is frequently estimated by applying the inertial dissipation method (Grant et al. 1962) to near-sediment ( $\sim 10$  cm) velocity data, as performed by Bryant et al. (2010; Ch.2) using acoustic Doppler velocimeter data. To quantify turbulence levels in the absence of more precise near-sediment velocity data for the current study, we used a correlation between the DBL, the viscous boundary layer (the cm-scale region immediately above the DBL), and friction velocity ( $u_*$ ) to estimate  $\varepsilon$ . According to Wüest and Lorke (2003),  $\delta_{\text{DBL}}$  and viscous boundary layer thickness ( $\delta_\nu$ ) are related by

$$\delta_{\text{DBL}} = \delta_\nu \left( \frac{D}{\nu} \right)^{1/3} \quad [\text{m}] \quad (4.3)$$

where  $\nu$  is the molecular viscosity of water ( $\text{m}^2 \text{s}^{-1}$ ). In turn,  $\delta_\nu$  is defined as a function of  $u_*$  (Schlichting 2000) via

$$\delta_\nu = \frac{11 \nu}{u_*} \quad [\text{m}] \quad (4.4)$$

Merging Eq. 4.3 and 4.4 allowed  $u_*$  to be related to  $\delta_{\text{DBL}}$ :

$$u_* = \frac{11 \nu \left( \frac{D}{\nu} \right)^{1/3}}{\delta_{\text{DBL}}} \quad [\text{m s}^{-1}] \quad (4.5)$$

The  $u_*$  values estimate the frictional stress of BBL currents on the sediment and thus, similar to  $\varepsilon$ , characterize BBL turbulence. Estimated  $u_*$  values obtained via Eq. 4.5 were used to calculate  $\varepsilon$  using the law-of-the-wall assumption (Lorke et al. 2003):

$$\varepsilon = \frac{u_*^3}{\kappa Z} \quad [\text{W kg}^{-1}] \quad (4.6)$$

where  $\kappa$  (the von Karman constant) is 0.41 and  $z$  is height above the sediment. For these estimations,  $\varepsilon$  was evaluated at an assumed  $z = 10$  cm to obtain near-sediment  $\varepsilon$  predictions and to allow for direct comparison with  $\varepsilon$  based on velocity measured at  $z = 10$  cm (Bryant et al. 2010; Ch. 2) to verify that  $\varepsilon$  estimates for this study were typical for a freshwater lake. Because sediment-side  $\delta_{\text{DBL}}$  is estimated as a function of  $J_{\text{O}_2}$  (Eq. 4.1), water-side  $\delta_{\text{DBL}}$  was used in  $\varepsilon$  calculations to allow for an independent evaluation of how  $J_{\text{O}_2}$  was affected by variations in turbulence.

## 4.4 Results and Discussion

**4.4.1 Vertical O<sub>2</sub> distribution at SWI** – During the 2008 campaign, the HOx was turned off for ~48 h in late June and in late August, as previously discussed (Fig. 4.2). Significant variation in the vertical O<sub>2</sub> distribution near the SWI was observed in response to halting oxygenation. Profiles (each of ~50 min duration) were collected continuously over the course of both 2008 week-long campaigns. A summary of profile results showing key trends in the response of the vertical O<sub>2</sub> distribution during the August C3 campaign is presented in Fig. 4.3. As shown in Fig. 4.3a, at the time the HOx was turned off (August 19 at ~14:00), O<sub>2</sub> levels were relatively high both in the water immediately above the sediment (~100  $\mu\text{mol L}^{-1}$ ) and within the sediment porewater (~90  $\mu\text{mol L}^{-1}$  at the SWI with  $z_{\text{max}}$  of 0.8 mm). A constant  $C_{\text{bulk}}$  and a defined DBL are also evident, indicating active BBL turbulence. However, as indicated by the 17:39 profile (time indicates the point at which the microsensor encountered the SWI), within a few hours of turning the HOx off O<sub>2</sub> started to become depleted from the sediment and overlying water. By 20:02 (~6 h following HOx turn-off), the sediment and overlying water column had become completely anoxic. Excluding a brief transient period on August 21 (profiles 15:11, 15:58) when near-sediment O<sub>2</sub> increased immediately after HOx operation resumed at ~14:00 August 21, conditions remained anoxic until August 29 (Fig. 4.3b; discussed below). A relatively rapid increase in O<sub>2</sub> is then observed on both sides of the SWI, with the vertical distribution returning to a structure similar to that at the beginning of the campaign (Fig. 4.3a).

Contour plots of O<sub>2</sub> microprofile and hypolimnetic O<sub>2</sub> data based on a Kriging interpolation scheme are shown in Fig. 4.4. While O<sub>2</sub> levels near the SWI changed substantially in response to turning off the HOx (Fig. 4.4a), O<sub>2</sub> remained relatively constant (~150  $\mu\text{mol L}^{-1}$ )

at 8 cm above the sediment (Fig. 4.4b). The water column was also affected minimally (Fig. 4.4c). The experiment was designed to minimize effects on hypolimnetic O<sub>2</sub> levels and thus preserve drinking water quality. This accounts for the short (~48 h) duration of the turn-off period. Previous work by Gantzer et al. (2009a) showed that turning the HOx off for a longer period (several weeks) can significantly decrease water quality. The fact that O<sub>2</sub> levels remained constant a few cm above the sediment during the period the HOx was not in operation indicates that HOx-induced turbulence plays a significant role in driving oxygenated water down to the SWI. Bryant et al. (2010; Ch. 2) similarly showed that seiche-induced turbulence was a controlling factor in maintaining oxic sediment conditions regardless of O<sub>2</sub> levels immediately above the SWI.

HOx operations are shown to have a significant influence on the vertical O<sub>2</sub> distribution at the SWI (Fig. 4.3, 4.4). A direct correlation between HOx operation and parameters quantifying the vertical O<sub>2</sub> distribution (O<sub>2</sub> at 5 cm above the sediment (C<sub>5</sub>), C<sub>SWI</sub>, and z<sub>max</sub>) is shown in Fig. 4.5. As C<sub>SWI</sub> dropped from ~125 to 0 μmol L<sup>-1</sup> after turning off the HOx on August 19 (Fig. 4.5a), z<sub>max</sub> also rapidly decreased from 1 to 0 mm as O<sub>2</sub> was depleted from the sediment (excluding the brief oxic period on August 21 after HOx operation resumed). Sediment porewater and the SWI remain anoxic and C<sub>5</sub> remains low until August 29 when oxic sediment conditions were re-established. We did not anticipate anoxic conditions to occur so rapidly following the halt of HOx operation during the initial June campaign; thus, we did not capture the initial O<sub>2</sub> depletion phase (Fig. 4.5b). However, the response of the vertical O<sub>2</sub> distribution to turning the HOx off and on is similar at CVCB (Fig. 4.5b) to that observed at C3 (Fig. 4.5a). Data obtained before and after each week-long campaign (e.g., August 12 and September 14 in Fig. 4.5a) compare well with average values of C<sub>SWI</sub> and z<sub>max</sub> during regular continuous HOx operation (C<sub>SWI</sub> = 94 ± 38 μmol L<sup>-1</sup> and z<sub>max</sub> = 1.4 ± 0.6 mm at C<sub>3</sub> (n = 22) and 61 ± 45 μmol L<sup>-1</sup> and 0.7 ± 0.4 mm (n = 15) at CVCB; full data set not shown).

Based on hypolimnetic O<sub>2</sub> data, it has been shown that it typically takes ~1 week for a similar HOx-equipped reservoir to return to ‘steady-state’ conditions after resuming oxygenation, with significantly higher O<sub>2</sub> depletion rates in the hypolimnion during the initial week (Gantzer 2002). Similarly, it took ~8 days for the SWI vertical O<sub>2</sub> distribution to re-establish during the C3 campaign and ~5 days during the CVCB campaign (Fig. 4.3-4.5). This delayed response may be attributed to both localized sediment resuspension and time required

for a uniform flow pattern in the reservoir to be re-established by the HOx plume. Sediment resuspension and subsequent introduction of reduced species into the hypolimnion, particularly near the HOx, likely occurs after turning on the HOx and prior to O<sub>2</sub> gas flow coming to equilibrium within the reservoir system. The time required for suspended particles to settle in the near field and the time required for HOx-induced mixing to re-establish the sediment-water vertical O<sub>2</sub> structure in regions farther away would both contribute to the delayed response.

A storm occurred on August 27; however, while O<sub>2</sub> levels increased in the metalimnion at approximately the same elevation as stream input at the back of CCR (9 m above the sediment; region of decreased O<sub>2</sub> in Fig. 4.4c), the bulk hypolimnion and near-sediment water were not affected (per CTD measurements; data not shown). Increased mixing in the hypolimnion was also not observed, indicating that the influence of the storm did not significantly affect results and observed variations in sediment O<sub>2</sub> availability may be legitimately related to changes in HOx operation.

**4.4.2 HOx flow and current velocity** – Current velocity time series (as measured via ADCP) in relation to HOx flow are presented in Fig. 4.6. In Fig. 4.6a, near-sediment velocities at ~1.5 m above the sediment are averages based on ~4-h time periods during the C3 August campaign. Average daily velocities at 3 m above the sediment (bulk hypolimnion) and 5 m below the water surface (bulk epilimnion) are also shown. While current velocities in the bulk hypolimnion and epilimnion do not seem to have been affected by HOx operations, near-sediment velocity (+1.5 m) dropped sharply soon after the HOx was turned off on August 19 (Fig. 4.6a). After the HOx was turned back on (August 21), near-sediment velocities are observed to increase though they remained quite variable. Near-sediment velocity returned to pre-campaign levels (~ 5 cm s<sup>-1</sup>; summer average was 6.2 cm s<sup>-1</sup>) on August 29, which directly corresponds with the timing of the re-established vertical O<sub>2</sub> structure at the SWI (Fig. 4.3-4.5). Although it took over a week before near-sediment velocities returned to pre-campaign levels mid-reservoir, near-sediment velocities at both CVCB and C3 were observed to increase immediately in both magnitude and degree of variation after resuming oxygenation (Fig. 4.6b; the period when the HOx was turned off is indicated in red) which clearly shows the influence of HOx-induced mixing.

Although the influence of wind-induced mixing (i.e., seiching) on the sediment-water vertical O<sub>2</sub> distribution (Bryant et al. 2010; Ch.2) was expected to be minimal due to relatively

mild average wind speeds and irregular basin geometry (Fig. 4.1), wind speed (based on National Oceanographic and Atmospheric Administration (NOAA) local climatological data for the Roanoke airport, located ~5 km from CCR) was assessed to determine if wind-induced seicheing was an influence in observed changes in current velocity (NOAA 2008). As anticipated, a correlation between average wind speed and current velocity (both near-sediment and in the epilimnion) was not observed (Appendix A.2; Fig. 4.6). Wind speed increased during the period of August 19 to 23 when the HOx was turned off, while near-sediment current velocity subsided in the absence of HOx-induced mixing (Fig. 4.6). Additionally, as current velocity and near-sediment O<sub>2</sub> levels increased back to pre-campaign levels on August 28-30, wind speed dropped significantly. Thus, seiche-induced turbulence was not a significant factor in sediment-water O<sub>2</sub> dynamics in CCR during our experimental campaigns.

**4.4.3 HOx-induced variation in sediment O<sub>2</sub> uptake** – While HOx are designed to remediate problems caused by O<sub>2</sub> depletion, conceptually these systems should also enhance O<sub>2</sub> flux into the sediment due to increased O<sub>2</sub> and turbulence levels in the lower hypolimnion and subsequent suppression of the DBL (discussed in Introduction and in Ch. 2; Bryant et. al 2010). The response of J<sub>O<sub>2</sub></sub> and the vertical O<sub>2</sub> distribution (as characterized by C<sub>SWI</sub> and δ<sub>DBL</sub>) to HOx operations closely parallels observed variation in current velocity and estimated turbulence levels (as characterized by ε; Fig. 4.7). During ongoing oxygenation (Fig. 4.2), average summer J<sub>O<sub>2</sub></sub> and δ<sub>DBL</sub> at C3 were 12.5 ± 7.6 mmol m<sup>-2</sup> d<sup>-1</sup> and 1.6 ± 0.9 mm, respectively (full data set not shown). However, in response to turning off the HOx on August 19, δ<sub>DBL</sub> increased from 0.7 mm to the point of becoming undefined (Fig. 4.7a; no discernable DBL was measurable at δ<sub>DBL</sub> > 5 mm; hence, a nominal maximum δ<sub>DBL</sub> = 5 mm was assumed for this study). Simultaneously, J<sub>O<sub>2</sub></sub> decreased from 8 to 0 mmol m<sup>-2</sup> d<sup>-1</sup> and C<sub>SWI</sub> dropped from ~130 to 0 μmol L<sup>-1</sup> as diffusive transport of O<sub>2</sub> was restricted and O<sub>2</sub> was depleted from the sediment. Once the DBL was suppressed back to a defined structure on August 29, J<sub>O<sub>2</sub></sub> increased to ~15 mmol m<sup>-2</sup> d<sup>-1</sup> (Fig. 4.7a). As indicated by Fig. 4.3b, elevated J<sub>O<sub>2</sub></sub> and decreased δ<sub>DBL</sub> are also observed briefly following HOx start-up on August 21, which may be attributed to a large internal wave induced by turning on the HOx. A peak in near-sediment current velocity is also observed at this time (Fig. 4.7b).

In Fig. 4.7b, near-sediment current velocity is shown to correlate significantly with  $\varepsilon$ , both of which decreased sharply during the 48-h period when the HOx was turned off. The clear relationship between ADCP velocity data and estimated  $\varepsilon$  values (based on independent O<sub>2</sub> microprofile data) supports our evaluation of  $\varepsilon$  as a function of  $\delta_{\text{DBL}}$  and highlights the influence of mixing (as quantified by near-sediment current velocity) on  $\delta_{\text{DBL}}$ . Our  $\delta_{\text{DBL}}$ -based  $\varepsilon$  estimates are within the same range as ADCP-based  $\varepsilon$  values obtained by Bryant et al. (2010; Ch. 2) characterizing seiche-induced mixing in a freshwater system.

HOx-induced mixing is further established by variations in temperature near the SWI (based on temperature microprofile data) which closely follow trends in  $\varepsilon$  and current velocity (Fig. 4.7b). HOx-induced mixing has been shown to result in elevated BBL temperature (Hess 1975; Gantzer et al. 2009a; Liboriussen et al. 2009). Our results (Fig. 4.7) thus clearly reveal the significant influence that HOx operation can have on the degree of mixing in the hypolimnion and resultant sediment O<sub>2</sub> uptake.

**4.4.4 J<sub>O2</sub> as a function of flow rate** – To evaluate the relationship between HOx flow rate and sediment O<sub>2</sub> uptake more comprehensively, we built on summer 2008 results by incorporating additional data from summer 2007. The 2008 off/on HOx experiments reveal that J<sub>O2</sub> and the sediment O<sub>2</sub> distribution responded directly to changes in HOx operation (Fig. 4.7). However, these results are based on data for the two flow rates used during the 2008 campaigns (0 and 51 m<sup>3</sup> h<sup>-1</sup>) and characterize two extremes of zero flow and high flow. We therefore included O<sub>2</sub> microprofile data obtained at C3 and CVCB while the HOx was operated at five different flow rates during 2007 – 2008 (Fig. 4.2; Table 4.1) to assess J<sub>O2</sub>, C<sub>SWI</sub>, and z<sub>max</sub> over a broader range of flow conditions.

As indicated in Fig. 4.7, J<sub>O2</sub> was strongly influenced by variation in HOx flow rate. J<sub>O2</sub> and HOx flow were found to be directly related for low to moderately-high flow rates in both the near field and mid-reservoir region; however, J<sub>O2</sub> decreased at flow rates greater than ~50 m<sup>3</sup> h<sup>-1</sup> (Fig. 4.8). While a similar J<sub>O2</sub> response was observed at both locations, data for the near field exhibited significant variation and were less correlated to HOx flow as compared to mid-reservoir data (CVCB R<sup>2</sup> = 0.79 versus C3 R<sup>2</sup> = 0.86; discussed below). Conceptually, J<sub>O2</sub> should increase in response to turbulence-induced decreases in  $\delta_{\text{DBL}}$  when sediment O<sub>2</sub> uptake is water-side controlled and limited by diffusive transport. However, reduced J<sub>O2</sub> at very high flow

rates could be attributed to time required for steady-state to re-establish, a change in processes governing sediment O<sub>2</sub> uptake, and/or sediment resuspension effects. We encountered mechanical difficulties operating the HOx at very high flow rates (>51 m<sup>3</sup> h<sup>-1</sup>) for extended periods of time. Hence, data were collected for shorter time periods (1-2 weeks) at these flow rates and steady-state conditions may have been less established than for lower flow rates. Laboratory studies focused on HOx-induced sediment O<sub>2</sub> uptake have shown that J<sub>O<sub>2</sub></sub> shifts from being water-side controlled to sediment-side controlled as O<sub>2</sub> uptake becomes substrate-limited (i.e., independent of O<sub>2</sub> concentration) at very high flow rates (Moore et al. 1996; Beutel 2003) or in the ocean (Glud et al. 2009). An in situ study focused on hypolimnetic oxygenation using a downflow bubble contact aerator (Speece Cone) yielded similar results (Moore 2003). Hence, sediment O<sub>2</sub> uptake may not have been controlled by diffusive J<sub>O<sub>2</sub></sub> at flow rates greater than 50 m<sup>3</sup> h<sup>-1</sup>. However, the fact that J<sub>O<sub>2</sub></sub> did not become constant but actually decreased at very high flow indicates that substrate-limitation of O<sub>2</sub> uptake may not have been the only factor in the observed J<sub>O<sub>2</sub></sub> response.

Elevated turbulence near the SWI has been shown to cause sediment resuspension, both in response to seiche-induced mixing (Davison et al. 1982; Charlton and Lean 1987; Kalnejais et al. 2007) and HOx operation (Moore et al. 1996; Gantzer et al. 2009b). Decreased J<sub>O<sub>2</sub></sub> at very high flow rates may hence also be attributed to elevated rates of HOx-induced mixing disturbing the sediment, particularly in the near field. Subsequent dispersion of resuspended sediment may have been a factor in mid-reservoir results as well. As near-sediment O<sub>2</sub> levels are depleted due to oxidation of resuspended reduced species, J<sub>O<sub>2</sub></sub> would subsequently decrease as the O<sub>2</sub> concentration gradient driving force at the SWI diminished. Furthermore, if the sediment were disturbed substantially, the defined DBL structure supporting diffusive transport would break down which would also result in significantly reduced J<sub>O<sub>2</sub></sub> (Fig. 4.7).

**4.4.5 Effect of HOx on sediment O<sub>2</sub> availability** – While induced J<sub>O<sub>2</sub></sub> can be problematic if not properly accounted for in HOx design and operation, increased J<sub>O<sub>2</sub></sub> is beneficial if sediment O<sub>2</sub> levels are sufficiently maintained to prevent the release of reduced soluble species into the water column (Beutel 2003). As shown in Fig. 4.9a, a moderate correlation (R<sup>2</sup> = 0.61) in estimated J<sub>O<sub>2</sub></sub> and C<sub>SWI</sub> was observed mid-reservoir (C3), with increased O<sub>2</sub> flux into the sediment corresponding to more oxic conditions at the SWI. A weaker correlation (R<sup>2</sup> = 0.47) is

again observed alongside the HOx at CVCB (discussed below). O<sub>2</sub> levels merely 5 cm above the SWI had much less of an influence on J<sub>O<sub>2</sub></sub> (Fig. 4.9b) with zero flux (J<sub>O<sub>2</sub></sub> = 0 mmol m<sup>-2</sup> d<sup>-1</sup>) occurring even when C<sub>5</sub> remains fairly high, as also observed in Fig. 4.4 and 4.5. Although hypolimnetic O<sub>2</sub> levels obviously must be high enough to act as an O<sub>2</sub> source to the sediment, a relationship between O<sub>2</sub> in the bulk hypolimnion (estimated from weekly CTD profiles) and J<sub>O<sub>2</sub></sub> was not found (data not shown). Thus, regardless of hypolimnetic and near-sediment O<sub>2</sub> levels, J<sub>O<sub>2</sub></sub> is shown to be much more strongly linked to O<sub>2</sub> directly at the SWI. These results emphasize the controlling role that turbulent mixing plays in driving the oxygenated hypolimnetic water down to the sediment (Fig. 4.7), as also shown by previous work (Glud et al. 2007; Bryant et al. 2010; Ch. 2).

Upon reaching the SWI, a balance between the rate at which O<sub>2</sub> is supplied to the sediment (quantified by J<sub>O<sub>2</sub></sub>) and the rate at which O<sub>2</sub> is consumed within the sediment (quantified by R<sub>O<sub>2</sub></sub>) establishes the sediment oxic zone (Jørgensen and Boudreau 2001; Higashino et al. 2004; Bryant et al. 2010; Ch.2). The extent of the sediment oxic zone (as quantified by z<sub>max</sub>) and HOx flow rate were found to be strongly related in both the near field and mid-reservoir region (CVCB R<sup>2</sup> = 0.96; C3 R<sup>2</sup> = 0.84), with sediment O<sub>2</sub> penetration increasing directly in response to elevated flow (Fig. 4.10). Unlike J<sub>O<sub>2</sub></sub> (Fig. 4.8), reduced z<sub>max</sub> at very high flow rates did not occur. This indicates that while J<sub>O<sub>2</sub></sub> decreased at very high flow rates, a sufficient level of O<sub>2</sub> reached the sediment to maintain oxic sediment conditions in both sampling regions. Taking into account results shown in Fig. 4.8-4.9, it is evident that HOx-induced increases in J<sub>O<sub>2</sub></sub> and C<sub>SWI</sub> facilitated an enhanced sediment oxic zone throughout CCR.

The response of z<sub>max</sub> to increased flow rate was quite similar in both regions, although sediment O<sub>2</sub> penetration was slightly lower near the HOx than mid-reservoir (Fig. 4.10). Average J<sub>O<sub>2</sub></sub> values were also comparable though slightly higher in the near field at CVCB than in the C3 mid-reservoir region (14.8 vs. 13.4 mmol m<sup>-2</sup> d<sup>-1</sup>; Table 4.2). J<sub>O<sub>2</sub></sub> and R<sub>O<sub>2</sub></sub> are equivalent at steady-state (Bryant et al. 2010; Ch. 2-3); hence, these results suggest that increased O<sub>2</sub> reached the near-field sediment but was then consumed more rapidly by sediment O<sub>2</sub> consumption processes, resulting in decreased z<sub>max</sub>. To complete the balance between J<sub>O<sub>2</sub></sub> and z<sub>max</sub>, sediment O<sub>2</sub> consumption was evaluated based on sediment O<sub>2</sub> microprofile data using the numerical procedure PROFILE (Berg et al. 1998; Bryant et al. 2010; Ch. 2). As shown in Table 4.2, R<sub>O<sub>2a</sub></sub> estimates based on PROFILE results verify that sediment O<sub>2</sub> consumption was similar

in both regions but also somewhat higher closer to the HOx. Near-field sediment has been found to have significantly higher levels of total organic carbon, Fe, and Mn in the bulk sediment which may result from enhanced oxide precipitation and sediment focusing near the HOx (Ch. 5). Thus, sediment in this deeper CCR region most likely has increased sources of electron acceptors and subsequently would have a greater capacity for O<sub>2</sub> consumption. However, the fact that fairly similar  $z_{\max}$  were observed in both the near field and mid-reservoir region indicates that oxygenation maintained a sufficient balance between sediment O<sub>2</sub> supply and consumption processes and the resultant sediment oxic zone. Conversely, the back region (CR; Fig. 4.1) is significantly less affected by HOx operations. As a result, J<sub>O<sub>2</sub></sub> was not maintained (Table 4.2) and the sediment became anoxic relatively early in summer 2008, subsequently becoming a source of soluble metals to the water column (as shown in Ch. 5).

**4.4.6 Influence of HOx proximity** – While HOx operations maintained a fairly uniform sediment oxic zone and average J<sub>O<sub>2</sub></sub> were comparable in both the near field and mid-reservoir region (Fig. 4.8, 4.10; Table 4.2), proximity to the HOx strongly influenced both the response time and variability in results. After the HOx was turned on, it took ~5 days for the vertical O<sub>2</sub> distribution to be restored in the near field and ~8 days mid-reservoir. Although the sediment-water vertical O<sub>2</sub> distribution was re-established more rapidly in the near-field region, consistently increased variability in near field results indicate that the overall structure was less stable during oxygenation. The degree of variation in sediment O<sub>2</sub> parameters (e.g., J<sub>O<sub>2</sub></sub>,  $z_{\max}$ , C<sub>SWI</sub>; Table 4.1) was typically higher and correlations between J<sub>O<sub>2</sub></sub> and both C<sub>SWI</sub> and HOx flow were weaker near the HOx (as indicated by R<sup>2</sup> values in Fig. 4.8, 4.9). While  $z_{\max}$  and flow rate were strongly correlated in both regions (Fig. 4.10), the relationship between J<sub>O<sub>2</sub></sub> and water-side  $\delta_{\text{DBL}}$  was also found to be less significant in the near field (CVCB R<sup>2</sup> = 0.44 versus C3 R<sup>2</sup> = 0.79; Appendix A.3).

Regarding response time, turning the HOx on most likely immediately stirred up the sediment in the near field (Gantzer 2002), introducing reduced species into the water column. Suspended sediment would have thus decreased O<sub>2</sub> levels both in the near field and at locations farther away if the reduced species were redistributed. The amount of time required for suspended sediment to settle and for near-sediment mixing to resume may have governed the re-establishment of oxic sediment conditions (Fig. 4.5, 4.7). The sediment-water O<sub>2</sub> distribution

was re-established more quickly near the HOx due to direct mixing effects. However, as indicated by decreased consistency in results (Fig. 4.8, 4.9; Appendix A.3), the O<sub>2</sub> distribution in the near field was less stable on a long-term basis which is likely due to flow instabilities and ongoing sediment resuspension. On the other hand, while the response mid-reservoir was more gradual after the HOx was turned on as it took longer for HOx-induced increases in O<sub>2</sub> and near-sediment turbulence to influence sediment O<sub>2</sub> conditions, once steady-state conditions were re-established the overall sediment-water O<sub>2</sub> distribution remained fairly stable due to negligible sediment resuspension and a relatively uniform flow pattern.

After steady-state conditions with oxygenation were established, it is likely that the spatial influence of oxygenation was still affected by sediment resuspension near the HOx and/or HOx plume detrainment in regions farther away. Because sediment resuspension can result in both decreased near-sediment O<sub>2</sub> levels and disturbance of the sediment-water O<sub>2</sub> structure, HOx-induced sediment resuspension may have contributed to both decreased correlation in near-field results (Fig. 4.8-4.9; Appendix A.3) and reduced J<sub>O<sub>2</sub></sub> at very high flow rates (Fig. 4.8). However, HOx-induced sediment disturbance may have facilitated non-diffusive O<sub>2</sub> transport at the SWI, thereby maintaining z<sub>max</sub> (Fig. 4.10). Sediment resuspension in response to HOx operations is indicated by CCR sediment trap data (Ch. 5; Gantzer et al. 2009b) showing increased sedimentation in the lower hypolimnion immediately over the HOx as compared to other locations, although this may be partially attributed to sediment focusing in the deeper region of the reservoir (Fig. 4.1; Schaller and Wehrli 1997). HOx-induced sediment resuspension is further supported by measurements of total and soluble Fe and Mn in the water immediately overlying the sediment showing that total and soluble metal levels were significantly higher near the HOx (Ch. 5).

Although suspended sediment may have been dispersed to other regions of the reservoir, deleterious sediment resuspension effects were likely much more significant in the near field. Furthermore, areas closer to the HOx may have been more negatively influenced by variable turbulence as opposed to the mid-reservoir region (McGinnis et al. 2004). Ideally HOx-induced turbulence establishes a well-mixed BBL (Singleton and Little 2006), which is evident in our results showing relatively similar current velocities throughout the reservoir (Fig. 4.6b). However, the area near the HOx can be affected by flow recirculation and intermittent stagnant zones, while regions mid-reservoir that are exposed to detrained water from the HOx bubble

plume are most likely closer to steady-state (Singleton et al., unpubl.). HOx plume model results by Singleton et al. (2007) showed that the region most directly influenced by the HOx was a detrainment region between the depth of maximum plume rise and the fallback elevation of equal density. C3 is located within this detrainment region, while CVCB is located below the fallback elevation. Thus, HOx-induced mixing is likely more disruptive close to the HOx than at distances farther away where the flow pattern established by plume detrainment is more uniform. As a result, especially when taking sediment resuspension effects into consideration, the vertical O<sub>2</sub> distribution at the SWI is more easily preserved farther away from the HOx. MP4 microprofile data obtained at C3 (Fig. 4.3) did typically maintain a more defined structure than those obtained closer to the HOx, particularly below the HOx at CC (data not shown). Nevertheless, as indicated by Fig. 4.8 and 4.9, while near-field results were less consistent general sediment O<sub>2</sub> availability was not significantly affected (Fig. 4.10).

**4.4.7 Effect on source water quality** – While HOx operations were found to increase sediment O<sub>2</sub> uptake, an O<sub>2</sub> balance performed on the CCR water column by Gantzer et al. (2009a) showed that oxygenation caused an overall decrease in background and HOx-induced hypolimnetic O<sub>2</sub> demand after several years of HOx operation. This indicates that while the amount of O<sub>2</sub> consumed by the sediment increased considerably in response to oxygenation, enough O<sub>2</sub> was supplied by the HOx to counteract this increased demand and prevent O<sub>2</sub> depletion within the water column. Model results by Singleton et al. (unpubl.) further validated that HOx can be successfully operated to minimize the influence of sediment O<sub>2</sub> uptake. Thus, as long as HOx-induced increases in J<sub>O<sub>2</sub></sub> are properly accounted for, our results support that HOx effectively replenish O<sub>2</sub> in thermally stratified water-supply reservoirs such as CCR (Beutel 2003; McGinnis et al. 2004). Furthermore, the sediment oxic zone was shown to be significantly enhanced by oxygenation both in the near field and mid-reservoir, thereby facilitating decreased sediment-water flux to the water column. By maintaining oxic conditions in the upper ~1-2 mm of sediment, soluble Fe and Mn fluxes from the sediment to the hypolimnion were suppressed (Ch. 5; also supported by Jørgensen and Boudreau 2001) and total and soluble metal concentrations in the source water were significantly decreased (Gantzer et al. 2009b).

## 4.5 Conclusions

In summary,  $J_{O_2}$  and sediment  $O_2$  availability were found to be directly influenced by HOx operations in CCR, particularly at low to moderately high flow rates (up to  $\sim 50 \text{ m}^3 \text{ h}^{-1}$ ). Reduced  $J_{O_2}$  was observed at higher flow rates which may be attributed to temporal dynamics of the reservoir, a shift from transport-limited to substrate-limited sediment  $O_2$  uptake, and/or sediment resuspension. Sediment resuspension effects could be reduced in future systems by elevating the diffuser lines to a greater height above the sediment. The sediment oxic zone (as characterized by  $z_{\text{max}}$ ) was substantially enhanced by HOx operations both in the near field and mid-reservoir, thus supporting the suppression of reduced chemical species to the water column. Although HOx operation resulted in both elevated near-sediment  $O_2$  and turbulence levels, sediment  $O_2$  uptake was found to be more strongly correlated to levels of near-sediment mixing than to  $O_2$  immediately overlying the sediment. Thus, regardless of hypolimnetic  $O_2$  levels, physical transport of the oxygenated water to the sediment surface governed sediment  $O_2$  availability (as also shown by Brand et al. (2009) and Bryant et al. (2010)). Near-sediment BBL mixing (as characterized by current velocity and estimated  $\varepsilon$ ) was found to vary in direct response to HOx operations, while wind-forced mixing effects appeared negligible. The influence of HOx on sediment  $O_2$  availability was emphasized by the CCR system response to turning the HOx off for  $\sim 48$  h. As  $\delta_{\text{DBL}}$  rapidly increased in the absence of near-sediment mixing and  $C_{\text{SWI}}$  decreased to negligible levels,  $J_{O_2}$  dropped to zero and the sediment became anoxic. After turning the HOx back on, it took  $\sim 1$  week for oxic sediment conditions to re-establish. Proximity to the HOx strongly influenced both how quickly the sediment-water vertical  $O_2$  distribution was restored and its long-term stability.

This work emphasizes the viability of using HOx to maintain an established sediment oxic zone and the importance of taking HOx-induced increases in  $J_{O_2}$  into account when designing and operating HOx systems. Understanding how variations in  $O_2$  and turbulence levels affect sediment-water fluxes is crucial for accurately quantifying  $J_{O_2}$ , optimizing water quality, and effectively managing lakes and reservoirs. By evaluating the influence of HOx on sediment  $O_2$  dynamics at a reservoir-wide scale, our results will contribute to successful HOx operations facilitating both elevated source water  $O_2$  levels and an oxic SWI for suppression of reduced chemical fluxes. Furthermore, while this study focused on HOx-induced changes in  $O_2$

and turbulence, variation in these parameters is frequently induced naturally (e.g., via fall overturn (Ch. 5), wind-induced seiching (Bryant et al. 2010; Ch. 2), and hydraulic inputs during storm events). Therefore, results should also be applicable on a much broader scale.

#### **4.6 Acknowledgements**

The authors thank Elizabeth Rumsey, Kevin Elam, and the staff at Western Virginia Water Authority who offered invaluable assistance in the field and with laboratory analyses. We also thank Daniel McGinnis and Peter Berg for discussion and advice on data interpretation.

We acknowledge financial support from the National Science Foundation (NSF IGERT Program) and the Western Virginia Water Authority. The research described in this paper was also partially funded by the United States Environmental Protection Agency (EPA) under the Science to Achieve Results (STAR) Graduate Fellowship Program. EPA has not officially endorsed this publication and the views expressed herein may not reflect the views of the EPA.

#### **4.7 References**

- Arega, F., and J. H. W. Lee. 2005. Diffusional mass transfer at sediment-water interface of cylindrical sediment oxygen demand chamber. *J. Env. Engr.* **131**: 755-766.
- Beutel, M. W. 2003. Hypolimnetic anoxia and sediment oxygen demand in California drinking water reservoirs." *Lake Reserv. Manage.* **19**: 208-221.
- Beutel, M. W., and A. J. Horne. 1999. A review of the effects of hypolimnetic oxygenation on lake and reservoir water quality. *J. Lake Reservoir Manage.* **15**: 285– 297.
- Bouldin, D. R. 1968. Models for describing the diffusion of oxygen and other mobile constituents across the mud-water interface. *J. Ecol.* **56**: 77-87.
- Brand, A., C. Dinkel, and B. Wehrli. 2009. Influence of the diffusive boundary layer on the solute dynamics in the sediments of a seiche-driven lake: A model study. *J. Geophys. Res.* **114**: G01010, doi:10.1029/2008JG000755.
- Bryant, L. D., C. Lorrai, D. F. McGinnis, A. Brand, A. Wüest, and J. C. Little. 2010. Variable sediment oxygen uptake in response to dynamic forcing. *Limnol. Oceanogr.* **55**: 950-964.

- Charlton, M. N., and D. R. S. Lean. 1987. Sedimentation, resuspension, and oxygen depletion in Lake Erie (1979). *J. Great Lakes Res.* **13**: 709-723.
- Dalsgaard, T. [ed.], L. P. Nielsen, V. Brotas, P. Viaroli, G. Underwood, D. B. Nedwell, K. Sundbäck, S. Rysgaard, A. Miles, M. Bartoli, L. Dong, D. C. O. Thornton, L. D. M. Ottosen, G. Castaldelli, and N. Risgaard-Petersen. 2000. Protocol handbook for NICE – Nitrogen Cycling in Estuaries: a project under the EU research programme: Marine Science and Technology (MAST III). National Environmental Research Institute, Silkeborg, Denmark.  
[http://www2.dmu.dk/LakeandEstuarineEcology/nice/NICE\\_handbook.pdf](http://www2.dmu.dk/LakeandEstuarineEcology/nice/NICE_handbook.pdf)
- Epping, E. H. G., and W. Helder. 1997. Oxygen budgets calculated from in situ microprofiles for Northern Adriatic sediments. *Cont. Shelf Res.* **17**:1737-1764.
- EPA (Environmental Protection Agency). 2000. Aquatic life water quality criteria for dissolved oxygen (saltwater): Cape Cod to Cape Hatteras. EPA report EPA-822-R-00-012.  
<http://www.epa.gov/waterscience/criteria/dissolved/dofacts.html>
- Gantzer, P. A. 2002. Diffuser operations at Spring Hollow Reservoir (master's thesis). Available from Digital Library and Archives database (<http://scholar.lib.vt.edu/theses/available/etd-05212002-163729/>).
- Gantzer, P. A., L. D. Bryant, and J. C. Little. 2009a. Effect of hypolimnetic oxygenation on oxygen depletion rates in two water-supply reservoirs. *Water Res.* **43**:1700-1710.
- Gantzer, P. A., L. D. Bryant, and J. C. Little. 2009b. Controlling soluble iron and manganese in a water-supply reservoir using hypolimnetic oxygenation. *Water Res.* **43**: 1285-1294.
- Gelda, R. K., M. T. Auer, and S. W. Effler. 1995. Determination of sediment oxygen demand by direct measurement and by inference from reduced species accumulation. *Mar. Freshwater Res.* **46**: 81-88.
- Glud, R. N., P. Berg, H. Fossing, and B. B. Jørgensen. 2007. Effect of the diffusive boundary layer on benthic mineralization and O<sub>2</sub> distribution: A theoretical model analysis. *Limnol. Oceanogr.* **52**: 547-557.
- Glud, R. N., H. Stahl, P. Berg, F. Wenzhöfer, K. Oguri, and H. Kitazato. 2009. In situ microscale variation in distribution and consumption of O<sub>2</sub>: A case study from a deep ocean margin sediment (Sagami Bay, Japan). *Limnol. Oceanogr.* **54**: 1-12.

- Grant, H. L., R. W. Stewart, and A. Moilliet. 1962. Turbulence spectra from a tidal channel. *J. Fluid Mech.* **12**: 241-263.
- Gundersen, J. K. and B. B. Jørgensen. 1990. Microstructure of diffusive boundary layers and the oxygen uptake of the sea floor. *Nature* **345**: 604-607.
- Hess, L. 1975. The effect of the first year of artificial hypolimnion aeration on oxygen, temperature, and the depth distribution of rainbow trout *Salmo gairdneri* in Spruce Knob Lake, West Virginia, U.S.A. *Proc. W. Va. Acad. Sci.* **47**:176-183.
- Higashino, M., C. J. Gantzer, and H. G. Stefan. 2004. Unsteady diffusional mass transfer at the sediment/water interface: Theory and significance for SOD measurement. *Water Res.* **38**(1): 1-12.
- Hondzo, M., T. Feyaerts, R. Donovan, and B. L. O'Connor. 2005. Universal scaling of dissolved oxygen distribution at the sediment-water interface: a power law. *Limnol. Oceanogr.* **50**: 166-1676.
- House, W. A. 2003. Factors influencing the extent and development of the oxic zone in sediments. *Biogeochemistry* **63**: 317-333.
- Jørgensen, B. B., and B. P. Boudreau. 2001. Diagenesis and sediment-water exchange, p. 211-244. *In* B. P. Boudreau and B. B. Jørgensen [eds.], *The benthic boundary layer: transport processes and biogeochemistry*. Oxford University Press.
- Jørgensen, B. B., and N. P. Revsbech. 1985. Diffusive boundary layers and the oxygen uptake of sediments and detritus. *Limnol. Oceanogr.* **30**: 111-122.
- Kalin, L., and M. M. Hantush. 2003. Evaluation of sediment transport models and comparative application of two watershed models. Cincinnati, Ohio, EPA National Risk Management Research Laboratory: 81 pp.
- Kalnejais, L. H., W. R. Martin, R. P. Signell, and M. H. Bothner. 2007. Role of sediment resuspension in the remobilization of particulate-phase metals from coastal sediments. *Environ. Sci. Technol.* **41**: 2282-2288.
- Lavery, P. S., C. E. Oldham, and M. Ghisalberti. 2001. The use of Fick's First Law for predicting porewater nutrient fluxes under diffusive conditions. *Hydrol. Process.* **15**: 2435-2451.
- Liboriussen, L., M. Søndergaard, E. Jeppesen, I. Thorsgaard, S. Grunfeld, T. S. Jakobsen, and K. Hansen. 2009. Effects of hypolimnetic oxygenation on water quality: results from five Danish lakes. *Hydrobiologia* **625**: 157-172.

- Lorke, A., B. Müller, M. Maerki, and A. Wüest. 2003. Breathing sediments: the control of diffusive transport across the sediment-water interface by periodic boundary-layer turbulence. *Limnol. Oceanogr.* **46**: 2077-2085.
- Mackenthun, A. A., and H. G. Stefan. 1998. Effect of flow velocity on sediment oxygen demand: Experiments. *J. Environ. Eng.-ASCE.* **124**: 222-230.
- McGinnis, D. F., and J. C. Little. 2002. Predicting diffused-bubble oxygen transfer rate using the discrete-bubble model. *Water Res.* **36**: 4627-4635.
- McGinnis, D. F., A. Lorke, A. Wüest, A. Stöckli, and J. C. Little. 2004. Interaction between a bubble plume and the near field in a stratified lake. *Water Resour. Res.* **40**: W10206, doi:10.1029/2004WR003038.
- Mobley, M. H., G. E. Hauser, D. F. McGinnis, and R. J. Ruane. 1997b. Diffuser system modeling and design for dissolved oxygen enhancement of reservoirs and releases. Proceedings of the 27th IAHR Congress, San Francisco, CA.
- Mobley, M. H., R. J. Ruane, and E. D. Harshbarger. 1997a. "And then it sank . . ." The development of an oxygen diffuser for hydropower. ASCE Technical Report. <http://www.mobleyengineering.com/publications.html>
- Moore, B. C. 2003. Downflow bubble contact aeration technology (Speece Cone) for sediment oxygenation. Proceedings of the Second International Conference on Remediation of Contaminated Sediments [eds. M. Pellei and A. Porta].
- Moore, B. C., P. H. Chen, W. H. Funk, and D. Yonge. 1996. A model for predicting lake sediment oxygen demand following hypolimnetic aeration. *Wat. Resour. Bull.* **32**:1-9.
- National Oceanographic and Atmospheric Administration. 2008. Local Climatological Data Report for Roanoke Regional / Woodrum Field Airport (KROA). June – May 2008. 10 October 2009. <http://www.ncdc.noaa.gov/oa/ncdc.html>.
- Nogami, M., T. Matsuno, T. Nakamura, and T. Fukumoto. 2000. Estimation of oxygen consumption rate using T-DO diagram in the benthic layer of Ohmura Bay, Kyushu, Japan. *J. Oceanogr.* **56**: 319-329.
- Rasmussen, H., and B. B. Jørgensen. 1992. Microelectrode studies of seasonal oxygen uptake in a coastal sediment: role of molecular diffusion. *Mar. Ecol. Prog.-Ser.* **81**: 289-303.

- Røy, H., M. Huettel, and B. B. Jørgensen. 2004. Transmission of oxygen concentration fluctuations through the diffusive boundary layer overlying aquatic sediments. *Limnol. Oceanogr.* **49**: 686-692.
- Schaller, T., and B. Wehrli. 1997. Geochemical-focusing of manganese in lake sediments – an indicator of deep-water oxygen conditions. *Aquat. Geochem.* **2**: 359-378.
- Schlichting, H. [ed.] 2000. *Boundary-layer theory*. McGraw-Hill. 9<sup>th</sup> ed.
- Singleton, V. L., and J. C. Little. 2006. Designing hypolimnetic aeration and oxygenation systems: a review. *Environ. Sci. Technol.* **40**: 7512-7520.
- Singleton, V. L., F. J. Rueda, and J. C. Little. 2010. A coupled bubble plume/reservoir model for hypolimnetic oxygenation. Unpubl.
- Steinberger, N., and M. Hondzo. 1999. Diffusional mass transfer at sediment-water interface. *J. Environ. Eng.-ASCE.* **125**: 192-200.
- Veenstra, J. N., and S. L. Nolen. 1991. In situ sediment oxygen demand in five southwestern U.S. lakes. *Water Res.* **25**: 351-354.
- Wetzel, R. G. 2001. *Limnology: Lake and River Ecosystems*. San Diego, Academic Press.
- Wu, R. S. S., B. Sheng Zhou, D. J. Randall, N. Y. S. Woo, and P. K. S. Lam. 2003. Aquatic hypoxia is an endocrine disruptor and impairs fish reproduction. *Environ. Sci. Technol.* **37**: 1137-1141.
- Wüest, A., N. H. Brooks, and D. M. Imboden. 1992. Bubble plume modeling for lake restoration, *Water Resour. Res.* **28**: 3235– 3250.
- Wüest, A., and A. Lorke. 2003. Small-scale hydrodynamics in lakes. *Annu. Rev. Fluid Mech.* **35**: 373-412.
- Zaw, M., and B. Chiswell. 1999. Iron and manganese dynamics in lake water. *Water Res.* **33**: 1900-1910.

Table 4.1. Average results for sediment oxygen uptake rate ( $J_{O_2}$ ), dissolved oxygen ( $O_2$ ) at the sediment-water interface ( $C_{SWI}$ ), and sediment oxic zone depth ( $z_{max}$ ) used for correlations between hypolimnetic oxygenation system (HOx) flow rate and  $J_{O_2}$  (Fig. 4.8) and  $z_{max}$  (Fig. 4.10). Average values are based on in situ  $O_2$  microprofile data from 2007-2008. Full (non-averaged) data set for  $J_{O_2}$  and  $C_{SWI}$  comparison shown in Fig. 4.9a. Standard deviations based on an assumed normal distribution.

$J_{O_2}^{(1)}$ (mmol m <sup>-2</sup> d <sup>-1</sup> )	$C_{SWI}$ ( $\mu$ mol L <sup>-1</sup> )	$z_{max}$ (mm)	Flow (m <sup>3</sup> h <sup>-1</sup> )	n samples
mid-reservoir (C3)				
0.0 ± 0.0	0.0 ± 0.0	0.0 ± 0.1	0	6
4.6 ± 0.9	25 ± 10	0.4 ± 0.1	25	2
12.5 ± 7.3	85 ± 25	1.2 ± 0.6	51	16
10.2 ± 2.9	140 ± 29	2.0 ± 0.7	68	2
5.8 ± 0.9	76 ± 7	1.5 ± 0.4	85	2
near field (CVCB)				
0.0 ± 0.0	0 ± 0	0.0 ± 0.0	0	4
38.4 ± 27.0	68 ± 12	0.5 ± 0.1	25	2
19.6 ± 7.5	82 ± 62	0.7 ± 0.4	51	9
6.1 ± 0.9	75 ± 7	1.0 ± 0.7	68	2
3.9 ± 0.6	43 ± 54	1.5 ± 1.1	85	2

<sup>(1)</sup>In order to prevent bias from the continuous profiling during the 2008 week-long campaigns, bi-daily averages from these campaigns were used to calculate average values. Two profiles were typically collected on monthly sampling dates as well. Data obtained during the transition period after the HOx was turned back on (to 51 m<sup>3</sup> h<sup>-1</sup>) but prior to when the vertical  $O_2$  distribution was re-established are also excluded from average  $J_{O_2}$  estimates as these data are not representative of normal operating conditions.

Table 4.2. Spatial variation in average  $J_{O_2}$  and areal sediment  $O_2$  consumption rate ( $R_{O_2a}$ ) during summer 2008. The near field is characterized by CVCB data, the mid-reservoir region by C3 data, and the back region by CR data.

Location	Date	$J_{O_2}^{(1)}$ (mmol m <sup>-2</sup> d <sup>-1</sup> )	$R_{O_2a}^{(1)}$ (mmol m <sup>-2</sup> d <sup>-1</sup> )
CVCB	6/08	9.7	10.6
CVCB	7/08	18.1	16.4
CVCB	8/08	26.8	21.2
CVCB	9/08	4.4	4.1
C3	6/08	4.6	3.8
C3	7/08	24.0	17.9
C3	8/08	9.0	8.1
C3	9/08	16.1	14.4
CR	6/08	6.5	6.1
CR	7/08	4.4	2.5
CR	8/08	0.3	0.0
CR	9/08	0.0	0.0

<sup>(1)</sup>Minor deviation in  $J_{O_2}$  (estimated via Eq. 4.1) and PROFILE-estimated  $R_{O_2a}$  values is most likely due to methodological differences (Ch. 3) rather than an indication of proximity to steady-state.

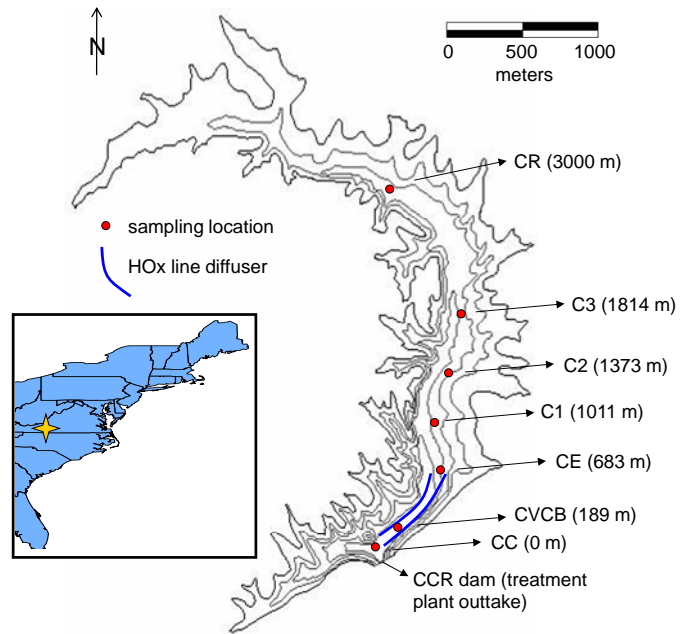


Figure 4.1. Map of Carvin's Cove Reservoir (CCR) showing sampling sites (near-field locations CC and CVCB; central, mid-reservoir locations CE, C1, C2, and C3; back-reservoir location CR) and linear bubble-plume hypolimnetic oxygenation system (HOx).

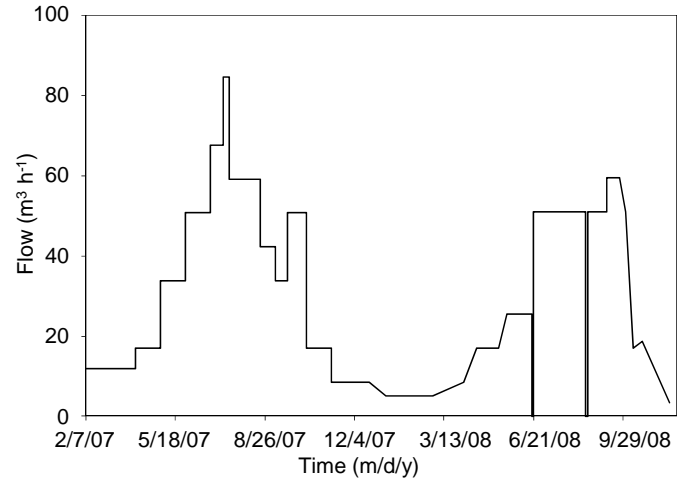


Figure 4.2. Variations in oxygen flow during CCR HOx operations in 2007 and 2008.

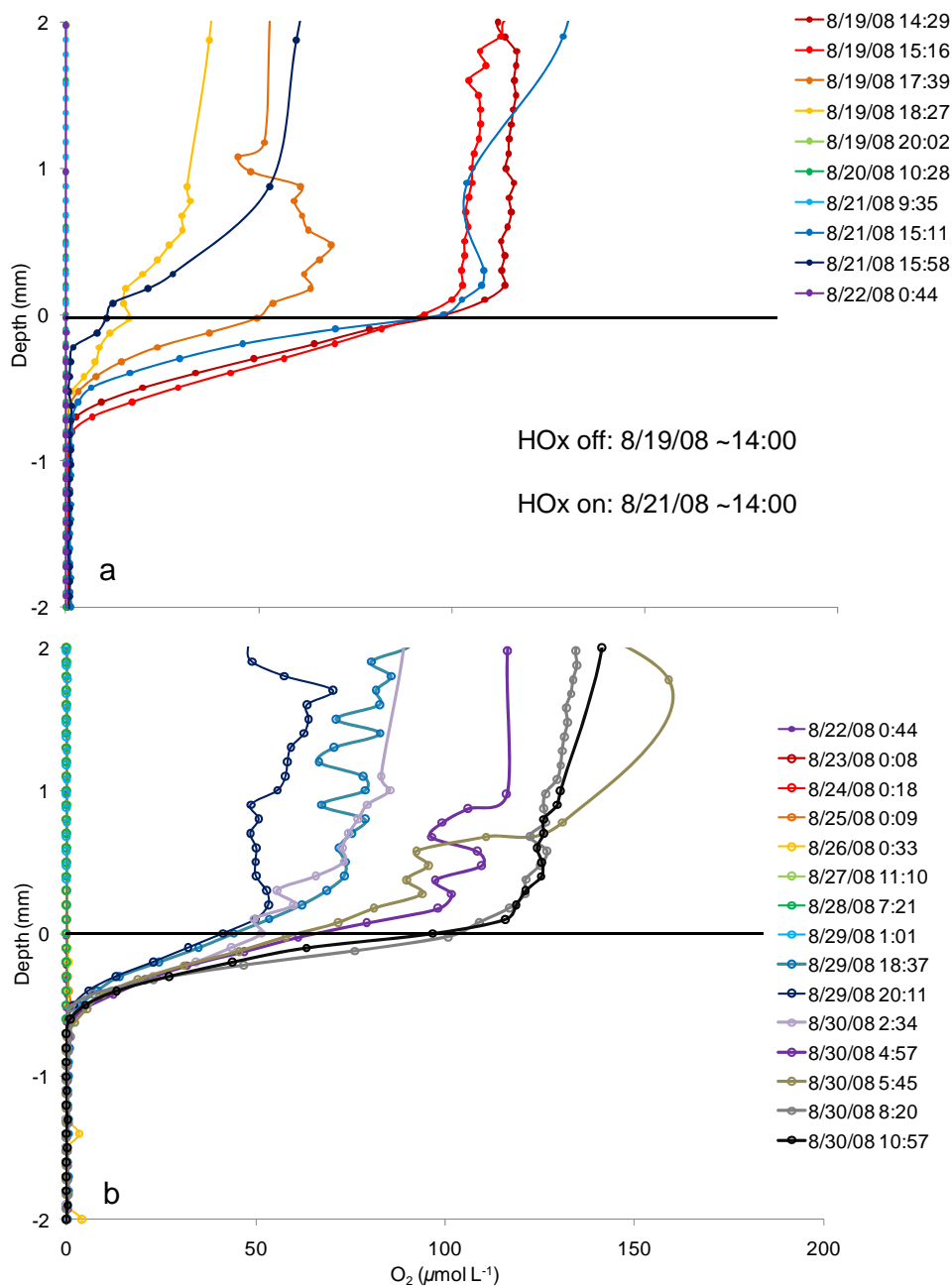


Figure 4.3. Summary of in situ dissolved oxygen ( $O_2$ ) profile data obtained at the sediment-water interface (SWI) with the MP4 microprofiler during the August 2008 campaign at C3. The HOx was turned off on August 19 (~14:00) and turned back on ~48 h later on August 21 (~14:00). Following the halt of HOx operations,  $O_2$  rapidly depleted from the sediment and the overlying water column (a). An oxic vertical  $O_2$  distribution was not re-established until August 29 (b), 8 days after the HOx was turned back on.

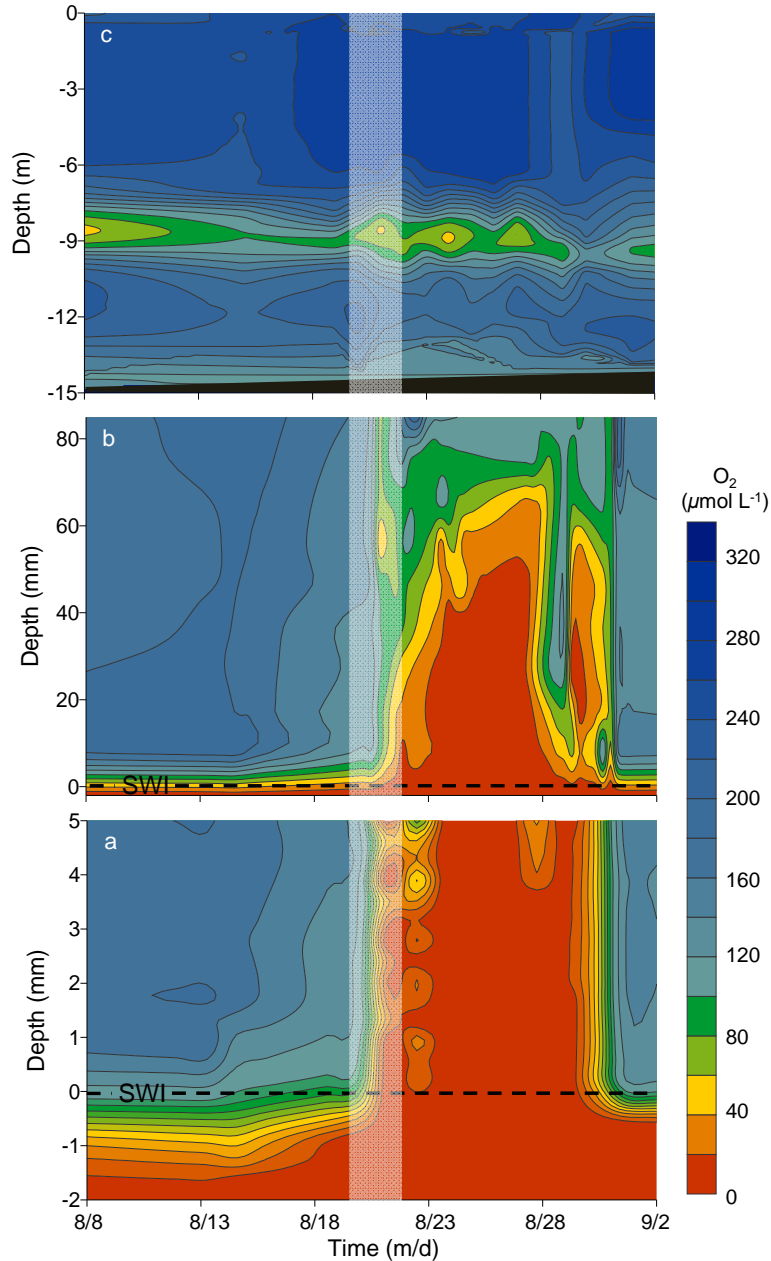


Figure 4.4. Contour plots of O<sub>2</sub> levels at the SWI (a; MP4 O<sub>2</sub> microsensor data), in the water overlying the sediment (b; MP4 O<sub>2</sub> microsensor data), and in the hypolimnion (c; CTD (conductivity-temperature-O<sub>2</sub> as a function of depth) profile data). Shaded region indicates period when HOx turned off. While O<sub>2</sub> is rapidly depleted from the sediment and water immediately above the SWI (a) after the HOx was turned off, O<sub>2</sub> levels were only minimally affected at ~8 cm above the sediment (b) and remained relatively constant in the bulk hypolimnion (c). In (a) and (b), depth indicates distance above (+) or below (-) the SWI, which is indicated by the dashed line. Depth in (c) indicates distance below the water surface.

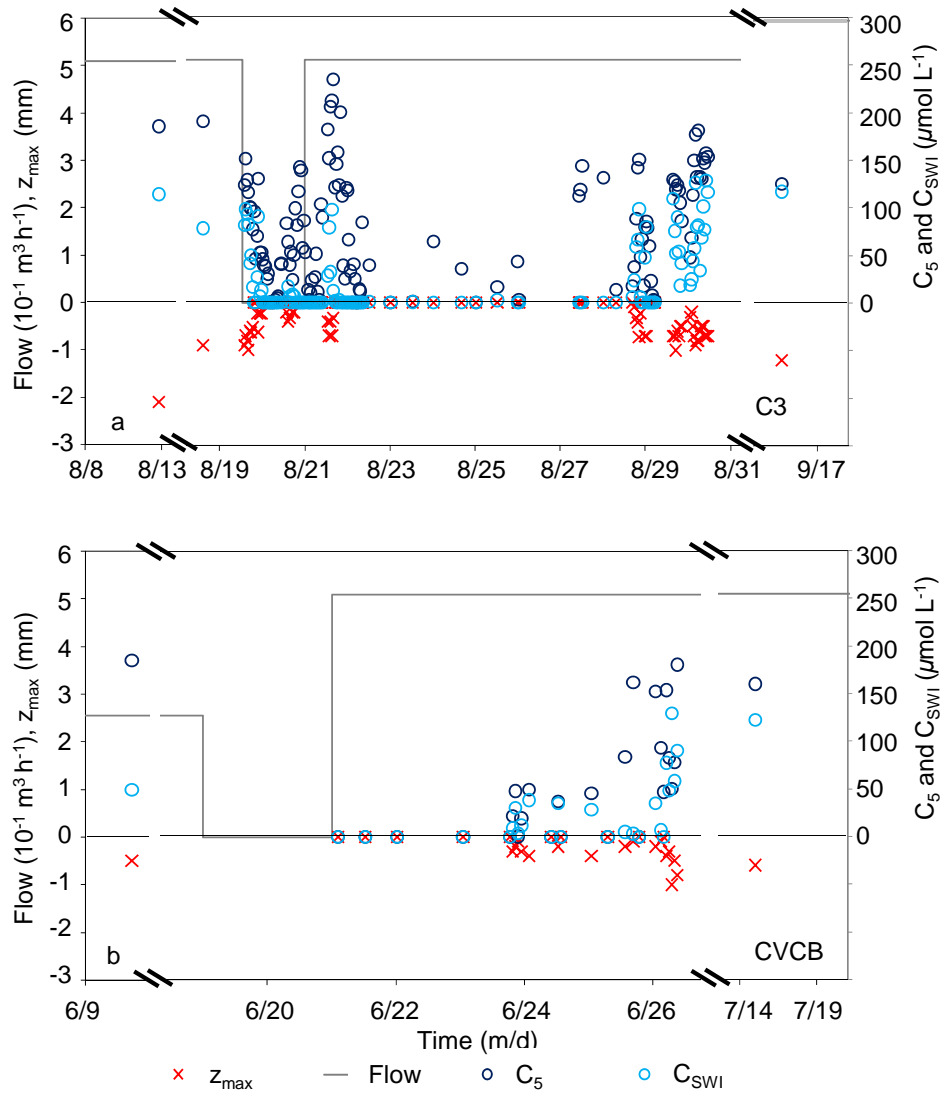


Figure 4.5. Variations in  $\text{O}_2$  levels at the SWI ( $C_{\text{SWI}}$ ), at 5 cm above the SWI ( $C_5$ ), and within the sediment (as characterized by sediment oxidic zone depth  $z_{\text{max}}$ ) in response to turning off the HOx. Similar trends are observed in data from both the August 2008 campaign at C3 (a) and also the June 2008 campaign at CVCB (b). During the period of zero flow when the HOx was not in operation,  $\text{O}_2$  levels dropped both at 5 cm above and directly at the SWI and the sediment went anoxic as  $\text{O}_2$  was depleted. After HOx operations resumed, it took  $\sim 5$  days for the vertical  $\text{O}_2$  distribution to re-establish near the HOx at CVCB and  $\sim 8$  days mid-reservoir at C3.

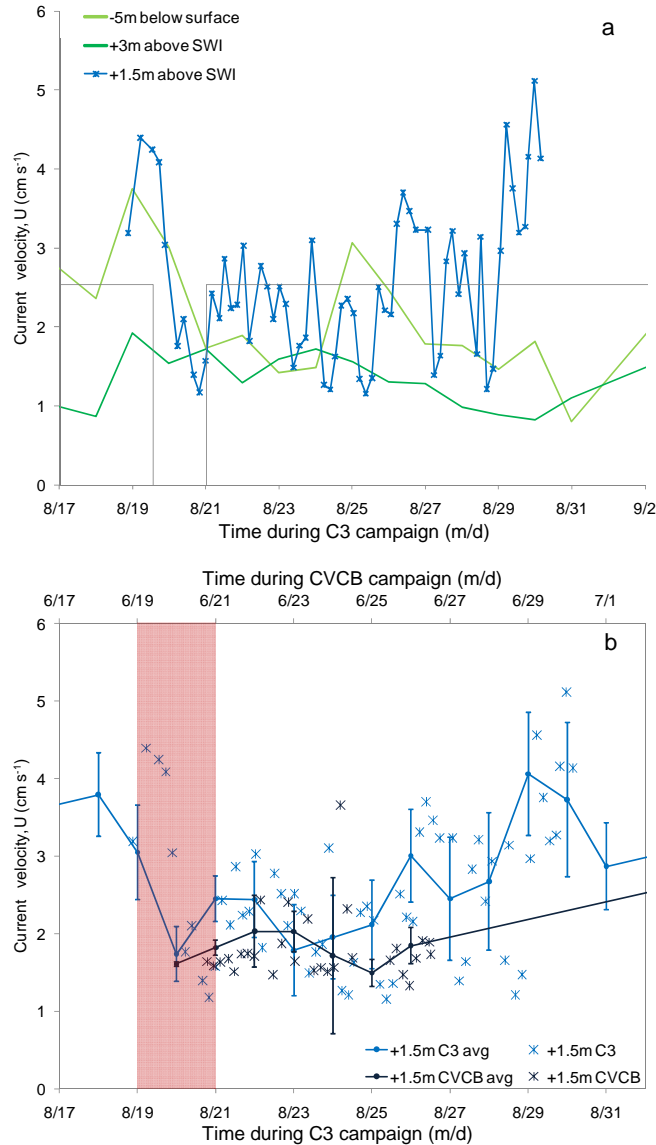


Figure 4.6. Current velocity time series (as measured via acoustic Doppler current profiler; ADCP) in relation to HO<sub>x</sub> flow during the August 2008 C3 campaign (a). Near-sediment velocities (+1.5 m above the sediment) as well as velocities in the bulk hypolimnion (+3 m above the sediment) and epilimnion (-5 m below the water surface) are shown. Increased near-sediment velocity observed at the end of the campaign correlates with the re-established vertical O<sub>2</sub> distribution shown in Fig. 4.3b. Similar results were obtained during the June 2008 CVCB campaign (b). The magnitude and degree of variation in near-sediment velocities increased after HO<sub>x</sub> operations were resumed after the period it was turned off (b; designated in red).

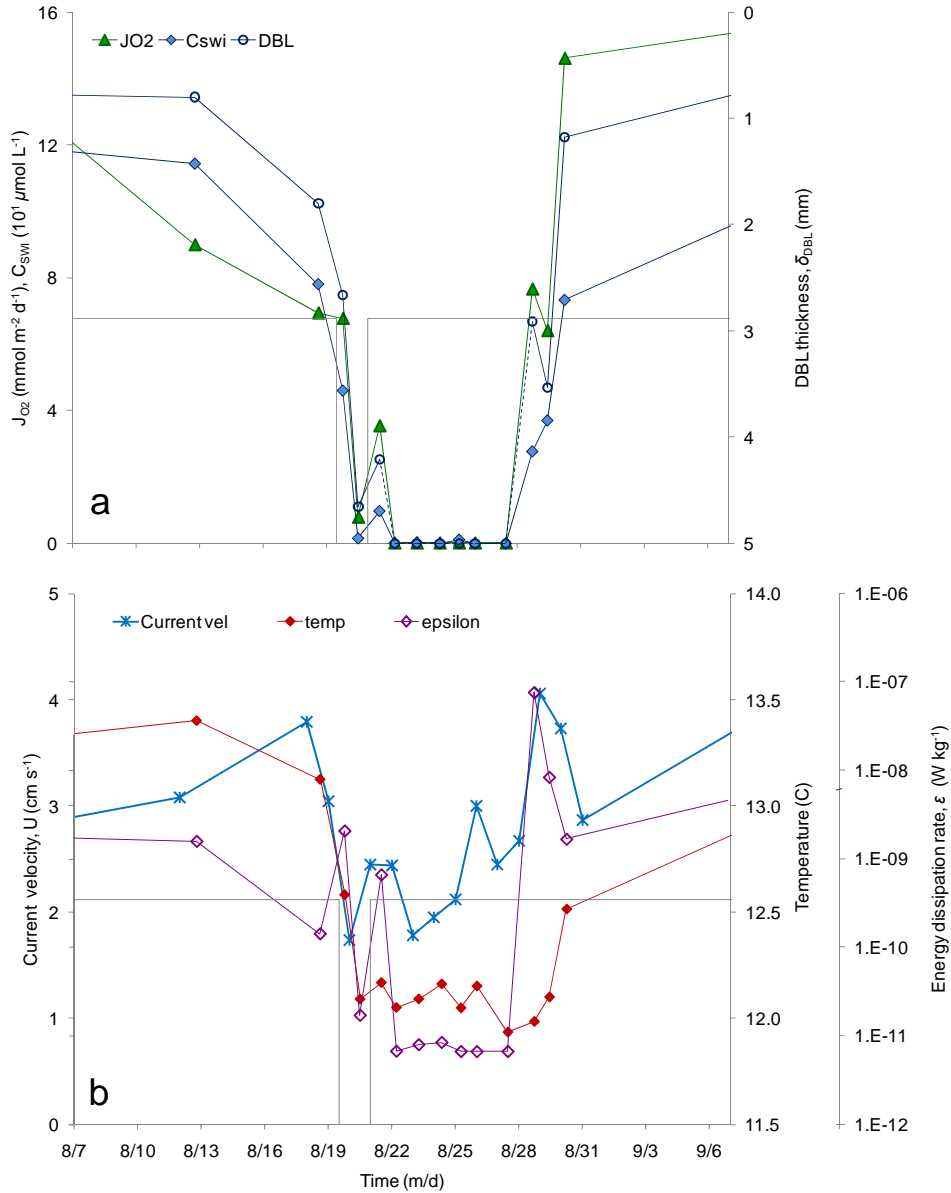


Figure 4.7. The response of  $J_{O_2}$  and the vertical  $O_2$  distribution at the SWI (a; as characterized by diffusive boundary layer thickness ( $\delta_{DBL}$ ) and  $z_{max}$ ) to turning off the HOx corresponds directly to variations in near-sediment mixing (b) as characterized by current velocity (obtained via ADCP) and turbulence (defined by energy dissipation rate  $\epsilon$ , which was estimated as a function of water-side  $\delta_{DBL}$ ). Results shown are based on in situ data obtained during the August 2008 campaign at C3; similar results were obtained from the June CVCB campaign. The analogous behavior of temperature at the SWI (b; obtained via MP4 temperature microsensors) further indicates that near-sediment mixing was significantly influenced by HOx operations.

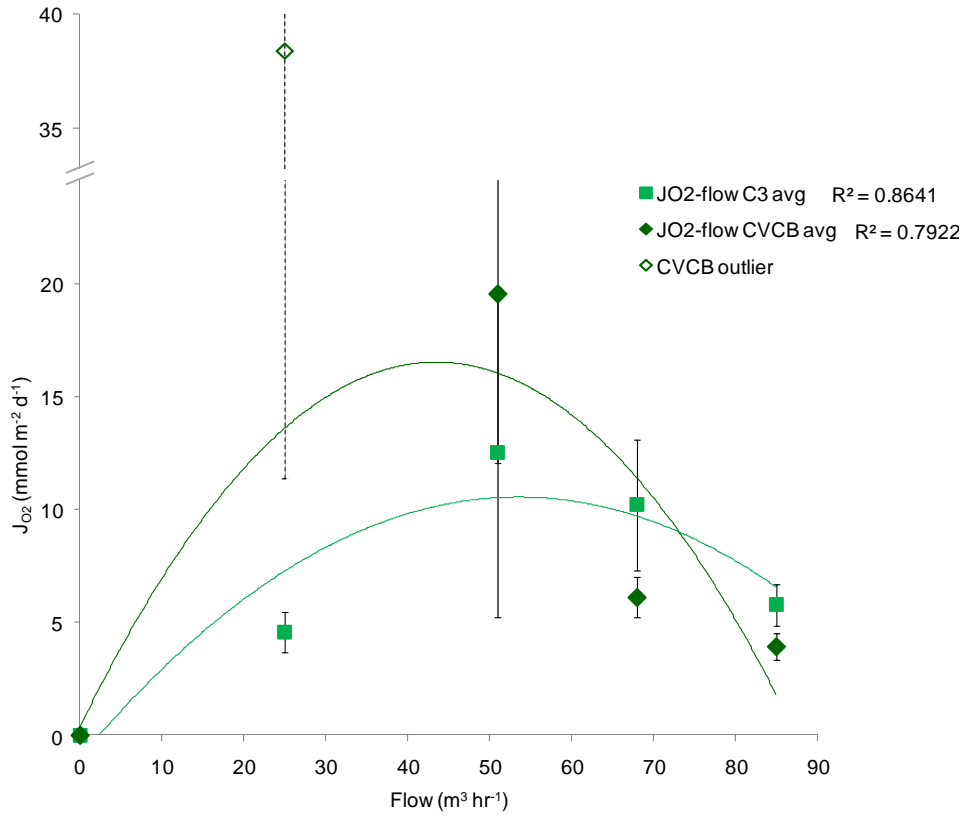


Figure 4.8. Variation in  $J_{O_2}$  as a function of HOx flow rate. Data shown are average values based on  $O_2$  microprofile data from 2007-2008 (Table 4.1). CVCB data for flow =  $25 \text{ m}^3 \text{ h}^{-1}$  were considered outliers (supported by  $J_{O_2}$  standard deviation data in Table 4.1; including outlier data decreased CVCB  $R^2$  value to 0.61).

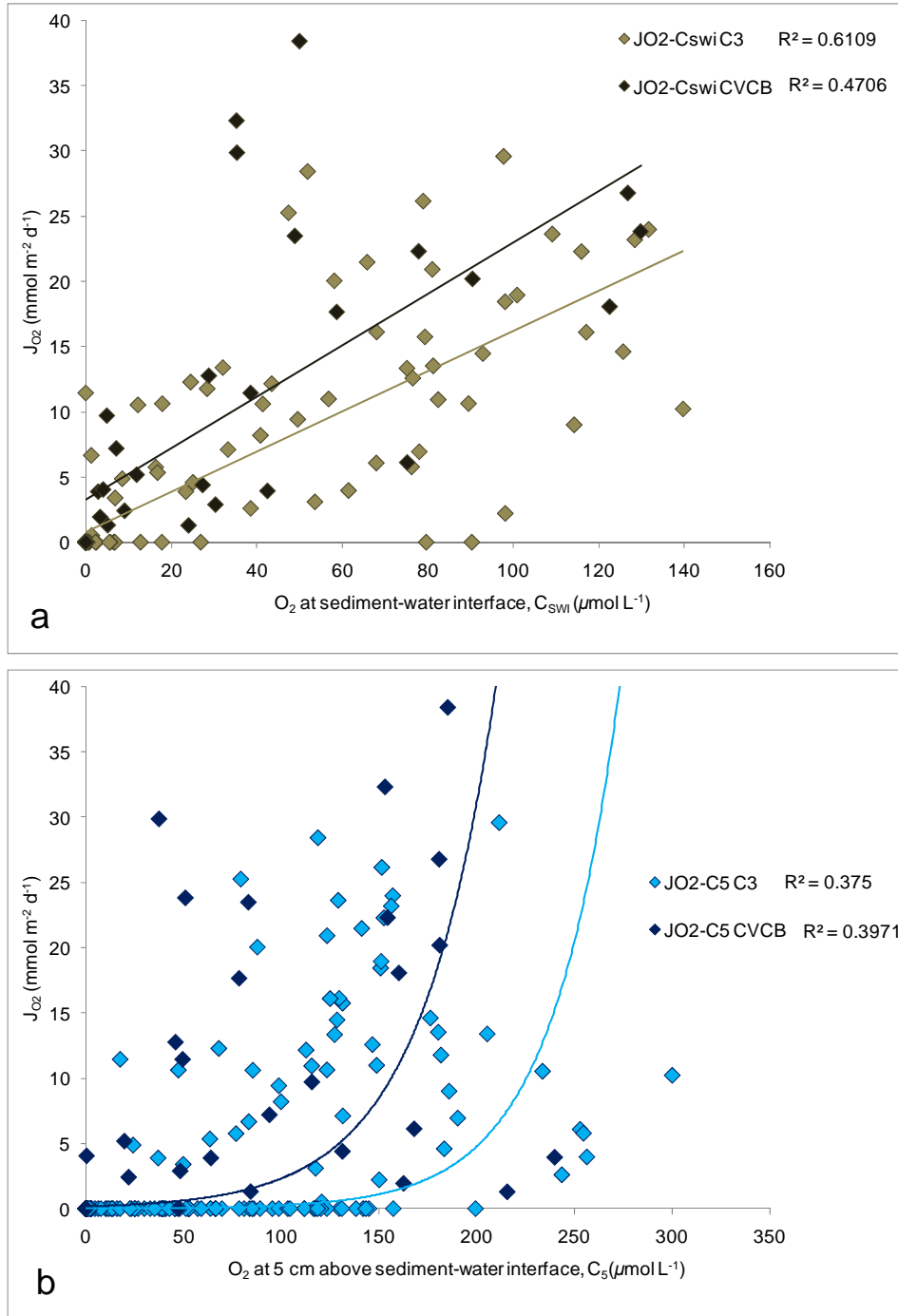


Figure 4.9. Correlation between  $J_{O_2}$  and both  $C_{SWI}$  (a) and  $C_5$  (b). Results shown based on full  $O_2$  microprofile data set from 2007-2008 (corresponding averages provided in Table 4.1).

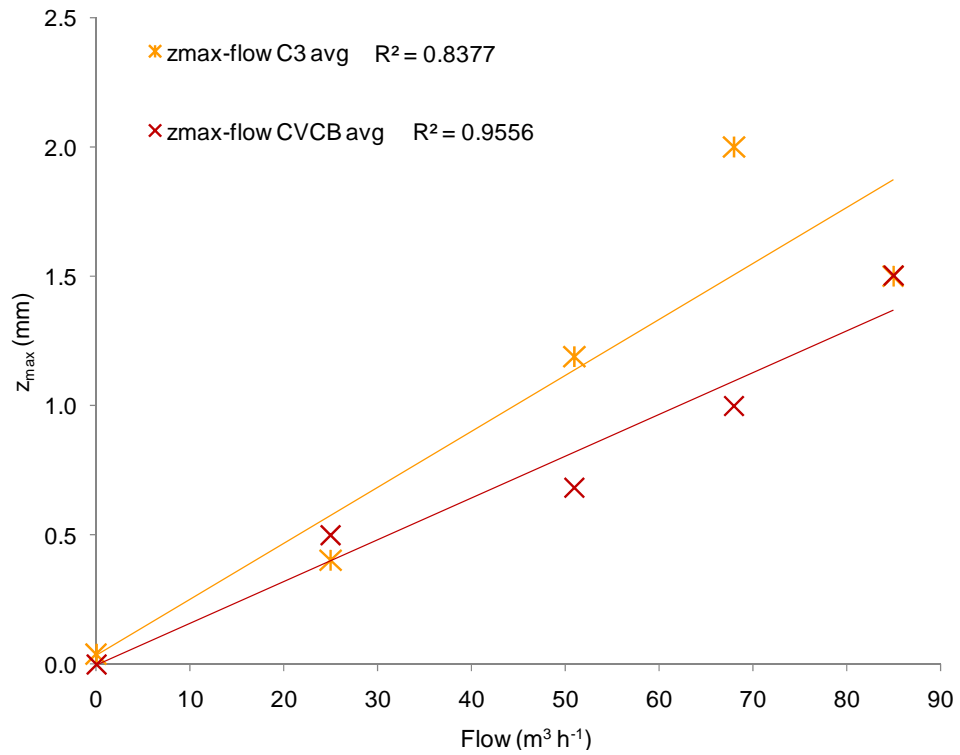


Figure 4.10. Variation in  $z_{\max}$  as a function of HOx flow rate. The sediment oxic zone is shown to increase in direct response to elevated HOx flow at both locations. Data shown are average values based on O<sub>2</sub> microprofile data from 2007-2008 (Table 4.1).

## Chapter 5 – Biogeochemical cycling of iron and manganese at the sediment-water interface in response to hypolimnetic oxygenation

Bryant, Lee D., Paul A. Gantzer\*, John C. Little  
Civil and Environmental Engineering, Virginia Tech, Blacksburg, Virginia, 24060, USA.  
\*Now at: Gantzer Water Resources LLC, Kirkland, Washington, 98084, USA.

To be submitted: *Water Research*

### 5.1 Abstract

One of the primary goals of hypolimnetic oxygenation systems (HOx) from a drinking-water perspective is to suppress sediment-water fluxes of reduced chemical species (e.g., iron (Fe) and manganese (Mn)) by replenishing dissolved oxygen ( $O_2$ ) in the hypolimnion. While it has been established that HOx increase sediment  $O_2$  uptake rates ( $J_{O_2}$ ) via elevated near-sediment  $O_2$  and turbulence levels, the influence of HOx on sediment-water fluxes of Fe and Mn ( $J_{Fe}$  and  $J_{Mn}$ , respectively) has not been comprehensively evaluated. We therefore performed a study focused on how HOx operations affect biogeochemical cycling of Fe and Mn. This study was based on  $O_2$ , Fe, and Mn data collected primarily in situ characterizing both the sediment and water column in a drinking-water-supply reservoir equipped with an HOx.

While soluble Fe was found to be controlled relatively easily as long as minimal levels of  $O_2$  remained near the sediment, soluble Mn levels in the lower hypolimnion increased significantly when the HOx was not in operation and the upper sediment became anoxic. However, continuous HOx operations maintained elevated near-sediment  $O_2$  levels and an oxic sediment-water interface which facilitated Fe and Mn suppression within the benthic region. Although  $J_{Fe}$  and  $J_{Mn}$  were enhanced by HOx operations, results indicate biogeochemical cycling supported by elevated  $O_2$  in the sediment and overlying water prevented released metals from reaching the bulk water. Increased amounts of Fe and Mn in the bulk sediment resulting from HOx-enhanced sedimentation further support benthic metal retention. These results emphasize that  $O_2$  allocated for the oxidation of enhanced fluxes of reduced species and subsequent incorporation of these species into the sediment must be taken into account for successful HOx operation. Results of this study should be of benefit to managers of HOx-equipped lake and reservoir systems for the optimization of HOx operations and source-water quality.

## 5.2 Introduction

Hypolimnetic oxygenation systems (HOx) are used by drinking water and hydropower utilities, as well as other lake and reservoir managers, to replenish dissolved oxygen ( $O_2$ ) while preserving stratification (Wüest et al. 1992; Singleton and Little 2006; Gantzer et al. 2009a). Increasing hypolimnetic  $O_2$  while maintaining stratification in drinking water reservoirs is desirable because this allows the oxygenated hypolimnetic water (which is relatively free of algal matter and other debris as compared to the epilimnion) to be used as source water (Gafsi et al. 2009). One of the primary goals of oxygenation from a drinking-water perspective is to improve source water quality by preventing hypolimnetic anoxia and the subsequent release of reduced chemical species (e.g., iron (Fe) and manganese (Mn)) from the sediment into the water column (Beutel 2003; Moore 2003). It has been established that oxygenation can significantly decrease soluble Fe and Mn levels in the hypolimnion (Chiswell and Zaw 1991; Gantzer et al. 2009b) as the reduced metals are oxidized by increased hypolimnetic  $O_2$  and precipitate to the sediment. However,  $O_2$  dynamics and biogeochemical transformation processes are highly variable at the sediment-water interface (SWI) due to the extremely steep gradients in chemical, physical, and microbial properties that occur in this region (Santschi 1990). Thus, as increased levels of oxide precipitates reach the sediment, potentially significant changes in the sediment  $O_2$  uptake rate ( $J_{O_2}$ ) and metal fluxes at the SWI may occur (Jørgensen and Revsbech 1985; Zhang et al. 1999). As a result, the influence of HOx on sediment-water fluxes of reduced species is not well understood.

Conceptually, HOx-induced increases in turbulence and near-sediment  $O_2$  and metal concentrations will have a direct effect on sediment-water diffusive flux. Mass transport of soluble species at the SWI is governed by diffusion through the diffusive boundary layer (DBL), a mm-scale laminar layer immediately above the sediment (Jørgensen and Revsbech 1985). Diffusive flux at the SWI is therefore controlled by the concentration gradient ( $\partial C/\partial z$ ) within the DBL, which is in turn regulated by turbulence in the overlying water of the bottom boundary layer (BBL) and DBL thickness ( $\delta_{DBL}$ ). Natural variation in turbulence has been shown to have a significant effect on  $\delta_{DBL}$  and sediment-water fluxes (Lorke et al. 2003; Brand et al. 2009; Bryant et al. 2010; Ch.2).

While previous work has shown that oxygenation increases  $J_{O_2}$  via elevated near-sediment  $O_2$  and turbulence levels (Moore 2003; Gafsi et al. 2009), the influence of HOx on sediment-water fluxes of Fe and Mn ( $J_{Fe}$  and  $J_{Mn}$ , respectively) has not been fully established. Some studies support the use of HOx for sediment-water flux suppression (Beutel 2003; Beutel et al. 2008); however, it has also been shown that technical lake management procedures such as oxygenation can fail to effectively decrease the release of reduced species from the sediment to the hypolimnion in some systems (Gächter and Wehrli 1998; A. Matzinger, unpubl.). Furthermore, much of the work that has been done on using oxygenation to improve water quality has largely focused on the water column (Chiswell and Zaw 1991; Matthews et al. 2006; Gantzer et al. 2009b) and many of the sediment-water flux studies that have been performed have been largely theoretical or laboratory-based (Moore et al. 1996; Beutel 2003). We therefore performed a study that assessed how HOx operations affect  $J_{Fe}$ ,  $J_{Mn}$ , and resulting water quality. Our study was based on  $O_2$ , Fe, and Mn data collected primarily in situ characterizing both the sediment and water column in a drinking-water-supply reservoir equipped with an HOx. By evaluating the vertical distribution of  $O_2$ , Fe, and Mn at the SWI, the incorporation of Fe and Mn into the bulk sediment, and subsequent source water quality as a function of HOx operation, we aim to promote greater understanding of (1) biogeochemical cycling at the SWI and (2) how to successfully manage HOx operation for the suppression of reduced chemical species in the benthic region.

### **5.3 Materials and methods**

**5.3.1 Study site and instrumentation** – Our study focused on Carvin’s Cove Reservoir (CCR), a drinking-water-supply reservoir managed by the Western Virginia Water Authority (WVWA) in Virginia, USA (Fig. 5.1). CCR is eutrophic and has a maximum depth of 23 m, width of ~600 m, and length of ~8000 m. A linear bubble-plume HOx (Mobley et al. 1997; Singleton et al. 2007) was installed by WVWA in CCR in 2005 and since that time ongoing field campaigns have been performed to monitor performance (Ch. 4; Gantzer et al. 2009a; Gantzer et al. 2009b). The CCR HOx is comprised of two parallel lines of porous tubing (each individual line consists of two tubes that are each ~1 cm in diameter and 625 m in length) located in the deepest section of the reservoir near the WVWA treatment plant outtake (Fig. 5.1).

To evaluate sediment-water fluxes in CCR, a network of in situ and laboratory measurements was obtained from 2005-2008. Focused field sampling typically lasted from March (at the start of stratification) through November (post fall turnover). Samples were obtained primarily from sites near the HO<sub>x</sub> (CC and CVCB), mid-reservoir (C3), and in the back region (CR) to characterize the influence of the HO<sub>x</sub> at a reservoir-wide scale. O<sub>2</sub> microprofiles of the SWI were obtained using both an in situ microprofiler and microsensor profiling of sediment cores in the laboratory. In-situ porewater analyzers (“peepers”; Hesslein 1976) were used to obtain soluble Fe and Mn profile data at the SWI. Bulk sediment samples were analyzed for total Fe, total Mn, and total organic carbon (TOC). Water samples from different elevations in the water column and also from water overlying the sediment of core samples was used to track changes in total and soluble Fe and Mn. Further details on primary measurements are provided below and in Ch. 4. Some additional data were collected for background information and companion studies. Water column profiles were obtained using a CTD (Conductivity-Temperature-O<sub>2</sub> as a function of Depth) probe to track water column O<sub>2</sub> levels and density stratification as a function of temperature. During the 2006 season, sediment samples from sediment cores were also routinely preserved for microbial analyses (Ch. 6).

*5.3.1.1 O<sub>2</sub> profiles at the SWI* – During 2005 and 2006, O<sub>2</sub> profiles at the SWI were measured via microsensor profiling of sediment cores. Sediment cores were obtained using a ball corer (Uwitec) with a core tube diameter of 90 mm and height of 120 cm. Following extraction, sediment cores were kept in the dark and on ice as they were transported to the laboratory and were typically profiled within ~1 h of extraction. Sediment cores were cut to an appropriate height (~20 cm) for profiling using a Uwitec core cutter. Sediment cores remained largely undisturbed during the extraction and cutting process and only undisturbed cores were profiled. Sediment cores were profiled using Clark-type O<sub>2</sub> microsensors (OX-100; Unisense A/S), which have an internal reference and a guard cathode. OX-100 microsensors have an extremely small tip size and depth resolution (100 μm), rapid response time (90% response in < 8 s), and negligible stirring sensitivity. The microsensors were manually controlled by a micromanipulator (M3301R; World Precision Instruments, Inc.) and were supported by a high-sensitivity picoammeter (PA2000; Unisense A/S). Mild mixing of the core water column was maintained during profiling. Cores were profiled in duplicate at 1-mm depth resolution; for each

profile, three measurements were obtained at each depth. For each core, a linear calibration of the microsensor was obtained using O<sub>2</sub> concentrations in the overlying core water column, as determined via Winkler titration, and in the anoxic sediment (Røy et al. 2004).

During 2007 and 2008, an autonomous microprofiler (MP4; Unisense A/S) equipped with microsensors (O<sub>2</sub> (OX-100), temperature (TP-100), and pH (PH-100); Unisense A/S) was used to obtain microprofiles at the SWI in situ. The MP4 OX-100 has the same characteristics as described for the laboratory microsensor. The thermo-coupled TP-100 has a spatial resolution of ~200 μm, resolution of ± 0.1 μV per °C, and 90% response time of < 3 s. The PH-100 is a miniaturized conventional pH electrode with a spatial resolution of ~200 μm, detection limit of ± 0.1 pH unit, and 90% response time of < 20 s. The pH microsensor was used solely to obtain single-point measurements and not profile data; hence the longer response time did not affect speed of profiling. Profiles were collected in duplicate at each sample site (excluding multi-day campaigns in 2008 where profiles were measured continuously), with a full profile obtained ~every 50 min. The profile sequence was as follows: 10-mm resolution from 10 cm to 1 cm above the SWI, 1-mm resolution from 1 cm to 0.5 cm above the SWI, 0.1-mm resolution from 0.5 cm above the SWI to 0.5 cm below the SWI. Ten measurements were typically taken at each depth (during the multi-day campaigns only three measurements were obtained per depth due to data storage limitations during overnight deployments). Following a pause between measurements for equilibration at each depth, microsensor data were collected at a rate of 1 Hz.

Sediment core O<sub>2</sub> profiles were used to quantify HO<sub>x</sub>-induced variations in the vertical O<sub>2</sub> distribution and J<sub>O<sub>2</sub></sub> prior to summer 2007 (when the MP4 microprofiler was acquired). However, in addition to issues with sediment disturbance during sampling, core profiling is not ideal because the sample does not reflect in situ turbulence, which is known to significantly influence sediment O<sub>2</sub> uptake (Lorke et al. 2003; Bryant et al. 2010; Ch. 2). To assess how in situ and sediment core data compared, an evaluation of J<sub>O<sub>2</sub></sub> estimates based on laboratory sediment core and in situ MP4 microprofile data was performed during summer 2007. While O<sub>2</sub> profiles from both methods were visually similar and overall trends in J<sub>O<sub>2</sub></sub> were well preserved, core-based estimates of J<sub>O<sub>2</sub></sub> were on average 50% (± 25%; Appendix B.1) less than MP4 estimates. Although the core water column was continually mixed during profiles, decreased J<sub>O<sub>2</sub></sub> estimates based on sediment core data were most likely a result of insufficient turbulence (as compared to in situ) within the core tube and subsequently increased δ<sub>DBL</sub>. Because sediment

core  $J_{O_2}$  estimates were consistently ~50% less than in situ estimates, a correction factor of 2.0 was applied to sediment core  $J_{O_2}$  data from 2005-2006.

During sediment core profiling, the SWI location was easily identified visually. In the absence of a video camera during in situ microprofiling, the SWI location was determined via both visual interpretations of  $O_2$  profile data (based on identifying linear DBL regions and kinks in the profile due to porosity differences between the sediment and the water column) and using standard deviations of  $O_2$  temporal fluctuations obtained at each sampling-depth increment (Bryant et al. 2010; Ch. 2). Standard deviations of solute concentration measurements decrease as the sensor approaches the sediment due to decreased turbulent diffusion near the SWI and these variances may be used to determine SWI location (Müller et al. 2002).

*5.3.1.2 Fe and Mn profiles at the SWI* – Peeper dialysis porewater samplers were used to obtain in situ soluble Fe and Mn profile data at the SWI. The peepers were constructed following Hesslein (1976), Urban et al. (1997), and Lewandowski et al. (2002). Each peeper consisted of two polypropylene sheets (a 13-mm-thick base plate and a 3-mm-thick cover plate) and a sheet of Millipore 0.45- $\mu$ m HV Durapore membrane; total peeper dimensions were 80 cm in height and 32 cm in width. Stainless steel fasteners were used to secure the two plates and membrane sheet together. Each peeper had a single column of forty sampling chambers (20-mL volume) with a vertical profile resolution of 1 cm. Peepers were filled with distilled water during construction and then kept in a nitrogen ( $N_2$ )-bubbling tank for deoxygenation until deployment. Immediately prior to deployment, peepers were inserted into an aluminum frame which, upon deployment (typically within ~1-2 minutes of removal from the deoxygenation tank), positioned the peeper vertically into the sediment so that half of the peeper chambers were exposed to the near-sediment water column and half of the chambers were exposed to sediment porewater. The frames were designed to prevent the aluminum from influencing peeper measurements and, based on data obtained from peepers deployed with and without the frame, the frames did not affect measurements. Peepers were deployed in duplicate for 2-4 weeks at a time (to allow for the peeper to come to equilibrium with in situ water) at locations CC (2006), CVCB (2007-2008), CE (2007-2008), and CR (2008). Immediately upon retrieval, water samples were obtained via sterilized pipettes from each peeper chamber, acidified, and analyzed for metals via inductively-coupled plasma (ICP) spectroscopy (Clesceri et al. 1998).

Concentrations of Fe and Mn in near-sediment water and porewater were characterized by soluble ( $< 0.45\text{-}\mu\text{m}$ ) peeper data which represents both the reduced, dissolved ( $< 0.20\text{-}\mu\text{m}$ ) and oxidized, colloidal ( $< 0.45\text{-}\mu\text{m}$ ) forms of these metals (Lienemann et al. 1999; Thompson et al. 2006). To evaluate how much of our soluble Fe samples were in the reduced  $\text{Fe}^{2+}$  form, ferrozine analyses (Stookey 1970) were performed on peeper samples from the 2006 field campaign.

*5.3.1.3 Water sample measurements* – Because peeper data could only be obtained on a bi-weekly basis, near-sediment water samples were obtained from sediment cores to increase measurement frequency for metals data. Samples were collected at  $\sim 5$  cm above the sediment in the water column of core samples using a syringe with attached tubing. Water samples were transferred directly to sterile plastic bottles. Immediately upon reaching the WVWA laboratory (typically within  $\sim 1\text{-}2$  h of sampling), samples for total metal analyses were acidified and samples for soluble metals were filtered through  $0.45\text{-}\mu\text{m}$  Millipore filter paper and then acidified. Samples were evaluated for total and soluble Fe and Mn via ICP (Clesceri et al. 1998).

Samples from the CCR hypolimnion were collected at 3m-increments using a Kemmerer bottle and analyzed for total and soluble Fe and Mn via ICP (Clesceri et al. 1998). Total metal samples were transferred directly from the Kemmerer bottle to pre-acidified plastic bottles. Soluble metal samples were filtered through  $0.45\text{-}\mu\text{m}$  Millipore filter paper prior to being transferred to pre-acidified plastic bottles.

*5.3.1.4 Bulk sediment measurements* – Bulk sediment samples were collected in the field from the top  $\sim 2$  cm of sediment core samples and transferred directly into sterile glass containers. Samples were analyzed following standard methods for total solids (SM2540B; Greenberg et al. 1992), total Fe and Mn (SW6010B; EPA 1996), and TOC (Lloyd Kahn; EPA 1988).

**5.3.2 Flux analyses** –  $\text{O}_2$  microprofile and peeper profile data were used to estimate  $J_{\text{O}_2}$ ,  $J_{\text{Fe}}$ , and  $J_{\text{Mn}}$ , respectively. While chemical and biological processes may influence sediment-water metal fluxes, solute flux models of the SWI are typically based on diffusive transport (Achman et

al. 1996; Lavery 2001). Diffusive flux ( $J_i$ ) for species (i) O<sub>2</sub>, Mn, and Fe was evaluated using Fick's first law of diffusion (Rasmussen and Jørgensen 1992; Higashino et al. 2004):

$$J_i = -\varphi D_{si} \left. \frac{\partial C}{\partial z} \right|_{\text{sed}} = -D_i \left. \frac{\partial C}{\partial z} \right|_{\text{water}} = D_i \frac{C_{\text{bulk}} - C_{\text{SWI}}}{\delta_{\text{DBL}}} \Bigg|_{\text{water}} \quad [\text{mmol m}^{-2} \text{d}^{-1}] \quad (5.1)$$

where  $\varphi$  is sediment porosity (m<sup>3</sup> voids m<sup>-3</sup> total volume),  $D_{si}$  is the species-dependent diffusion coefficient in sediment (m<sup>2</sup> s<sup>-1</sup>), and  $D_i$  is the species-dependent diffusion coefficient in water (m<sup>2</sup> s<sup>-1</sup>).  $C$  indicates the respective species concentration,  $\partial C/\partial z$  is the linear concentration gradient in the DBL immediately above or below the SWI ( $\mu\text{mol m}^{-4}$ ),  $C_{\text{bulk}}$  is the concentration in the bulk BBL ( $\mu\text{mol L}^{-1}$ ), and  $C_{\text{SWI}}$  is the concentration at the SWI ( $\mu\text{mol L}^{-1}$ ), as shown in Fig. 2.1a of Ch. 2. Diffusive transport is hence defined in the sediment by the second term in Eq. 5.1 and in the water by the third and fourth terms. Water-side profile data is frequently more difficult to evaluate due to rapid turbulence-induced variation in  $\delta_{\text{DBL}}$  (Bryant et al. 2010; Ch. 2). Additionally, measuring fluxes representative of in situ conditions is problematic based on sediment core profiling where turbulence is controlled. Because sediment-side data is less directly influenced by variations in turbulence (Ch. 3),  $J_i$  was evaluated from porewater data using the second term in Eq. 5.1.

Sediment cores from the primary sampling locations (Fig. 5.1) were evaluated for  $\varphi$  following Dalsgaard et al. (2000) and  $\varphi$  values of 0.95-0.97 were obtained. Values for  $D_{\text{O}_2}$  were based on  $D_{\text{O}_2} = 1.97 \times 10^{-9} \text{ m}^2 \text{ s}^{-1}$  at 20°C (Arega and Lee 2005). The simplifying assumption was made for metal flux calculations that soluble Fe and Mn peeper data were completely in the dissolved, reduced forms of Fe<sup>2+</sup> and Mn<sup>2+</sup>. This assumption may have resulted in slightly overestimated  $J_{\text{Fe}}$  and  $J_{\text{Mn}}$  values due to  $D_i$  and colloidal transport effects (Achman et al. 1996); however, its validity is supported by ferrozine results showing that typically ~70% of near-surface soluble Fe was Fe<sup>2+</sup>. Due to the close pairing of Fe-Mn redox kinetics (Santschi et al. 1990; Fossing et al. 2004; Duckworth et al. 2009) and the ease with which oxidized Mn reduces relative to Fe (Davison 1985), an even greater percentage of Mn was likely in the reduced form in the largely anoxic upper cm of sediment (excluding the ~1-2 mm oxic zone). Values for metal  $D_i$  were hence based on  $D_{\text{Fe}^{2+}} = 7.19 \times 10^{-10} \text{ m}^2 \text{ s}^{-1}$  and  $D_{\text{Mn}^{2+}} = 6.88 \times 10^{-10} \text{ m}^2 \text{ s}^{-1}$  at 25°C (Li and Gregory 1974). All  $D_i$  and corresponding  $D_{si}$  values were corrected for temperature using the

Stokes-Einstein relationship (Li and Gregory 1974).  $D_{si}$  was defined as  $D_{si} = \phi D_i$  to correct for sediment tortuosity as a function of  $\phi$  (Berg et al. 1998; Glud 2008; Ch. 3).

The temporal change in  $O_2$  concentration ( $\partial C/\partial t$ ) was evaluated for our series of in situ  $O_2$  profiles by comparing profiles immediately before and after one another and calculating the rate of change in  $O_2$  at each depth.  $\partial C/\partial t$  was found to be on average <5% of  $J_{O_2}$ , establishing that our profiles were at quasi-steady state and that turbulence conditions in CCR were changing slowly relative to the duration of an  $O_2$  microprofile. Quasi-steady-state conditions were assumed for peeper data based on the extended deployment period.

## 5.4 Results and Discussion

**5.4.1 Sediment-water vertical Fe and Mn distribution** – Soluble Fe and Mn peeper data from the 2007 season are shown in Fig. 5.2. The distinct peaks near the SWI are indicative of the anoxic-oxic boundary where active redox cycling between precipitated oxides and reduced soluble species occurs (Davison 1982; Belzile et al. 1996). Sediment Fe and Mn levels steadily increased as the season progressed; hence, as Fe and Mn precipitated out of the oxygenated water column, these particles likely were transformed to soluble Fe and Mn as they reached the more reducing near-sediment environment. Additionally, enhanced oxidation of sediment organic matter due to elevated near-sediment  $O_2$  may have contributed to reductive remobilization of Fe and Mn (Zhang et al. 1999). While CCR soluble Mn and Fe porewater concentrations were relatively high in comparison to other freshwater studies (Urban et al. 1997; Schaller et al. 1997; Schaller and Wehrli 1997), they are on the same order of magnitude and regional geology is known to have high levels of Fe and Mn (Stose et al. 1919, Carpenter et al. 1971; Mussman et al. 1986).

**5.4.2 Fe and Mn response near the SWI** – Contour plots based on a Kriging interpolation scheme and peeper data at site CVCB (directly beside the HOx; Fig. 5.1) in correlation with HOx flow during 2006-2008 are shown in Fig. 5.3. Near-sediment soluble Fe levels remained consistently low during HOx operations (Fig. 5.3a-c). Increased Fe is observed up to ~10 cm in the water column for a brief period following a reduction in HOx flow in 2007 (Fig. 5.3b). Near-surface porewater Fe levels also slightly increased when the HOx was turned off for extended

periods during June and November 2006 (Fig. 5.3a) and fall 2007 (Fig. 5.3b). Nevertheless, Fe tends to remain in the oxidized form even under reducing conditions (Davison 1993; Crittenden et al. 2005) and soluble Fe levels were only mildly affected even during periods when the sediment went anoxic after the HOx was turned off. Conversely, soluble Mn levels at the SWI varied significantly in response to changes in HOx operation. As shown in Fig. 5.3d, when the HOx was turned off for one month in 2006, soluble Mn levels both in the water overlying the sediment and in sediment porewater increased substantially. Similar results were obtained during 2007 in response to decreased HOx flow (Fig. 5.3e). Mn reduces much more easily than Fe (Balzer 1982; Davison 1985), which most likely explains the Mn response observed during periods when the HOx was turned off.

Although soluble Fe and Mn levels increased when the HOx was turned off in 2006-2007 (Fig. 5.3a-b, d-e), near-sediment concentrations of both metals remained low during continuous HOx operation in 2008 (Fig. 5.3c, 5.3f). Similar results were also observed mid-reservoir at C3 (Appendix B.2). These results indicate that Fe and Mn were oxidized in the water column and incorporated into the sediment during oxygenation (Jørgensen and Boudreau 2001). While Fe is easily oxidized in oxic environments, chemical oxidation of Mn is more difficult at the pH of natural waters, which is typically 7 – 9, and depends largely on microbial and/or surface-catalyzed reactions under such conditions (Santschi et al. 1990; Belzile et al. 1996; Crittenden et al. 2005). MP4 microsensor pH data confirmed that pH remained ~8 – 9 at the SWI in CCR and a correlation between Mn and pH at the SWI was not found (data not shown). Therefore, Mn oxidation and decreases in soluble Mn (Fig. 5.3; Appendix B.2) were likely controlled by biological processes (Nealson et al. 1988; Jørgensen and Boudreau 2001) and/or adsorption onto particulate matter (Santschi et al. 1990). The influence of sediment microbes on Fe and Mn dynamics in CCR is further explored in Ch. 6.

In addition to peeper data, core-water data provided independent verification of HOx-induced variation in near-sediment metal concentrations. Both total and soluble Fe and Mn levels increased substantially during periods when HOx flow was reduced, particularly in regions most directly affected by the HOx (Fig. 5.4). Similar results were obtained during 2006 (Fig. 5.4) and 2008 (Appendix B.3). A strong response to turning the HOx off and a consistent fractionation of total and soluble Fe and Mn is observed. Excluding the periods when the HOx was turned off, metal concentrations remained relatively constant at all sampling locations. As

shown by Fig. 5.3 and 5.4, Mn levels were more affected by HOx operations than Fe. Additionally, while ~50% of total Fe was soluble, indicating a significant solid fraction, Mn remained almost completely soluble. The fact that Mn stayed predominantly soluble while Fe was largely in the solid form highlights the ease with which Fe remains oxidized under low O<sub>2</sub> conditions relative to Mn.

In Fig. 5.5, the relationship among near-sediment metal concentrations, O<sub>2</sub> at the SWI, and HOx flow is emphasized. After the HOx was turned off from 19-21 August 2008, SWI O<sub>2</sub> levels dropped to 0 μmol L<sup>-1</sup> for over a week until the vertical O<sub>2</sub> distribution was finally re-established (Ch. 4). A significant increase in total and soluble Fe and Mn is observed during this anoxic period (Fig. 5.5; full data set provided in Appendix B.3), which clearly reveals the controlling influence that HOx operations have on sediment O<sub>2</sub> availability and metal cycling near the SWI.

Although HOx-induced variation in metal concentrations was observed throughout the reservoir as indicated by data from CVCB (directly alongside the HOx; Fig. 5.3, 5.4a) and C3 (mid-reservoir; Fig. 5.4b, 5.5), the response was not uniform. As shown by Fig. 5.4c, near-sediment metal concentrations at C2 were relatively unaffected. While C3 is located farther away from the HOx than C2, it is also at a higher elevation and HOx plume detrainment in the C3 region may have been an influence (Fig. 5.1; Ch. 4). These results indicate that the influence of the HOx was at least partially dependent on reservoir bathymetry.

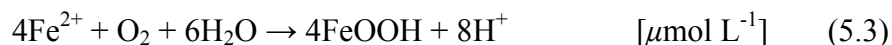
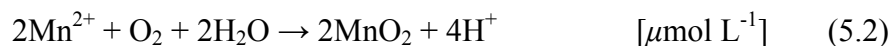
**5.4.3 HOx-induced variation in J<sub>O<sub>2</sub></sub>, J<sub>Fe</sub>, and J<sub>Mn</sub>** – Overall, a strong correlation between J<sub>O<sub>2</sub></sub>, J<sub>Fe</sub>, and J<sub>Mn</sub> was observed throughout the reservoir (Fig. 5.6). All three fluxes are shown to increase when the HOx was in operation and decrease when HOx flow was significantly reduced or halted for an extended period (e.g., November 2005 and June 2006 in Fig. 5.6a and September 2007 in Fig. 5.6a,b). Following an extended period of oxygenation, J<sub>Mn</sub> peaked at 0.67 mmol m<sup>-2</sup> d<sup>-1</sup>, with maximum J<sub>Fe</sub> = 1.53 mmol m<sup>-2</sup> d<sup>-1</sup> and J<sub>O<sub>2</sub></sub> = 26.8 mmol m<sup>-2</sup> d<sup>-1</sup> at CC in August 2008 (Fig. 5.6a). When the HOx was turned off for one month in July 2007, fluxes dropped to minimum values of J<sub>Mn</sub> = 0.34 mmol m<sup>-2</sup> d<sup>-1</sup>, J<sub>Fe</sub> = 0.40 mmol m<sup>-2</sup> d<sup>-1</sup>, and J<sub>O<sub>2</sub></sub> = 0.0 mmol m<sup>-2</sup> d<sup>-1</sup>. Estimates of J<sub>Mn</sub>, J<sub>Fe</sub>, and J<sub>O<sub>2</sub></sub> shown in Fig. 5.6 are comparable to values obtained from similar freshwater lake systems (Johnson et al. 1991; Belzile et al. 1996; Lorke et al. 2003).

While fluxes were influenced by whether or not the HOx was in operation, a relationship between metal flux and actual HOx flow rate is not evident, which may be attributed to the relatively small number of peeper samples obtained for each flow rate. An additional factor may have been that O<sub>2</sub> levels at the SWI typically remained relatively high regardless of flow rate during HOx operation (Ch. 4; Beutel 2003). Due to the complex biogeochemical controls on J<sub>Fe</sub> and especially J<sub>Mn</sub>, these fluxes were likely not as directly influenced by the actual HOx flow rate as long as sufficient sediment O<sub>2</sub> was available. An evaluation of our more extensive O<sub>2</sub> profile data set did reveal a correlation between flow rate and J<sub>O<sub>2</sub></sub> at low to moderately high flow rates however (Ch. 4). J<sub>Fe</sub> is shown to correlate more directly with J<sub>O<sub>2</sub></sub> than J<sub>Mn</sub>, as observed by Zaw and Chiswell (1999), which may be a function of redox kinetics (Bouldin 1986; Davison 1993).

As indicated by the different sign of J<sub>O<sub>2</sub></sub> compared to J<sub>Fe</sub> and J<sub>Mn</sub> in Fig. 5.6, J<sub>O<sub>2</sub></sub> represents the rate at which O<sub>2</sub> is transported into the sediment while J<sub>Fe</sub> and J<sub>Mn</sub> represent the rate at which Fe and Mn diffuse out of the sediment. BBL O<sub>2</sub> levels are typically much higher than in the sediment while porewater metal concentrations are significantly greater than in the water column. J<sub>O<sub>2</sub></sub> into the sediment is hence increased by HOx operations due to elevated near-sediment O<sub>2</sub> levels and subsequently increased O<sub>2</sub> driving force through the DBL (Ch. 4). Concurrently, water-column levels of Fe and Mn are significantly reduced (Gantzer et al. 2009b) and sediment concentrations increased as the metals are oxidized and settle to the sediment. As evidenced by peeper profiles (Fig. 5.2) and corresponding J<sub>Fe</sub> and J<sub>Mn</sub> estimates (Fig. 5.6), HOx operation therefore also increased  $\partial C/\partial z$  (albeit in the opposing direction of that for O<sub>2</sub>) for diffusive transport of Fe and Mn out of the sediment into the water column. As observed for J<sub>O<sub>2</sub></sub> (Ch. 4), HOx-induced suppression of  $\delta_{DBL}$  would have additionally enhanced J<sub>Fe</sub> and J<sub>Mn</sub> out of the sediment. Conversely, J<sub>Fe</sub> and J<sub>Mn</sub> decreased when the HOx was turned off which may be attributed to decreased  $\partial C/\partial z$  as near-sediment soluble metals increased significantly (Fig. 5.3-5.5) and the DBL was no longer maintained (Bryant et al. 2010; Ch. 2; Ch. 4).

The release of Fe<sup>2+</sup> and Mn<sup>2+</sup> as the sediment became anoxic would contribute to observed decreases in J<sub>O<sub>2</sub></sub> (Fig. 5.6) as these reduced metals were subsequently oxidized in the water column (Glud et al. 2007). Additionally, an initial increase in J<sub>Fe</sub> and J<sub>Mn</sub> very likely occurred immediately after HOx operations were halted and Fe and Mn were released as the sediment went anoxic (Fig. 5.5). The temporal scale of peeper measurements (two-week deployment period), however, did not facilitate capturing such rapid changes in flux.

**5.4.4 Amount of  $J_{O_2}$  allocated to  $J_{Fe}$  and  $J_{Mn}$  suppression** – The percentage of  $J_{O_2}$  used for the oxidation of released  $Fe^{2+}$  and  $Mn^{2+}$  was evaluated based on  $J_{Fe}$  and  $J_{Mn}$  estimates (Fig. 5.6) and stoichiometric relationships defined by Eq. 5.2 – 5.3 (Berg et al. 2003; Glud et al. 2007) following Adams et al. (1982).



Using Eq. 5.2-5.3,  $J_{Fe}$  and  $J_{Mn}$  were converted to equivalent values of hypothetical  $J_{O_2}$  ( $J_{O_2-Fe}$  and  $J_{O_2-Mn}$ , respectively). As shown in Fig. 5.7 and Table 5.1, hypothetical  $J_{O_2}$  based on total metal flux ( $J_{O_2-T} = J_{O_2-Fe} + J_{O_2-Mn}$ ) and also solely on Fe and Mn contributions ( $J_{O_2-Fe}$  and  $J_{O_2-Mn}$ ) are compared to measured  $J_{O_2}$  (Fig. 5.6). This approach is based purely on diffusive flux estimates and does not take into account Fe and Mn oxidation processes associated with surface-mediated reactions and/or microbial activity. Furthermore, because  $J_{Fe}$ ,  $J_{Mn}$ , and the estimates of  $J_{O_2-Fe}$  and  $J_{O_2-Mn}$  were based on the assumption that soluble metals were in the reduced form, results may over-estimate the proportion of  $J_{O_2}$  actually used for reduced metal oxidation. However, the influence of  $J_{Fe}$  and  $J_{Mn}$  on the overall  $O_2$  balance should be preserved in the comparisons.

During periods of summer stratification,  $J_{O_2-T}$  made up 10-15% of  $J_{O_2}$ , indicating that a moderate amount of total diffusive sediment  $O_2$  uptake (as defined by  $J_{O_2}$ ) was devoted to oxidation of  $J_{Fe}$  and  $J_{Mn}$  near the SWI (Fig. 5.7; Table 5.1). During the winter period following turnover (indicated by blue rectangles in Fig. 5.7), the percent of  $J_{O_2}$  used for reduced metal oxidation decreased to 1-2%. While  $J_{Fe}$  was found to be consistently higher than  $J_{Mn}$  (Fig. 5.6), a trend in  $J_{Fe}$  and  $J_{Mn}$  contributions to overall  $J_{O_2-T}$  was not observed. Previous work has shown that the proportion of  $J_{O_2}$  allocated to re-oxidation of reduced Fe and Mn was insignificant as compared to other reduced species such as nitrite, ammonium, and methane (Maerki et al. 2009; A. Matzinger, unpubl.). The fact that a measurable (up to 15%) amount of  $J_{O_2}$  was estimated for  $J_{Fe}$  and  $J_{Mn}$  oxidation (and subsequent suppression from the hypolimnion) indicates the relatively substantial role Fe and Mn play in the CCR redox cycle. Based on the traditional sequence of

redox reactions, denitrification and subsequent N<sub>2</sub> release occurs prior to Fe and Mn release as O<sub>2</sub> is depleted (Santschi et al. 1990); hence, extensive N<sub>2</sub> flux may be paired with J<sub>Fe</sub> and J<sub>Mn</sub>. Additional reduced species not considered here likely contribute significantly to sediment O<sub>2</sub> uptake and re-oxidation processes.

**5.4.5 Biogeochemical cycling effects** – Sediment-water metal flux results (Fig. 5.6) may appear to be in direct conflict with the overall goal of using HOx to reduce Fe and Mn levels in the water column. However, as shown by Mn data in Fig. 5.8, although J<sub>Mn</sub> and Mn levels near the sediment (both at the SWI and 1 m above) typically increased in response to HOx operation, Mn levels in the bulk hypolimnion (4 m above the sediment) remained negligible excluding the period when the HOx was turned off. Similar results for J<sub>Mn</sub> and J<sub>Fe</sub> (Fe data not shown) were observed both near the HOx (CVCB; Fig. 5.8a) and mid-reservoir (C3; Fig. 5.8b). Hence, our results indicate that while HOx operations increase soluble metal fluxes out of the sediment, elevated levels of O<sub>2</sub> maintained by HOx operation oxidize the soluble metals as they diffuse from the sediment. Following oxidation, metal oxide particles settle back to the sediment, thereby sustaining an HOx-enhanced Fe and Mn redox cycle in the near-sediment water.

Simple mass balance calculations were performed to further evaluate the influence of near-sediment biogeochemical cycling on hypolimnion water quality. Maximum bulk hypolimnetic Fe and Mn concentrations were estimated based on CC 2006 Fe and Mn flux data shown in Fig. 5.6, total Fe and Mn sediment trap data for the lower hypolimnion over the HOx (P. Gantzer, unpubl.), hypolimnetic Fe and Mn levels at the beginning of the 2006 season, and average volumes of both the bottom meter and the full depth of the hypolimnion. Based on sediment trap data, Fe and Mn sedimentation rates of 3.9 and 2.6 mmol m<sup>-3</sup> d<sup>-1</sup>, respectively, were estimated for August through November 2006. It was assumed that no Fe or Mn was removed via oxidation/precipitation; thus, all metals diffusing out of the sediment and/or settling from the bulk water were retained in the volume assessed (benthic (1m) region or full hypolimnion). As shown in Fig. 5.9a, while actual Mn levels at 1 m above the sediment initially approached the maximum Mn levels at 1 m, the maximum Mn surpassed actual Mn levels considerably by mid-season. Average hypolimnetic Mn data (based on water samples obtained mid-hypolimnion at 7 m above the sediment) remained low and fell far below maximum Mn at 7 m, with the deviation indicating a net gain of Mn to the sediment. These rough calculations

characterizing the influence of biogeochemical cycling indicate that while moderate Mn suppression occurred in the near-sediment region, biogeochemical cycling and/or dilution prevented enhanced Mn levels released by  $J_{Mn}$  from reaching the bulk hypolimnion. Similar Fe results show that actual hypolimnetic Fe levels were insignificant compared to maximum estimates (Fig. 5.9b). Thus, while the previously discussed results show increased  $J_{Mn}$  and  $J_{Fe}$  from the sediment due to HOx operation (Fig. 5.6), overall suppression of metals from the bulk water is maintained via biogeochemical cycling and elevated  $O_2$  in the benthic region.

**5.4.6 Influence of HOx on bulk sediment** – Bulk sediment data were used to assess how HOx-induced variation in  $J_{Fe}$  and  $J_{Mn}$  influenced Fe and Mn retention in the sediment. Bulk sediment total metal data and soluble metal and  $O_2$  concentrations at the SWI from the 2008 field season are presented in Fig. 5.10. While bulk sediment levels of total Fe and Mn were comparable mid-reservoir (Fig. 5.10b) and in the back region (Fig. 5.10c), total metals, particularly Mn, were substantially higher near the HOx (Fig. 5.10a). The percentage of soluble Mn relative to total Mn is also relatively low at CVCB, indicating that more Mn was retained in the oxide form in this region. Although total Mn levels were much lower at C3 and  $O_2$  levels at the SWI were comparable, the percentage of Mn in the soluble form was significantly greater mid-reservoir (Fig. 5.10a,b). Enhanced sediment Mn retention at CVCB may be a result of oxidation and adsorption processes due to increased levels of oxide particles in the region closest to the HOx and/or sediment focusing effects in the deeper CCR region (Fig. 5.1; Balzer 1982; Santschi et al. 1990). Sediment traps deployed throughout CCR in the lower hypolimnion showed elevated sedimentation rates in the near field region during summer oxygenation in 2007 (Gantzer et al. 2009b). Accelerated oxidation and precipitation of Fe and Mn and geochemical focusing in deeper regions as a result of oxygenation have also been observed by Schaller and Wehrli (1997) and Zaw and Chiswell (1999).

Despite the differing proportions of Mn at the various sample sites (Fig. 5.10a-c), a clear relationship between soluble and total Mn is typically observed. However, a similar correlation for Fe was not evident. While actual Fe and Mn kinetics are highly complex and affected by many variables (e.g., pH, microbial processes), these results do indicate that Mn release may have been at least partially dependent on total Mn concentration while Fe kinetics was zero-order with respect to total Fe. Mn oxidation kinetics are frequently assumed to be a function of solid

Mn ( $\text{MnO}_2(\text{s})$ ) while Fe oxidation is typically defined solely as a function of the dissolved  $\text{Fe}^{2+}$  form (Crittenden et al. 2005).

In addition to sedimentation effects, data from the back region (CR) suggest that horizontal migration of soluble metals may also influence metal distribution in CCR. CR went anoxic fairly early in summer 2008 (as indicated by sediment oxic zone depth,  $z_{\text{max}}$ ; Fig. 5.10c) due largely to distance from the HOx. While soluble Mn levels remained relatively constant, soluble Fe increased significantly during this anoxic period. As discussed by Gantzer et al. (2009b), elevated Mn in the upper hypolimnion in the central CCR basin (at approximately the same elevation as CR) may be a result of horizontal migration of Mn released from anoxic sediment in the back region. This is supported by Belzile et al. (1996). It is likely that both soluble Fe and Mn were released from CR during the anoxic period and rapidly transported toward the central basin. However, average  $J_{\text{Fe}}$  was significantly higher than  $J_{\text{Mn}}$  (0.7 and 0.3  $\text{mmol m}^{-2} \text{d}^{-1}$ , respectively) at CR. Fe would thus have been more rapidly resupplied in response to losses from horizontal transport which could explain the deviation in soluble Fe and Mn late season (Fig. 5.10c). Horizontal transport from the back region may also have been a factor in enhanced levels of soluble Mn (as compared to Fe) mid-reservoir (Fig. 5.10b). Due to slow Mn oxidation kinetics, influent soluble Mn would have remained prevalent in the oxic C3 region while soluble Fe would have rapidly oxidized. A correlation between Mn levels in the lower hypolimnion at CR and C3 was observed (data not shown). Interestingly, it has been shown that the lithospheric average ratio of Fe:Mn in sedimentary rocks is approximately equivalent to the kinetic oxidation rates of these two metals (Davison 1982).

Historical bulk sediment data characterizing the near field region from before the HOx was turned on in 2005 through summer 2008 are shown in Fig. 5.11. These data support HOx-induced increases in oxidation and precipitation near the HOx shown in Fig. 5.10a. Following the start of HOx operations in July 2005, total Fe, Mn, and TOC levels increased substantially in the sediment near the HOx. However, after the first year of HOx operation, bulk sediment measurements have remained relatively constant. Similar results, though with a less significant initial increase in total Fe, Mn, and TOC, were observed at other locations as well (C3 and CR; data not shown). The observed peak in TOC in 2006 may likely be a result of seasonal organic matter deposition (Berg et al. 2007).

CCR is largely isolated from allochthonous input and variation in annual nutrient loading is likely minimal. Hence, results in Fig. 5.11 indicate that after background levels of soluble Fe and Mn were oxidized in the first year of HOx operation, new steady-state conditions based on HOx operation were established. From a mass-balance perspective, incorporating increased levels of Fe and Mn into the sediment over time should decrease soluble metal concentrations and subsequent O<sub>2</sub> demand in the hypolimnion. Our sediment-side results support previous work based on water-column data showing reduced hypolimnetic O<sub>2</sub> demand as a result of long-term oxygenation (Moore et al. 1996; Matthews and Effler 2006). TOC data indicate that HOx operation initially resulted in increased deposition of organic matter in the hypolimnion to the sediment, possibly due to enhanced precipitation of metal oxides. However, a significant decrease in hypolimnetic TOC was not observed (data not shown). Because sediment TOC levels have stayed fairly constant since 2006, a balance between increased TOC loading via increased precipitation of oxide particles and enhanced burial efficiency due to increased O<sub>2</sub> exposure time may have been established (Sobek et al. 2009).

Based on 2005-2008 peeper data, seasonal Fe and Mn porewater concentrations and average  $J_{Fe}$  and  $J_{Mn}$  have remained relatively constant throughout HOx operations (Fig. 5.2, 5.6; full peeper-profile data set not shown). Paired with bulk sediment data in Fig. 5.11, these results indicate that while hypolimnetic metal concentrations were decreased by suppressing soluble metal fluxes to the benthic region, the potential sediment O<sub>2</sub> demand (Bryant et al. 2010; Ch. 2) has not been significantly decreased by oxygenation due to the accumulation of precipitated and subsequently reduced metals in the sediment (Yagi 1996). However, while a substantial source of reduced metals may remain in the sediment during oxygenation (A. Matzinger, unpubl.), maintaining elevated near-sediment O<sub>2</sub> levels and an established sediment oxic zone (Fig. 5.3-5.5, 5.10) should prevent the release of these soluble species into the overlying water, as shown by Jørgensen and Boudreau (2001) and Liboriussen et al. (2009).

**5.4.7 Effect of  $J_{Fe}$  and  $J_{Mn}$  on water column** – Our results have established that continuous oxygenation enhanced  $J_{Fe}$  and  $J_{Mn}$  out of the sediment (Fig. 5.6, 5.8) by increasing the  $\partial C/\partial z$  driving force via both reduced metal concentrations in the near-sediment water (Fig. 5.2-5.5) and elevated metal concentrations in the sediment porewater (Fig. 5.2, 5.3). However, as indicated by mid-hypolimnion water sample data (Fig. 5.8, 5.9) and simple flux calculations (Fig. 5.9),

near-sediment biogeochemical cycling maintained by HOx-increased O<sub>2</sub> levels prevented Fe and Mn released from the sediment from reaching the bulk hypolimnion. These results are further supported by water sample data characterizing the water column on a reservoir-wide scale. As shown in Fig. 5.9, average soluble Mn and Fe levels in the hypolimnion remained at ~10 and <1 μmol L<sup>-1</sup>, respectively, during 2006 oxygenation. Similar results were obtained during 2008, with a notable exception when the HOx was turned off in late August (Fig. 5.5). During this period, while soluble Fe increased immediately above the sediment (Fig. 5.5b), little change was observed in hypolimnetic Fe (data not shown). Conversely, soluble Mn concentrations in the lower hypolimnion increased significantly to ~50 μmol L<sup>-1</sup> (Mn<sub>1m</sub> in Fig. 5.8), though higher elevations were largely unaffected due to the relatively brief period that the HOx was turned off (Mn<sub>4m</sub> in Fig. 5.8). These results support the findings of Gantzer et al. (2009b) which show that hypolimnetic Mn levels are strongly influenced by HOx-induced variation in hypolimnetic O<sub>2</sub>. The overall effect of oxygenation on source water quality is revealed by CCR historical data showing that annual hypolimnetic Fe and Mn levels have decreased significantly since the start of HOx operations in 2005 (Gantzer et al. 2009b).

It should be acknowledged that while the use of HOx to improve water quality has been established (McGinnis et al. 2002; Beutel 2003; Singleton et al. 2006), the effect of HOx may be relatively modest in comparison to ‘natural oxygenation’ caused by fall turnover (Steichen et al. 1979). Our results show that Fe and Mn were sufficiently suppressed and elevated hypolimnetic O<sub>2</sub> was maintained throughout summer stratification in 2008 (Fig. 5.12). However, Fe and particularly Mn increased as hypolimnetic O<sub>2</sub> decreased approaching fall turnover. Following turnover in mid-November 2008, hypolimnetic O<sub>2</sub> increased significantly while Fe and Mn dropped to minimum concentrations due to dilution via mixing of hypolimnion water (relatively low in O<sub>2</sub> and high in soluble species) and epilimnion water (relatively high in O<sub>2</sub> and low in soluble species); hence, the natural oxygenation effect of turnover is demonstrated. However, hypolimnetic concentrations of soluble species would have been substantially increased without summer oxygenation. Overall results from this study clearly show the beneficial effect that HOx can have on Fe and Mn during summer stratification when water quality typically decreases significantly as a result of seasonal anoxia and the subsequent release of reduced species from the sediment (Davison et al. 1982).

## 5.5 Conclusions

This study shows that HOx can be used to improve drinking water quality by decreasing source water Fe and Mn levels. Soluble Fe was controlled relatively easily as long as minimal levels of O<sub>2</sub> remained near the sediment; however, soluble Mn levels in the lower hypolimnion increased significantly when the HOx was not in operation and the sediment became anoxic. Although  $J_{\text{Fe}}$  and  $J_{\text{Mn}}$  were enhanced by HOx operation, results indicate biogeochemical cycling supported by elevated O<sub>2</sub> in the benthic region and in the sediment prevented released metals from reaching the bulk water. Oxygenation techniques using artificial destratification to increase hypolimnetic O<sub>2</sub> may not maintain an oxic zone that facilitates biogeochemical cycling as close to the sediment as HOx due to sediment resuspension effects (Gafsi et al. 2009). Increased amounts of Fe and Mn in the bulk sediment resulting from enhanced sedimentation were found to be retained in the sediment via HOx operation. Furthermore,  $J_{\text{Fe}}$  and  $J_{\text{Mn}}$  were estimated to constitute up to 15% of  $J_{\text{O}_2}$  during summer stratification. While only Fe and Mn were evaluated in this study, additional species (e.g., nitrite, methane) may also contribute to sediment O<sub>2</sub> uptake (Maerki et al. 2009). Our results emphasize that O<sub>2</sub> allocated for the oxidation of enhanced fluxes of reduced species and subsequent incorporation of these species into the sediment must be taken into account for successful HOx operation.

Ultimately, source water levels of Fe and Mn were shown to be substantially reduced by HOx operation (Fig. 5.3-5.5, 5.8, 5.9), thus decreasing treatment required at the plant. This work (Ch. 5) and the studies on  $J_{\text{O}_2}$  (Ch. 4) and the CCR sediment microbial community (Ch. 6) were intended as scientific and conceptual evaluations of the effect of HOx on sediment-water fluxes and water quality. The companion works by Gantzer et al. (2009a,b) were intended to serve as a more applied guide to HOx operation. Our combined works, which comprehensively assess oxygenation from both a sediment and source-water perspective, will be used to optimize CCR HOx operations and source-water quality and should also be of benefit to managers of similar lake and reservoir systems.

## 5.6 Acknowledgements

The authors thank Elizabeth Rumsey, Kevin Elam, and the staff at Western Virginia Water Authority who offered invaluable support in the field and with laboratory samples. We also thank Robert Rebodos for assistance with ferrozine analyses and to Peter Berg for valuable discussion. We acknowledge financial support from the National Science Foundation (NSF IGERT Program) and the Western Virginia Water Authority. The research described in this paper was partially funded by the United States Environmental Protection Agency (EPA) under the Science to Achieve Results (STAR) Graduate Fellowship Program. EPA has not officially endorsed this publication and the views expressed herein may not reflect the views of the EPA.

## 5.7 References

- Achman, D. R., B. J. Brownawell, and L. Zhang. 1996. Exchange of polychlorinated biphenyls between sediment and water in the Hudson River Estuary. *Estuaries* **19**: 950-965.
- Adams, D. D., G. Matisoff, and W. J. Snodgrass. 1982. Flux of reduced chemical constituents (Fe<sup>2+</sup>, Mn<sup>2+</sup>, NH<sub>4</sub><sup>+</sup>, and CH<sub>4</sub>) and sediment oxygen demand in Lake Erie. *Hydrobiologia* **92**: 405-414.
- Balzer, W. 1982. On the distribution of iron and manganese at the sediment / water interface: thermodynamic versus kinetic control. *Geochem. Cosmochim. Acta* **46**: 1153-1161.
- Belzile, N., J. Pizarro, M. Filella, and J. Buffle. 1996. Sediment diffusive fluxes of Fe, Mn, and P in a eutrophic lake: contribution from lateral vs bottom sediments. *Aquat. Sci.* **58**: 327-354.
- Beutel, M. W. 2003. Hypolimnetic anoxia and sediment oxygen demand in California drinking water reservoirs. *Lake and Reservoir Mgmt.* **19**: 208-221.
- Beutel, M. W., A. J. Horne, W. D. Taylor, R. F. Losee, and R. D. Whitney. 2008. Effects of oxygen and nitrate on nutrient release from profundal sediments of a large, oligo-mesotrophic reservoir, Lake Mathews, California. *Lake and Reservoir Mgmt.* **24**: 18-29.
- Berg, P., D. Swaney, S. Rysgaard, B. Thamdrup, and H. Fossing. 2007. A fast numerical solution to the general mass-conservation equation for solutes and solids in aquatic sediments. *J. Mar. Res.* **65**: 317-343.

- Bouldin, D. R. 1968. Models for describing the diffusion of oxygen and other mobile constituents across the mud-water interface. *J. Ecol.* **56**: 77-87.
- Brand, A., C. Dinkel, and B. Wehrli. 2009. Influence of the diffusive boundary layer on the solute dynamics in the sediments of a seiche-driven lake: a model study. *J. Geophys. Res.* **114**: G01010, doi:10.1029/2008JG000755.
- Bryant, L. D., C. Lorrai, D. F. McGinnis, A. Brand, A. Wüest, and J. C. Little. 2010. Variable sediment oxygen uptake in response to dynamic forcing. *Limnol. Oceanogr.* **55**: 950-964.
- Carpenter, R. H., J. M. Fagan, and H. Wedow. 1971. Evidence on the age of barite, zinc, and iron mineralization in the lower Paleozoic rocks of east Tennessee. *Econ. Geol.* **66**: 792-798.
- Chiswell, B., and M. Zaw. 1991. Lake destratification and speciation of iron and manganese. *Environ. Monit. Assess.* **19**: 433-447.
- Clesceri, L. S., A. E. Greenberg, and A. D. Eaton. 1998. Standard methods for the examination of water and wastewater, 20<sup>th</sup> ed. pp. 3-2 and 3-44. American Public Health Association.
- Crittenden, J. C., Trussell, R. R., D. W. Hand, K. J. Howe, and G. Tchobanoglous. 2005. *Water Treatment: Principles and Design*. John Wiley & Sons, Inc.
- Davison, W. 1982. Transport of iron and manganese in relation to the shapes of their concentration-depth profiles. *Hydrobiologia* **92**: 463-471.
- Davison, W. 1985. Conceptual models for transport at a redox boundary. *In*: Stumm, W. [Ed.], *Chemical Processes in Lakes*. John Wiley & Sons.
- Davison, W. 1993. Iron and manganese in lakes. *Ear. Sci. Rev.* **34**: 119-163.
- Davison, W., C. Woof, and E. Rigg. 1982. The dynamics of iron and manganese in a seasonally anoxic lake; direct measurement of fluxes using sediment traps. *Limnol. Oceanogr.* **27**: 987-1003.
- Duckworth, O. W., J. R. Bargar, and G. Sposito. 2009. Coupled biogeochemical cycling of iron and manganese as mediated by microbial siderophores. *Biometals* **22**:605-613.
- EPA (Environmental Protection Agency). 1988. Determination of total organic carbon in sediment (Lloyd Khan method). EPA Region II.  
[www.dnr.mo.gov/ENV/hwp/docs/part4sec5\\_lloydkahn\\_tocmethod.pdf](http://www.dnr.mo.gov/ENV/hwp/docs/part4sec5_lloydkahn_tocmethod.pdf)
- EPA. 1996. Test methods for evaluating solid waste: physical/chemical methods, SW 846. Method 6010B: Inductively coupled plasma-atomic emission spectrometry, Rev. 2.  
[www.epa.gov/epaoswer/hazwaste/test/main.htm](http://www.epa.gov/epaoswer/hazwaste/test/main.htm)

- Fossing, H., P. Berg, B. Thamdrup, S. Rysgaard, H. M. Sørensen, and K. Nielsen. 2004. A model set-up for an oxygen and nutrient flux model for Aarhus Bay (Denmark). NERI Technical Report No. 483. National Environmental Research Institute, Denmark. [www.dmu.dk](http://www.dmu.dk)
- Gächter, R., and B. Wehrli. 1998. Ten years of artificial mixing and oxygenation: no effect on the internal phosphorus loading of two eutrophic lakes. *Environ. Sci. Technol.* **32**: 3659-3665.
- Gafsi, M., A. Kettab, S. Benmamar, and S. Benziada. 2009. Comparative studies of the different mechanical oxygenation systems used in the restoration of lakes and reservoirs. *J. Food Agric. Environ.* **7**: 815-822.
- Gantzer, P. A., L. D. Bryant, and J. C. Little. 2009a. Effect of hypolimnetic oxygenation on oxygen depletion rates in two water-supply reservoirs. *Water Res.* **43**:1700-1710.
- Gantzer, P. A., L. D. Bryant, and J. C. Little. 2009b. Controlling soluble iron and manganese in a water-supply reservoir using hypolimnetic oxygenation. *Water Res.* **43**: 1285-1294.
- Glud, R. N., P. Berg, H. Fossing, and B. B. Jørgensen. 2007. Effect of the diffusive boundary layer on benthic mineralization and O<sub>2</sub> distribution: A theoretical model analysis. *Limnol. Oceanogr.* **52**: 547-557.
- Greenberg, A. E., L. S. Clesceri, and A. D. Eaton. 1992. Standard methods for the examination of water and wastewater. Inductively coupled plasma-atomic emission spectrometry, Method SM2540B, 18th ed. American Public Health Association.
- Hesslein, R. 1976. An in-situ sampler for close interval porewater studies. *Limnol. Oceanogr.* **21**: 912-914.
- Higashino, M., C. J. Gantzer, and H. G. Stefan. 2004. Unsteady diffusional mass transfer at the sediment/water interface: Theory and significance for SOD measurement. *Water Res.* **38**: 1-12.
- Johnson, C. A., M. Ulrich, L. Sigg, and D. M. Imboden. 1991. A mathematical model of the manganese cycle in a seasonally anoxic lake. *Limnol. Oceanogr.* **36**: 1415-1426.
- Jørgensen, B. B., and B. P. Boudreau. 2001. Diagenesis and sediment-water exchange, p. 211-244. *In* B. P. Boudreau and B. B. Jørgensen [eds.], *The benthic boundary layer: transport processes and biogeochemistry*. Oxford University Press.
- Jørgensen, B. B., and N. P. Revsbech. 1985. Diffusive boundary layers and the oxygen uptake of sediments and detritus. *Limnol. Oceanogr.* **30**: 111-122.

- Lavery, P., C. Oldham, and M. Ghisalberti. 2001. The use of Fick's First Law for predicting porewater nutrient fluxes under diffusive conditions. *Hydrol. Process.* **15**: 2435-2451.
- Liboriussen, L., M. Søndergaard, E. Jeppesen, I. Thorsgaard, S. Grünfeld, T. S. Jakobsen, and K. Hansen. 2009. Effects of hypolimnetic oxygenation on water quality: results from five Danish lakes. *Hydrobiologia* 625: 157-172.
- Lienemann, C.-P., M. Monnerat, J. Dominik, and D. Perret. 1999. Identification and stoichiometric iron-phosphorous colloids produced in a eutrophic lake. *Aquat. Sci.* **61**: 133-149.
- Lorke, A., B. Müller, M. Maerki, and A. Wüest. 2003. Breathing sediments: The control of diffusive transport across the sediment-water interface by periodic boundary-layer turbulence. *Limnol. Oceanogr.* **46**: 2077-2085.
- Maerki, M., B. Müller, C. Dinkel, and B. Wehrli. 2009. Mineralization pathways in lake sediments with different oxygen and organic carbon supply. *Limnol. Oceanogr.* **54**: 428-438.
- Matthews, D. A., and S. W. Effler. 2006. Assessment of long-term trends in the oxygen resources of a recovering urban lake, Onondaga Lake, New York. *Lake and Reservoir Mgmt.* **22**:19-32.
- Matzinger, A., B. Müller, P. Niederhauser, M. Schmid, and A. Wüest. 2010. Hypolimnetic oxygen consumption by sediment-based reduced substances in former eutrophic lakes. Unpubl.
- McGinnis, D. F., A. Lorke, A. Wüest, A. Stöckli, and J. C. Little. 2004. Interaction between a bubble plume and the near field in a stratified lake. *Water Resour. Res.* **40**: W10206, doi:10.1029/2004WR003038.
- Mobley, M. H., G. E. Hauser, D. F. McGinnis, and R. J. Ruane. 1997. Diffuser system modeling and design for dissolved oxygen enhancement of reservoirs and releases. Proceedings of the 27th IAHR Congress, San Francisco, CA.
- Moore, B. C. 2003. Downflow bubble contact aeration technology (Speece Cone) for sediment oxygenation. Proceedings of the Second International Conference on Remediation of Contaminated Sediments [eds. M. Pellei and A. Porta].
- Moore, B. C., P. H. Chen, W. H. Funk, and D. Yonge. 1996. A model for predicting lake sediment oxygen demand following hypolimnetic aeration. *Wat. Resour. Bull.* **32**:1-9.

- Mussman, W. J., and J. F. Reid. 1986. Sedimentology and development of a passive- to convergent-margin unconformity: Middle Ordovician Knox unconformity, Virginia Appalachians. *Geol. Soc. Am. Bull.* **97**: 282-295.
- Nealson, K. H., B. M. Tebo, and R. A. Rosson. 1988. Occurrence and mechanisms of microbial oxidation of manganese. *Adv. Appl. Microbiol.* **33**: 279-318.
- Santschi, P., P. Höhener, G. Benoit, and M. Buchholtz-ten Brink. 1990. Chemical processes at the sediment-water interface. *Mar. Chem.* **30**: 269-315.
- Schaller, T., H. C. Moor, and B. Wehrli. 1997. Reconstructing the iron cycle from the horizontal distribution of metals in the sediment of Baldeggersee. *Aquat. Sci.* **59**: 326-344.
- Schaller, T., and B. Wehrli. 1997. Geochemical-focusing of manganese in lake sediments – an indicator of deep-water oxygen conditions. *Aquat. Geochem.* **2**: 359-378.
- Scholkovitz, E. 1985. Redox-related geochemistry in lakes; alkali metals, alkaline-earth elements, and  $^{137}\text{Cs}$ . *In*: Stumm, W. [ED.], *Chemical Processes in Lakes*. John Wiley & Sons.
- Singleton, V. L., and J. C. Little. 2006. Designing hypolimnetic aeration and oxygenation systems: a review. *Environ. Sci. Technol.* **40**: 7512-7520.
- Singleton, V. L., P. A. Gantzer, and J. C. Little. 2007. Linear bubble plume model for hypolimnetic oxygenation: full-scale validation and sensitivity analysis. *Water Resour. Res.* **43**(2): W02405.
- Sobek, S., E. Durisch-Kaiser, R. Zurbrügg, N. Wongfun, M. Wessels, N. Pasche, and B. Wehrli. 2009. Organic carbon burial efficiency in lake sediments controlled by oxygen exposure time and sediment source. *Limnol. Oceanogr.* **54**: 2243-2254.
- Steichen, J. M., J. E. Garton, and C. E. Rice. 1979. The effect of lake destratification on water quality. *Jour. AWWA* **71**: 219-225.
- Stose, G. W., H. D. Miser, F. J. Katz, and D. F. Hewitt. 1919. Manganese deposits along the west foot of the Blue Ridge in Virginia. Virginia Geological Survey Series of Reports. Bulletin No. XVII.
- Stookey, L. L. 1970. Ferrozine – a new spectrophotometric reagent for iron. *Anal. Chem.* **42**: 779-781.
- Thompson, A., O. A. Chadwick, S. Boman, and J. Chorover. 2006. Colloid mobilization during soil iron redox oscillations. *Environ. Sci. Technol.* **40**: 5743-5749.

- Urban, N. R., C. Dinkel, and B. Wehrli. 1997. Solute transport across the sediment surface of a eutrophic lake: I. Porewater profiles from dialysis samplers. *Aquat. Sci.* **59**: 1-25.
- Wüest, A., N. H. Brooks, and D. M. Imboden. 1992. Bubble plume modeling for lake restoration. *Wat. Resour. Res.* **28**: 3235-3250.
- Yagi, A. 1996. Manganese flux associated with dissolved and suspended manganese forms in Lake Fukami-Ike. *Wat. Res.* **30**: 1823-1832.
- Zaw, M., and B. Chiswell. 1999. Iron and manganese dynamics in lake water. *Water Res.* **33**: 1900-1910.
- Zhang, H, W. Davison, and C. Ottley. 1999. Remobilisation of major ions in freshly deposited lacustrine sediment at overturn. *Aquat. Sci.* **61**: 354-361.

Table 5.1. Estimation of proportion of measured sediment O<sub>2</sub> uptake rate (J<sub>O<sub>2</sub></sub>; based on microprofile data) utilized for oxidation of iron (Fe) and manganese (Mn) fluxes (J<sub>Fe</sub> and J<sub>Mn</sub>; based on peeper data). J<sub>Fe</sub> and J<sub>Mn</sub> were converted to theoretical J<sub>O<sub>2</sub></sub> (J<sub>O<sub>2</sub>-Fe</sub> and J<sub>O<sub>2</sub>-Mn</sub>) using stoichiometry defined by Eq. 5.2 and 5.3. The sum of J<sub>O<sub>2</sub>-Mn</sub> and J<sub>O<sub>2</sub>-Fe</sub> yields the total theoretical J<sub>O<sub>2</sub></sub> (J<sub>O<sub>2</sub>-T</sub>) allocated to oxidation of reduced Mn and Fe released from the sediment.

Date	Season	Measured J <sub>Mn</sub>	Theoretical J <sub>O<sub>2</sub>-Mn</sub>	Measured J <sub>Fe</sub>	Theoretical J <sub>O<sub>2</sub>-Fe</sub>	Total theoretical J <sub>O<sub>2</sub>-T</sub>	Measured J <sub>O<sub>2</sub></sub>
9/22/05	fall	0.04	0.02	0.28	0.07	0.09	1.8
10/13/05	fall	0.30	0.15	0.42	0.10	0.25	10.4
11/3/05	fall	0.25	0.13	0.36	0.09	0.22	10.0
1/13/06	winter	0.34	0.17	1.51	0.38	0.55	8.2
2/14/06	winter	0.28	0.14	1.62	0.41	0.55	10.1
3/23/06	spring	0.32	0.16	1.32	0.33	0.49	11.3
4/19/06	spring	0.23	0.11	0.53	0.13	0.25	10.8
5/31/06	spring	0.31	0.16	0.63	0.16	0.31	7.9
7/5/06	summer	0.22	0.11	0.47	0.12	0.23	0.0
8/9/06	summer	0.18	0.09	0.40	0.10	0.19	3.9
8/28/06	summer	0.37	0.19	0.61	0.15	0.34	3.7
10/18/06	fall	0.48	0.24	0.65	0.16	0.40	3.7
12/5/06	winter	0.29	0.15	0.44	0.11	0.26	21.6
4/19/07	spring	0.20	0.10	0.15	0.04	0.14	3.0
5/2/07	spring	0.02	0.01	0.11	0.03	0.04	3.4
5/14/07	spring	0.12	0.06	0.59	0.15	0.21	3.2
6/11/07	summer	0.16	0.08	0.49	0.12	0.20	6.8
6/26/07	summer	0.29	0.15	0.84	0.21	0.36	3.9
7/9/07	summer	0.24	0.12	0.70	0.17	0.29	8.2
8/7/07	summer	0.17	0.09	0.51	0.13	0.21	4.9
6/15/08	summer	0.30	0.15	0.61	0.15	0.30	19.4
7/15/08	summer	0.61	0.31	0.82	0.21	0.52	15.5
8/12/08	summer	0.67	0.33	0.64	0.16	0.49	12.0
9/14/08	fall	0.42	0.21	0.46	0.11	0.32	6.8

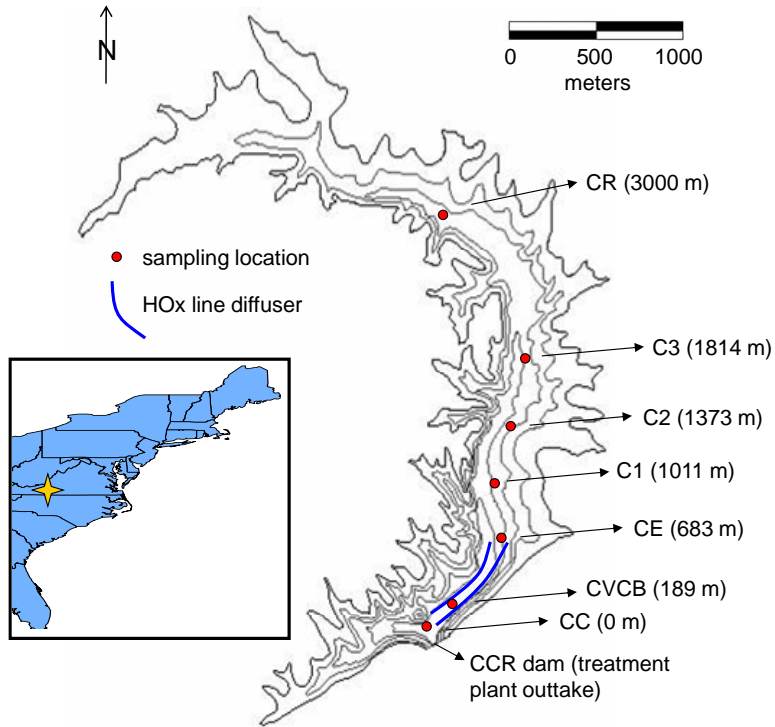


Figure 5.1. Map of Carvin's Cove Reservoir (CCR) showing locations of the seven sampling sites (CC, CVCB, CE, C1, C2, C3, and CR) and the hypolimnetic oxygenation system (HOx).

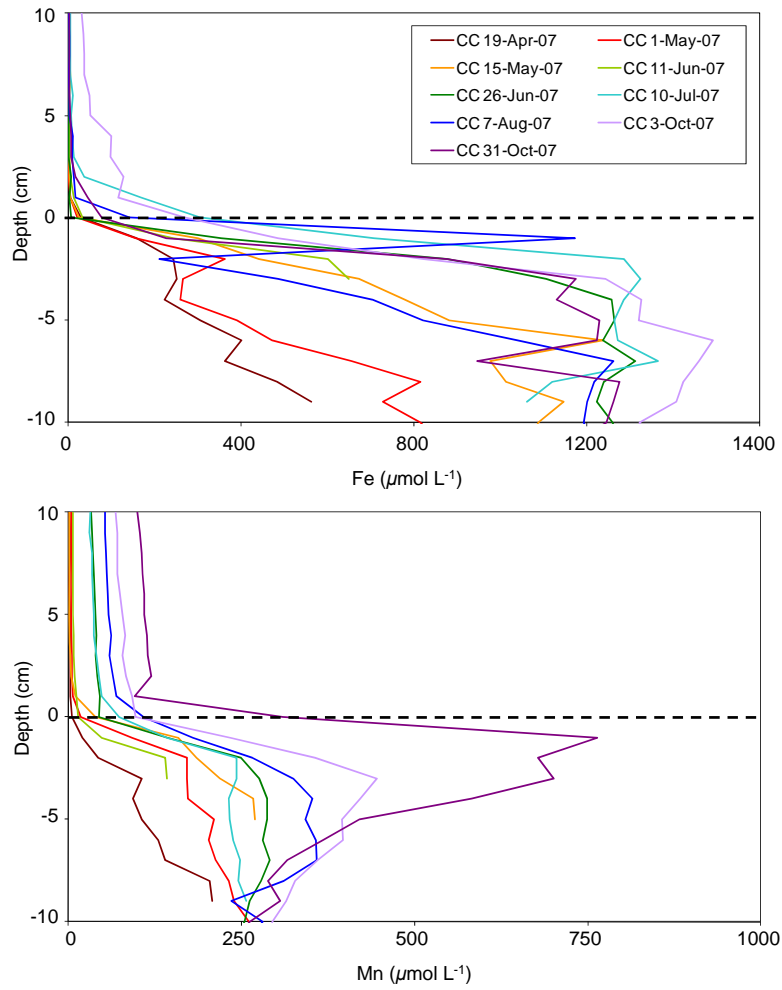


Figure 5.2. Profiles of soluble iron (Fe) and manganese (Mn) at the sediment-water interface (SWI) were obtained using in situ porewater analyzers (peepers). Data shown are from site CC during 2007 campaign.

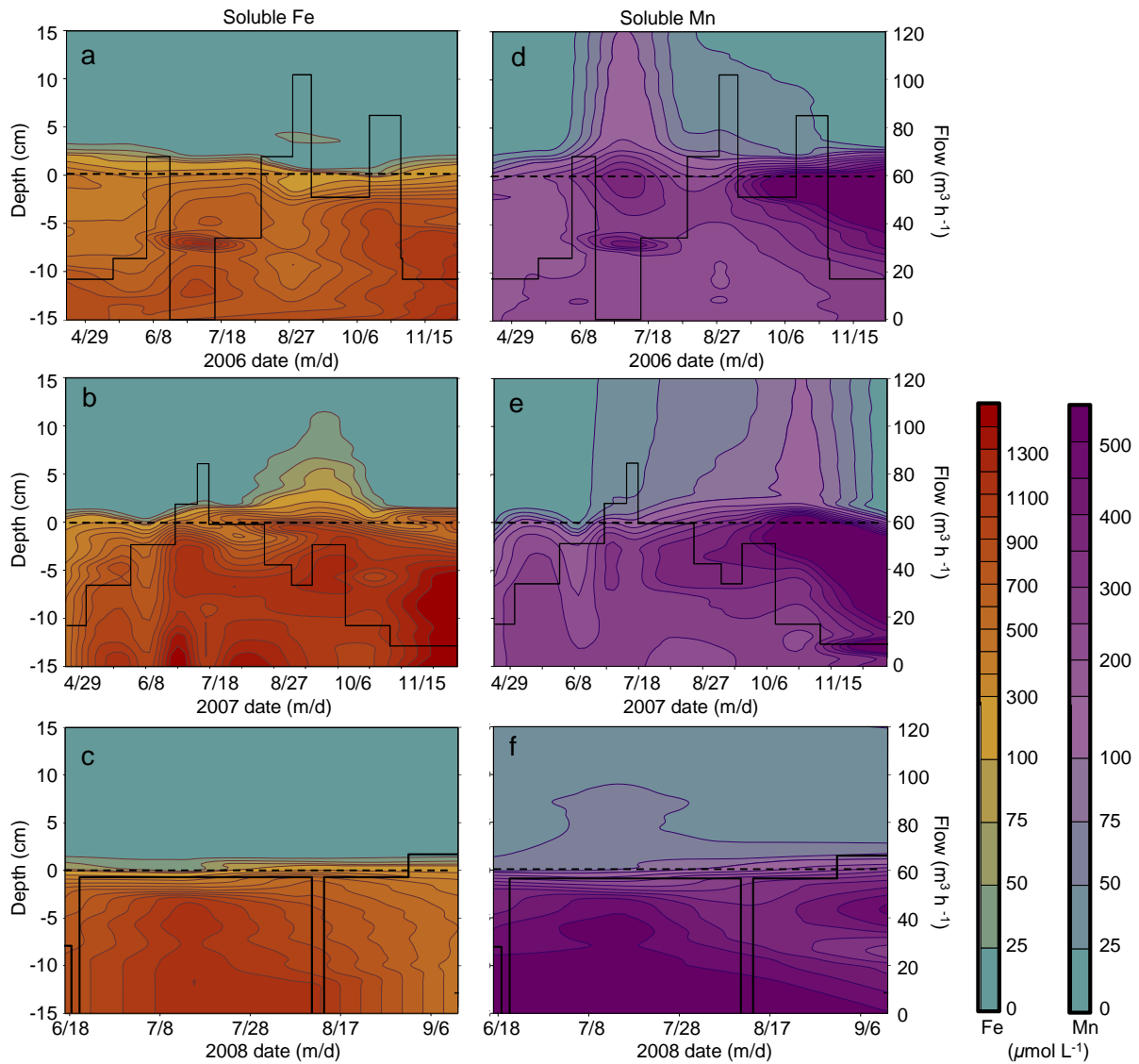


Figure 5.3. Contour plots based on peeper data obtained near the HOx at site CC in 2006 (a and d) and at site CVCB in 2007 (b and e) and 2008 (c and f). Corresponding variations in HOx flow are also shown. Analogous contour plots for site C3 (mid-reservoir) for the 2007 and 2008 campaigns are provided in Appendix B.2. Dashed line indicates SWI.

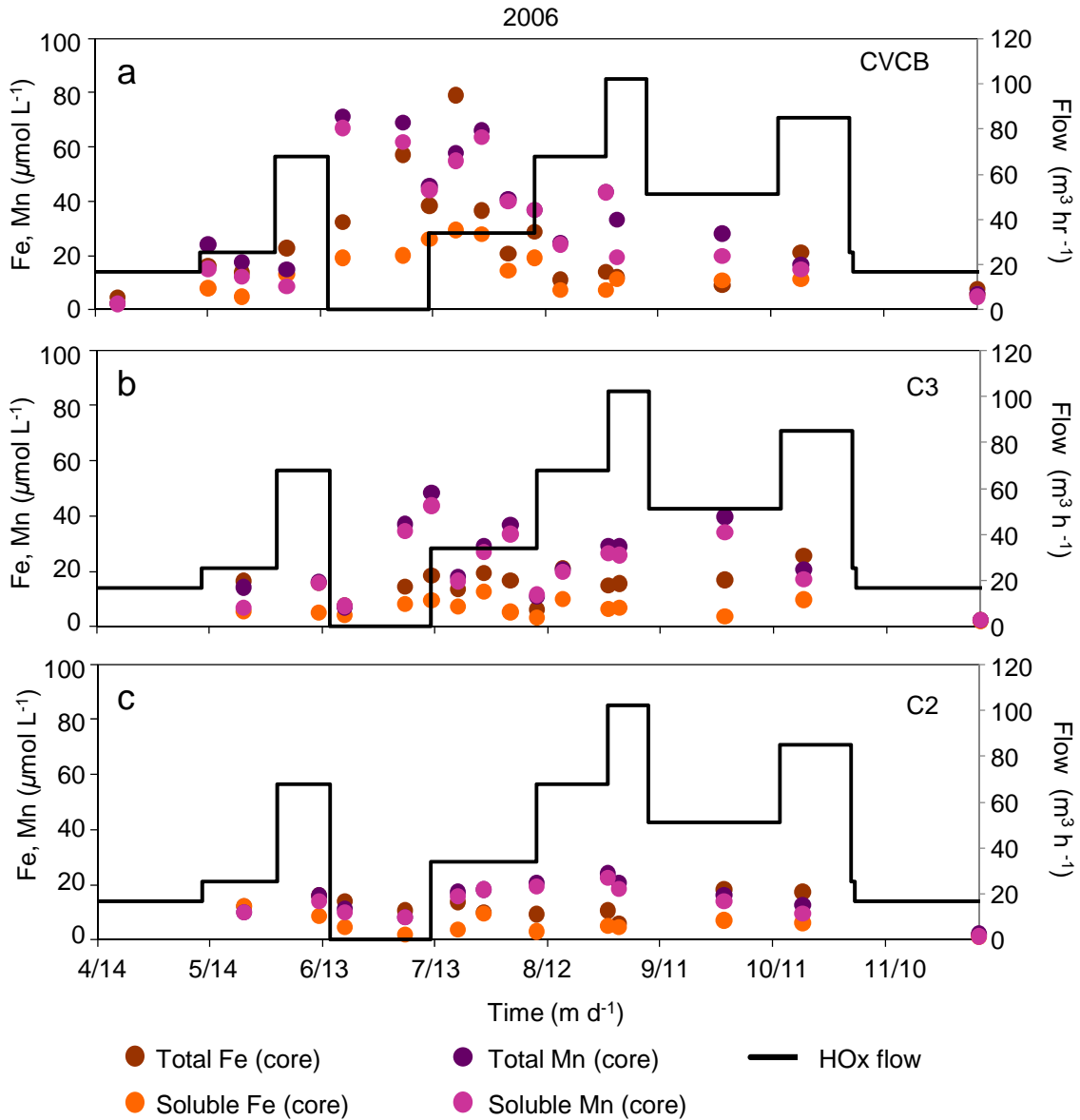


Figure 5.4. Total and soluble Fe and Mn data obtained from near-sediment core water samples collected throughout 2006 HOx operations. Samples were collected near the HOx (a; site CVCB) and mid-reservoir at sites C3 (b) and C2 (c). Analogous data for 2008 HOx operations are provided in Appendix B.3.

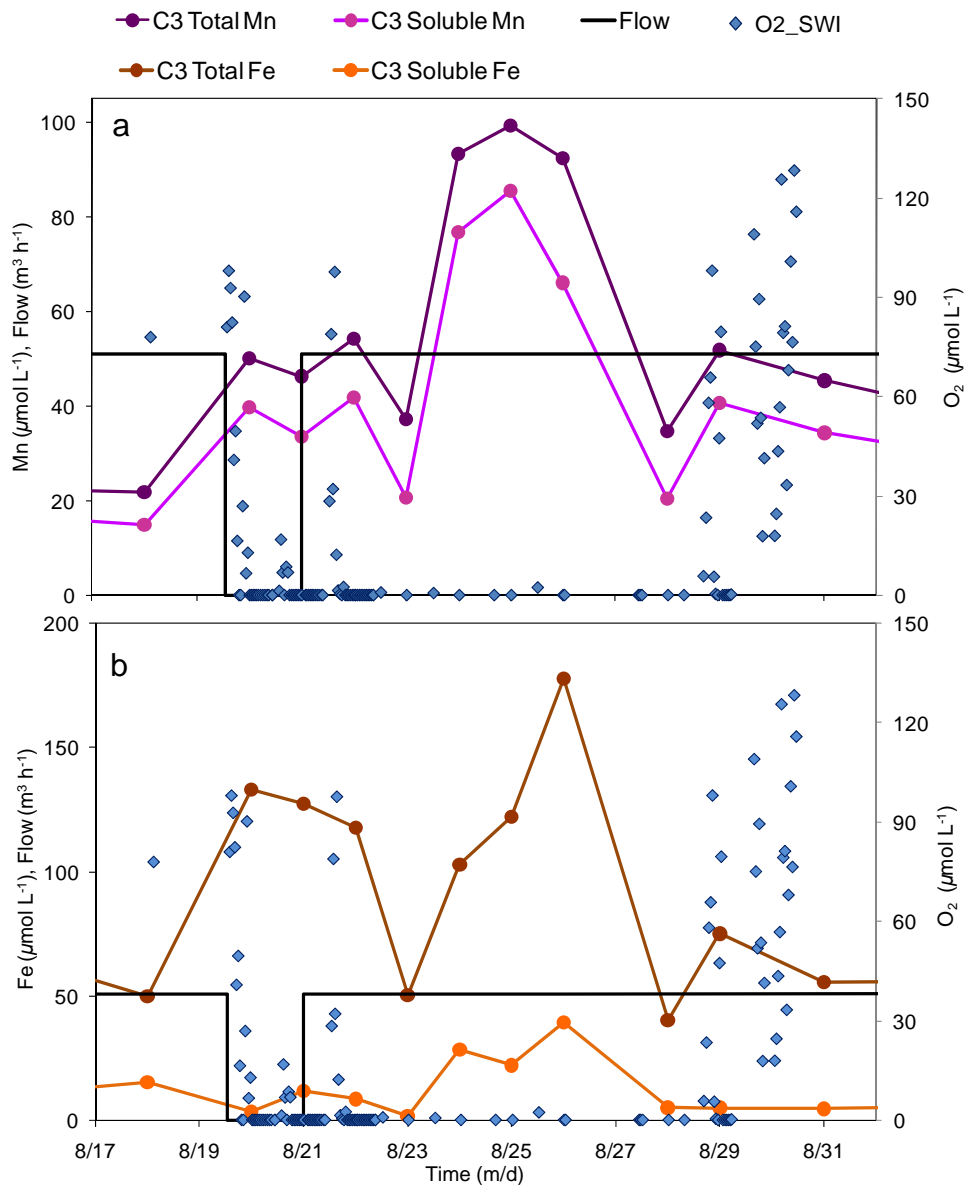


Figure 5.5. Correlation between near-sediment Fe and Mn levels (as characterized by sediment core water sample data), HOx flow, and dissolved oxygen (O<sub>2</sub>) levels at the SWI (as characterized by MP4 microprofile data) during the August 2008 campaign at C3. The proportion of total Mn in the soluble form is shown in (a) and corresponding Fe data are shown in (b).

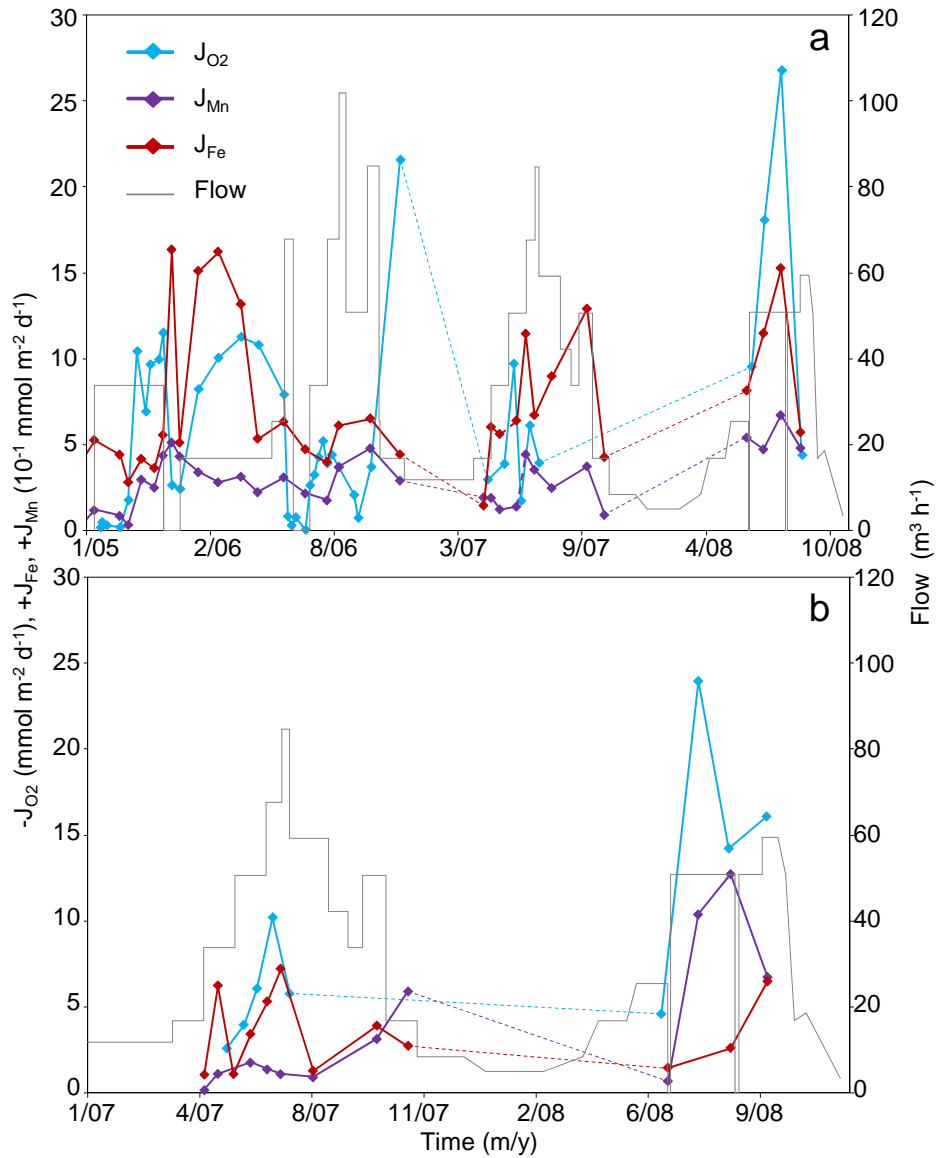


Figure 5.6. Time series of sediment O<sub>2</sub> uptake rate ( $J_{O_2}$ ), diffusive fluxes of soluble Fe and Mn ( $J_{Fe}$  and  $J_{Mn}$ , respectively) at the SWI, and HOx flow rate both near the HOx (a; site CVCB) and mid-reservoir (b; site C3). Dashed lines indicate periods between seasons of focused field sampling.

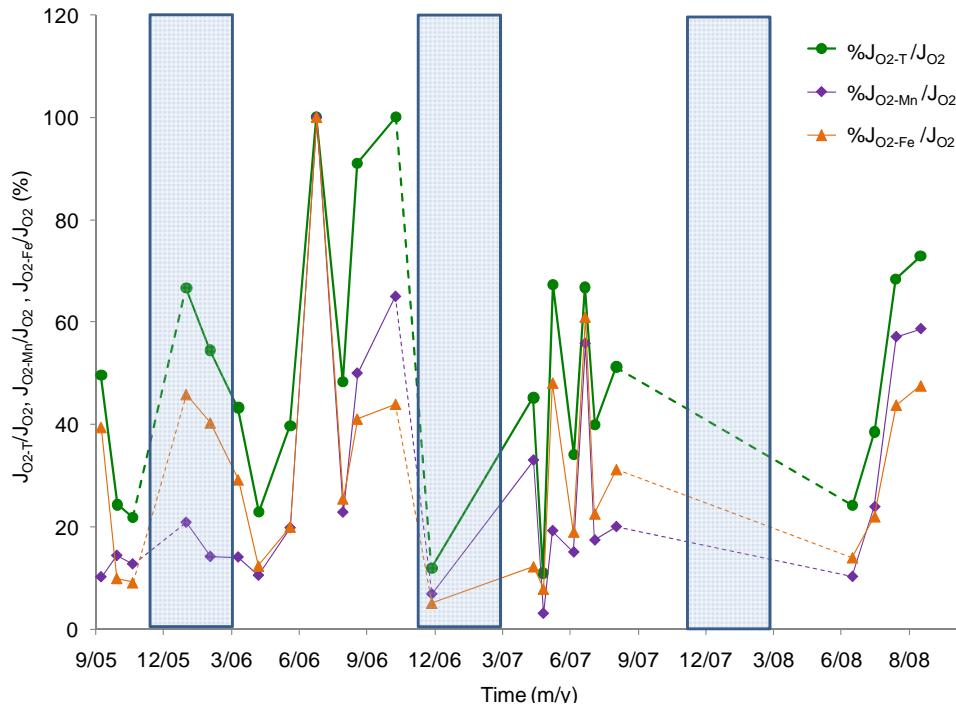


Figure 5.7. Evaluation of the proportion of measured  $J_{O_2}$  utilized for oxidation of reduced Fe and Mn (based solely on diffusive fluxes  $J_{Fe}$  and  $J_{Mn}$ ; the additional influence of microbial and surface-mediated processes were not taken into account). Results shown are presented percentages of theoretical  $J_{O_2}$  (based on stoichiometric conversion of  $J_{Fe}$  and  $J_{Mn}$ ) relative to measured  $J_{O_2}$ . The winter period (November thru March) is designated by blue shaded regions.

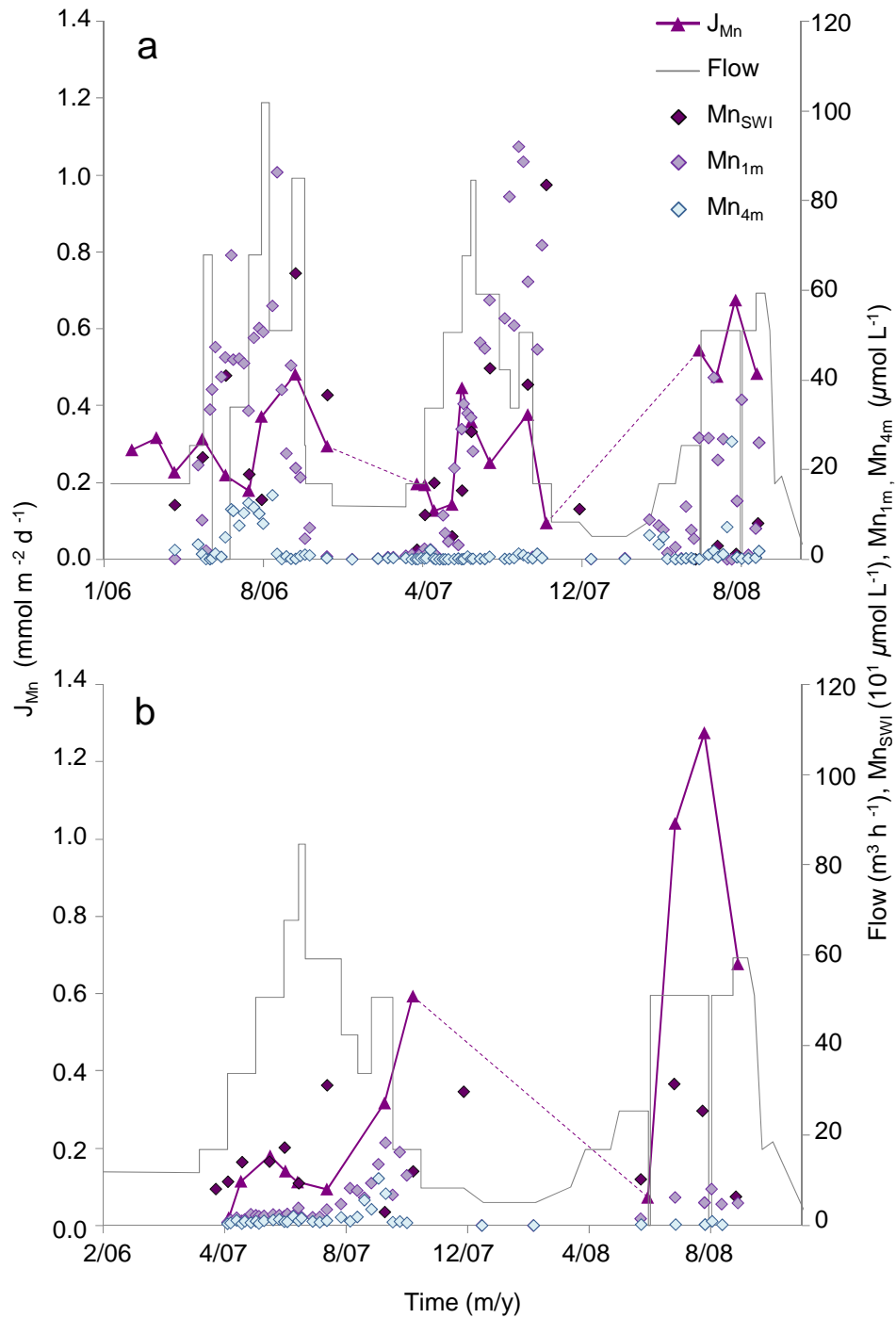


Figure 5.8. Correlation between  $J_{Mn}$ , HOx flow, and Mn concentrations directly at the SWI, 1 m above the sediment (benthic region), and 4 m above the sediment (mid-hypolimnion). Data obtained near the Hox are presented in (a) and mid-reservoir in (b). Dashed lines indicate periods between seasons of focused field sampling.

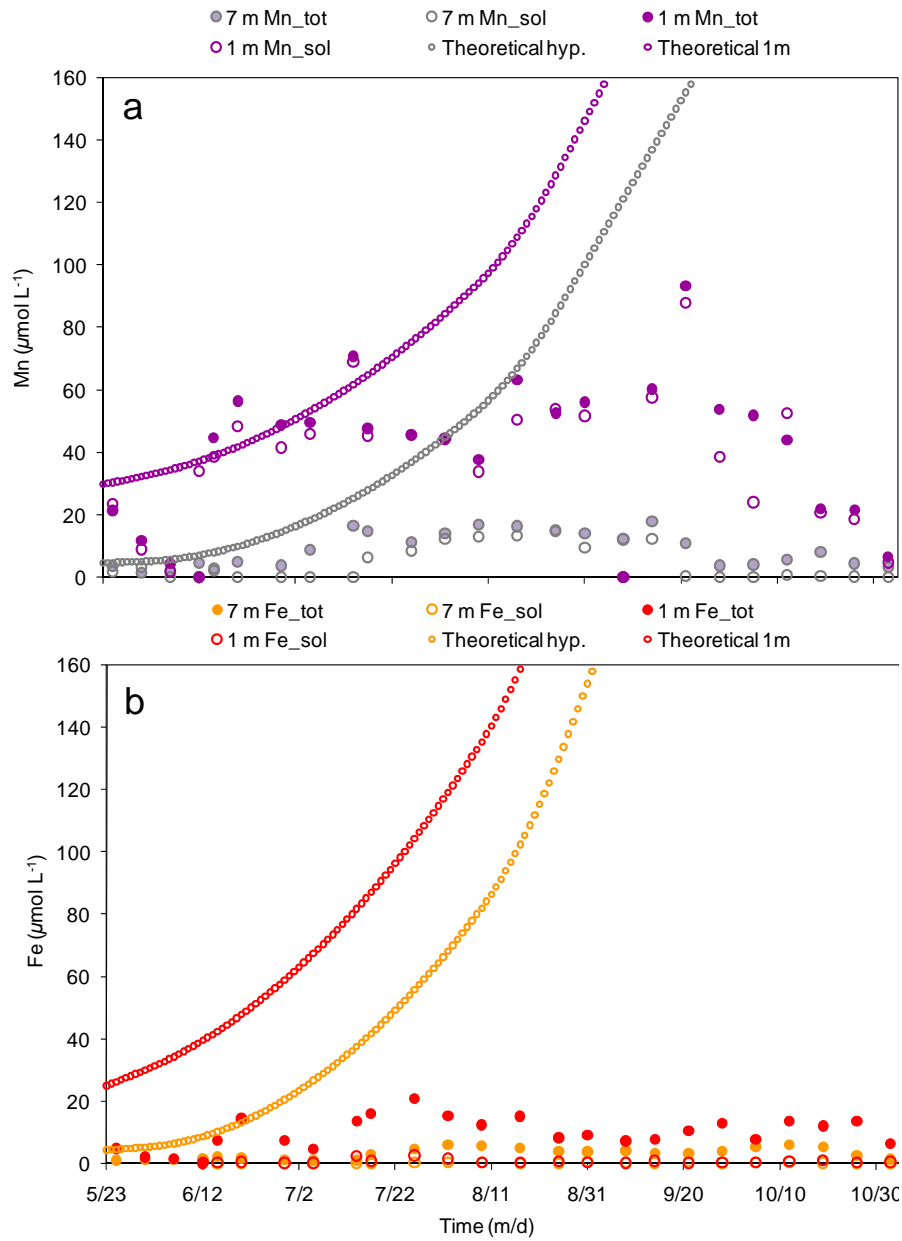


Figure 5.9. The effect of near-sediment biogeochemical cycling was evaluated using a mass balance based on  $J_{\text{Mn}}$  (a),  $J_{\text{Fe}}$  (b), and average volume of the benthic region (1m depth) and the average hypolimnion (7m depth).

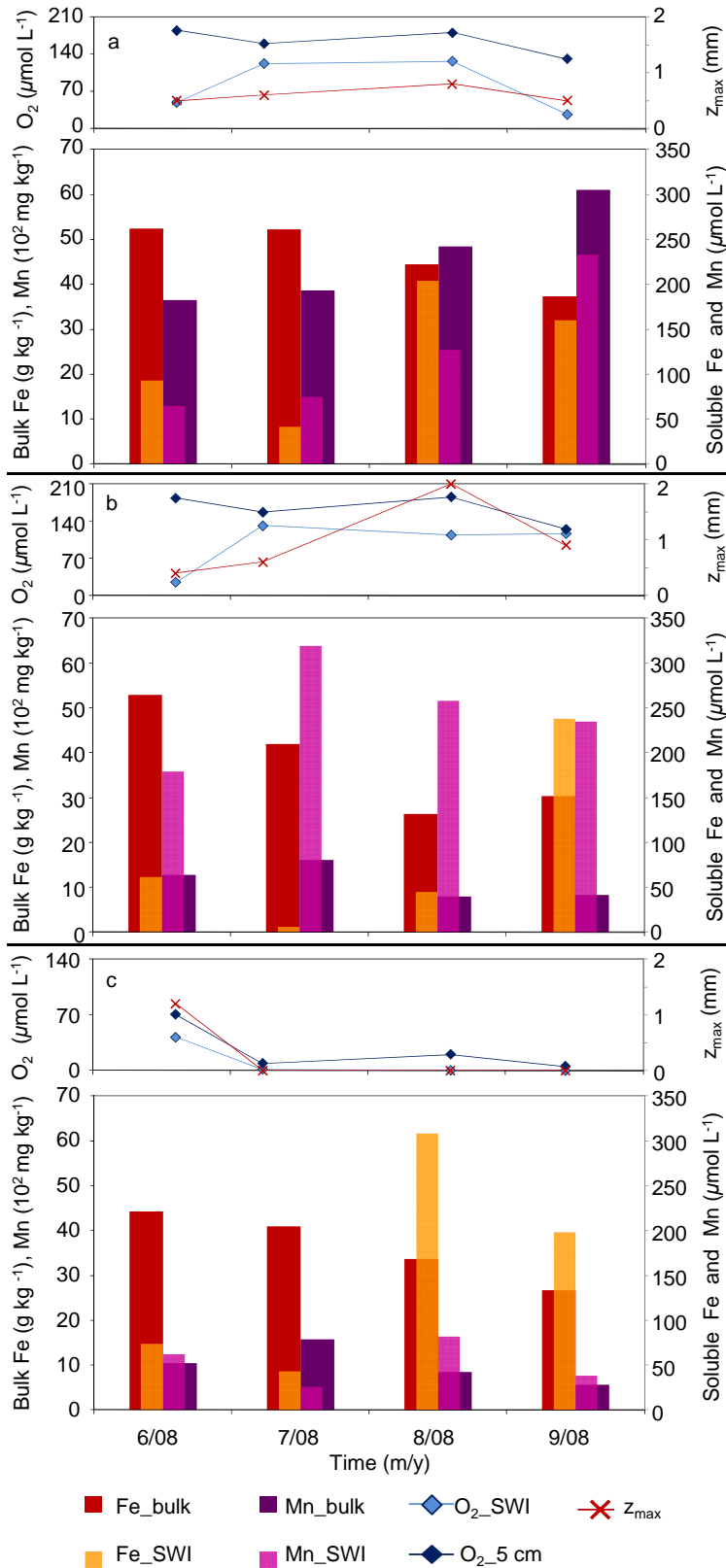


Figure 5.10. Bulk sediment total Fe and Mn data, soluble Fe and Mn concentrations at the SWI (peeper data), and corresponding sediment O<sub>2</sub> conditions as characterized by depth of the sediment oxidic zone (Z<sub>max</sub>) and O<sub>2</sub> concentration 5 cm above and directly at the SWI (microprofile data). Data obtained near the HOX (a; CVCB), mid-reservoir (b; C3), and from the back region (c; CR) during 2008 are compared.

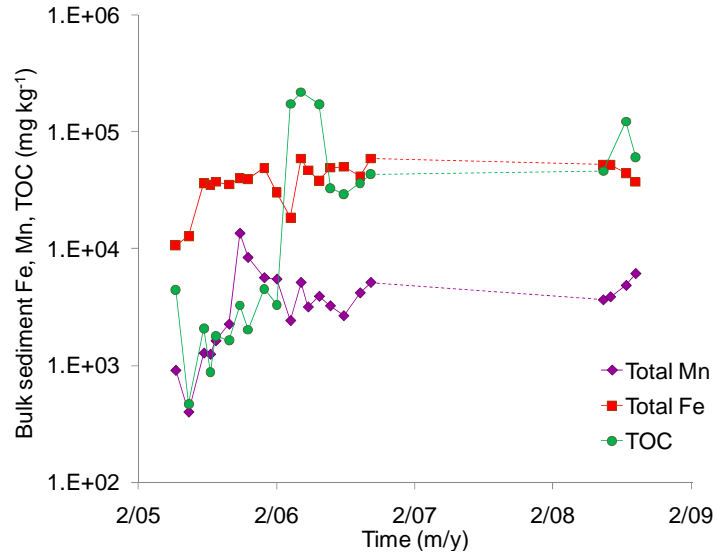


Figure 5.11. Time series of total organic carbon (TOC), total Fe, and total Mn in bulk sediment characterizing the near field region from before CCR HOx operations began in 2005 through 2008 (no data collected in 2007).

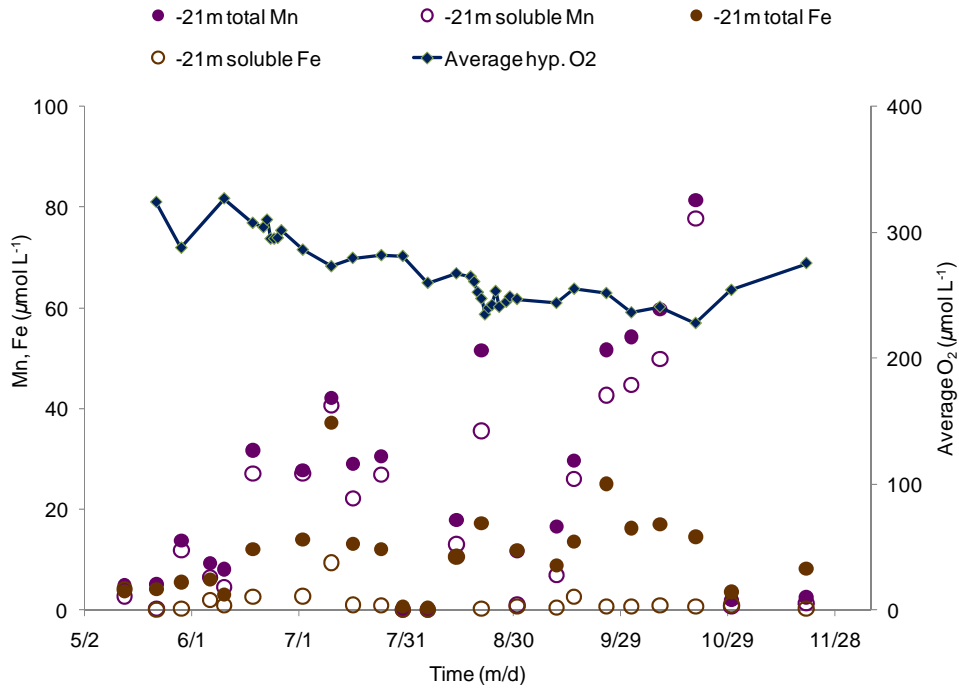


Figure 5.12. The influence of fall turnover as compared to HOx on total and soluble Fe and Mn concentrations in the lower hypolimnion and average hypolimnetic O<sub>2</sub>. Metals data are from hypolimnion water samples and O<sub>2</sub> data are from CTD (conductivity-temperature-O<sub>2</sub> as a function of depth) profiles obtained at site CC in 2008.

## **Chapter 6 – Variations in sediment microbial community structure in response to hypolimnetic oxygenation**

Bryant, Lee D.<sup>1</sup>, Helmut Bürgmann<sup>2</sup>, John C. Little<sup>1</sup>

1) Civil and Environmental Engineering, Virginia Polytechnic Institute and State University, Blacksburg, Virginia, United States of America (USA) 24060.

2) Eawag, Surface Waters - Research and Management, Kastanienbaum, Switzerland CH-6047.

### **6.1 Abstract**

It has been shown that microbially-mediated sediment-water metal fluxes often have a greater influence on water quality than allochthonous sources. As alternative approaches for improving water quality are being explored to address the emerging global water crisis, hypolimnetic oxygenation systems (HOx) are being increasingly used to elevate dissolved oxygen levels in the hypolimnion and suppress sediment-water fluxes of soluble metals (e.g., iron (Fe) and manganese (Mn)). However, while HOx-induced changes in sediment oxygen uptake and soluble metal fluxes have been evaluated in terms of chemical and physical processes in previous work, the influence of sediment microbial processes has not been assessed. Therefore, we performed a study focused on using microbial techniques to quantify changes in microbial community structure and corresponding biogeochemical cycling on a reservoir-wide scale as a function of HOx operations.

Results show a moderate phylogenetic trend in samples obtained near the HOx at the end of the 2006 oxygenation period. Increased nucleic acid concentration was also observed at this location throughout the 4-month campaign. A distinct trend in sediment microbial community structure in response to HOx operation was not found, however. This may be attributed to abiologic controls on Fe and Mn cycling, the adaptability of many bacteria to variations in prevalent electron acceptors, and/or background HOx effects. Nevertheless, insight was obtained on the relative significance of different environmental and geochemical variables on community composition. Our results suggest that while the sediment microbial community may not be drastically affected by HOx, some HOx-induced variation may occur (particularly in the near field following continuous oxygenation) that merits further investigation.

## 6.2 Introduction

In current microbial studies, environmental influences are often used as a factor for shaping microbial community structure and biogeochemical fluxes (Snoeyenbos-West et al. 2000; Stein et al. 2002; Yannarell and Triplett 2005). Significant environmental variability may be observed at the sediment-water interface (SWI) in aquatic systems due to the extremely steep gradients of chemical, physical, and microbial properties and subsequent biogeochemical transformation processes that occur in this region (Santschi 1990). Fluxes of reduced chemical species from the sediment can significantly reduce the quality of the overlying water and are one of the primary sources of reduced metals in the hypolimnion of stratified lakes and reservoirs (Zaw and Chiswell 1999; Zhang et al. 1999; Beutel 2003). It has been shown that microbially mediated sediment-water metal fluxes often have a greater influence on water quality than allochthonous sources (Christian and Lind 2007).

In light of the imminent water crisis and the acknowledged need for alternative approaches for improving water quality (NRC 2004), hypolimnetic oxygenation systems (HOx) are being more frequently used to improve water quality by increasing O<sub>2</sub> levels in the hypolimnion of stratified lakes and reservoirs. HOx systems have been shown to not only increase O<sub>2</sub> levels in the water column and at the SWI (Gantzer et al. 2009a; Ch. 4) but to also have significant influence on suppression of iron (Fe) and manganese (Mn) fluxes out of the sediment (Gantzer et al. 2009b; Ch. 5). However, while HOx-induced changes in sediment O<sub>2</sub> uptake and soluble metal fluxes have been evaluated in terms of chemical and physical processes by these studies and previous work (Beutel 2003), the influence of sediment microbial processes has not been assessed. It is established that sediment microbial communities can change in terms of both population size and structure as a function of sediment O<sub>2</sub> availability (House 2003). Thus, the effect of HOx-induced variation in sediment microbial community structure and corresponding biologically controlled redox processes may be significant. Furthermore, while metal cycling (particularly Mn) is frequently controlled by sediment microbial processes, very little is known about the actual physiology and metabolic diversity in sediment microbial communities (DiChristina and Delong 1993; Stein et al. 2001; Stein et al. 2002). We therefore

conducted a study using microbial techniques to relate changes in microbial community structure on a reservoir-wide scale to HOx operations.

### **6.3 Materials and procedures**

**6.3.1 Study site and instrumentation** – An HOx was installed in Carvin’s Cove Reservoir (CCR), one of the primary drinking-water-supply reservoirs for Roanoke, Virginia, in 2005 by the Western Virginia Water Authority. Throughout 2006 CCR HOx operations, sediment cores were obtained at sites CC, CVCB, CE, and C3 ranging from directly alongside the HOx to ~2,000 m upstream from the HOx (Fig. 6.1). Samples were obtained at all four sample sites on four dates covering a range of HOx flow rates to establish a network of samples characterizing the influence of the HOx on a reservoir-wide basis (Fig. 6.1, 6.2). As shown by HOx flow rates and microbial sampling dates for 2006 in Fig. 6.2, sediment samples were obtained during both anoxic periods after the HOx had been turned off and also oxic periods after continuous oxygenation. Following the sampling method detailed in Ch 5, sediment cores were obtained using a Uwitec corer. Core sub-samples (~12 mL) were collected via sampling with a Uwitec core-cutter as follows: 0-2 mm, 2-4 mm, 4-6 mm, and 1-1.2 cm relative to the sediment surface (SWI = 0 mm; Table 6.1). Each sub-sample was subsequently divided into three ~4 mL subsamples. Sub-samples were immediately placed in sterile glass bottles, sealed, and frozen at -80°C until analysis (excluding shipment (on ice) to Eawag, the institute where microbial work was performed).

**6.3.2 Analytical methods** – Nucleic acids were extracted from CCR sediment samples and then evaluated using a PicoGreen (Invitrogen Quant-iT) quantification to assess DNA concentration. Polymerase chain reaction (PCR) amplification was performed on extracted nucleic acid samples to obtain a high number of copies of a defined piece of ribosomal RNA (rRNA) gene which is an established phylogenetic marker (Fisher and Triplett 1999). PCR products were then assessed using ribosomal intergenic spacer analysis (RISA) to obtain a fingerprint of the sediment microbial community structure. The presence of Mn-oxidizing bacteria in CCR sediment was evaluated using the Leukoberbelin Blue (LBB) method (Tebo et

al. 2007). Detailed procedures for the microbial techniques used are provided below and in Appendix C.

*6.3.2.1 Nucleic acid extraction from CCR sediment* – Nucleic acids were extracted from sediment samples following the method of Bürgmann et al. (2001) and the protocol included in Appendix C.1. Approximately 0.5 g of each sediment sample (Table 6.1) was used for extraction. Nucleic acid extracts were stored at -20°C prior to subsequent PicoGreen quantification and PCR and RISA analyses.

*6.3.2.2 DNA quantification with PicoGreen* – Extracted nucleic acid concentrations were quantified using a PicoGreen quantification (Appendix C.2) based on the Quant-it dsDNA quantitation kit (Invitrogen P7589). The purity of the extracted DNA was assessed spectrophotometrically from the absorbance ratio at 260 and 280 nm (Sigler et al. 2002). Nucleic acid samples were diluted to concentrations of 5, 10, and 20 ng  $\mu\text{L}^{-1}$  for PCA and RISA analyses.

*6.3.2.3 Nucleic acid amplification via PCR* – Amplification of 16S ribosomal RNA gene fragments was performed using Touchdown PCR (Appendix C.3; Stein et al. 2001; Sigler et al. 2002) with universal bacterial-specific primers (forward primer 27f and reverse primer 1492r; Stein et al. 2001). As defined in Appendix C.3, the PCR reaction mix consisted of 418  $\mu\text{L}$  H<sub>2</sub>O, 65  $\mu\text{L}$  PCR buffer, 78  $\mu\text{L}$  MgCl<sub>2</sub>, 1.3  $\mu\text{L}$  forward primer, 1.3  $\mu\text{L}$  reverse primer, 5.2  $\mu\text{L}$  dNTP, 65  $\mu\text{L}$  BSA, and 3.3  $\mu\text{L}$  Taq. Each sample for PCR amplification consisted of 1  $\mu\text{L}$  sample of diluted nucleic acids and 49  $\mu\text{L}$  PCR reaction mix. Following initial denaturing at 94 °C for 5 min, thirty-five PCR cycles were performed under the following conditions: denaturing at 94 °C for 30 sec, annealing at 55 °C for 1 min, extension at 72 °C for 1.5 min, with a 5-min completion period at 72 °C at the end of the cycles.

Amplified rRNA products were then screened on agarose gel for densitometric screening. Primers ARISA-16S-1406f / ARISA-23r (Yannarell et al. 2003; Yannarell and Triplett 2005) were used for PCR-amplification of the ribosomal intergenic spacer region for RISA. Additional PCR products were obtained using primers specific to the 16S rRNA genes of *Geobacter metallireducans* (49f / 825r; Andersen et al. 2003) and *Shewanella putrefaciens* (SW.783f /

SW.1245r; Snoeyenbos-West et al. 2000). The abundance of these targets was assessed via quantitative real-time PCR (q-PCR) for future work focused specifically on the response of Fe- and Mn-reducing bacteria to HO<sub>x</sub>.

*6.3.2.4 Community composition via RISA* – Banding patterns obtained via RISA were used to characterize microbial community structure (Fisher and Triplett 1999; Sigler et al. 2002). The 16S-23S intergenic region shows significant variation in terms of length and nucleotide sequence that can be used to distinguish between different bacterial phylotypes (Fig. 6.3) although the specific species is not defined. Each band's relative intensity was used to determine relative abundance of each observed phylotype.

For RISA, the rRNA spacer region was amplified as described above and 5  $\mu$ L of sample (mixed with 3  $\mu$ L bromphenol blue/sucrose loading dye) was loaded onto 5% bis-acrylamide gels. Gel electrophoresis was then performed in a 1  $\times$  TAE buffer at 35°C for 15 min at 30V and then 4 h at 200V. Following electrophoresis, staining was performed by gently agitating the gel in 50 mL of 1  $\times$  TAE with a dilution of 1:5,000 SYBR Green dye (Molecular Probes Inc.) for 30 min. RISA band patterns (Fig. 6.3) were then analyzed using the Gel Doc high-resolution gel documentation system and Quantity One software (Bio Rad Laboratories). Densitometric data for each gel was exported to Microsoft Excel and manually assembled into a single dataset. All community analyses reported here are based on presence-absence data.

*6.3.2.5 Correlation to CCR geochemical data* – Results from microbial analyses were correlated to several other data sets from our 2006 CCR experimental campaign to explain observed variance in phylogenetic data. Sediment-water O<sub>2</sub> profile data obtained via an in situ microprofiler (MP4; Unisense A/S; Ch. 2-5), sediment-water Fe and Mn (soluble) profile data obtained via in situ porewater analyzers (“peepers”; Hesslein 1976; Ch. 5), and total organic carbon (TOC), phosphorus (P<sub>tot</sub>), Fe (Fe<sub>tot</sub>), and Mn (Mn<sub>tot</sub>) data obtained from bulk sediment samples (Ch. 5) were all used to evaluate microbial results. Details on sampling and analytical procedures for geochemical data are included in Ch. 5. Ordination analysis was performed using the statistical software R (R Development Core Team 2009) with packages vegan (Oksanen et al. 2009) and Biodiversity R (Kindt and Coe 2005).

*6.3.2.6 Identification of Mn-oxidizers via LBB* – Although RISA yields quantitative data on the different phylogenies represented in a given community, qualitative data identifying the bacteria species is not obtained. Because we were specifically interested in Fe and Mn biogeochemical cycling in CCR, the presence of Mn oxidizers in CCR was assessed based on the LBB method following the Manual of Environmental Microbiology (Tebo et al. 2007). Sediment samples taken from the upper 2 cm of cores from CC, CVCB, CE, and C3 were plated on agar plates of Mn-containing media described by Stein et al. (2001). Probable Mn-oxidizing colonies, visually identified as a dark brown or orange irregularly-shaped mass, were selected and streaked to obtain isolates. Fourteen isolated colonies were then inoculated in Mn broth (Stein et al. 2001). Isolate samples were analyzed using a 1:5 ratio with LBB, a color indicator that chemically reacts with oxidized Mn. Controls of LBB solution were maintained to ensure that the oxidation observed was biological rather than chemical. Absorption measurements of isolate samples and controls were taken using a Hitachi Digital Spectrophotometer at 620 nm. A potassium permanganate calibration curve was employed to relate oxidized Mn to absorption.

## **6.4 Results and discussion**

**6.4.1 Relative concentrations of DNA** – As shown in Fig. 6.4, several trends in nucleic acid concentration may be discerned from PicoGreen data although a defined temporal or spatial relationship is not evident. Nucleic acid concentrations can be used as an indicator for microbial biomass as shown by Pesaro et al. (2002). Nucleic acid concentration was typically highest at CVCB, the site located immediately alongside the HOx in the deepest CCR region (site CC is located slightly downstream from the HOx; Fig. 6.1). Thus, increased O<sub>2</sub> levels due to HOx proximity and accumulated organic matter due to sediment focusing may have supported a denser sediment microbial community. Increased nucleic acid concentrations were frequently observed at the deepest sample depth (1-1.2 cm), particularly at site CE, which may possibly be due to accumulation of recently deposited material with relatively low biomass at the sediment surface during certain periods of the campaign. Additionally, nucleic acid concentration is shown to increase at all locations by the end of the campaign, with the exception of site CVCB which remained relatively constant. This may be attributed to either HOx-induced increases in

sediment O<sub>2</sub> and/or elevated levels of organic matter following late-summer algal matter deposition.

**6.4.2 Phylogenetic hierarchy** – Hierarchical clustering of the RISA community fingerprints showed that the CCR sediment samples were fairly similar in terms of bacterial community structure as indicated by the large grouping of samples in green in Fig. 6.5. However, samples obtained close to the HOx (sites CC and CVCB) at the end of the experimental campaign formed a separate cluster (C4 and B4 grouping in orange in Fig. 6.5). The sediment in this region is influenced by the HOx more directly, which may have contributed to the observed similarity. Hypolimnetic O<sub>2</sub> levels remained extremely high throughout the summer and early fall prior to turnover, which occurred in mid-November 2006. This facilitated elevated O<sub>2</sub> in the upper sediment layers and also precipitation of Fe- and Mn-oxide particles as reduced Fe and Mn oxidized in the water column (Gantzer et al. 2009a,b; Ch. 5).

In addition to HOx effects on sediment composition, natural sediment focusing may have also been a factor in the observed phylogenetic similarity. These CC and CVCB samples were obtained from the deepest part of CCR in mid-October; thus, this region likely had much higher levels of freshly-accumulated organic matter as a result of settled spring and summer algal matter and terrestrial sediment focusing. Bulk sediment data (Ch. 5) showed that total organic carbon, Fe, and Mn levels were greater at CVCB than in shallower regions (e.g., C3) farther from the HOx. The influence of near-field sediment composition is further supported by the fact that within the October CC-CVCB sample group, even greater similarity is observed in the samples obtained from the sediment surface (B41 and C41; designated in red in Fig. 6.5). The sediment microbe community in the upper sediment would obviously be most directly affected by both the accumulation of newly deposited material (resulting from HOx operations, algal settling, and/or sediment focusing) and also increased hypolimnetic O<sub>2</sub> levels. These results are supported by PicoGreen data showing enhanced nucleic acid concentration at CVCB (Fig. 6.4).

**6.4.3 Correlation between microbial community structure, geochemical cycling, and HOx operation** – Canonical correspondence analyses (CCA; Ter Braak 1986) were performed to relate sediment microbial composition to environmental (geochemical) variables. Axes for each variable were plotted via CCA to explain variance in the dataset. Proximity of a sample or

phylogroup to a specific axis indicates correlation. Initially, a constrained CCA based on the full set of CCR samples was performed using an environmental dataset based on global experimental and system characteristics (Fig. 6.6a). In this analysis, 17% of the variance in microbial community structure identified by RISA can be explained. As also indicated by the phylogenetic hierarchy in Fig. 6.5, CCA results in Fig. 6.6 show increased correlation between the upper-sediment samples obtained near the HOx in mid-October (B4 and C4 samples) and the variables time and flow (which are directly related as flow was changed over the duration of the experiment; Fig. 6.2). Moderate correlation between sites closer to the HOx and O<sub>2</sub> levels at the SWI (O2\_d) is also observed. Conversely, samples from the site farthest from the HOx (C3 or D sample set; Table 6.1) were logically most strongly related to distance but far less correlated to HOx flow and SWI O<sub>2</sub> levels. However, bacterial phylogroups were ultimately not found to be strongly associated with any of the environmental variables assessed in the initial CCA model.

Because the variance explained by the constrained CCA model was low, an unconstrained analysis with detrended correspondence analysis (DCA) was also performed (Fig. 6.6b). The DCA indicated that ~35% of the variance is explained by the first two axes of the ordination. This relatively low value of explained variance indicates that more than just one or two common trends in species distribution contributed to the observed variance. Passively fitting environmental variables indicated that flow, time, and O<sub>2</sub> at the SWI were closely correlated in their effect on community composition, while distance and depth were found to be independent (Fig. 6.6). Slightly increased correlation between bacterial phylogenies and the variables SWI O<sub>2</sub> and time/flow was also observed.

To evaluate the relationship between community composition and corresponding CCR sediment geochemical data, a constrained CCA was performed on a reduced dataset that excluded samples for which geochemical data was unavailable. In addition to the environmental variables shown in Fig. 6.6 (though time was omitted due to the correlation with flow), TOC, P<sub>tot</sub>, Fe<sub>tot</sub>, and Mn<sub>tot</sub> data were assessed as additional constraining variables (Fig. 6.7). CCA based on the reduced dataset and supporting geochemical data explained an additional ~19% of the variance, with distance, flow, and Mn<sub>tot</sub> found to be the most significant variables. The considerable increase in the explained variance indicates the importance of local sediment conditions relative to the global system properties. The increased influence of Mn<sub>tot</sub> as compared to Fe<sub>tot</sub> may be attributed to the fact that Mn redox kinetics is largely dominated by

microbial processes while Fe kinetics are typically chemically controlled. TOC was the most insignificant variable, which does not support the theoretical influence of organic matter deposition and sediment focusing in the deeper CCR region (previously discussed).

An additional CCA ordination was performed based only on site CC sample data and corresponding soluble Fe and Mn porewater data (CC was the sole site at which in situ peepers were deployed in 2006 due to equipment limitations). O<sub>2</sub>, Fe, and Mn levels at the SWI and HOx flow were found to be the most significant variables (Fig. 6.8). However, the degree of variance explained by these environmental variables was not significant, which is most likely due to the small sample size and small environmental gradient sampled.

In summary, the multiple CCA ordinations explained low proportions of the overall variance in our sample set as a function of the environmental and geochemical variables evaluated. The unconstrained ordination also indicated, however, that the community structure is not influenced by an easily discernable trend but rather by independent changes of many phylotypes (Fig. 6.6-6.8). Regardless, in comparison to results from other CCA studies (Yannarell and Triplett 2005; Bürgmann, pers. comm.), a relatively small part of the variance in the community dataset was explained by our overall CCA ordinations in general and by our environmental variables specifically. This indicates that either there are important drivers not considered here (e.g., pH, temperature, sediment total:soluble metal ratios), sediment geochemical data did not sufficiently represent microbial sediment samples due to localized sediment heterogeneity, operational errors during laboratory analyses occurred, and/or that a large part of the observed variance is simply random or related to methodological noise. We opted to analyze presence-absence data only in our analysis since this approach is considered more robust against PCR and other biases inherent to microbial fingerprinting methods. However, this analysis also masks more gradual environmental influences on the relative abundances of prevalent microbial taxa. Considering the high overall uniformity of the sediment microbial community structure that was observed, incorporating the information on relative band intensities as a proxy for relative abundance of microbial species might have allowed for a better correlation of environmental and community datasets.

**6.4.4 Presence of metal-oxidizers and reducers** – Fe- and Mn-reducers and also Mn-oxidizers were confirmed to be members of the CCR sediment microbial community. Fe- and

Mn-reducers *G. metallireducans* and *S. putrefaciens* were successfully detected via q-PCR. While the Mn-oxidizers were not qualitatively identified, their presence was confirmed via LBB analyses. Three of the fourteen selected colonies were identified as Mn-oxidizers by the LBB method. These samples exhibited Mn-oxidation rates of approximately three times the background levels. The presence of these bacterial colonies confirms that Fe and Mn redox processes in CCR are at least partially influenced by Fe- and Mn-specific bacteria. Additionally, these results indicate that Fe- and Mn-specific bacteria are phylogenetic members of the community structure defined by RISA (Fig. 6.5-6.8). Further investigations, however, are needed to understand how oxygenation influences Fe- and Mn-specific bacteria and other members of the CCR sediment microbial community in order to optimize suppression of soluble Fe and Mn flux from the sediment.

## 6.5 Conclusions

A moderate response of the microbial community structure to oxygenation was observed in samples obtained near the HOx at the end of the 2006. Additionally, nucleic acid concentrations were typically elevated immediately alongside the HOx throughout the campaign and at all locations at the end of the campaign following ongoing oxygenation. However, a strong link between sediment microbial community structure and environmental variables in response to HOx operation was not found. Because a correlation between the environmental variables themselves (e.g., O<sub>2</sub> at the SWI and total and soluble metal concentrations in the sediment) and HOx operations was observed in previous work (Ch. 4 and 5, respectively), our microbial results indicate that sediment geochemical processes and the general microbial community composition may have been largely decoupled during certain time periods. Thus, while the CCR sediment microbial community is diverse (as indicated by the large number of phylotypes identified via RISA) and long-term HOx operation has the capacity to fundamentally affect the microbial community via changes in sediment O<sub>2</sub> availability, variation in community composition could not be sufficiently linked to HOx-induced changes in sediment O<sub>2</sub> concentration and other geochemical properties. The absence of an evident short-term shift in the microbial community structure in response to oxygenation may indicate that the significant HOx-induced variation in sediment-water Fe and Mn fluxes revealed in Ch. 5 was largely

abiologically controlled (Stein et al. 2002). Conversely, our results may be attributed to the ability of many bacteria to adapt to variations in sediment O<sub>2</sub> levels and utilize various electron acceptors, particularly over relatively short time scales (Thamdrup 2000). The microbial community may have easily adapted to both the month-long period when the sediment went anoxic after the HOx was turned off and also subsequent re-oxygenation (Fig. 6.2; Ch. 5). Long-term oxygenation combined with late-season influx of fresh organic matter may have been necessary to induce the changes in the microbial community observed at the final October sampling date.

The full effect of HOx-induced variation in sediment O<sub>2</sub> availability on community composition may also have been masked by the influence of background HOx operations. CCR had been continually oxygenated for the year prior to this field campaign and an oxic SWI had been maintained throughout the reservoir. The influence of HOx operation on sediment microbial community structure may have been more evident if microbial data from sediment in a back region of CCR that remains unaffected by HOx were also taken into account.

Through this study, insight was obtained on the relative significance of the environmental and geochemical variables assessed in the CCR system. Of the variables evaluated, HOx flow, distance from the HOx, sediment O<sub>2</sub> availability, and total Mn levels in the sediment were shown to have the greatest influence on variation in community composition. Our results suggest that while the sediment microbial community may not be drastically affected by HOx, some HOx-induced variation may occur (particularly in the near-field region following ongoing oxygenation) that merits further investigation. Characterizing the influence of sediment microbial and chemical processes on soluble metal flux suppression in response to HOx operations will ultimately help optimize lake and reservoir management.

## **6.6 Acknowledgements**

The authors are extremely grateful to Francisco Vasquez and Krista Koellner who offered invaluable advice and support in the laboratory with microbial techniques. We thank Mary-Theresa Pendergast, Deric Learman, Jose Manuel Cerato, and Joseph Falkingham for assistance in identification of manganese-oxidizing bacteria. Kevin Elam, Elizabeth Rumsey, and the staff at Western Virginia Water Authority provided help in the field and with laboratory samples.

We acknowledge financial support from the National Science Foundation (NSF IGERT Program) and the Western Virginia Water Authority. The research described in this paper has also been funded in part by the United States Environmental Protection Agency (EPA) under the Science to Achieve Results (STAR) Graduate Fellowship Program. EPA has not officially endorsed this publication and the views expressed herein may not reflect the views of the EPA.

## 6.7 References

- Anderson, R. T., H. A. Vronis, I. Ortiz-Bernad, C. T. Resch, P. E. Long, R. Dayvault, K. Karp, S. Marutzky, D. R. Metzler, A. Peacock, D. C. White, M. Lowe, and D. R. Lovley. 2003. Stimulating the in-situ activity of *Geobacter* species to remove uranium from the groundwater of a uranium-contaminated aquifer. *Appl. and Env. Microbiol.* **69**: 5884-5891.
- Beutel, M. W., and A. J. Horne. 1999. A review of the effects of hypolimnetic oxygenation on lake and reservoir water quality. *J. Lake Reservoir Manage.* **15**: 285– 297.
- Bürgmann, H., M. Pesaro, M. Widmer, and J. Zeyer. 2001. A strategy for optimizing quality and quantity of DNA extracted from soil. *J. Microbiol. Meth.* **45**: 7-20.
- DiChristina, T. J., and E. F. DeLong. 1993. Design and application of rRNA-targeted oligonucleotide probes for the dissimilatory iron- and manganese-reducing bacterium *Shewanella putrefaciens*. *Appl. and Env. Microbiol.* **59**: 4152-4160.
- Fisher, M. M., and E. W. Triplett. 1999. Automated approach for ribosomal intergenic spacer analysis of microbial diversity and its application to freshwater bacterial communities. *Appl. and Env. Microbiol.* **65**: 4630-4636.
- Gantzer, P. A., L. D. Bryant and J. C. Little (2009a). Effect of hypolimnetic oxygenation on oxygen depletion rates in two water-supply reservoirs. *Water Res.* **43**: 1700-1710.
- Gantzer, P. A., L. D. Bryant and J. C. Little (2009b). Controlling soluble iron and manganese in a water-supply reservoir using hypolimnetic oxygenation. *Water Res.* **43**: 1285-1294.
- Hesslein, R. 1976. An in-situ sampler for close interval porewater studies. *Limnol. Oceanogr.* **21**: 912-914.

- Kindt, R., and R. Coe. 2005. Tree diversity analysis: a manual and software for common statistical methods for ecological and biodiversity studies. World Agroforestry Centre (ICRAF), Nairobi. ISBN 92-9059-179-X.
- NRC (National Research Council). 2004. Confronting the Nation's Water Problems: The Role of Research. Washington, D.C., National Academies Press.
- Oksanen, J., R. Kindt, P. Legendre, B. O'Hara, G. L. Simpson, P. Solymos, M. H. H. Stevens, and H. Wagner. 2009. vegan: community ecology package. R package version 1.15-3. <http://CRAN.R-project.org/package=vegan>
- Pesaro, M., H. Bürgmann, F. Widmer, and J. Zeyer. 2002. Soil DNA content - a novel quantitative bulk parameter for description of microbiological soil characteristics. Proceedings of COST Action 831, Biotechnology of soil: Monitoring, Conservation and Remediation, Workshop "Managing Soil Quality", Budapest, Hungary, Sept. 2002.
- R Development Core Team. 2009. R: A language and environment for statistical computing. R Foundation for Statistical Computing, Vienna, Austria. ISBN 3-900051-07-0. [www.R-project.org](http://www.R-project.org)
- Santschi, P., P. Höhener, G. Benoit, and M. Buchholtz-ten Brink. 1990. Chemical processes at the sediment-water interface. *Mar. Chem.* **30**: 269-315.
- Sigler, W. V., S. Crivii, and J. Zeyer. 2002. Bacterial succession in glacial forefield soils characterized by community structure, activity and opportunistic growth dynamics. *Microb. Ecol.* **44**: 306-316.
- Snoeyenbos-West, O., K. P. Nevin, R. T. Anderson, and D. R. Lovley. 2000. Enrichment of *Geobacter* species in response to stimulation of Fe(III) reduction in sandy aquifer sediments. *Microb. Ecol.* **39**: 153-167.
- Stein, L. Y., M. T. La Duc, T. J. Grundl, and K. H. Nealson. 2001. Bacterial and archaeal populations associated with freshwater ferromanganous micronodules and sediments. *Environ. Microbiol.* **3**: 10-18.
- Stein, L. Y., G. Jones, B. Alexander, K. Elmund, C. Wright-Jones, and K. H. Nealson. 2002. Intriguing microbial diversity associated with metal-rich particles from a freshwater reservoir. *FEMS Microbiol. Ecol.* **42**: 431-440.

- Tebo, B. M., B. G. Clement, and G. J. Dick. 2007. Biotransformations of Manganese. *In* C. Hurst, R. Crawford, J. Garland, D. Lipson, A. Mills, and L. Stetzenbach [Eds.], *Manual of Environmental Microbiology* (3<sup>rd</sup> ed.). Blackwell Publishing.
- Ter Braak, C. J. F. 1986. Canonical correspondence analysis: a new eigenvector technique for multivariate direct gradient analysis. *Ecology* **67**: 1167-1179.
- Thamdrup, B. 2000. Bacterial manganese and iron reduction in aquatic sediments. *In* B. Thamdrup [ed.], *Advances in Microbial Ecology*. Kluwer Academic / Plenum Publishers.
- Yannarell, A. C., A. D. Kent, G. H. Lauster, T. K. Kratz, and E. W. Triplett. 2003. Temporal patterns in bacterial communities in three temperate lakes of different trophic status. *Microb. Ecol.* **46**: 391-405.
- Yannarell, A. C., and E. W. Triplett. 2005. Geographic and environmental sources of variation in lake bacterial community composition. *Appl. and Env. Microbiol.* **71**: 227-239.
- Zaw, M., and B. Chiswell. 1999. Iron and manganese dynamics in lake water. *Water Res.* **33**: 1900-1910.
- Zhang, H., W. Davison, and C. Ottley. 1999. Remobilisation of major ions in freshly deposited lacustrine sediment at overturn. *Aquat. Sci.* **61**: 354-361.

Table 6.1. Sediment sampling strategy and nomenclature used in microbial analytical techniques. Canonical correspondence analysis (CCA) sample identification based on the first digit to identify location (C, B, D, and E identifying sites CC, CB, C3, and CE, respectively), the second digit to identify sampling date in chronological order (i.e., 1 represents first sampling date July 12, 2006), and the third digit to indicate depth below the sediment surface in order of increasing depth (i.e., 2 represents second depth from sediment surface at 2-4 mm).

site	date	depth (mm)	general sample ID	CCA sample ID
CB	7/12/06	0-2	CB-B1	B11
CB	7/12/06	2-4	CB-B2	B12
CB	7/12/06	4-6	CB-B3	B13
CB	7/12/06	10-12	CB-B4	B14
CB	8/2/06	0-2	CB-B1	B21
CB	8/2/06	2-4	CB-B2	B22
CB	8/2/06	4-6	CB-B3	B23
CB	8/2/06	10-12	CB-B4	B24
CB	8/28/06	0-2	CB-B1	B31
CB	8/28/06	2-4	CB-B2	B32
CB	8/28/06	4-6	CB-B3	B33
CB	10/19/06	0-2	CB-B1	B41
CB	10/19/06	2-4	CB-B2	B42
CB	10/19/06	4-6	CB-F3	B43
CC	7/12/06	0-2	CC-B1	C11
CC	7/12/06	2-4	CC-B2	C12
CC	7/12/06	4-6	CC-B3	C13
CC	7/12/06	10-12	CC-B4	C14
CC	8/2/06	0-2	CC-B1	C21
CC	8/2/06	2-4	CC-R2	C22
CC	8/2/06	4-6	CC-R3	C23
CC	8/2/06	10-12	CC-B4	C24
CC	8/28/06	0-2	CC-R1	C31
CC	8/28/06	2-4	CC-B2	C32
CC	8/28/06	4-6	CC-B3	C33
CC	10/19/06	0-2	CC-B1	C41
CC	10/19/06	2-4	CC-B2	C42
CC	10/19/06	4-6	CC-B3	C43

site	date	depth (mm)	general sample ID	CCA sample ID
C3	7/12/06	0-2	C3-B1	D11
C3	7/12/06	4-6	C3-B3	D13
C3	7/12/06	10-12	C3-B4	D14
C3	8/2/06	0-2	C3-B1	D21
C3	8/2/06	2-4	C3-B2	D22
C3	8/2/06	4-6	C3-B3	D23
C3	8/2/06	10-12	C3-B4	D24
C3	8/28/06	0-2	C3-B1	D31
C3	8/28/06	2-4	C3-F2	D32
C3	8/28/06	4-6	C3-F3	D33
C3	10/19/06	0-2	C3-B1	D41
C3	10/19/06	4-6	C3-B3	D43
CE	7/12/06	0-2	CE-R1	E11
C3	7/12/06	2-4	C3-B2	E12
CE	7/12/06	2-4	CE-R2	E12
CE	7/12/06	4-6	CE-B3	E13
CE	7/12/06	10-12	CE-R4	E14
CE	8/2/06	0-2	CE-R1	E21
CE	8/2/06	2-4	CE-R2	E22
CE	8/2/06	4-6	CE-B3	E23
CE	8/2/06	10-12	CE-B4	E24
CE	8/28/06	0-2	CE-F1	E31
CE	8/28/06	2-4	CE-B2	E32
CE	8/28/06	4-6	CE-B3	E33
CE	10/19/06	0-2	CE-B1	E41
C3	10/19/06	2-4	C3-B2	E42
CE	10/19/06	2-4	CE-B2	E42
CE	10/19/06	4-6	CE-B3	E43

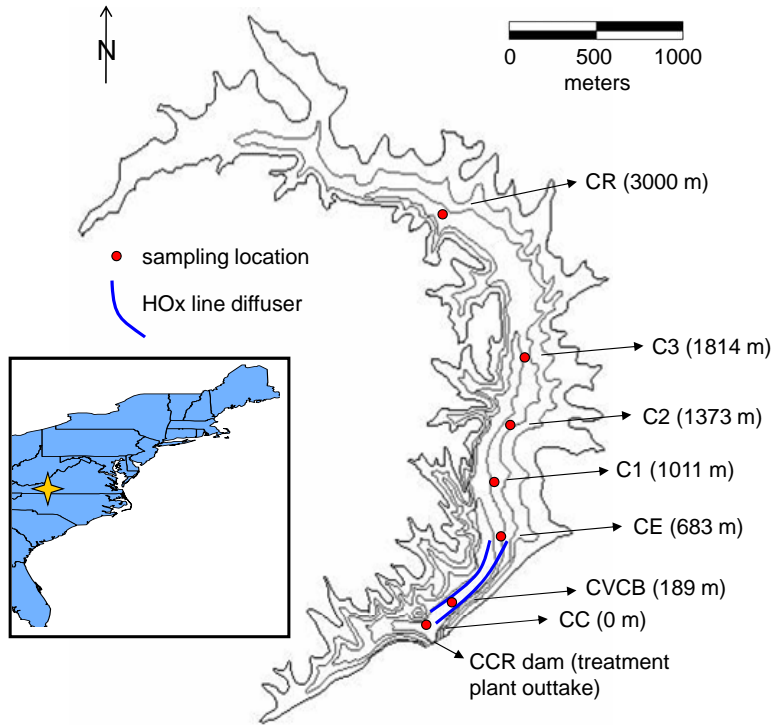


Figure 6.1. Map of Carvin's Cove Reservoir (CCR) showing sampling sites for microbial analyses (near field locations CC and CVCB; central, mid-reservoir locations C1, C2, C3, and CE; back-reservoir location CR) and linear bubble-plume hypolimnetic oxygenation system (HO<sub>x</sub>).

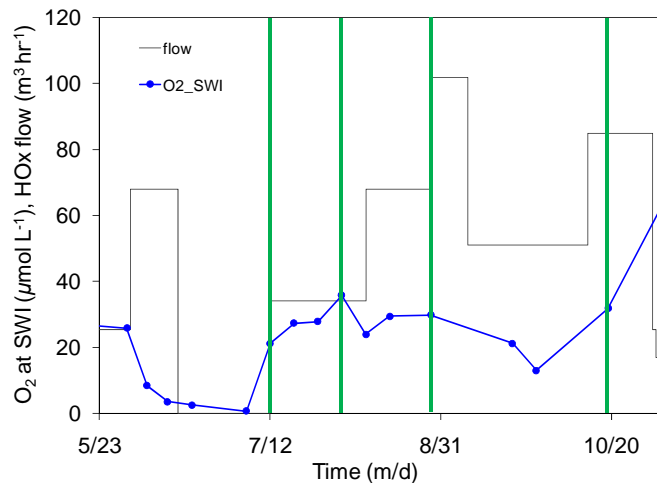


Figure 6.2. Oxygen flow rates of the CCR HOx and dates of sediment core sampling. The HOx was turned off in CCR from mid-June to mid-July 2006 to re-establish anoxic conditions. Following this period, HOx operations were resumed and oxygen gas flow was increased to the maximum possible flow rate ( $\sim 100 \text{ m}^3 \text{ hr}^{-1}$ ). This experiment was designed to demonstrate how increasing levels of turbulence and dissolved oxygen ( $\text{O}_2$ ) in the overlying water column impacted sediment-water fluxes (Fe, Mn,  $\text{O}_2$ ) at the sediment-water interface and microbial communities within the sediment. Sediment samples for microbial analyses were collected on the dates indicated by vertical green lines.

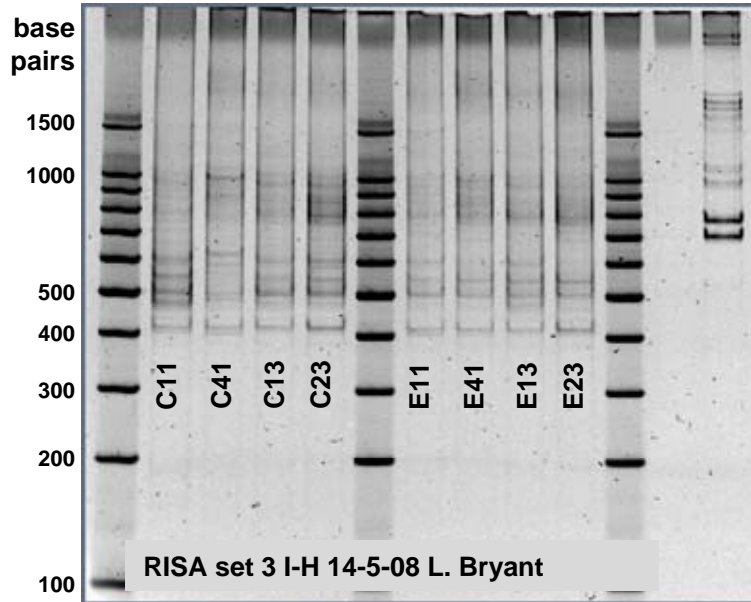


Figure 6.3. Gel image of ribosomal intergenic spacer analysis (RISA) of rRNA isolated from CCR sediment showing variable banding patterns indicating different sediment bacteria phylotypes. Lanes 1, 6, and 11 contain size markers (sizes indicated by base pairs at left) and lanes 12 and 13 are positive and negative controls. Samples (corresponding dates and depths from sites CC (lanes 2-5) and CE (lanes 7-10)) are coded per canonical correspondence analysis (CCA) sample labels defined in Table 6.1.

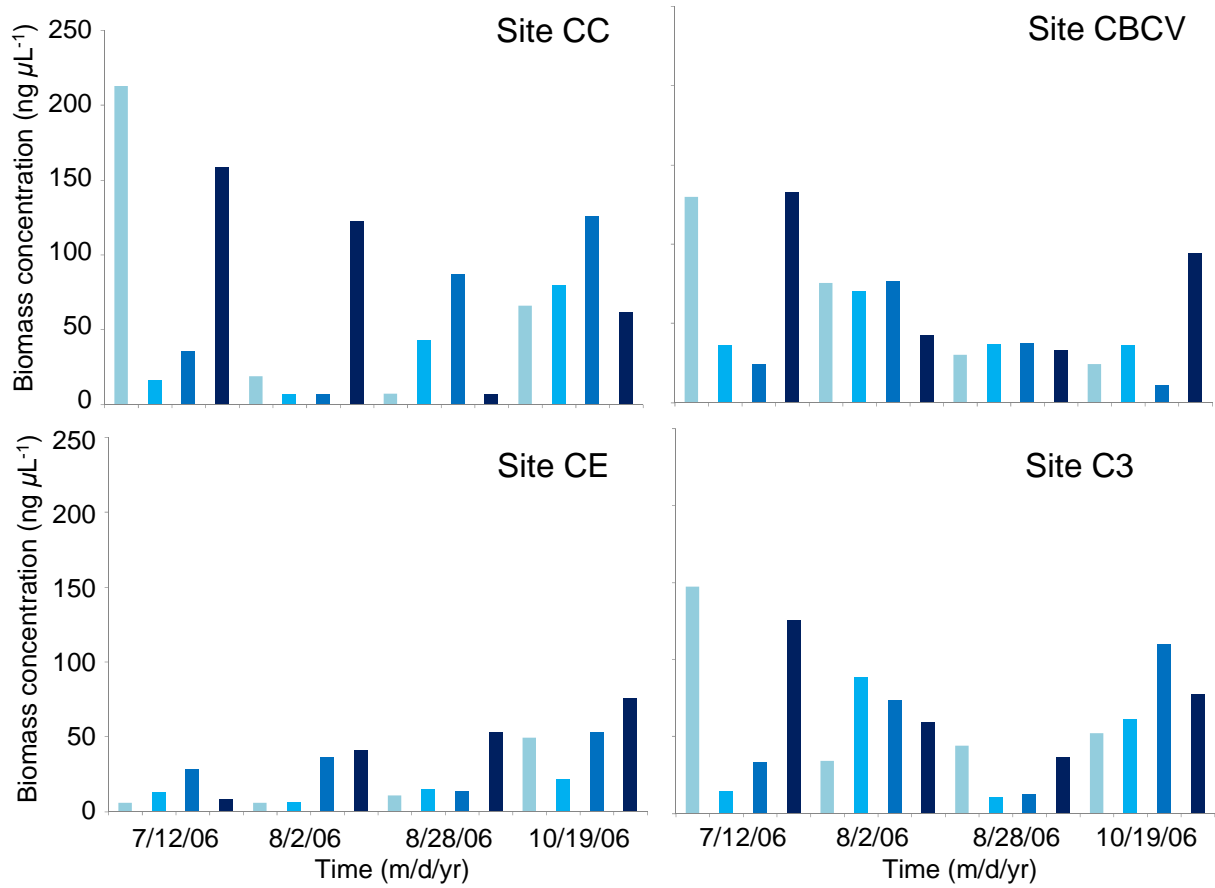


Figure 6.4. Nucleic-acid-concentration data obtained via PicoGreen analyses. Per sampling date, increasing sample depth is indicated by a darker shade of blue: light blue (0-2 mm), turquoise (2-4 mm), medium blue (4-6 mm), and dark blue (1-1.2 mm).

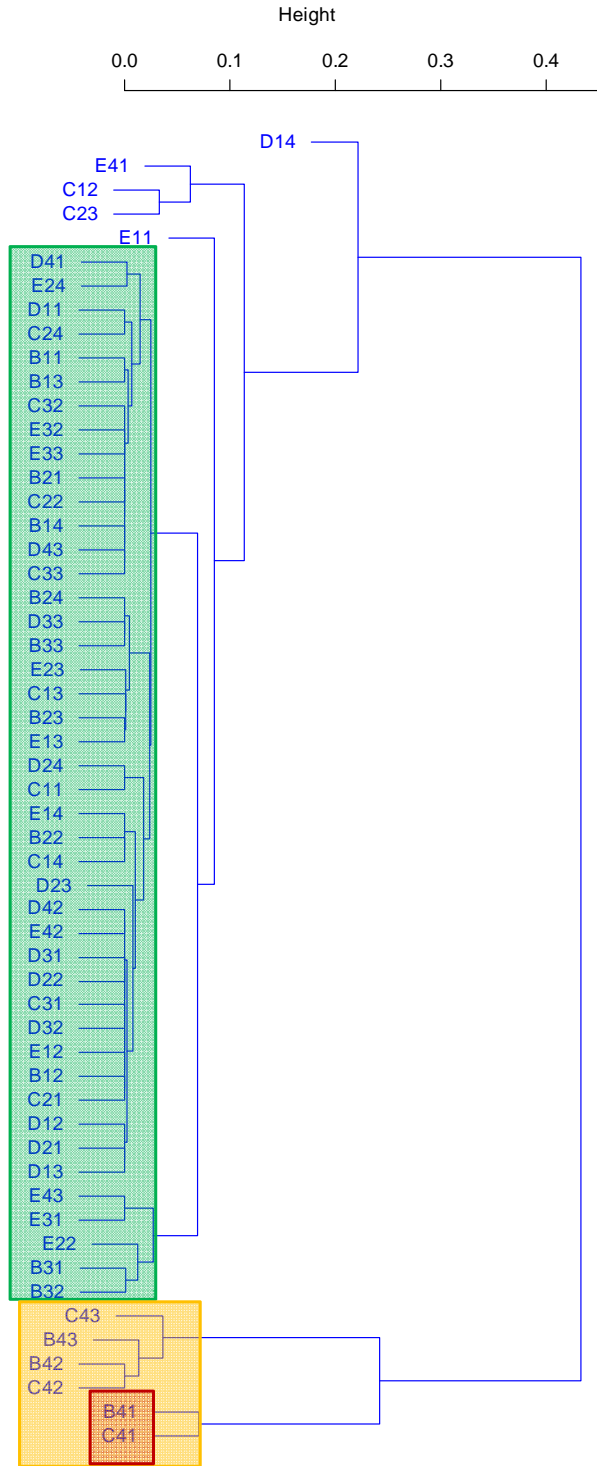


Figure 6.5. Average linkage hierarchical cluster analysis of community similarity (Raup-Crick distances) of CCR sediment samples based on presence-absence data of RISA phylotypes. Sampling site, depth and date are coded per CCA sample labels defined in Table 6.1.

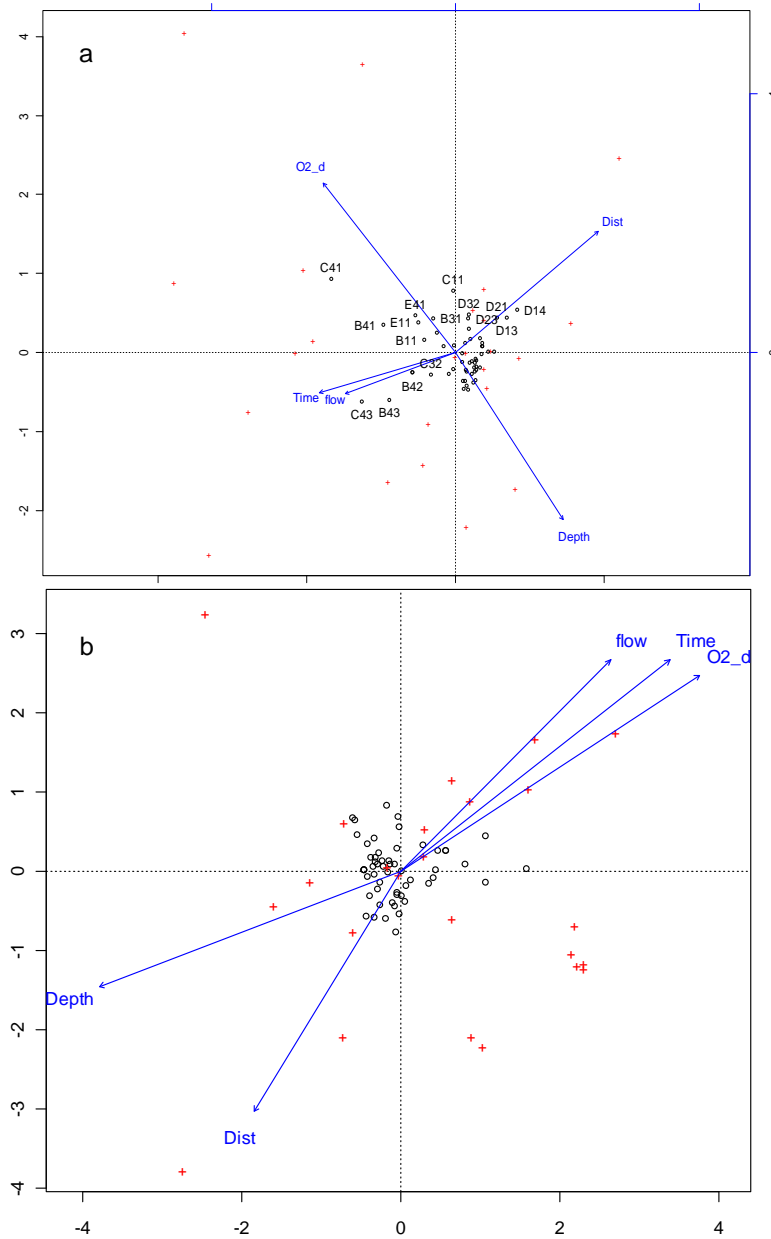


Figure 6.6. Biplots of ordination analysis of the RISA community dataset and environmental variables. (a) CCA using a constrained model to analyze the full set of CCR samples. RISA community composition data are correlated to variables time, HOx flow, distance from the HOx (Dist), sample depth, and O<sub>2</sub> (O2\_d) at the sediment surface (as indicated by blue axes). (b) Detrended (unconstrained) correspondence analysis (DCA) of the same dataset. Environmental variables are passively fitted. Black open circles are samples and red crosses are individual bacterial phylotypes identified by RISA bands. CCA (a) and DCA (b) sample labels are identically coded per CCA sample labels in Table 6.1.

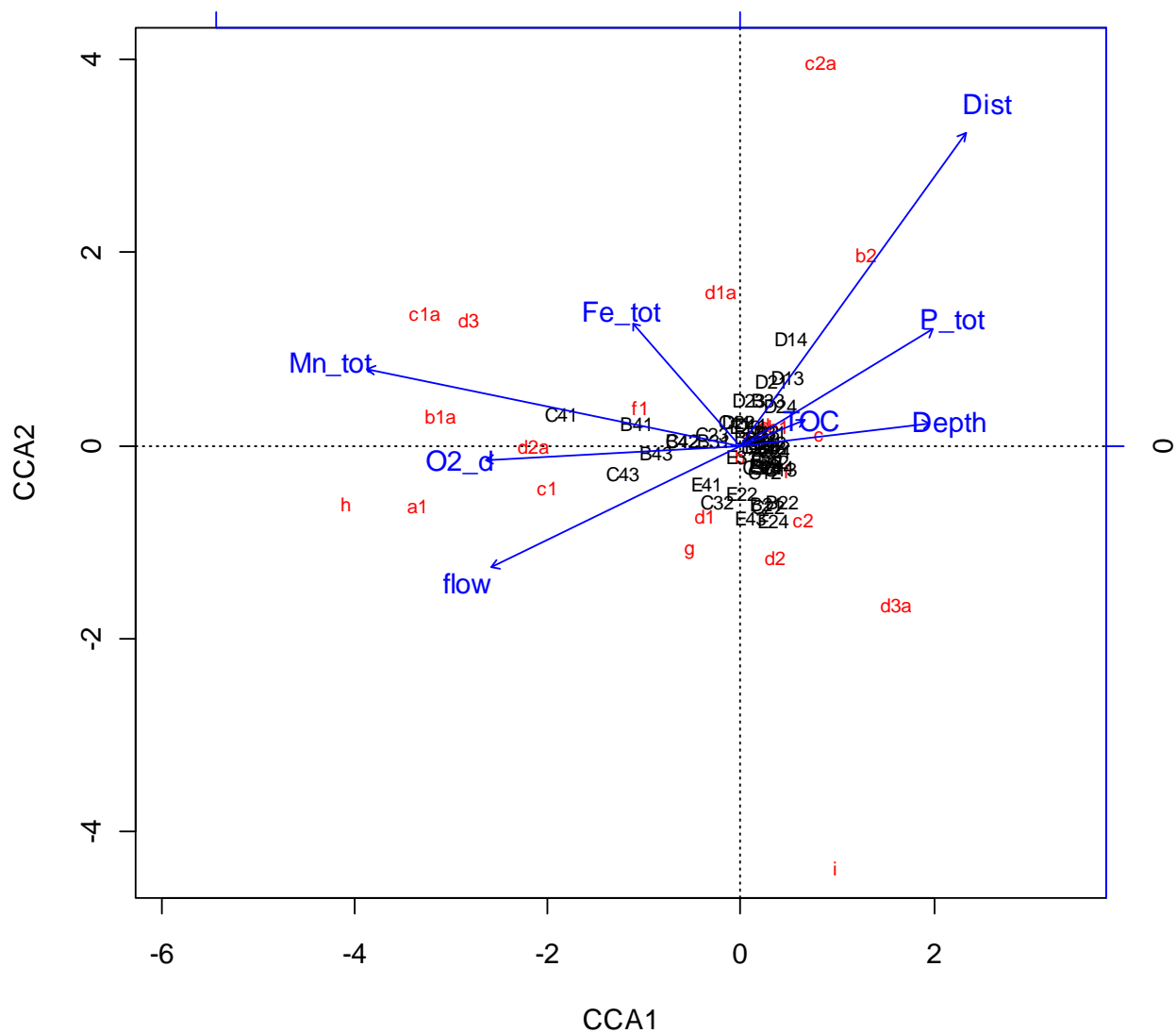


Figure 6.7. Constrained CCA ordination including all environmental (geochemical) variables. A reduced dataset excluding samples for which geochemical data were not available was used for this CCA. Time variable omitted due to correlation with HOx flow. Samples coded per CCA sample labels in Table 6.1.

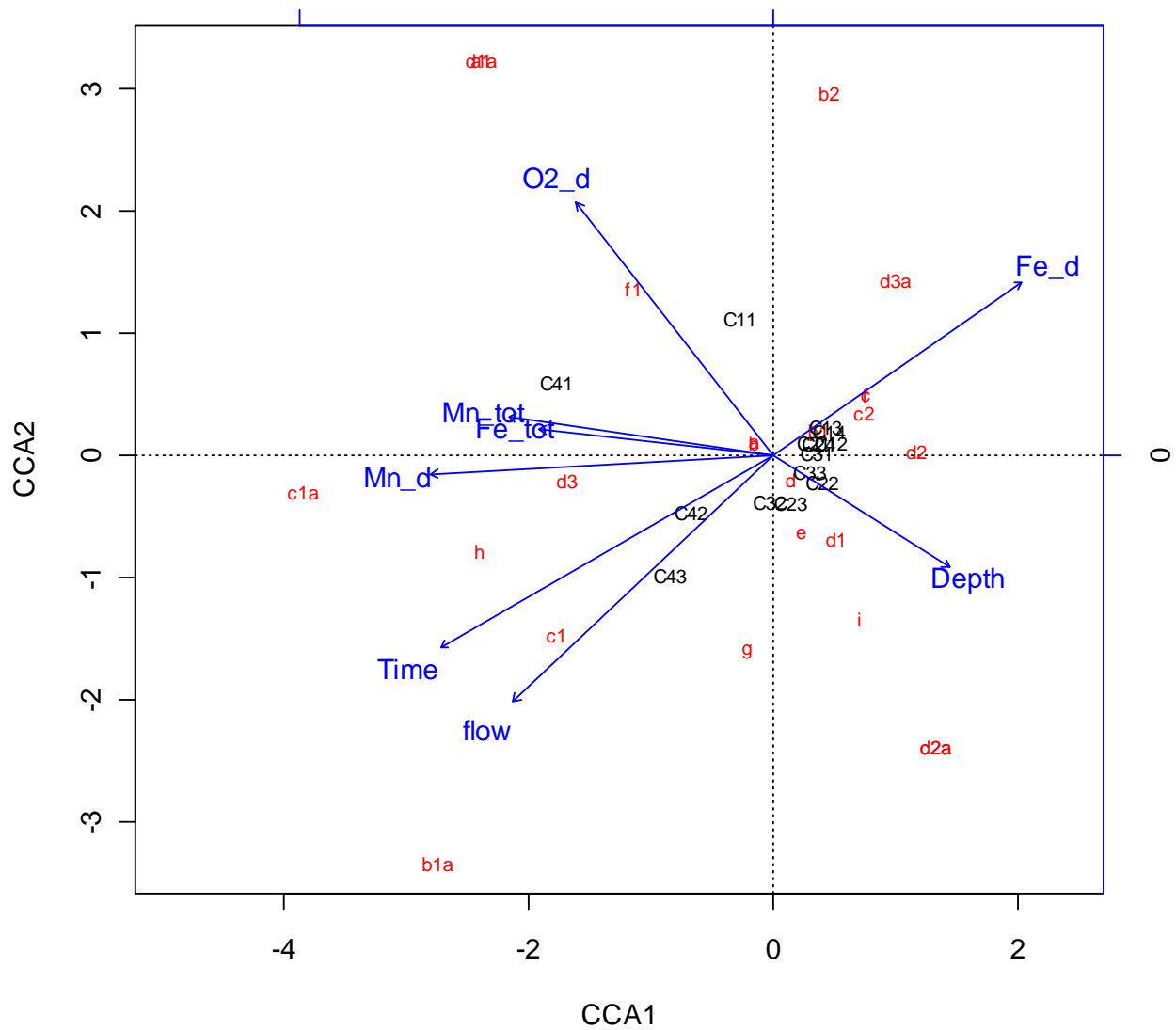


Figure 6.8. Constrained CCA ordination specifically for site CC which includes soluble Fe and Mn data obtained via in situ porewater analyzer (peeper). Samples coded per CCA sample labels in Table 6.1.

## Chapter 7 – Global impacts and future work

### 7.1 Global impacts

Current water supply issues become even more significant in light of climate change (Arnell 1999). For example, global warming will likely cause enhanced thermal stratification in many water bodies, which could lead to unprecedented increases in deep-water anoxia (Jankowski et al. 2006). Water quality and aquatic biodiversity are strongly affected by decreased O<sub>2</sub> levels (Glud 2008), as supported by our results showing significantly increased fluxes of soluble metals from the sediment during periods when the sediment became anoxic. The full extent to which sediment microbial community structure adapts to variable sediment O<sub>2</sub> availability has yet to be determined. Climate-change-induced shifts in microbial communities controlling carbon flux could contribute even further to the global warming crisis as decreased O<sub>2</sub> levels cause increased fluxes of reduced species (e.g., methane) from the sediment in aquatic systems. Greenhouse gas emissions from lake and reservoir surfaces are estimated to already be equivalent to ~7% of the global warming potential from anthropogenic sources (St. Lois et al. 2000); hence, this could be a considerable issue. As emphasized by our research, (1) understanding the mechanisms controlling sediment-water fluxes under dynamic environmental and/or limiting O<sub>2</sub> conditions and (2) evaluating alternative approaches to preserving hypolimnetic O<sub>2</sub> and subsequent water quality are therefore critical to alleviating future demands on our water supplies, which are already approaching a critical state (Berndes 2002).

Many of the insights on the mass transfer and redox mechanisms defining sediment-water fluxes of O<sub>2</sub>, Fe, and Mn gained through this research can be used to elucidate biogeochemical cycling of other chemical species as well. HOx can be used to address issues with increased levels of soluble species such as phosphorus, ammonia, hydrogen sulfide, and methane resulting from O<sub>2</sub> depletion. Furthermore, it has recently been shown that elevated Mn levels are creating an additional threat to some areas of Bangladesh where arsenic (As) poisoning from groundwater-supplied drinking water is prevalent; paired As and Mn release was found to be strongly controlled by the redox environment of the groundwater (Buschmann et al. 2007). Results from our research will clearly be applicable to drinking water issues on a global scale.

## 7.2 Future work

This research promotes the use of an interdisciplinary approach for the management of our water supplies, from both a water quality and ecosystem perspective. Two longer-term goals of this project are to (1) develop specific guidelines for water utilities to optimize design and operational parameters of HOx and (2) quantify improvements to overall aquatic ecosystem health via such measures as benthic biodiversity counts, species richness and health assessments of fish populations, and a survey of recreational patrons of CCR (e.g., boaters, fishermen).

Based on a proposal the author wrote building on this doctoral work, she will be funded by NSF to perform postdoctoral research that further explores the complexity of the Mn redox cycle, the influence of microbial activity at the SWI, and how these processes relate with respect to source and drinking water quality. During this postdoctoral work, recently-developed voltammetric microelectrodes specific for O<sub>2</sub>, Fe<sup>2+</sup>, and Mn<sup>2+</sup> (Brendel and Luther 1995) will be used to more-precisely quantify Fe and Mn dynamics at the SWI. Additional microbial work will be performed to comprehensively characterize how O<sub>2</sub> availability affects microbial processes controlling Mn cycling, with focus on Mn-reducers. The proposed combination of analytical methods will allow assessment of the general impact of oxygenation on microbial community structure (e.g., using general bacterial or group-specific protocols) and specific tracking of microbes known to be involved in Mn release (e.g. *G. metallireducens*, *S. putrefaciens*, using quantitative tools such as q-PCR). A one-dimensional model utilizing the sediment module of the aquatic system modeling program AQUASIM will also be developed to enable accurate predictions of Mn biogeochemical fluxes and sediment oxic zone depths (Reichert 1994; Brand et al. 2009).

Ultimately, our work will hopefully contribute to the shifting perspective on how we consume and protect our water resources. This highly-interdisciplinary doctoral research characterized sediment-water fluxes and subsequent effects on water quality using knowledge and theory from the fields of limnology, aquatic physics, biogeochemistry, soil science, microbiology, and environmental engineering. In doing so, the importance of approaching a research problem from many different scientific perspectives in order to obtain comprehensive and innovative solutions is emphasized. The closing line of an article on “The Practical Value of Science” appropriately reflects the interdisciplinary and societal aspects of this work; ironically,

the article was published 130 years ago in the very first issue of *Science*. “An Industry attains higher stages of its development as its processes become more complicated and refined, and the sciences are dragged in, one by one, to take their share in the fray” (Huxley 1880).

### 7.3 References

- Arnell, N. W. 1999. Climate change and global water resources. *Global Environ. Chang.* **9**: S31-S49.
- Berndes, G. 2002. Bioenergy and water – the implications of large-scale bioenergy production for water use and supply. *Global Environ. Chang.* **12**: 253-271.
- Brand, A., C. Dinkel, and B. Wehrli. 2009. Influence of the diffusive boundary layer on the solute dynamics in the sediments of a seiche-driven lake: A model study. *J. Geophys. Res.* **114**: G01010, doi:10.1029/2008JG000755.
- Brendel, P. J., and G. W. Luther. 1995. Development of gold mercury amalgam microelectrodes for the determination of dissolved Fe, Mn, O<sub>2</sub> and S(-II) in porewaters or marine and freshwater sediments. *Environ. Sci. Technol.* **29**: 751-761.
- Buschmann, J., M. Berg, C. Stengel, and M. L. Sampson. 2007. Arsenic and manganese contamination of drinking water resources in Cambodia: coincidence of risk areas with low relief topography. *Environ. Sci. Technol.* **41**: 2146-2152.
- Glud, R. N. 2008. Oxygen dynamics of marine sediments. *Mar. Biol. Res.* **4**: 243-289.
- Huxley, T. H. 1880. The Practical Value of Science. *Science* **1**: 3.
- Jankowski, T., D. M. Livingstone, H. Bührer, R. Forster, and P. Niederhauser. 2006. Consequences of the 2003 European heat wave for lake temperature profiles, thermal stability, and hypolimnetic oxygen depletion: Implications for a warmer world. *Limnol. Oceanogr.* **51**: 815–819.
- Reichert, P. 1994. AQUASIM - a tool for simulation and data analysis of aquatic systems. *Water Sci. Tech.* **30**: 21-30.
- St. Lois, V. L., C. A. Kelly, E. Duchemin, J. W. M. Rudd, and D. M. Rosenberg. 2000. Reservoir surfaces as sources of greenhouse gases to the atmosphere: a global estimate. *Bioscience* **50**: 766-775.

## **Appendix A – Supporting data for Chapter 4 (Oxygenation-induced variation in sediment oxygen uptake)**

Figure A.1 – Correlation between diffusive boundary layer thickness ( $\delta_{\text{DBL}}$ ) estimates obtained using in situ water-side ( $\delta_{\text{DBL-W}}$ ) and sediment-side ( $\delta_{\text{DBL-S}}$ ) oxygen ( $\text{O}_2$ ) microprofile data.

Figure A.2 – Comparison of near-sediment current velocity and wind speed time series. Average wind speed based on three-hour time blocks.

Figure A.3 – Correlation between  $J_{\text{O}_2}$  and water-side  $\delta_{\text{DBL}}$  based on in situ MP4 data from 2007-2008.

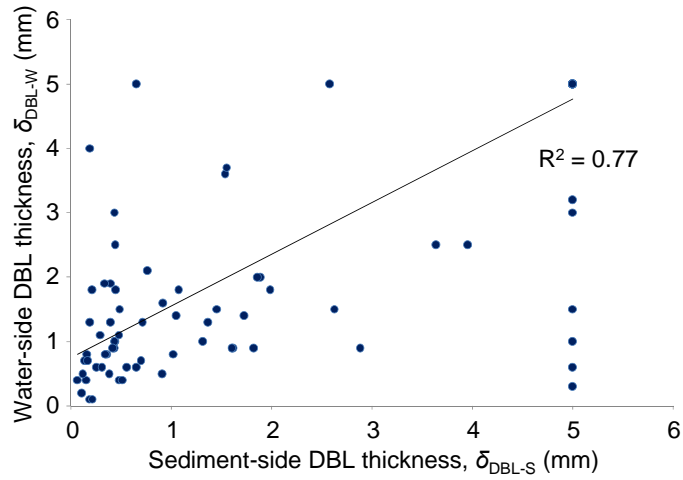


Figure A.1. Correlation between diffusive boundary layer thickness ( $\delta_{\text{DBL}}$ ) estimates obtained using in situ water-side ( $\delta_{\text{DBL-W}}$ ) and sediment-side ( $\delta_{\text{DBL-S}}$ ) oxygen ( $\text{O}_2$ ) microprofile data.

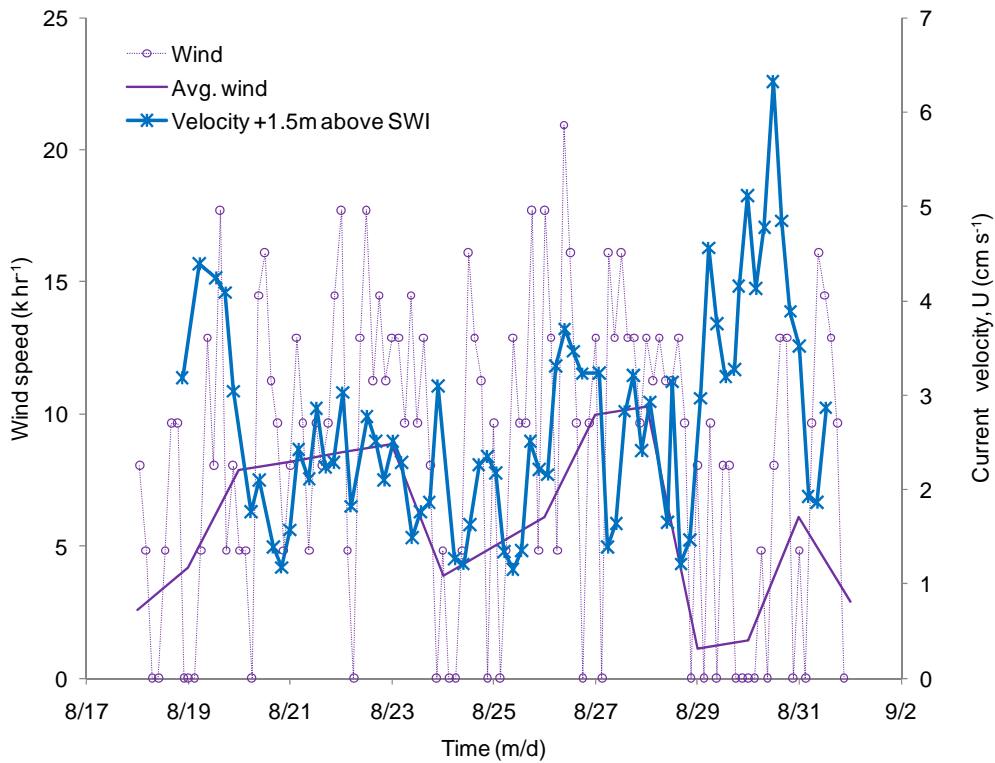


Figure A.2. Comparison of near-sediment current velocity and wind speed time series. Average wind speed based on three-hour time blocks.

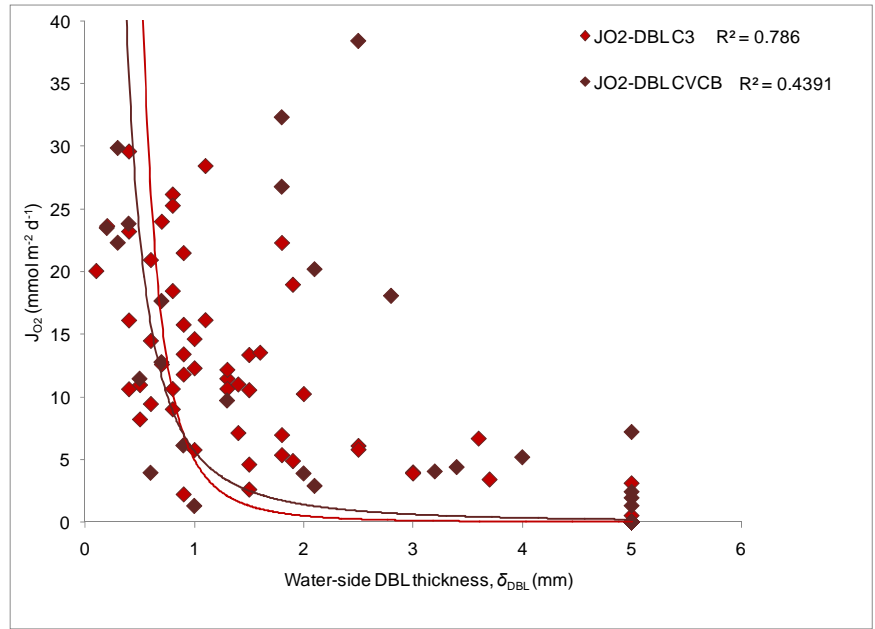


Figure A.3. Correlation between  $J_{O_2}$  and water-side  $\delta_{DBL}$  based on  $O_2$  microprofile data from 2007-2008.

## **Appendix B – Supporting data for Chapter 5 (Biogeochemical cycling of iron and manganese at the sediment-water interface in response to hypolimnetic oxygenation)**

Table B.1 – Comparison of sediment core and in situ MP4 microprofiler data from summer 2007. Hypolimnetic oxygenation flow rate is in  $\text{m}^3 \text{hr}^{-1}$ , sediment oxygen uptake rate ( $J_{\text{O}_2}$ ) is in  $\text{mmol m}^{-2} \text{d}^{-1}$ , oxygen concentration at the sediment-water interface ( $C_{\text{SWI}}$ ) is in  $\mu\text{mol L}^{-1}$ , and diffusive boundary layer thickness ( $\delta_{\text{DBL}}$ ) and depth of the sediment oxic zone ( $z_{\text{max}}$ ) are in mm.

Figure B.2 – Contour plots based on peeper data obtained mid-reservoir (site C3) and corresponding HOx flow pattern during 2007 and 2008. C3 peeper data for 2006 were unavailable due to equipment limitations.

Figure B.3 – Total and soluble Fe and Mn data obtained from near-sediment core water samples collected throughout 2008 HOx operations. Samples were collected near the HOx (site CVCB; a) and mid-reservoir at sites C3 (b) and C2 (c). Corresponding peeper data (for profile depth 5 cm above the SWI) are included to verify core water sample data. As discussed in Ch. 4, an experimental campaign focused specifically on site CVCB was performed in June 2008, hence the increased number of data points during this period in (a). A similar campaign was performed at C3 during August 2008 (b). Data characterizing the back-region of the reservoir (CR; Fig. 5.1) is provided in (c).

Table B.1. Comparison of sediment core and in situ MP4 microprofiler data from summer 2007. Hypolimnetic oxygenation flow rate is in  $\text{m}^3 \text{hr}^{-1}$ , sediment oxygen uptake rate ( $J_{\text{O}_2}$ ) is in  $\text{mmol m}^{-2} \text{d}^{-1}$ , oxygen concentration at the sediment-water interface ( $C_{\text{SWI}}$ ) is in  $\mu\text{mol L}^{-1}$ , and diffusive boundary layer thickness ( $\delta_{\text{DBL}}$ ) and depth of the sediment oxic zone ( $z_{\text{max}}$ ) are in mm.

			In situ MP4				Sediment cores			
Date	Site	Flow	$C_{\text{SWI}}$	$J_{\text{O}_2}$	$\delta_{\text{DBL}}$	$z_{\text{max}}$	$C_{\text{SWI}}$	$J_{\text{O}_2}$	$\delta_{\text{DBL}}$	$z_{\text{max}}$
5/22/07	CVCB	34	2.9	3.9	2.0	0.0	7.8	0.6	5.0	1.0
6/6/07	CVCB	51	4.9	9.7	1.3	0.0	17.2	1.3	5.0	2.0
6/18/07	CVCB	51	24.1	1.7	1.0	1.0	65.0	1.0	5.0	5.0
7/2/07	CVCB	68	75.3	6.1	0.9	1.0	65.6	4.9	2.0	2.0
7/17/07	CVCB	85	42.5	3.9	0.6	1.5	118.8	2.0	2.0	5.0
5/22/07	C3	34	38.6	2.6	1.5	2.2	57.7	0.7	3.0	3.0
6/6/07	C3	51	61.5	4.0	3.0	2	40.6	2.8	5.0	4.0
6/18/07	C3	51	68.0	6.1	2.5	1.4	19.5	3.2	5.0	4.0
7/2/07	C3	68	139.7	10.2	2.0	2.0	98.8	6.1	2.5	4.0
7/17/07	C3	85	66.9	5.8	2.5	1.5	76.2	4.5	2.0	4.0

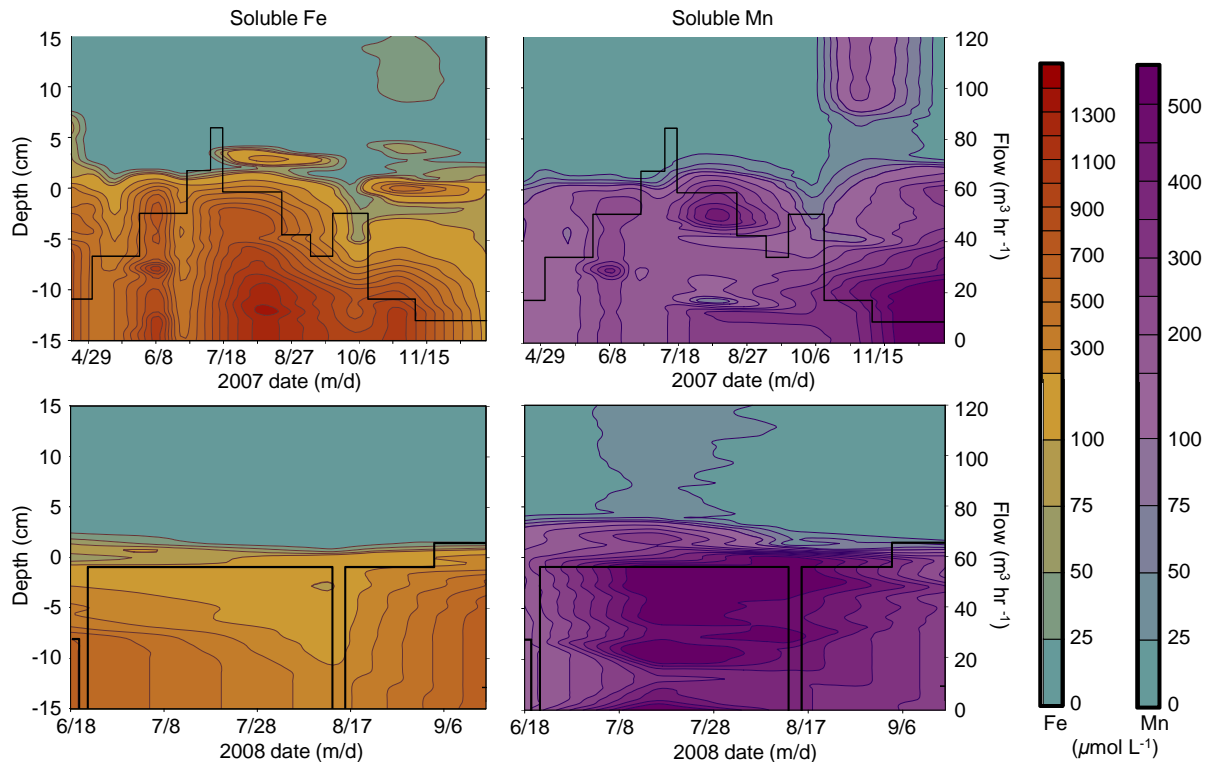


Figure B.2. Contour plots based on peeper data obtained mid-reservoir (site C3) and corresponding HOx flow pattern during 2007 and 2008. C3 peeper data for 2006 were unavailable due to equipment limitations.

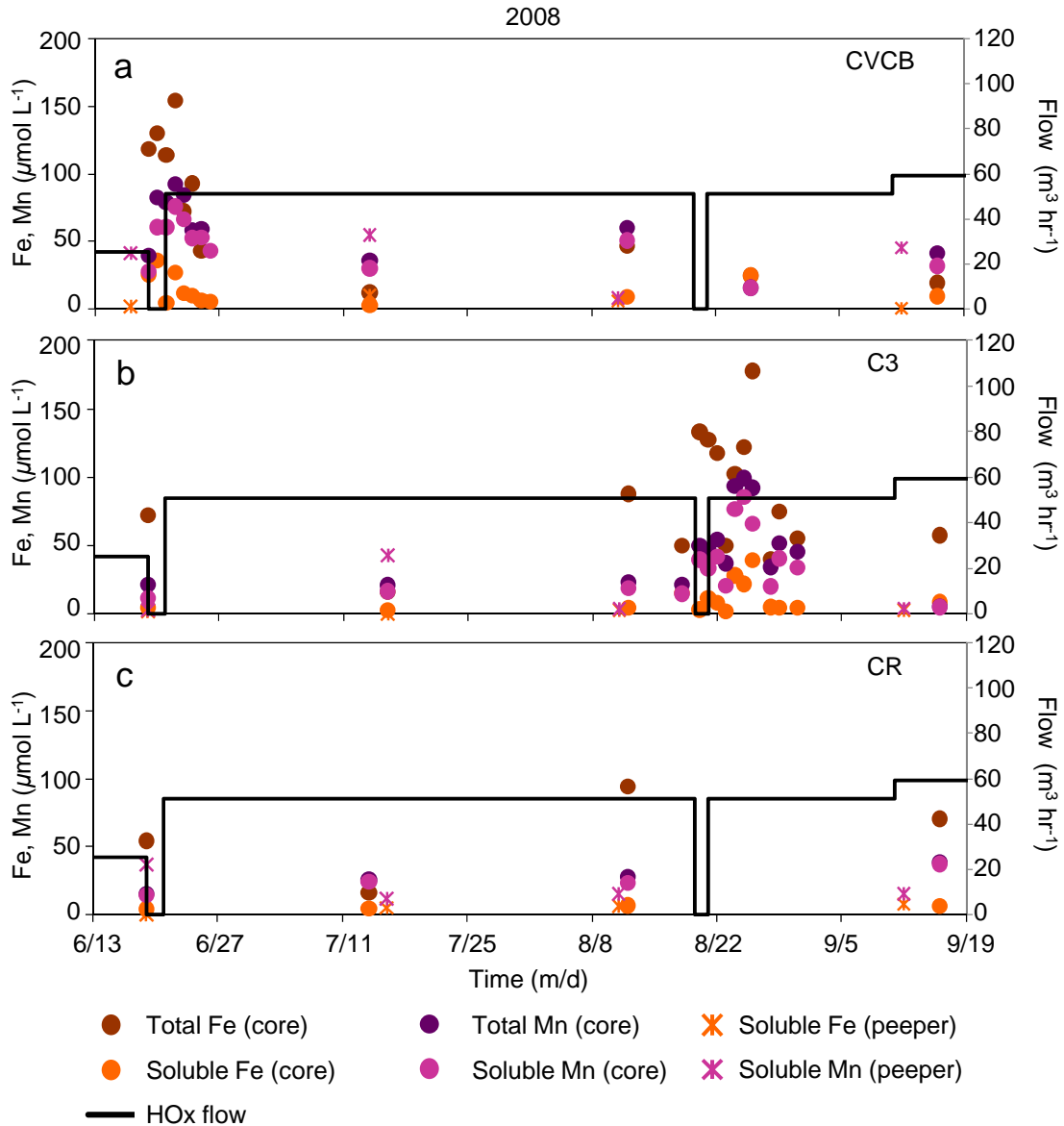


Figure B.3. Total and soluble Fe and Mn data obtained from near-sediment core water samples collected throughout 2008 HOx operations. Samples were collected near the HOx (site CVCB; a) and mid-reservoir at sites C3 (b) and C2 (c). Corresponding peeper data (for profile depth 5 cm above the SWI) are included to verify core water sample data. As discussed in Ch. 4, an experimental campaign focused specifically on site CVCB was performed in June 2008, hence the increased number of data points during this period in (a). A similar campaign was performed at C3 during August 2008 (b). Data characterizing the back-region of the reservoir (CR; Fig. 5.1) is provided in (c).

## **Appendix C – Microbial method procedures**

Appendix C.1 – Nucleic acid extraction

Appendix C.2 – DNA quantification with PicoGreen

Appendix C.3 – PCR program

## Appendix C.1 – Nucleic acid extraction

### Detailed protocol for DNA extraction

Lake Sediment version, Sept. 2007

By Helmut Bürgmann

Reference to Bürgmann et al. 2001, 2003

#### Reagents:

"CTAB+ Buffer" (Manuel Pesaro):

CTAB	0,2% (w/v)
Na-PO <sub>4</sub> -Buffer, pH 8,0	0,2M
NaCl	0,1M
EDTA	50mM
H <sub>2</sub> O, PCR grade, sterile, RNase free	
DTT (add fresh)	1mM

Substance	Amount for 500 ml	Comments
Na <sub>2</sub> HPO <sub>4</sub>	13.23 g	Phosphate Buffer, pH 8 200 mM
(oder Na <sub>2</sub> HPO <sub>4</sub> *2 H <sub>2</sub> O)	16.59 g )	
NaH <sub>2</sub> PO <sub>4</sub> * 2 H <sub>2</sub> O	1.06 g	
CTAB (Hexadodecyltrimethyl- ammonium bromide)	1 g	0.2%
DTT (1 M aq solution)	0.5 ml	from frozen stock
NaCl (keep a clean stock for molecular work)	2.92 g	0.1 M
Na-EDTA	9.31 g	50 mM

Sterilize by filtration (0,2 µm). Add DTT fresh, and use for no more than two weeks after adding DTT.

Store all buffers at 4°C. Dissolve precipitates prior to use.

## Appendix C.1 – Nucleic acid extraction

### **Phenol (pH 8.0)**

is prepared using RNase-free Tris-Buffer (pH 8). Available commercially, prepare as described by manufacturer. Check pH prior to use, and keep under a layer of buffer.

### **Chloroform-Isoamyl alcohol (CIA):**

Mix 1 part isoamylalcohol and 24 parts chloroform (puriss.). Prepare in baked or chloroform-rinsed volumetric cylinder (e.g. 240 ml chloroform, make to 250 ml with isoamylalcohol (3-methyl-1butanol). Store in baked glassware.

### **DEPC treated H<sub>2</sub>O:**

Autoclave H<sub>2</sub>O bidest. Add 0,1% (v/v) DEPC. Incubate 12h at 37°C. Autoclave again.

### **PEG precipitation solution (PEG):**

<i>PEG 6000</i>	<i>20% (w/v)</i>
<i>NaCl</i>	<i>2,5M</i>

*H<sub>2</sub>O, PCR grade, sterile*

Treat with 0,1% DEPC before autoclaving

**Ethanol 70%**, from 36 ml EtOH puriss. Made to 50 ml with 0,1% DEPC treated or certified water. Mix in sterile Falcon Tube

**Isopropanol (puriss.)**, in baked glassware

**Glass beads** (0,10-0,11mm diameter), bake at 200°C for 12 h.

**Ice**

### ***Material:***

Fastprep Machine

Eppendorf tubes, 2 / 1,5 / 0,5 ml

Pipettes for 1ml, 200µl, 100µl, with filter tips.

Suction device for removing supernatants.

Microcentrifuge

Hood

**Protocol:**

*General: Work under a hood (phenol and chloroform are poisonous). If possible keep centrifuge in the hood too (it generates a lot of phenol-aerosol). Wear gloves to protect tubes from RNase from your skin. Powder-free gloves are best. Use fresh, autoclaved plasticware, and use gloves to handle it. If using glassware sterilize and decontaminate it before use (Rinse with Chloroform and bake at 250°C for 12h). Wipe workplace with 70% Ethanol and 3% H<sub>2</sub>O<sub>2</sub> for decontamination. Be careful to keep reagents RNase free (use DEPC where possible (but not with TRIS!)), keep sterile, store in fridge, prepare small volumes). Work as quick and as cool as possible to minimize RNase activity. Calculate 5-7h to complete protocol.*

**Nucleic acid extraction:**

- Remove Phenol and CTAB+ buffer from fridge and bring to room temperature. Dissolve all precipitates in buffer. Add DTT, if using fresh buffer.
- Weigh 0.75g glass beads into 2 ml Eppendorf tubes.
- Weigh 0.5g wet sediment into the tubes (In order to calculate DNA or RNA content, determine water content for separate soil sample).
- Add 1.25 ml cold CTAB+ buffer (pipette 2 x 625 µl).
- In dismembrator, process 3 x 80 s at 3000rpm. Cool on ice for 1 min between beatings. Centrifuge for 5 min at 13200 rpm (max speed).
- Transfer supernatant (ca. 1000 µl) to new 2 ml tube . Add 400µl Phenol (pH 8) and 400 µl CIA. Vortex for 15 s (or until suspension forms). Centrifuge 5 min at max speed (13200 rpm), 25°C.
- Transfer supernatant to fresh 2 ml tube (ca. 950 µl). Do not touch interface with pipette tip.
- Add 800 µl CIA. Vortex for 20 s, centrifuge 5 min at 13200 rpm, 25°C.
- Transfer 900 µl of supernatant to fresh 2 ml tube (Store at –80°C if necessary). Add one volume (ca. 900 µl) PEG. Mix by inverting. Incubate for 1h at 37°C. Centrifuge 30 min at max speed (13200 rpm) at 25°C. Pellet should be light to dark brown in color.
- Pre-cool centrifuge to 4°C.
- Remove supernatant with aspirator.
- Add 500 µl ice-cold Ethanol swirl gently to wash pellet (Store at –80°C if necessary). Centrifuge 5 min at max speed (13200 rpm). Remove supernatant with aspirator.
- Let pellet dry on air for a few minutes (or Speedvac), protect from dust by covering loosely with aluminum foil or placing in laminar flow chamber. As soon as Ethanol is no longer visible, add 50 µl TE. Vortex well to dissolve. Keep on ice, store at -20°C (-80°C if work with RNA is planned).

## Appendix C.2 – DNA quantification with PicoGreen

### DNA quantitation with PicoGreen

Bürgmann Lab 2007

*Based on Quant-it dsDNA quantitation kit from Invitrogen (P7589)*

*(Difference to kit protocol: We dilute the sample, and we use pre-diluted standards instead of diluting standards on the plate)*

#### Material:

Quant-it dsDNA quantitation kit (PicoGreen, lambda DNA stock (100 ug / ml), 20x TE)

Sterile (Nanopur, autoclaved) H<sub>2</sub>O

Black 96 well plates

Plate reader (Synergy HT) and software (KC4)

PCR workbench (Work in sterile bench while loading 96 well plate)

#### Protocol:

1. Take kit from fridge. Allow PicoGreen to thaw completely. Keep picogreen away from light.
2. Use PicoGreen calculation sheet to calculate Master Mix and needed standards.
  - 1 µl sample recommended for extracts high in humi acids
  - 5 µl or higher for clean but low concentration samples
  - For easy pipetting and calculation, use same volume for standards and samples.
3. Set up your plate in KC4 software. Load picogreen method. Setup plate layout. Save method with date in your folder. Print out plate layout at the end.
4. Prepare standards:
  - quantify stock solution on nanodrop
  - prepare dilution series as calculated
  - keep standards on ice
5. Prepare the Master Mix (required amount as calculated)
6. Distribute Master Mix on plate (refer to plate layout) using pipette, stepper or multichannel pipette as appropriate (volume according to calculation sheet, usually 399 or 395 µl).
7. Add sample (per sheet, usually 1 or 5 µl) to each well (refer to and mark plate layout you printed to keep track of samples, if necessary).
8. Start read in KC4 software, fill out the info window, load your plate.
9. After read has finished, print and save your results. Remove plate and wash it.
10. Store Kit and standard stock at 4°C.

## Appendix C.3 – PCR program

PCR general protocol:

- 1) Take mix supplies out of fridge – thaw.
- 2) Make dilutions of samples (200 uL tubes).
- 3) Make reaction mix (H<sub>2</sub>O, PCR buffer, Mg CL<sub>2</sub>, primer forward, primer reverse, dNTP, BSA). Gently centrifuge.
- 4) Add 44 uL of mix (step 2) and 1 uL of sample to new small tube: PCR sample.
- 5) Prepare positive (e.coli) and negative (water) samples (1 uL each) with 44 uL reaction mix for positive and negative controls.
- 6) Remove Taq from freezer. Gently centrifuge. Prepare H<sub>2</sub>O and buffer for Taq mix. Add 5 uL Taq **last** to H<sub>2</sub>O/buffer mix. Mix by flicking.
- 7) Put tubes in PCR machine. (DNA samples, +/- controls, and 100 bp marker at beginning and end)
- 8) Add 5 uL of Taq **mix** to each tube.
- 9) Start PCR (~ runs about 3-4 hours).
- 10) Run PCR product samples on agarose gels.

## Appendix C.3 – PCR program

<b>Date</b>	4/23/2008		<b>Program</b>	27F_1492R		<b>Nr. Cycles</b>	
<b>PCR</b>	Universal				<b>T (°C)</b>	<b>Time [mm:ss]</b>	
<b>Forward Primer</b>	27f						
<b>Reverse Primer</b>	1492r						
<b>Expected size of Product:</b>	1465						
<b>Total Reaction Volume</b>	50 µl						
<b>Amount of DNA sample</b>	1 µl						
<b>Number of reactions</b>	11 samples and controls						
<b>Summe</b>							
<b>dNTP stock</b>	100 mM					You need:	
<b>Total dNTP needed</b>	Prepare: 10 µl of each dNTP stock solution + 60 µl H2O (PCR grade)					5.2 µl minimum	dNTP
<b>Given final concentrations:</b>							
	<b>Stock solution</b>	<b>Final Concentration</b>	<b>Per reaction</b>	<b>Prepare for all:</b>			
<b>Reaction mix Volume</b>			50.00 µl				
<b>H2O</b>			32.15 µl	417.95 µl	H2O		
<b>PCR Buffer</b>	10 times	1 times	5.00 µl	65.00 µl	PCR Buffer		
<b>Mg Cl2</b>	25 mM	3 mM	6.00 µl	78.00 µl	Mg Cl2		
<b>Primer forward</b>	100 µM (each)	0.2 µM	0.10 µl	1.30 µl	Primer forward		
<b>Primer reverse</b>	100 µM (each)	0.2 µM	0.10 µl	1.30 µl	Primer reverse		
<b>dNTP</b>	25 mM (each)	0.2 mM	0.40 µl	5.20 µl	dNTP		
<b>BSA</b>	10 mg/ml	1 mg/ml	5.00 µl	65.00 µl	BSA		
<b>Taq</b>	5 u/µl	0.025 u/µl	0.25 µl	3.25 µl	Taq		
<b>Summe</b>			49.00 µl/tube	637.00 µl			
<b>DNA sample</b>			1 µl/tube				
<b>Summe</b>			50.00 µl/tube				
<b>Given Volumes per Reaction:</b>							
	<b>Stock solution</b>	<b>Per Reaction</b>	<b>Final Concentration</b>	<b>Prepare for all:</b>			
<b>Reaction mix Volume</b>		50 µl					
<b>H2O</b>		32.15 µl		417.95 µl	H2O		
<b>PCR Buffer</b>	10 times	5.00 µl	1.00 times	65.00 µl	PCR Buffer		
<b>Mg Cl2</b>	25 mM	6.00 µl	3.00 mM	78.00 µl	Mg Cl2		
<b>Primer forward</b>	100 µM (each)	0.10 µl	0.20 µM (each)	1.30 µl	Primer forward		
<b>Primer reverse</b>	100 µM (each)	0.10 µl	0.20 µM (each)	1.30 µl	Primer reverse		
<b>dNTP</b>	25 mM (each)	0.40 µl	0.20 mM (each)	5.20 µl	dNTP		
<b>BSA</b>	10 mg/ml	5.00 µl	1.00 mg/ml	65.00 µl	BSA		
<b>Taq</b>	5 u/µl	0.25 µl	0.025 u/µl	3.25 µl	Taq		
<b>Summe</b>		49.00 µl mix / tube		637.00 µl			
<b>DNA Sample</b>		1 µl sample / tube					
<b>Summe</b>		50.00 µl/tube					
<b>Final volume correct?</b>		50.00 µl					

## **Appendix D – Copyright permission**

Official permission from the journal *Limnology & Oceanography* to reproduce material in Chapter 2 of this dissertation. Copyright permission was obtained for this chapter as this work was published prior to submission of this dissertation document to Virginia Tech.

Delete Reply Reply All Forward Redirect View Source Move to: This message to Message 3 of 1248

Date: Wed, 24 Mar 2010 10:29:15 -0500  
From: Jo Davis <jdavis@sgmeet.com>  
To: lebryan1@vt.edu  
Subject: Fwd: ASLO Copyright Permission

2 text/html 3.48 KB [unnamed](#)

Dear Ms. Bryant,

On behalf of the American Society of Limnology & Oceanography, you can use the text as well as the figure.

Sincerely,

Mrs. Jo Davis  
ASLO Business Office  
c/o The Schneider Group

Date: Wed, 24 Mar 2010 09:13:32 -0500  
To: lebryan1@vt.edu  
From: Jo Davis <jdavis@sgmeet.com>  
Subject: ASLO Copyright Permission

To: Ms. Lee D. Bryant,

On behalf of the American Society of Limnology and Oceanography, we are happy to grant permission to use the figures from Limnology & Oceanography per your application below.

When reproducing the article/figure(s), please cite according to the references that follow:

All copyrighted works, whether displayed electronically or in print, should be properly acknowledged as follows:

"Copyright (Year) by the American Society of Limnology and Oceanography, Inc."

Once permission is granted to use an article or any part thereof of a work from L&O, the full citation must include:

1. Name(s) of the author(s);
2. Journal title (Limnology & Oceanography or L&O)
3. Publication date
4. Volume number
5. Issue number
6. Chapter or article name

7. Pages on which the articles, data, and/ or figure(s) appear

For your records, the American Society of Limnology and Oceanography is a nonprofit organization. (Taxpayer I.D. Number: 38-1710020)

If you have additional requests or have any questions in regard to this request, you can contact me directly via e-mail at [jdavis@sgmeet.com](mailto:jdavis@sgmeet.com).

Sincerely,

Jo Davis  
ASLO Business Office

Will the copyrighted material appear in a for-profit publication?

no

Will the copyrighted material appear in a not-for-profit publication?    yes

Proposed Publication Date: April 2010

**REQUESTOR INFORMATION**

Requestor: Ms. Lee D. Bryant

Contact's Name (if different):

Institution: Virginia Tech

Department: Civil and Environmental Engineering

Mailing Address:

418 Durham Hall

Blacksburg, Virginia 24061

USA

Telephone: 865-803-7716

Fax: 540-231-7916

Email: [lebryan1@vt.edu](mailto:lebryan1@vt.edu)

**INTENDED USE**

Publication in which material will appear:

Lee Bryant's doctoral dissertation entitled "Dynamic forcing of oxygen, iron, and manganese fluxes at the sediment-water interface in lakes and reservoirs"

Publisher: Virginia Tech via UMI Company

**MATERIAL TO BE USED**

Author(s) Name(s): Bryant, L. D., C. Lorrai, D. F. McGinnis, A. Brand, A. Wuest, and J. C. Little

Journal Title: Limnology and Oceanography

Publication Date: 2010

Volume: 55

Issue: 2

Chapter, article or figure name or title: Variable sediment oxygen uptake in response to dynamic forcing

Pages on which articles, data or figures appear: 950-964

Special notes: